



This work is protected by copyright and other intellectual property rights and duplication or sale of all or part is not permitted, except that material may be duplicated by you for research, private study, criticism/review or educational purposes. Electronic or print copies are for your own personal, non-commercial use and shall not be passed to any other individual. No quotation may be published without proper acknowledgement. For any other use, or to quote extensively from the work, permission must be obtained from the copyright holder/s.

AUGER ELECTRON AND CHARACTERISTIC ENERGY

LOSS SPECTROSCOPY OF SELECTED METALS,

SEMI-METALS AND COMPOUNDS

A thesis presented for the degree of Doctor of Philosophy  
at the University of Keele

by

SURJIT SINGH, B.Sc., MSc., A.R.C.S.

Physics Department,  
University of Keele,  
Staffordshire.

September, 1976.

**BEST COPY AVAILABLE.**

**VARIABLE PRINT QUALITY**

## CONTENTS

	Page
ACKNOWLEDGEMENTS	
ABSTRACT	
CHAPTER 1 INTRODUCTION	1
1.1 Surface Science	4
1.2 Experimental Techniques of Surface Science	7
CHAPTER 2 AUGER ELECTRON SPECTROSCOPY	13
2.1 Introduction	13
2.2 The Auger Process	14
2.3 Auger Electron Spectroscopy	15
2.4 Excitation of Auger Electrons	16
2.4.1 Electron Induced Ionization	16
2.4.2 X-ray Induced Ionization	17
2.4.3 Proton and Ion induced Ionization	17
2.5 Energy of Auger Electrons	18
2.6 Intensity of Auger Transitions	22
2.6.1 Coster Kronig Transitions	22
2.6.2 Effect of Primary Electron Energy	23
2.6.3 The Backscattering Effect	23
2.6.4 Dependence of the Auger Yield on Angle of Incidence	24
2.7 Instrumentation in A.E.S.	25
2.8 Quantitative A.E.S.	27
2.9 Chemical Effects in A.E.S.	29
2.10 Electron Beam Artifacts	32
2.11 Interatomic Auger Transitions	32
2.12 Uses of A.E.S.	33



	Page
4.4.2 The Argon Ion Source	59
4.4.3 Cold Cathode Inert Gas Sputtering	61
4.4.4 Thin Film Evaporation	62
4.5 Design of a Cylindrical Mirror Analyser	62
4.5.1 Introduction	62
4.5.2 Theory of the CMA	63
4.5.3 Design	65
4.6 Construction of the CMA	67
4.6.1 Assembly	68
4.6.2 Magnetic Shielding	70
4.7 Operation of the CMA	70
4.7.1 Detection Circuit for $\frac{dN}{dE}$	72
4.7.2 Detection Circuit for $\frac{d^2N}{dE^2}$	73
4.7.3 Detection Circuit for $N(E)$	74
4.8 Experimental Properties of the CMA	76
4.8.1 Resolution	76
4.8.2 Effect of the Amplitude of Modulation	78
4.9 Comparison with other Analysers	80
4.10 Summary and General Comments	80
CHAPTER 5 AUGER ELECTRON SPECTROSCOPY OF STAINLESS STEEL (EN58E)	 83
5.1 Introduction	83
5.2 Experimental	83
5.3 Results and Discussion	84
5.4 Summary	88
CHAPTER 6 THE AUGER AND CHARACTERISTIC ENERGY LOSS SPECTROSCOPY OF GOLD	 89

	Page
6.1 Auger Spectroscopy of Gold	89
6.1.1 Introduction	89
6.1.2 Experimental	89
6.1.3 Results and Discussion	90
6.2 Energy Loss Spectroscopy of Gold	93
6.2.1 Introduction	93
6.2.2 Experimental	93
6.2.3 Results and Discussion	94
6.3 Summary	96
 CHAPTER 7	
MOLYBDENUM	97
7.1 Introduction	97
7.2 Auger Spectroscopy of Molybdenum	98
7.2.1 Experimental	98
7.2.2 Results and Discussion	98
7.3 The Effect of Contaminants on the Auger Spectra of Mo	101
7.3.1 Carbon Contamination	101
7.3.2 Sulphur Contamination	103
7.3.3 Oxygen Contamination	104
7.4 Electron Beam Effects	104
7.5 Adsorption of Oxygen on to Polycrystalline Molybdenum	106
7.5.1 Introduction	106
7.5.2 Experimental	106
7.5.3 Results	107
7.5.4 The Initial Sticking Coefficient	108
7.6 Energy Loss Spectroscopy of Molybdenum	111
7.6.1 Introduction	111
7.6.2 Experimental	111

	Page
7.6.3 Results and Discussion	111
7.7 Summary	115
CHAPTER 8 AUGER ELECTRON AND ENERGY LOSS SPECTROSCOPY OF ANTIMONY, ANTIMONY OXIDE AND ANTIMONY SULPHIDE	117
8.1 Antimony	117
8.1.1 Introduction	117
8.1.2 Experimental	118
8.1.3 Results and Discussion of the Auger Spectra	119
8.1.4 Results and Discussion of the Energy Loss Spectra	121
8.1.5 Adsorption of Oxygen on to the Sb (100) Face	124
8.2 Antimony Oxide ( $Sb_2O_3$ )	125
8.2.1 Introduction	125
8.2.2 Experimental	125
8.2.3 Results and Discussion of the Auger Spectra of $Sb_2O_3$	126
8.2.4 Electron Beam Effects in the Auger Spectra of $Sb_2O_3$	128
8.2.5 Results and Discussion of the Energy Loss Spectra	129
8.2.6 Electron Beam Effects in the Loss Spectra	132
8.3 Antimony Sulphide	133
8.3.1 Introduction	133
8.3.2 Experimental	133
8.3.3 Results and Discussion of the Auger Spectra from $Sb_2S_3$	134
8.3.4 Electron Beam Effects	135
8.3.5 Results and Discussion of the Energy Losses of $Sb_2S_3$	137
8.4 Summary	139

	Page	
CHAPTER 9	AUGER ELECTRON AND ENERGY LOSS SPECTROSCOPY	
	OF BISMUTH AND BISMUTH OXIDE	140
9.1	Bismuth	140
	9.1.1 Introduction	140
	9.1.2 Experimental	141
	9.1.3 Results and Discussion of the Auger Spectrum of Bismuth	142
	9.1.4 Results and Discussion of the Energy Losses of Bismuth	143
9.2	Bismuth Oxide	145
	9.2.1 Experimental	145
	9.2.2 Results and Discussion of the Auger Spectrum of Bismuth Oxide	146
	9.2.3 Results and Discussion of the Energy Losses of Bismuth Oxide	148
9.3	Summary	150
CHAPTER 10	GENERAL CONCLUSIONS AND SUGGESTIONS FOR FURTHER WORK	151
REFERENCES		

## ACKNOWLEDGEMENTS

The author wishes to express his gratitude to:

Professor D. J. E. Ingram and Professor W. Fuller for the use of the laboratory facilities of the Physics Department.

The University of Keele for the appointment of Demonstrator.

Dr. E. B. Pattinson for his supervision, encouragement and guidance throughout the course of this work.

Dr. M. Suleman, Dr. B. Wright and Mr. W. R. C. Stewart and other colleagues in the Physics Department for useful suggestions and discussions.

The technical staff of the department and in particular Mr. F. Rowerth, Mr. G. Dudley of the workshop, Mr. W. Brearley, and members of the electronics workshop for their helpful assistance throughout this work.

Mr. M. Daniels for his photographic work.

Judy Gill for her efficient typing of this thesis.

My parents for their encouragement.

## ABSTRACT

The topics of interest in surface science are introduced together with some of the experimental techniques used in their investigation. In particular the techniques of Auger Electron Spectroscopy (A.E.S.) and Characteristic Energy Loss Spectroscopy (C.E.L.S.) are outlined in detail with an appraisal of recent developments in these subjects.

The design and construction of an apparatus suitable for performing electron stimulated surface investigations is described. The apparatus incorporates a double pass cylindrical mirror type of energy analyser with a minimum operating resolution of 0.7%, suitable for AES and CELS. Additional features of the apparatus are in-situ target cleaning facilities and a pure gas admittance system. A suitable pumping arrangement to evacuate the apparatus to ultra high vacuum pressures ( $\sim 10^{-10}$  Torr.) is outlined as well as the electronic detection circuitry needed to obtain an output proportional to  $N(E)$ ,  $N'(E)$  or  $N''(E)$  of the secondary electron emission spectrum.

The apparatus constructed was used to perform experiments on a number of selected materials. Detailed Auger spectra of Au, Mo, Sb,  $Sb_2O_3$ ,  $Sb_2S_3$ , Bi and  $Bi_2O_3$  are presented together with measurements of their characteristic energy losses. Transitions are assigned to the observed Auger peaks and the characteristic losses are interpreted, by comparison with optical properties, in terms of volume plasmons, surface plasmons and interband transitions. The Auger spectra of an EN58E stainless steel surface is also presented.

A number of interesting results emerged from the experiments performed. A previously undetected surface plasmon oscillation on a molybdenum surface was identified and the strong bismuth Auger peak

( $\sim 100$  eV) was found to contain considerable fine structure. The adsorption of pure oxygen on polycrystalline molybdenum investigation showed that the initial sticking coefficient increased by a factor of about one hundred when sulphur contamination was introduced on to the clean Mo surface.

Chemical shifts of the Sb MNN Auger peaks from antimony oxide are reported. The energy shift is interpreted as partially due to a change in the binding energy of the core level electrons and partially due to a decrease ( $\sim 5$  eV) in the extra atomic relaxation energy as a consequence of the chemical combination.

Considerable electron beam induced effects on molybdenum, antimony oxide and antimony sulphide are reported. The thesis concludes with suggestions for future studies.

## CHAPTER 1

### INTRODUCTION

It has been known for some time that when a solid surface is bombarded with radiation it may emit electrons. If the incident radiation is in the form of photons, the emitted electrons are termed photoelectrons and when it consists of electrons or other particles the resulting electrons are called the secondary electrons. Basically the incident particles dissipate their energy by undergoing many interactions and excitations within the solid resulting in the emission of electrons and other particles. In particular the emitted electrons can contain useful information about the surface such as the electronic structure, the species of atoms present and the chemical environment of these atoms.

We are concerned in this thesis with the study of selected material surfaces by stimulating the emission of electrons with incident electrons of energy up to 3 Kev. Fig. 1.1 shows schematically the secondary electron emission (SEE) spectrum excited, by a monoenergetic primary electron beam of energy  $E_p$ . Most of the secondary electrons emitted are due to random processes within the solid (the true secondaries) but two features are present in the SEE spectrum which make it important for surface investigations. Firstly superimposed on the large SEE background are several small peaks identified as being due to the excitation of Auger processes, from these the atomic species present on the surface can be identified. The characteristic losses observed just below the elastically reflected primaries are the other important feature of the SEE spectrum and from the losses important information about the loosely bound electrons of the solid can be deduced. These

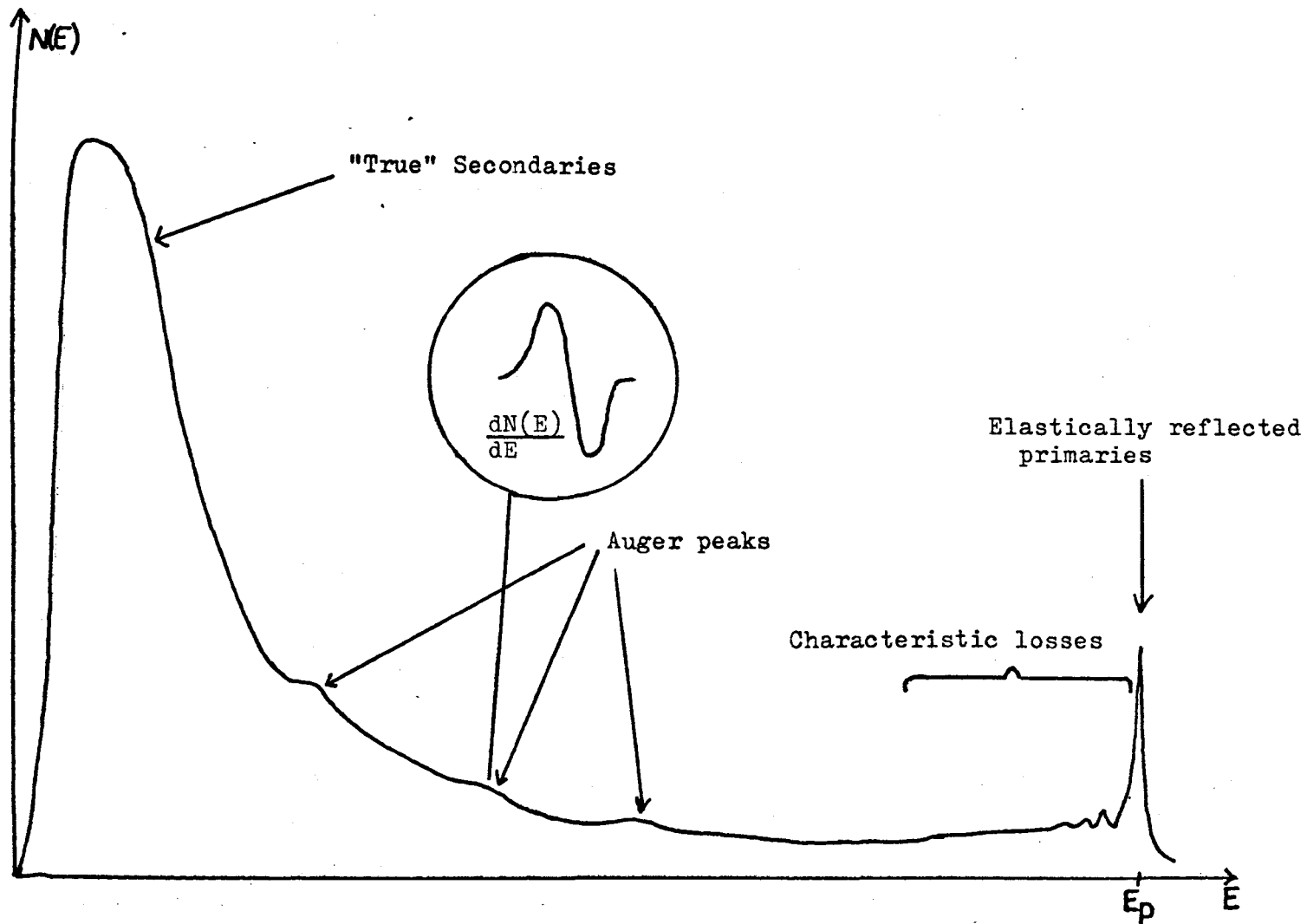


Fig.1-1. The secondary electron emission (SEE) spectrum excited by primary electrons of energy  $E_p$ .

two properties of the SEE spectrum have been fairly recently developed into the surface sensitive techniques of Auger Electron Spectroscopy (A.E.S.) and Characteristic Energy Loss Spectroscopy (C.E.L.S.) and both are of considerable current research interest.

Characteristic energy losses in solids have been observed since the 1930's whereas the Auger process has only become a useful tool for surface analysis since 1968. A.E.S. is particularly important because the atomic species present on a surface can be identified hence a "clean" surface characterised for other measurements to be performed. There has been considerable work on the study of elements using these two techniques independently and since 1968 a number of investigations have been reported in which the two spectroscopies have been used in conjunction. The presence of surface contaminants can influence the characteristic losses observed so that it is important to record loss measurements from an A.E.S. characterised surface.

The subject matter of this thesis is intended as a contribution to the surface study of selected materials. We aim particularly at obtaining detailed Auger and energy loss spectra from pure elements and then proceeding to observe the changes produced upon chemical combination. To realise these aims, a suitable high resolution, high sensitivity apparatus was designed and constructed as a part of the research programme.

Surface science is a multi-disciplinary subject which has undergone rapid development in the past few years. In the following sections of this chapter some of the phenomenon occurring at surfaces and the techniques used in their investigation are briefly described. In Chapter Two Auger Electron Spectroscopy is reviewed with Chapter Three devoted to Characteristic Energy Loss Spectroscopy, particular emphasis being placed on the more recent developments in these

techniques. Chapter Four describes the design, construction and operation of a suitable apparatus for A.E.S. and C.E.L.S. The remaining chapters are devoted to presenting the results from the solid surfaces: stainless steel, gold, molybdenum, antimony, its oxide and sulphide, and finally bismuth and its oxide. The final chapter is concerned with general conclusions and suggestions for further work.

\* \*

## 1.1 Surface Science

The properties of a bulk material are determined by the number, relative positions and types of atoms it contains. Some properties can be related in a straight forward manner to the chemical composition and to the crystal structure by using the band theory of solids, for example the division of crystalline solids into insulators, semi-conductors and conductors. This century has seen an enormous progress in the understanding of the bulk properties of solids so that concentration has begun to be focussed on to understanding the surface properties. The subject of surface science is the study of the chemical compositions and atomic arrangements at the surfaces of solids and the theory and observation of their mechanical, electronic and chemical properties. As in the study of bulk solids the ultimate aim is to understand the relationship between the properties, the composition and the structure of surfaces.

The surface is normally thought of as the top few atomic layers of a solid. Now bulk properties are determined by a three-dimensional arrangement of atoms whereas at a surface there is only a two-dimensional arrangement with the additional influence of the interface. The measurement and understanding of phenomena at a surface is one of great scientific interest and enormous technological significance, however it is only since the improvement in vacuum technology has allowed ultra high vacuum pressures to be obtained as a matter of routine together with the development of A.E.S., L.E.E.D. (Low Energy Electron Diffraction), and other related techniques to characterise a surface that an explosive growth in surface science has occurred.

The variety of processes occurring at a surface is so large and involves such a wide spread of academic disciplines that only a few of

the important areas of research can be mentioned in this introduction:-

(i) Surface States. These are localised electron energy levels occurring at a crystal surface which may be explained as a consequence of the electron wave function matching which needs to occur at an interface<sup>1,2</sup>. The importance of surface states is in semi-conductor device technology since they strongly influence the characteristics of all planer devices, for instance in the field effect transistor the surface state density needs to be reduced for successful device operation.

(ii) Atomic and Molecular Events at the Solid-Gas Interface. The interaction of gases with a solid surface is of technological importance in catalysis, corrosion and oxidation. The two main types of interaction between the solid and gas, i.e. chemisorption or physisorption and the role of surface structure and chemical composition on rates of reaction are of importance but, as yet, not well understood.

(iii) Surface Thermodynamics and Kinetics. Supposing a surface is formed by cutting through a solid parallel to a chosen plane. The atoms of the exposed surface will undergo re-arrangement to an equilibrium, in accordance with the principles of thermodynamics, to minimise the surface energy. The phenomenon of nucleation at surfaces and the migration of atoms on a surface are important in crystal growth and the preparation of epitaxial thin films, as the growth generally involves the deposition of atoms upon single crystal surfaces under such conditions that the arriving atoms can diffuse about and build up a three-dimensional array. Thus the kinetics of adsorbed atoms on single crystal surfaces is fundamental to an understanding of crystal growth.

(iv) Electron Emission and Reflection. A beam of electrons or other energetic particles striking a solid surface can stimulate many interactions and excitations which may result in the emission of electrons. For a surface bombarded with a beam of electrons of energy  $E_p$  (the primary beam) the ejected electron distribution is referred to as the secondary electron emission (S.E.E.) spectrum, as shown in Fig. 1-1. As mentioned previously these ejected electrons can contain considerable useful information about the surface; in addition the secondary electron yield, which is the total number of electrons emitted per incident electron, also depends on the surface properties. The study of electron and photon stimulated emission from solids has led to and is still leading to the development of many, quite sophisticated, instruments for surface investigation.

Another area of interest is thermionic emission from surfaces. This is important in electronic devices and as a source of electrons in oscilloscope tubes and electron microscopes. The number of electrons emitted at a given temperature depends not only on the material but also on the presence of any chemical contaminants and the crystallographic orientation of the emitting face.

(v) Electrochemical Properties, Solid-Liquid Interface.

Many chemical reactions take place when an electrical current is passed through a solution. The electric current is usually passed by inserting two electrodes into a solution. The nature of the electrode material and its surface structure affect the transfer of charge between the solid and electrolyte and hence the nature and rate of any reaction occurring at the interface.

(vi) Atomic Structure of Crystal Surfaces. A number of important questions arise about the atomic structure of crystal surfaces. When a crystal is cleaved do the atoms in the top layer retain the same positions as in the bulk or does some rearrangement occur? What is the lattice parameter for surface atoms? On adsorption what kind of super lattice do the atoms form? Where do the adsorbed atoms sit relative to the substrate atoms? These are all fundamental questions of broad interest in surface science.

## 1.2 Experimental Techniques of Surface Science

A number of techniques have been developed over the past ten years to study surfaces. Two of the most fundamental questions asked about a surface are firstly what is its surface composition and secondly how are the surface atoms arranged? Consequently two of the most widely used techniques in surface science are low energy electron diffraction (L.E.E.D.) by means of which the surface structure can be determined and A.E.S. which can identify the species of atoms present. In Table 1-1 a number of other methods used in surface analysis are summarised on the basis of the incident and ejected particles. The techniques available commercially are underlined in this table.

Each method of investigation provides different information about a surface and the applicability of the various techniques for determining the different physical properties, are summarised in Table 1-2. The usefulness of a technique will depend on the particular property of interest and the material to be investigated, generally it is best to use several techniques in conjunction. It

TABLE 1-1. Methods of Surface Analysis

Incident Particle	Emergent Particle		
	XR	e <sup>-</sup>	IONS
UV	-	<u>UPS</u>	(PD)
XR	<u>(XRF)</u>	<u>XPS</u>	-
e <sup>-</sup>	APS	<u>AES</u> , IS	(ED)
IONS	IEX	INS	<u>ISS</u> , <u>SIMS</u>

- UPS - Ultraviolet Photoelectron Spectroscopy
- PD - Photodesorption
- XRF - X-ray Fluorescence
- XPS - X-ray Photoelectron Spectroscopy
- APS - Appearance Potential Spectroscopy
- AES - Auger Electron Spectroscopy
- IS - Ionisation Spectroscopy
- ED - Electron Desorption
- IEX - Ion Excited X-rays
- INS - Ion Neutralisation Spectroscopy
- ISS - Ion Scattering Spectroscopy
- SIMS - Secondary Ion Mass Spectroscopy

TABLE 1-2. Commonly used techniques for measuring the chemical, geometric and electronic properties of surfaces in ultra high vacuum

<u>Physical Property</u>	<u>Tip Geometry</u>	<u>Plane Geometry</u>
Atomic identity of surface species	Atom probe	A.E.S., X.P.S., I.S.S., S.I.M.S.
Atomic geometry of surface species	F.I.M.	L.E.E.D., S.E.M. R.H.E.E.D.
Surface diffusion	F.I.M.	L.E.E.D.
Surface electronic excitation spectra and valence band spectra	F.E.M. with electron energy distribution	U.P.S., X.P.S., I.N.S., A.P.S., C.E.L.S., A.E.S.

must be stressed that the methods of investigation mentioned in Tables 1-1 and 1-2 are normally used in an ultra high vacuum environment.

Tables 1-3 and 1-4 summarise the properties of the incident and emergent particles of the various techniques and Table 1-5 displays the volume of material analysed in a typical application of a technique. Some spectrosopes are more sensitive than others and Table 1-6 presents figures for the smallest concentration of a typical element which can be detected by a particular technique. These tables are based on a series of lectures the author attended at an S.R.C. summer school on surface science<sup>3</sup>.

We now proceed to give brief descriptions of a few of the important techniques used in surface science.

(i) LEED. (Low Energy Electron Diffraction). This is used to study the structure of surfaces and the structural changes produced during a surface reaction. The electrons are normally incident on a crystal surface, and are only of sufficient energy ( $\sim 500$  eV) to penetrate the first few atomic layers. About 1% of the incident electrons undergo elastic collisions with the surface atoms (the elastic peak in Fig. 1-1) and these give rise to the diffraction pattern. The inelastically scattered electrons are filtered out by a grid, the elastically reflected electrons penetrate this grid and are then accelerated to a high voltage ( $\sim 5$  KeV) and impinge upon a fluorescent screen to produce a light spot. The diffraction pattern obtained can be used to determine the surface structure.

(ii) RHEED. (Reflection High Energy Electron Diffraction). This technique is also used to study the structure of surfaces.

TABLE 1-3. Properties of the Incident Particles

<u>Technique</u>	<u>Particle</u>	<u>Energy</u>	<u>Incident Flux</u>
UPS	Photons	HeI : 21.2 eV HeII : 40.8 eV NeI : 16.8 eV NeII : 26.9 eV	
XPS	Photons	AlK $\alpha$ : 1486.6 eV MgK $\alpha$ : 1253.6 eV	Source power Variable 100- 1000 watts
APS	Electrons	0-1500 eV, variable during expt.	1-6 mA emission
AES	Electrons	2-5 keV, fixed	10 <sup>-3</sup> -10 $\mu$ A
IS	Electrons	0-1500 eV, variable	1-50 $\mu$ A
IEX	Ions, Ar <sup>+</sup> , N <sup>+</sup> , C <sup>+</sup> , protons, etc.	20-500 keV, fixed	10 <sup>-9</sup> -10 <sup>-6</sup> A/cm <sup>2</sup>
INS	Ions, He <sup>+</sup>	$\sim$ 5 eV, fixed	10 <sup>-9</sup> A
ISS	Ions, He <sup>+</sup> , Ar, Ne	2-40 keV, fixed	10 <sup>-8</sup> -10 <sup>-6</sup> A
SIMS	Ions, Ar <sup>+</sup>	1-4 keV, fixed	10 <sup>-9</sup> -10 <sup>-6</sup> A/cm <sup>2</sup>

TABLE 1-4. Properties of the Emergent Analysed Particles

<u>Technique</u>	<u>Particle</u>	<u>Energy</u>
UPS	Photoelectrons	0 - 20 eV
XPS	Photoelectrons and Auger electrons	0 - 1500 eV
APS	Soft X-ray photons (thresholds)	0 - 1500 eV
AES	Auger electrons	0 - 2000 eV
IS	Characteristic Loss	0 - 1000 eV
IEX	X-ray photons	0 - 10,000 eV
INS	Auger electrons (valence band)	0 - 20 eV
ISS	Elastically scattered ions	$E_I/E_P = 0 \rightarrow 1$
SIMS	Secondary Ions (positive or negative)	0 - 500 amu

TABLE 1-5. Volume of Analysed Region

<u>Technique</u>	<u>Depth of analysis, monolayers</u>	<u>Spatial resolution</u>
UPS	1 - 6	Large area
XPS	1 - 8	0.1 - 30 mm <sup>2</sup>
APS	1 - 5	Large area
AES	1 - 4	10 <sup>-8</sup> - 0.1 mm <sup>2</sup>
IS	1 - 6	10 <sup>-8</sup> - 0.1 mm <sup>2</sup>
IEX	1 - 50	1 - 6 mm <sup>2</sup>
INS	1 - 6	Large area
ISS	1	1 - 3 mm <sup>2</sup>
SIMS	1 - 2	3 mm <sup>2</sup>

TABLE 1-6. Elemental Sensitivities

<u>Technique</u>	<u>Ultimate Sensitivity monolayers</u>
UPS	0.5 ?
XPS	$\sim 10^{-3}$
APS	$\sim 10^{-2}$
AES	$\sim 10^{-3}$
IS	$\sim 10^{-2}$
IEX	$\sim 10^{-5}$
INS	$\sim 5 \times 10^{-2}$
ISS	$\sim 10^{-3}$
SIMS	$\sim 10^{-6}$

A high energy electron beam ( $\sim 40$  KeV) is incident on a specimen at grazing incidence so that it is reflected and diffracted only by the surface atomic layers. Surface imperfections normal to the surface can be investigated using this technique.

More recently SHEED (Scanning High Energy Electron Diffraction) has become commercially available from Vacuum Generators Ltd.<sup>4</sup>

(iii) A.E.S.<sup>5,6</sup> and C.E.L.S. A.E.S. is a widely used technique to identify the species of atoms present on a surface. These two techniques are more fully discussed in Chapters Three and Four. For the case of electron stimulated emission from surfaces (Fig. 1-1), the Auger peaks appear small in comparison with the large SEE background and they may be enhanced by differentiating the emission spectrum. The electron stimulated A.E.S. technique is easy to use and commercial apparatus of good sensitivity and resolution are available. The characteristic energy losses appear as structure just below the elastic peak in the SEE spectrum, whereas the losses are fixed in energy relative to the elastic peak, the Auger features are fixed in position relative to the energy zero.

(iv) XPS<sup>7</sup> and UPS (X-ray and Ultra Violet Photoelectron Spectroscopy). Photons of energy  $h\nu$  from a suitable source (Table 1-3) strike the specimen exciting several processes within the solid. A photo electron can be emitted with kinetic energy  $T = h\nu - E_B$  where  $E_B$  is the binding energy of the electron or an Auger transition may be excited. X-rays can also be emitted from depths up to  $20,000 \text{ \AA}^0$  (XRF in Table 1-1). Because of the higher energy of the X-ray photons XPS will probe electrons in the core levels of the atoms whereas UPS will only excite the valence band electrons of solids. By analysing the ejected

particles the binding energy of the electrons within the specimen can be deduced so that elemental identification, at least with XPS, is possible. Additionally chemical effects on the binding energy of the electrons can be studied. Photons cause less radiation damage than electrons and little or no surface charging of the specimen but the cross-section for photo-electron emission is small and intense sources cannot be obtained so that long counting times are needed for photo-electron spectroscopy, nevertheless XPS and UPS are powerful techniques for probing the electronic structure of solids.

(v) F.I.M. (Field Ion Microscopy). This technique was originated by Muller (1951)<sup>8</sup> and has the ability to detect directly the positions of atoms on a surface. The specimen is prepared in the form of a sharp tip to which a positive potential is applied so that a field of the order of  $5 \times 10^8$  volts  $\text{cm}^{-1}$  is present at the tip surface. Molecules of the imaging gas (usually He or Ne at a pressure of  $\sim 2 \times 10^{-3}$  Torr.) move towards the tip and collide with it losing an electron, to the tip, by quantum mechanical tunnelling. The resultant +ve ion is accelerated away from the tip in the large electric field and strikes a fluorescent screen. The spots of light can in the ultimate obtained resolution correspond to individual atoms on the tip. A Field Emission Microscope (F.E.M.) has also been developed. The field on the tip is now reversed and no imaging gas is used, electrons are then accelerated out of the surface by the very high local field towards the fluorescent screen. FIM and FEM have the disadvantage that a special tip geometry is required nevertheless the techniques are useful for studying the diffusion of atoms on a surface.

(vi) The Atom Probe. By combining a field ion microscope with an aperture and mass spectrometer Muller and Tsong (1969)<sup>9</sup> were able to detect and identify individual atoms. This is the ultimate in chemical sensitivity, but again the technique is limited to rather special geometries.

(vii) S.I.M.S. and I.S.S. In SIMS (Secondary Ion Mass Spectroscopy)<sup>10</sup> ions of a rare gas ( $\text{Ar}^+$ ,  $\text{Ne}^+$ ,  $\text{He}^+$ ) are formed into a beam and focused on to the surface of a solid. If the incident ions are sufficiently energetic ( $\sim 500 \text{ eV}$ ) they interact in a nearly classical manner with the atoms knocking them into the vacuum with billiard ball like collisions. Some of the ejected particles are ionized and can be detected by a mass spectrometer. The high sensitivities of quadrupole mass spectrometers and electrom multipliers means that  $10^{-6}$  of a monolayer can be detected by this method. However, the technique is surface destructive although the rate of removal of atoms can be controlled and in fact made quite small. Another similar spectroscopy is I.S.S. (Ion Scattering Spectroscopy) in which a primary beam of nearly mono-energetic ions is incident on the specimen surface. Some of these are scattered by the surface without neutralisation and the scattered current, in a particular direction, is measured as a function of energy with a suitable energy analyser and detector. The interesting feature of the scattered ion current is the occurrence of peaks corresponding to energy losses of the primary which are characteristic of the masses of the surface atoms. The collisions can be treated as two body elastic collisions and from the energy of the incident particle and its mass and the energy of the peak, the mass of the surface atom

can be computed and hence the atom identified.

(viii) A.P.S. (Appearance Potential Spectroscopy)<sup>10,11</sup>. A solid surface is bombarded with electrons and the total soft X-ray yield is detected as a function of the incident electron energy, (SXAPS). When the energy of the incident electrons is in excess of the binding energy of a core electron, there is the possibility of exciting this electron to an empty state above the Fermi level. It is normally assumed that the de-excitation process leads to a contribution to the observed X-ray intensity. The technique can be used to probe the empty states above the Fermi level.

(ix) I.N.S. (Ion Neutralisation Spectroscopy). This has been developed by Hagstrum<sup>12</sup>. Slow Helium or Neon ions are directed at clean metal surfaces, for an ion in contact with the metal surface an electron can tunnel through the potential barrier between the metal surface potential and the ionic potential and neutralise the ion. Its excess energy being used to eject another electron from the conduction band. The process is strongly analogous to an Auger transition. The interpretation of INS information is difficult and the data requires long recording times so that extremely low pressures of  $\sim 10^{-12}$  Torr are needed. So far the technique appears to be used only by Hagstrum and his co-workers.

In conclusion, we have briefly outlined why surfaces are studied and some of the techniques which may be used in their investigation. We now proceed to consider the important features of Auger Electron Spectroscopy in more detail as this technique is particularly relevant to the work presented in this thesis.

## CHAPTER 2

### AUGER ELECTRON SPECTROSCOPY

#### 2.1 Introduction

One of the most important surface characterization techniques is that of Auger Electron Spectroscopy which forms the subject matter of this chapter. Using this technique the atomic species in the first few atomic layers of a solid can be identified with sensitivities down to  $10^{-3}$  of a monolayer. AES is a surface sensitive technique because the inelastic mean free path of electrons in the energy range of Auger transitions (0 - 1000 eV) is only about  $10\text{\AA}$  so that the Auger signal originates predominantly from the top few atomic layers of a material. The small mean free path for electrons in this energy range is illustrated by Fig. 2-1 which displays the results for the attenuation length of electrons in a solid as a function of their energy. This diagram is reproduced from the review of attenuation lengths of electrons in solids published by Powell (1974)<sup>13</sup> and is a summary of the results obtained by a large number of workers on different materials.

In any investigation of a surface it is fundamentally important to know the species of atom present on a surface. Apart from the use of AES to determine surface atomic species there are current developments to obtain the concentration of a particular species from the intensity of the observed Auger signal and the chemical environment of the atoms from the energy and fine structure of the observed peaks.



## 2.2 The Auger Process

This is a radiationless relaxation process by means of which an excited atom loses energy. It was first discovered in 1925 by Pierre Auger<sup>14</sup> while studying particle tracks in a cloud chamber with white X-rays. He detected not only photoelectrons but also electrons of constant energy irrespective of the X-ray exciting energy. These electrons are called the Auger electrons.

The process can be explained by considering a neutral atom which is then excited above its ground state by the creation of a "hole" or vacancy within one of its inner shells. This can be most efficiently done by electron impact although ions and X-rays are also suitable. The created hole has a long lifetime in comparison with the characteristic time of ionization so that the de-excitation of the ion will be independent of the means or energy of excitation. The excited atom may decay towards the ground state by an electron from an outer level occupying the vacancy the difference in energy being emitted as a photon (X-ray fluorescence) or as an electron (the Auger effect), Fig. 2-2. In the Auger effect the atom is left in a doubly ionized state and may continue to de-excite by X-ray or Auger processes, in the absence of externally supplied electrons.

If the binding energy of the electron removed to create the vacancy is less than about 1 KeV, the probability of de-excitation by photon production has been shown by Burhop<sup>15</sup>, for initial ionization of K and L Shells, to be small and then the Auger process is the dominant mechanism of relaxation. The same is believed true for initial ionization of the other shells in the binding energy range of 0 - 1000 eV.

The Auger transitions are normally designated according to the

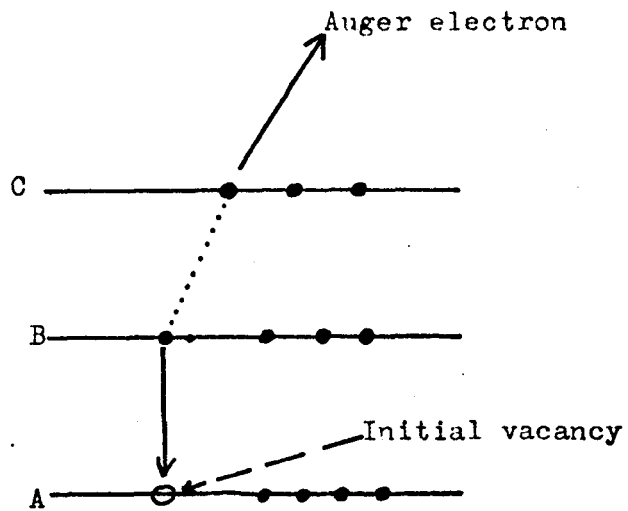


Fig 2-2. Schematic diagram of the Auger process involving the energy levels A, B and C.

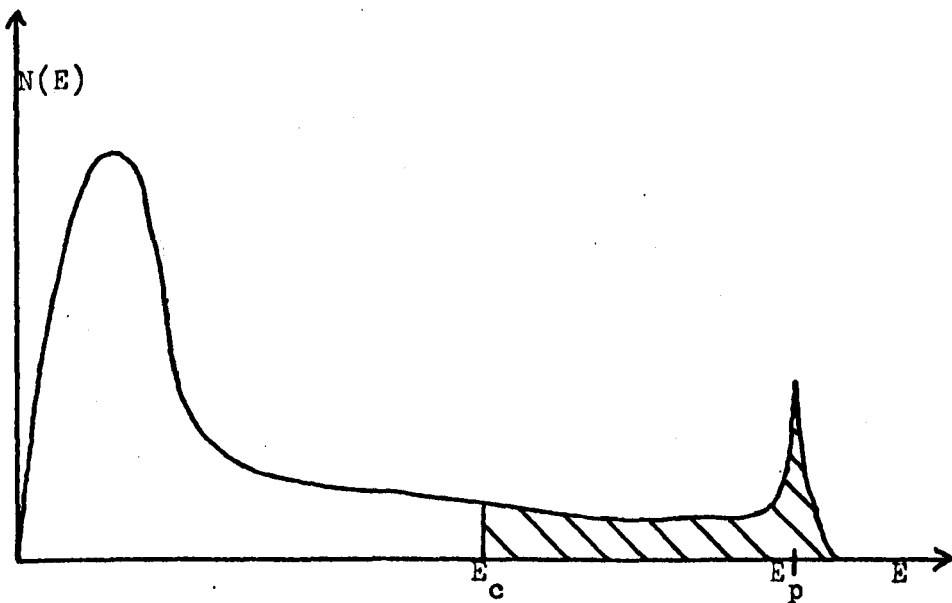


Fig 2-3. The backscattering contribution.

three levels participating in the process. This is done with the aid of the X-ray level notation: K - 1s, L<sub>1</sub> - 2s, L<sub>2</sub> - 2p<sub>1/2</sub>, L<sub>3</sub> - 2p<sub>3/2</sub>, M<sub>1</sub> - 3s, M<sub>2</sub> - 3p<sub>1/2</sub>, M<sub>3</sub> - 3p<sub>3/2</sub>, M<sub>4</sub> - 3d<sub>3/2</sub>, M<sub>5</sub> - 3d<sub>5/2</sub> etc. Thus if a hole is created in the K shell and an electron from the L<sub>1</sub> shell relaxes to fill this vacancy, giving the difference in energy to an electron in the L<sub>2</sub> shell, the transition is designated KL<sub>1</sub>L<sub>2</sub>. The Auger transition in Fig. 2-2 is an ABC transition.

### 2.3 Auger Electron Spectroscopy

The first person to point out the potential of the Auger process as a technique for surface analysis was Lander in 1953<sup>16</sup> who suggested that the technique provided a complement to X-ray emission for the determination of energy band densities of states. However Lander's work went virtually unnoticed (perhaps due to the lack of ultrahigh vacuum technology) until 1968 when Harris<sup>5,17</sup> made the most decisive advancement in the use of the Auger process by detecting the Auger peaks in the S.E.E. spectrum. The Auger peaks appear as small features on a large background in S.E.E., Harris overcame the lack of sensitivity by obtaining electronically the differential of the energy distribution, i.e.  $dN(E)/dE$ .

Harris used a 127° dispersive type of analyser not now so commonly used. The work of Weber and Peria<sup>18</sup> and Palmberg (1969)<sup>19</sup> demonstrated the use of existing retarding field type LEED equipment for obtaining Auger spectra from solid targets by electron excitation and the development of a cylindrical mirror analyser for AES by

Palmberg, Bohn and Tracy (1969)<sup>20</sup>, contributed to rapid developments in the investigation and application of Auger Electron Spectroscopy. More recently the subject has been reviewed by several authors<sup>21,22,6,23,24</sup>, and its application to metallurgy, thin films and materials analysis outlined.

## 2.4 Excitation of Auger Electrons

The initial vacancy in an inner atomic level can be created by several methods. We concentrate on electron induced ionization although other methods are also briefly discussed.

### 2.4.1 Electron Induced Ionization

This is the most common means of exciting Auger spectra because a primary electron beam of high intensity  $\sim 100\mu\text{A}$  in a spot size of  $5\mu\text{m}$  and with energies up to 5 keV can easily be obtained<sup>4</sup>. Such a beam can be readily focussed and deflected into position by electrostatic fields. The high intensities make possible measurements at good signal to noise ratios and therefore high recording speeds are possible for Auger spectra.

The cross-section for ionization by an electron is quite large  $\sim 10^{-19} \text{ cm}^2$  and remains constant over a wide range of primary electron energies of 2 - 6 times the binding energy of a core electron<sup>22</sup>.

The disadvantage of electron induced ionization is that the high currents can induce adsorption and desorption effects as well as the cracking of molecules on to the specimen surface. Electron induced ionization gives rise to a large secondary background upon which the Auger peaks are superimposed so that differentiation of the spectrum is

necessary to readily observe these features. An additional complication is that a large number of rediffused secondary electrons constitute a back scattered current which is capable of producing additional ionization so that the measured Auger current will not be simply related to the primary current and ionization cross-section.

#### 2.4.2 X-ray Induced Ionization

There has been some work on the excitation of Auger spectra by X-rays normally from Al K $\alpha$  or Mg K $\alpha$  sources. There are certain advantages in that the spectra can be recorded directly in the N(E) mode because the strong "rediffused" primary electron background is absent. Also the interaction of X-rays with the surface under bombardment is much weaker than in the electron excited case so less degradation is to be expected. The spectra recorded with X-ray excitation normally has many peaks due to core level excitations in addition to the Auger peaks, this can be an advantage as core level binding energies participating in the Auger process can be determined simultaneously with the Auger transition energy.

The X-ray excitation method has the disadvantage that long scan times are needed to record the spectra due to the unavailability of high intensity X-ray sources. Also the primary excitation energy of the photons is fixed so that maximisation on the ionization cross-section is not possible to observe a particular transition. The cross-section for X-ray induced ionization decreases with reduced energy whereas it increases for electron induced ionization, Barrie(1975)<sup>25</sup>:

#### 2.4.3 Proton and Ion induced Ionization

High energy protons (4 Mev)<sup>26</sup> or ions (60 Kev)<sup>27</sup> can also be used to produce core holes in the surface region within the escape depth

incident particles largely eliminate the back scattering contribution of the electron impact excitation but the method has the disadvantage that a high energy accelerator is needed for the incident particles and only low beam currents ( $\sim 1\mu\text{A}$ ) are obtainable. Additionally some sputtering of the surface layers cannot be avoided. Nevertheless the study of Auger transitions by ion and proton bombardment is increasing in popularity and recently there have been two reviews of surface analysis by heavy ion induced Auger electrons, one by Groeneve (1975)<sup>29</sup> and the other by Viel et al(1976)<sup>27</sup>.

## 2.5 Energy of Auger Electrons

There are a number of semi-empirical formulae for calculating the kinetic energies of the Auger electrons. Now the electrons in an atom are in different levels having different binding energies. Referring to Fig. 2-2, the initial vacancy is created in level A of the atom with the electrons having a binding energy  $E_A$ , the electron which fills this vacancy comes from level B and has a binding energy  $E_B$ , the Auger electron is emitted from level C having a binding energy  $E_C$ . Then the simplest formula for the kinetic energy  $T$  of the emitted electron is,

$$T = E_A - E_B - E_C \quad \text{Eq. 2-1.}$$

Now  $E_C$  is the binding energy of the electron when the atom is already singly ionized. Burhop<sup>15</sup> suggested that as an approximation to the binding energy of an electron such as C in a singly charged ion, one can use the binding energy of the equivalent electron in the atom of the next higher atomic number. This is the equivalent core approximation, then

of low energy Auger electrons. The straight line trajectories of the incident particles largely eliminate the back scattering contribution of the electron impact excitation but the method has the disadvantage that a high energy accelerator is needed for the incident particles and only low beam currents ( $\sim 1\mu\text{A}$ ) are obtainable. Additionally some sputtering of the surface layers cannot be avoided. Nevertheless the study of Auger transitions by ion and proton bombardment is increasing in popularity and recently there have been two reviews of surface analysis by heavy ion induced Auger electrons, one by Groeneve (1975)<sup>29</sup> and the other by Viel et al(1976)<sup>27</sup>.

### 2.5 Energy of Auger Electrons

There are a number of semi-empirical formulae for calculating the kinetic energies of the Auger electrons. Now the electrons in an atom are in different levels having different binding energies. Referring to Fig. 2-2, the initial vacancy is created in level A of the atom with the electrons having a binding energy  $E_A$ , the electron which fills this vacancy comes from level B and has a binding energy  $E_B$ , the Auger electron is emitted from level C having a binding energy  $E_C$ . Then the simplest formula for the kinetic energy  $T$  of the emitted electron is,

$$T = E_A - E_B - E_C \quad \text{Eq. 2-1.}$$

Now  $E_C$  is the binding energy of the electron when the atom is already singly ionized. Burhop<sup>15</sup> suggested that as an approximation to the binding energy of an electron such as C in a singly charged ion, one can use the binding energy of the equivalent electron in the atom of the next higher atomic number. This is the equivalent core approximation, then

$$T = E_A(Z) - E_B(Z) - E_C(Z + 1) \quad \text{Eq. 2-2}$$

From a knowledge of the binding energies of the electron levels the kinetic energy of an Auger electron can be calculated. The binding energies of the electrons of an atom as deduced from X-ray emission data have been published by Bearden and Burr (1967)<sup>30</sup> and more recently by Servier (1972)<sup>31</sup>, who summarises the values obtained from photoelectron spectroscopy and X-ray emission. Using equation 2-2 and the binding energy values published by Bearden and Burr, Packer and Wilson<sup>32</sup> have compiled the energies of possible Auger transitions for the elements  $3 < Z < 88$ , in the energy range 0 - 1550 eV.

Other formulae have also been proposed for the kinetic energy of the Auger electron. Bergstrom and Hill (1954)<sup>33</sup> suggested the use of a correction factor  $\Delta E(\text{BH})$  to obtain agreement between measured and calculated values where

$$\Delta E(\text{BH}) = \Delta Z (E_C(Z) - E_C(Z + 1))$$

Then,

$$T = E_A(Z) - E_B(Z) - E_C(Z) - \Delta E(\text{BH}) \quad \text{Eq. 2-3}$$

This formula attempts to account for the fact that the Auger electron is escaping from the field of two holes. Bergstrom and Hill found that values of  $\Delta Z$  between 0.54 - 0.76 were needed to obtain agreement with their experimental KLL Auger energies from mercury.

Chung and Jenkins (1970)<sup>34</sup> have proposed a modification to equation 2-2 based on the following argument. If a direct transition is described as the one shown in Fig. 2-2 for which the down and up electrons originate in levels B and C respectively, then there is also an exchange transition in which the down electron originates in level C and the up electron originates in level B. As the Auger energy is the difference between the initial and final states of the atom, that

energy must be the same regardless of how the electron re-arrangement came about, i.e. whether the Auger emission occurred via a direct or exchange transition. Quantum mechanically the two possibilities cannot be simply distinguished by measuring the Auger electron energy. Chung and Jenkins pointed out that equation 2-2 and 2-3 will give two different values for the energy of an Auger electron originating from direct and exchange transitions, consequently they proposed a modification of eq. 2-2 to give the arithmetic mean of the direct and exchange transitions kinetic energy. Then,

$$T = E_A(Z) - \frac{1}{2}(E_B(Z) + E_B(Z+1)) - \frac{1}{2}(E_C(Z) + E_C(Z+1))$$

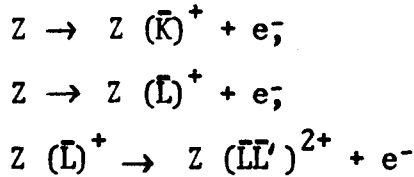
Eq. 2-4

Using this formula a set of Auger transitions in the energy range 10 - 3000 eV have been compiled by Coghlan and Clausing (1972)<sup>35,36</sup> for the elements with atomic number Z given by  $3 < Z < 92$ . They have also made a crude estimate of the intensity of each Auger transition from the product of the number of electrons in the three levels involved. This product called the multiplicity is normalised to a maximum of 100 for the largest such product for a given element.

It is difficult to be catagorical about the applicability of either formula 2-2 or 2-4 as they both give the energy of an Auger transition within a few percent of the experimentally determined value. The experimentally determined energies are additionally complicated by the work function correction of the analyser which is expected to be the work function of the entrance slit of the analyser = 4 - 5 eV.

The formulae described so far have been of a semi-empirical nature, Shirley (1973)<sup>37</sup> has attempted to obtain the energies of the KLL Auger transitions by theoretical calculation. Shirley's model is based on regarding the Auger process as a series of simple steps.

The steps for a KLL' transition for element Z are,



Then the energy for the Auger transition is expressed as:

$$T = E_K - E_L - E_{L'} - F_{KLL'} + R_S, \quad \text{Eq. 2-5}$$

where  $E_K$ ,  $E_L$ ,  $E_{L'}$  are the binding energies of the electrons in the neutral atom.  $F_{KLL'}$  is a final state interaction term depending of the Auger transition and the final state of the atom.  $R_S$  is the static relaxation energy corresponding to a reduction in the binding energy of the emitted Auger electron due to relaxation of the remaining electrons towards the vacancy created in the process.

Shirley was able to calculate theoretical values for KLL Auger energies for the elements  $10 < Z < 100$  and obtained good agreement with the experimental values. Similar calculations have been performed for the  $L_{2,3} MM$  Auger series of arsenic and selenium by Roberts, Weightman and Johnson (1975)<sup>38, 39</sup>.

Shirley's formula has more of a quasi-atomic approach, a similar formula but with a more solid state flavour has been proposed by Matthews (1973)<sup>40</sup>. The kinetic energy of a KLL' Auger transition is then given by,

$$T = E_K - E_L - E_{L'} - H + P, \quad \text{Eq. 2-6}$$

again  $E_K$ ,  $E_L$ ,  $E_{L'}$  are the binding energies of the electrons as say determined from X.P.S.,  $H$  is the extra energy needed to remove the second electron from the ion core due to interaction with the other core electrons and  $P$  is the extra conduction or valence electron polarization energy associated with a double core hole relative to the sum of the polarization energies of two individual holes.

## 2.6 Intensity of Auger Transitions

The intensity of a given Auger peak (ABC) is equal to:-

Rate of production of the particular core hole involved  $\times \frac{\sigma(\text{ABC})}{\sigma(\text{Total})}$

Where  $\sigma(\text{ABC})$  is the specific transition probability

and  $\sigma(\text{Total})$  is total transition probability for an Auger process, involving that core level.

The observed intensity will additionally depend on the instrument response function at the energy concerned as well as other factors which will be now briefly discussed.

### 2.6.1 Coster Kronig Transitions

A Coster-Kronig Auger transition is one in which the initial and a final hole are in the same shell, eg.  $L_1L_2M$ ,  $L_1L_2L_3$ ,  $M_1M_2M_3$  etc. It is generally believed that electron impact produces core holes in the various subshells of a particular shell in rough proportion to their occupation numbers. Thus for the L shell ionization, the initial vacancy distribution is 1:1:2 for the  $L_1:L_2:L_3$  subshells. There are three things which can happen to the  $L_1L_2$  holes. They can undergo X-ray or Auger de-excitation by combining with electrons in a higher lying shell or they can move to a higher lying subshell  $L_1 + L_2$ ,  $L_2 + L_3$ , by a Coster-Kronig transition releasing the energy to a weakly bound outer electron. These Coster-Kronig processes are extremely rapid where they are energetically possible, McGuire<sup>41,42</sup> has calculated for Ti that the  $L_1$  vacancy lifetime is 20 times shorter than the  $L_2$  or  $L_3$  vacancy lifetimes and the probability for filling a  $L_1$  hole from  $L_2$  or  $L_3$  subshell electrons by a Coster-Kronig transition is 90%. Thus as fast as  $L_1$  holes are created they

are shifted to  $L_2$ ,  $L_3$  holes. Hence the vacancy distribution appropriate for comparison with experiment is probably more like 1:15:25 for the  $L_1$ ,  $L_2$ ,  $L_3$  subshells. For Ag McGuire (1972)<sup>43</sup> has calculated for the M shell that an initial hole distribution of 1:6:10 for  $M_1$ :  $M_{2,3}$ :  $M_{4,5}$  subshells becomes 1:15:280 by the action of Coster-Kronig transitions enhancing the intensity of the  $M_{4,5}$  series of Auger transitions. Tracy (1973) was able to measure the intensity of the  $L_{2,3}$  VV phosphorus Auger peak versus primary beam energy and recorded a kink at the ionization energy of the  $L_1$  level due to enhancement of the intensity by Coster-Kronig transitions.

### 2.6.2 Effect of Primary Electron Energy.

The strength of an observed Auger peak depends on the primary electron energy  $E_p$  due to the ionization cross-section being energy dependent. A qualitative result has been deduced, for most materials studied so far, that the Auger electron yield rises abruptly above the threshold for core hole production to a maximum value at about 2 - 6 times the threshold energy and then remains constant. These results for the energy of maximum ionization cross-section do not agree with theoretically determined values which tend to reach a maximum at lower values of energy, closer to the threshold, and then decrease rapidly as the exciting energy is further increased, Neave, Foxon and Joyce (1972)<sup>45</sup>.

### 2.6.3 The Backscattering Effect

When a surface is bombarded with a beam of electrons of energy  $E_p$  ionization of the surface atoms will occur. Now an atom with electrons having binding energy  $E_c$ , where  $E_c < E_p$ , can be ionized not only by the primary electrons but also by all the secondary electrons within the solid which have suffered inelastic collisions but whose

energy is still greater than  $E_c$ , that is, all those secondary electrons with energy  $E_s$  when  $E_c < E_s < E_p$ . The contribution of these electrons to the Auger intensity is referred to as the backscattering contribution, Fig. 2-3. Gallon (1972)<sup>46</sup> measured the  $L_{2,3}$  W Auger yield from bulk Si and proceed to construct a model in which the Auger signal current is given by

$$I_A = C I_p (\phi + \alpha\beta).$$

Where  $C$  = Constant,  $I_p$  = Primary electron current,

$\phi$  = Energy dependent ionization cross-section,

$\alpha$  = Ionization cross-section integrated over the range of energies present in the backscattered contribution.

$\beta$  = A geometric term.

$$\alpha(E_p) = \int_{E_c}^{E_p} \phi(E) N(E) dE.$$

Gallon used an iterative procedure to calculate the backscattering contribution to the Auger current and showed it to be about 30% for Ge and 20% for Si<sup>46</sup>. Other values which have been quoted in the literature are: 20% for Si, 30% for Ge by Meyer and Vrakking (1972)<sup>47</sup>; Tarng and Wehner (1973)<sup>48</sup> obtained a 40% backscattering contribution to the intensity of the 120 eV peak of molybdenum. The backscattering contribution has been shown to change with primary beam energy, from a value of 20% at  $E_p/E_c = 2$ , to 30% for  $E_p/E_c = 5$ , Meyer and Vrakking (1975)<sup>49</sup>.

#### 2.6.4 Dependence of the Auger Yield on Angle of Incidence

P.W. Palmberg (1968)<sup>50</sup> has investigated the effect of varying the angle of incidence of the primary electrons on the Auger yield from overlayers and substrates. His results indicate that the Auger yield for the overlayer is very much enhanced relative to the substrate when

the primary beam is incident on the sample near grazing incidence. As the angle of grazing incidence is decreased the primary electrons spend more time traversing the overlayer and thus have an increased probability of producing ionization within the escape depth of Auger electrons. The overall strength of the signal is attenuated at very near grazing incidence ( $\sim 7^\circ$ ) probably because of surface roughness.

## 2.7. Instrumentation in A.E.S.

There are two main types of instrument widely used in A.E.S. One is the retarding field analyser (R.F.A.) as used in LEED systems, this is fairly well described in the literature<sup>18,19</sup> and several such instruments have been constructed within our own laboratory<sup>51,52</sup>. The RFA has essentially spherical, as constructed by Harris<sup>52</sup>, or hemispherical symmetry<sup>51</sup> and in its simplest form consists of three grids in front of a collector with the target at the centre. The first and third grids are at earth potential and a negative voltage  $E_g$  is applied to the second grid so that only electrons having an energy greater than  $E_g$  are transmitted to be collected; this type is thus referred to as a high pass analyser. RFA's have a constant energy window  $\Delta E$  over the entire range of energies and the derivative of the secondary electron emission is obtained by modulating the second grid with a sinusoidal signal of frequency  $w$  and detecting the component of the collector current at frequency  $2w$ . This component is proportional to  $dN(E)/dE$ , the first derivative of the SEE spectrum. In this type of analyser nearly all the electrons emitted from the surface can be collected so that it is particularly sensitive to structure in the low energy true secondary peak of the SEE spectrum<sup>53,54</sup>.

The other type of instrument used is the dispersive analyser, which is referred to as a band pass analyser because only electrons having a narrow spread of energies close to the electron energy being analysed are focussed at the exit collector, so that potentially such an analyser is capable of a better signal/noise ratio than a R.F.A. The cylindrical mirror analyser, described in Chapter 4, is of this type and the derivative of the SEE spectrum is obtained by modulating the focussing voltage with a sinusoidal signal of frequency  $\omega$  and detecting the component of the collector current at the same frequency, i.e.  $I_c(\omega)$ , which is proportional to  $\frac{dN(E)}{dE}$ . These analysers have a constant instrumental resolution  $R_0$  so that the energy window of the analyser  $\Delta E (= R_0 E)$  is a function of the energy analysed, and it is obvious that  $\Delta E$  deteriorates with higher analysed energies.  $\Delta E$  is an important parameter for an instrument because it determines whether two peaks close together are resolved.

Both types of analyser, with good resolutions, are commercially available. More recent instrumental advances have been in developing scanning Auger microscopes capable of operation as a S.E.M. (Scanning Electron Microscope) and as an Auger spectrometer. Powell et al<sup>55</sup> have recently developed such an instrument which uses two separate guns, one to produce the S.E.M image and the other is used to excite the Auger spectra. Physical Electronics Industries<sup>56</sup> are also marketing a scanning Auger Microprobe (S.A.M.) instrument. With these instruments elemental identification at a specific location on the S.E.M. image is possible so that considerable applications to metallurgy and electronic device analysis are expected.

## 2.8 Quantitative A.E.S.

The peak to peak heights in the derivative Auger spectra contain quantitative information on the number of atoms of a particular type in the surface region. This area of A.E.S. is of considerable current interest and controversy as there are a number of parameters involved in establishing a relationship between the recorded peak height and the concentration of the atomic species present. Since the excitation probabilities for the Auger transitions and the escape depths of the excited electrons cannot as yet be deduced from theory a number of semi-empirical methods have been developed to obtain quantitative information and these are now briefly outlined.

(i) By Calibration. To determine the concentration of a particular element a signal from the surface under investigation is compared with the Auger signal obtained from a pure element under identical conditions and a direct ratio is used as an estimation of the concentration. This method is open to the criticism that different targets have to be used so that it will be difficult to position them in identical positions in the spectrometer to record the Auger spectra. Also the targets should have the same surface topography as roughness can influence the Auger yield.

(ii) It has been shown by breaking metallic alloys of known compositions in an ultra high vacuum environment and immediately recording the Auger spectra that the ratio of the peak heights is proportional to the concentration. The results of Bowman et al (1972)<sup>57</sup> obtained from the platinum-tin alloys are shown in Fig. 2-4, such a graph can be used as a calibration for subsequent study of the surface, for instance to detect surface enrichment upon sample heating, or the preferential sputtering of a particular element on an alloy

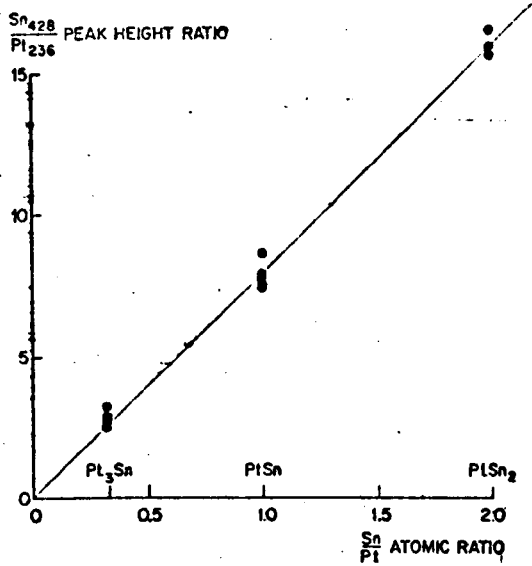


Fig.2-4. The Ratio of the Observed Auger Peak Heights for Different Concentrations of the Pt/Sn System, from Bouwman et. al. (1972)<sup>56</sup>.

surface. Similar graphs to Fig. 2-4 have been obtained for the Ni-Pd and the Ag-Pd system by Mathieu et al (1975)<sup>58</sup>.

(iii) In adsorption studies the heights of the Auger peaks are monitored as a function of the exposure to a particular gas and a number of authors have assigned structure in the Auger peak height versus exposure graph to one monolayer coverage of the substrate by the adsorbing gas: Florio and Robertson (1969)<sup>59</sup> identified saturation of the chlorine Auger peak signal in the adsorption of Cl on Si as one monolayer coverage; Musket and Ferrante (1970)<sup>60</sup> also identified the saturation coverage of O<sub>2</sub> on W (110) as detected by the Auger signal peak height with one monolayer; Jackson et al (1973)<sup>61</sup> proposed a layer model in which structure in the Auger peak height v exposure graph can be identified with the build up of monolayers on the surface. More recently Kirby and Lichman (1974)<sup>62</sup> identify the saturation of the Auger peak of oxygen with exposure as one monolayer coverage of the silicon surface.

There are many parameters to be considered in quantitative A.E.S. which make it a complex topic. The variation of the escape depth of Auger electrons with energy, the Auger peak widths and transition probabilities, the influence of fine structure, all need to be considered in quantitative A.E.S. Additionally, there are instrumentation problems particularly with cylindrical mirror type of analysers as two Auger peaks at different energies are recorded with different analyser energy windows and electron multiplier gains. These are just some of the factors which make quantitative A.E.S. a stimulating topic for current debate.

## 2.9 Chemical Effects in A.E.S.

A major area of current activity in A.E.S. is the excitation and analysis of spectra from chemical compounds. In the past few years the prominent features in the Auger spectra from most of the elements have been identified and research is now in progress on the changes produced in the Auger emission when the elements are in chemical combination. The aim of the research is to determine and interpret the changes in energy and shape of the observed Auger features of the elements which are produced as a result of the charge transfer which accompanies chemical bond formation. Other effects which may be observed are the appearance or disappearance of structure either due to plasmons or changes in valence band density of states.

There are two types of chemical effects which need to be distinguished in the AES of compounds. There are the changes produced in Auger peaks involving the valence band, these will be strongly affected by the alterations in the valence band produced as a result of the chemical combination. Such peaks will undergo a shift in energy as well as a possible change in shape. Whereas the chemical effects on the Auger transitions involving the core levels of an element are expected to undergo a shift in energy only.

Some of the results obtained by workers, studying chemical effects in A.E.S., are briefly mentioned. Szalowski and Somorjai (1974)<sup>63</sup> have measured the chemical shift of the  $L_3 M_{2/3} M_{2/3}$  inner shell transition from various vanadium compounds, and obtained values ranging from - 2.3 eV in  $V_2O_4$  to - 0.55 eV for  $VSi_2$ . Haas, Grant and Dooley (1972)<sup>64</sup> have measured Auger peak shifts in the oxides of Ta, Mo, Nb which ranged from - 0.2 to - 1.5 eV for the NNN peaks of Ta, - 0.2 to - 0.9 eV for the MN peaks of Mo and

## 2.9 Chemical Effects in A.E.S.

A major area of current activity in A.E.S. is the excitation and analysis of spectra from chemical compounds. In the past few years the prominent features in the Auger spectra from most of the elements have been identified and research is now in progress on the changes produced in the Auger emission when the elements are in chemical combination. The aim of the research is to determine and interpret the changes in energy and shape of the observed Auger features of the elements which are produced as a result of the charge transfer which accompanies chemical bond formation. Other effects which may be observed are the appearance or disappearance of structure either due to plasmons or changes in valence band density of states.

There are two types of chemical effects which need to be distinguished in the AES of compounds. There are the changes produced in Auger peaks involving the valence band, these will be strongly affected by the alterations in the valence band produced as a result of the chemical combination. Such peaks will undergo a shift in energy as well as a possible change in shape. Whereas the chemical effects on the Auger transitions involving the core levels of an element are expected to undergo a shift in energy only.

Some of the results obtained by workers, studying chemical effects in A.E.S., are briefly mentioned. Szalowski and Somorjai (1974)<sup>63</sup> have measured the chemical shift of the  $L_3 M_{2/3} M_{2/3}$  inner shell transition from various vanadium compounds, and obtained values ranging from - 2.3 eV in  $V_2O_4$  to - 0.55 eV for  $VSi_2$ . Haas, Grant and Dooley (1972)<sup>64</sup> have measured Auger peak shifts in the oxides of Ta, Mo, Nb which ranged from - 0.2 to - 1.5 eV for the NNN peaks of Ta, - 0.2 to - 0.9 eV for the MN peaks of Mo and

- 0.2 to - 0.5 eV for the MN peaks of Nb; the changes in shape of the metal Auger peaks produced on carbide formation are also mentioned. Baker et al (1972)<sup>65</sup> detected a shift of - 4 eV in the Auger peaks of Yttrium on the absorption of oxygen, but found no corresponding shift in the Auger peaks of Molybdenum; Barrie (1975)<sup>66</sup> has measured the energies of the KLL, KLV Auger transitions in Na and NaO. Solomon and Baum (1975)<sup>67</sup> studied the LMV peak of Ti, TiO, TiO<sub>2</sub> and detected differences which were interpreted as due to the change produced in the valence band. Holloway (1976)<sup>68</sup> detects a shift of - 4 eV in the Si, L<sub>2/3</sub> VV peak and a shift of - 5 eV in the Si, KL<sub>2/3</sub>, L<sub>2/3</sub> peak from silicon nitride, (SiN) whereas from silicon oxide (SiO<sub>2</sub>) a shift of - 13 eV was observed in the L<sub>2/3</sub> VV transition. The Fe, M<sub>2/3</sub> M<sub>4/5</sub> M<sub>4/5</sub> peak shifts, from 47 eV to 44 eV on oxide formation<sup>69</sup> and the Ge peaks are found to shift by - 4 eV on the formation of GeO<sub>2</sub>, Wang et al (1975)<sup>70</sup>.

The Auger spectra can be used to distinguish between different oxides of a metal for instance in the titanium oxides already mentioned<sup>67</sup>; also Seo et al (1975)<sup>68</sup> has obtained distinct Auger spectra for the oxides of iron: Fe<sub>2</sub>O<sub>3</sub> and Fe<sub>3</sub>O<sub>4</sub>. The KLL Auger peak of C also has a distinct shape depending on whether the C is in the form of a graphite, diamond or a carbide<sup>64</sup>.

When an atom combines chemically with another atom a certain amount of charge transfertakes place so that the valence shell charge density is altered. This re-arrangement of the outer electrons (generally electrons transfer from the metal atom to the non-metal atom) will cause a slight increase in the binding energy of the metallic core level electrons, so that on the simplified picture of equation 2-1 the kinetic energy of the Auger electron will shift by an amount  $\Delta E_{ABC}$ , given by

$$\Delta E_{ABC} = \Delta E_A - \Delta E_B - \Delta E_C,$$

Where  $\Delta E_A$ ,  $\Delta E_B$ ,  $\Delta E_C$  are the shifts in the binding energy of the electrons in individual levels. As the core electron binding energy shifts are nearly equal<sup>64</sup>

$$\Delta E_A \approx \Delta E_B \approx \Delta E_C \approx \Delta E' \quad \text{Eq. 2-7}$$

This is a shift of a few electron volts. The observed energy shift for an Auger transition involving the core levels is usually greater than the shifts in the individual levels and this additional contribution has been interpreted as a change in the final state term  $F_{BC}$  and the static relaxation term  $R_S$  of Shirley's equation 2-5. so that

$$\Delta E_{ABC} \text{ (observed)} = \Delta E' - \Delta F + \Delta R_S \quad \text{Eq. 2-8}$$

Kowalczyk et al (1973)<sup>72</sup> proposes the separation of the static relaxation energy into two components, an atomic relaxation energy  $R_1$  and an extra-atomic relaxation energy  $R_2$ . So that

$$R_S = R_1 + R_2,$$

where  $R_2$  is the contribution due to relaxation of the lattice electrons towards the hole and it is this term which should be most sensitive to the chemical environment of the atom. Thus

$$\Delta E_{ABC} \text{ (observed)} = \Delta E' + \Delta R_2 \quad \text{Eq. 2-9}$$

Then the observed shift in the position of an Auger peak involving the core levels can be interpreted as being due to a shift in the binding energy of the electrons involved together with the change in the extra atomic relaxation energy produced.

## 2.10 Electron Beam Artifacts

In AES an electron beam is normally used as the investigating probe. Now a typical beam used to record Auger spectra may have energy 1 - 3 KeV, a beam current of 10 - 50 $\mu$ A and a spot diameter of 0.1 - 1mm, such a beam represents a considerable load ( $\sim$  15 watts/sq. cms.) on to the surface under investigation. Such a load can introduce electron beam artifacts because it will cause local heating of the target, if it is a poor conductor, and induce effects such as dissociation of compound surfaces, surface diffusion within the region of bombardment, and electron induced desorption and adsorption. Consequently care needs to be exercised in any studies performed and electron beam artifacts must be looked for when ever electron stimulated AES is used. In some situations it may be best to use a diffused beam of low current to reduce the surface load. There are numerous reports of electron beam induced effects in the literature amongst whom are Florio and Robertson (1969)<sup>59</sup>, who report Cl desorption from Si and Musket and Ferrante (1970)<sup>60</sup>, who report oxygen desorption from tungsten surfaces by the action of the electron beam. Considerable electron beam effects are reported in later chapters of the present work.

## 2.11 Interatomic Auger Transitions

Interatomic transitions, or cross transitions, can occur when two atoms are in chemical combination with one another. A hole created in a core level of one atom relaxes by an Auger transition in which the electrons from the neighbouring atoms participate by a

tunnelling mechanism. They were originally proposed for structure observed in X-ray emission spectra and it was Gallon and Matthew (1970)<sup>73</sup> who first interpreted structure in the Auger spectra of LiF as being due to interatomic processes. Interatomic transitions have been reported in the Auger spectra of MgO<sup>74,75</sup> and Citrin (1974)<sup>76</sup> has interpreted the low energy structure in the Auger spectrum of MgF<sub>2</sub> as being primarily due to interatomic transitions of the form Mg (L<sub>2/3</sub>) F (L<sub>2/3</sub>) F (L<sub>2/3</sub>), Mg (L<sub>2/3</sub>) F (L<sub>2/3</sub>) F (L<sub>1</sub>), Mg (L<sub>1</sub>) Mg (L<sub>2/3</sub>) F (L<sub>1</sub>) etc.

## 2.12 Uses of A.E.S.

In this section we mention briefly some of the uses to which Auger electron spectroscopy has been applied.

- (i) Depth profiling - in which Auger spectra are recorded from a surface which is being simultaneously sputtered away at a constant rate by Argon ion bombardment. Using the peak-peak Auger signal height as a qualitative estimate of the concentration of a particular element, a depth v concentration profile can be obtained. This is useful for instance in determining the thickness of an oxide film on a surface. A non-destructive technique for obtaining depth profiles has been proposed by Meyer and Vrakking (1974)<sup>134</sup> based on recording Auger spectra as a function of the primary beam energy.
- (ii) Valence band determination - in spite of the complexity of the Auger process, a number of authors have attempted to use the Auger peak shapes for the determination of the valence band density of occupied states. Usually the peak selected for study

is an ABV type of transition, where A and B are inner levels and one of the final holes is in the valence band of the solid. Barrie et al (1975)<sup>66</sup> used the  $KL_1^V$  and  $KL_{2/3}^V$  Auger peaks to obtain the valence band of Na in moderate agreement with UPS and XPS determinations; Sickafus (1973)<sup>78</sup>, in his study of NiS, was able to relate the features in the Ni (MV) and S (LW) Auger peaks to the valence band density of states of nickel sulphide; Amelio (1970) used the  $L_{2/3}^{VV}$  peak of Si and Salmeron et al (1975)<sup>80</sup> used the  $L_1L_{2/3}^V$  Auger peak to obtain the valence band of silicon; Solomons (1975)<sup>67</sup> work on the LMW Auger peaks from titanium oxides has already been mentioned.

Although there has been some success in obtaining the valence band density of states for some solids other workers report transitions involving the valence band to have a quasi-atomic nature. Kowalczyk (1973)<sup>72</sup> reports the absence of any valence band influences on the  $L_{2/3}^{VV}$  Auger transitions from copper and zinc; Bassett et al (1973)<sup>81</sup> report a similar result for the  $M_{4/5}^{VV}$  transition of silver. Joyner and Roberts (1973)<sup>82</sup> detected no valence band influences on  $N_{6/7}^{VV}$  Auger transition of gold. It has been suggested by Salmeron et al<sup>83</sup> that this atomic behaviour may be connected with the presence of d electrons in the valence band.

(iii) Technological Applications - the technological applications of AES have been reviewed by Gjostein and Chauka (1973)<sup>84</sup> and by Stein (1975)<sup>85</sup>. These authors summarize the phenomenon such as segregation of impurities to surfaces, thin film growth, fracture surfaces, surface diffusion, to which AES can be applied. Other applications are in the study of wear and friction,<sup>86</sup> surface sputtering<sup>87</sup> and corrosion.

One of the latest areas of research in Auger spectroscopy is angle resolved emission from solid surfaces<sup>88,89</sup>.

To briefly summarize this chapter the subject of Auger electron spectroscopy has been introduced and some of the latest developments outlined. The subject matter of the next chapter is concerned with characteristic energy loss spectroscopy, which is the other important technique used in the present work.

3.1 Introduction

A solid contains a large number of electrons some of which are in discrete energy levels of the atoms while the rest are in the conduction and valence bands of the material. The electrons in the deeper energy levels of an atom remain more or less unchanged when this atom comes together with other atoms to form a solid, whereas the electrons in the outer energy levels interact strongly with one another to form the electron energy bands characteristic of the solid. These outer loosely bound electrons in the solid are of considerable interest as they determine properties such as the electrical and thermal conductivity and are responsible for the subdivision of solids into conductors, insulators and semi-conductors.

Characteristic energy loss spectroscopy probes these outer electrons which constitute one of the highest densities of charged particles ( $\approx 10^{22}$  electrons  $\text{cm}^{-3}$ ) available. This high density solid state plasma is a sea of strongly interacting particles upon which many-body theories can be tested and additionally there are suggestions to exploit this plasma for solid state device applications<sup>90</sup>. Another important property of these outer electrons is that they strongly influence the reflection and transmission of electromagnetic radiation by a material.

Characteristic energy losses in solids have been studied since the 1930's, most of the earlier measurements were made on freshly evaporated films, in vacuum of  $10^{-6}$  Torr. A number of techniques have been developed for CEL investigations: transmission of electrons through

thin films, reflection of electrons from solid surfaces and optical transmission and reflection from solids. Simultaneously with the experimental studies theoretical analysis of the electron plasma excitation modes provided a basis for the interpretation of the experimental results. There are two excellent reviews available on the subject one by R  ther (1965)<sup>91</sup> and the other by Servier (1972)<sup>31</sup>. The theoretical work, on the elementary excitations in solids induced by photon and electron bombardment of a surface, has been summarised by Pines<sup>92</sup>.

### 3.2 Methods of Investigating CEL in Solids

#### 3.2.1 Optical Methods

In this technique electromagnetic radiation of known wavelength is incident on the surface to be investigated. Ideally the surface should be pure and clean and in an ultra high vacuum environment. From measurements of the reflectivity of the light, or the transmission through thin films the complex dielectric constant  $n + jk$  can be deduced. Measurements at different wavelengths will allow  $n$  and  $k$  to be determined as function of the photon energy. From these results the complex dielectric constant  $\epsilon$  where

$$\begin{aligned}\epsilon &= (n + jk)^2 \\ &= \epsilon_1 + \epsilon_2\end{aligned}$$

can be obtained.

For the idealised case of a solid containing a free electron gas the dielectric constant can be calculated to be a frequency dependent expression<sup>91</sup>

$$\epsilon(\omega) = 1 - \frac{\omega_p^2}{\omega^2} \left( \frac{1}{1 - j\omega\tau_c} \right), \quad \text{Eq. 3-1}$$

where  $\omega_p^2 = \frac{Ne^2}{M\epsilon_0}$  ,  $N =$  Number of electrons per  $m^3$   
 $M =$  Electron mass  
 $\epsilon_0 =$  Permittivity of free space  
 $T_c$  is a relaxation time

The dielectric constant consists of a real term,

$$\epsilon_1(\omega) = 1 - \frac{\omega_p^2}{\omega^2} \left( \frac{1}{1 + \frac{1}{\omega^2 T_c^2}} \right) \quad \text{Eq. 3-2}$$

and an imaginary term

$$\epsilon_2(\omega) = \frac{\omega_p^2}{\omega^2} \cdot \frac{1}{\omega T_c} \left( \frac{1}{1 + \frac{1}{\omega^2 T_c^2}} \right) \quad \text{Eq. 3-3}$$

Fig. 3-1 shows the variation of  $\epsilon_1$ ,  $\epsilon_2$  with frequency  $\omega$  for a free electron gas.

Now the results obtained from optical measurements are of importance because Pines<sup>92</sup> has shown that the probability of a fast charge, moving through an electron gas, losing energy is proportional to  $-\text{Im} \left( \frac{1}{\epsilon(k, \omega)} \right)$ . To a good approximation it may be assumed that the momentum transfer during an electron interaction with the gas is negligible, so that  $k \rightarrow 0$ , then the probability of a fast moving charge losing energy is proportional to  $-\text{Im} \left( \frac{1}{\epsilon(0, \omega)} \right)$  and this quantity can be obtained from the optical measurements as

$$-\text{Im} \left( \frac{1}{\epsilon} \right) = \frac{\epsilon_2}{\epsilon_1^2 + \epsilon_2^2} \quad \text{Eq. 3-4}$$

Thus we should be able to correlate characteristic losses as measured by electron bombardment with structure in  $-\text{Im} \left( \frac{1}{\epsilon} \right)$  as deduced from photon bombardment.

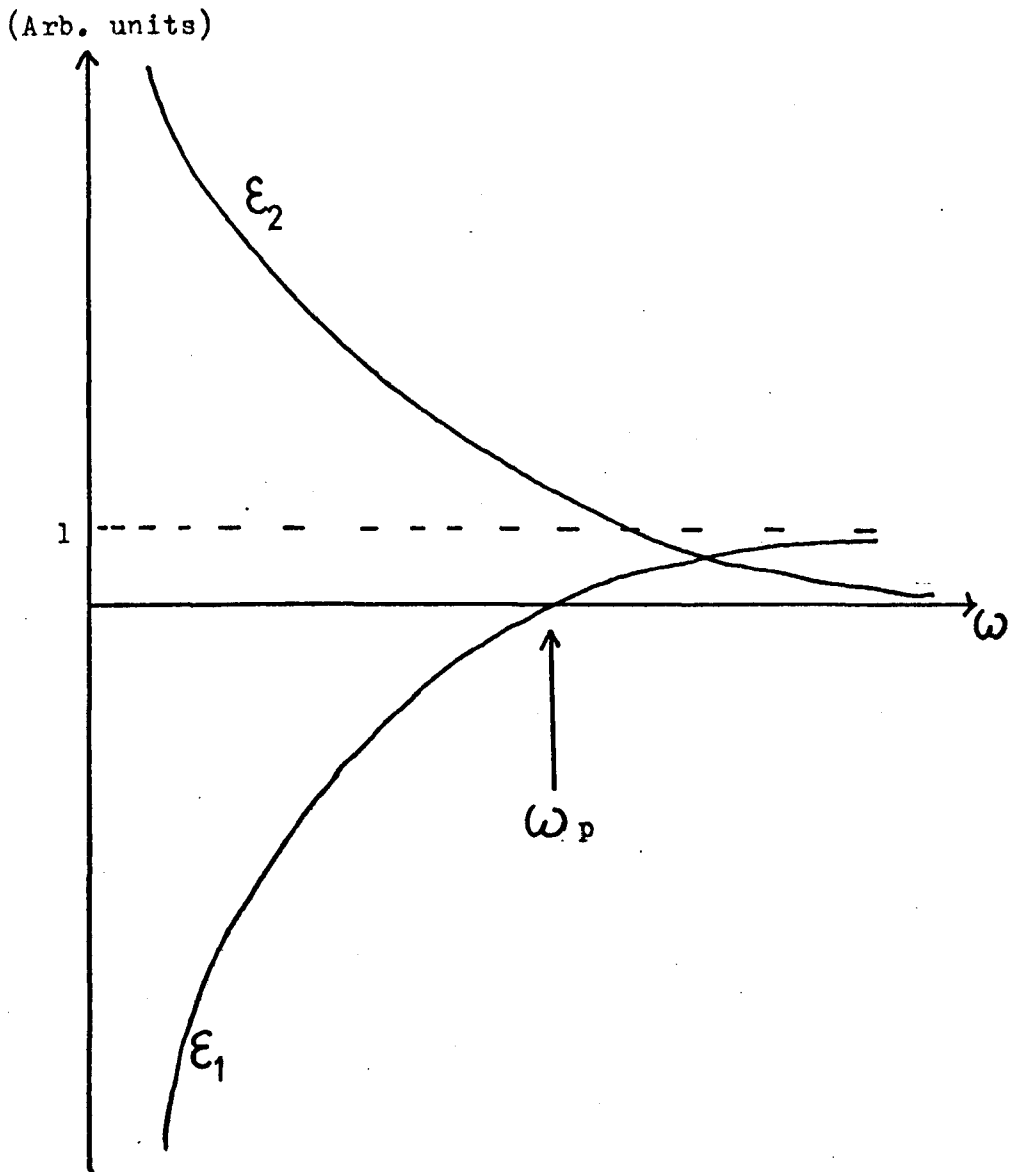


Fig.3-1. Dielectric behavior of a free electron gas.

### 3.2.2 Transmission of High Energy Electrons

High energy monoenergetic electrons (30-50 Kev) are passed through thin specimens ( $\approx 2000\text{\AA}$ ) and the transmitted beam is energy analysed to determine the characteristic losses suffered by the primary electrons. Using this technique measurements can be made of the energy loss v scattering angle to deduce the dispersion relation for characteristic losses and also because thin specimens are used multiple losses are not excited.

### 3.2.3 Reflection of Low Energy Electrons

The surface, which need not be a thin specimen, is bombarded with monoenergetic electrons, usually of energy less than 1000 eV, and the secondary electrons emitted are energy analysed. The characteristic losses are detected on the low energy side of the elastic peak as shown in Fig. 1-1. The observation of a loss by this method involves two events, that is the excitation of the loss plus the elastic scattering of the exciting electron into the entrance slit of the energy analyser. Primary beam energies as low as 50 eV can be used and surface sensitive features are much more readily observed using this method of investigation. Also the same energy analyser can be used as an Auger spectrometer so that the surface under study can be characterized.

## 3.3 Characteristic Excitations in Solids

We now outline some characteristic losses which can be excited in a solid.

The collection of loosely bound electrons together with the ion cores in a solid, form a plasma of high density. These electrons are capable of collective oscillation with a high eigenfrequency of energy  $\sim 10$  eV. This oscillation is a longitudinal density fluctuation and the quanta of this oscillation is called a plasmon. Now for a free electron gas of density  $N$  per unit volume the plasmon energy has been calculated to be<sup>91,92</sup>

$$\hbar\omega_p = \hbar \left( \frac{Ne^2}{m\epsilon_0} \right)^{\frac{1}{2}}, \quad \text{Eq. 3-5}$$

where  $m$  is the electron mass,

$\epsilon_0$  is the permittivity of free space,

$\hbar$  is Planck's constant/ $2\pi$ .

and  $N$  is the density of electrons.

The study of plasmons is important for XPS and AES as some of the satellite structure appearing on the low energy side of the major peaks can be attributed to electrons from the major peaks having lost a characteristic amount of energy by exciting a plasmon while exiting from the solid.

Electron impact is one of the best methods of studying plasmon behaviour in solids. It has been shown theoretically by Quinn<sup>93</sup> that the mean free path  $\lambda$  for plasmon excitation in a free electron gas is given by

$$\lambda = \frac{2A_0 E_0}{\hbar\omega_p} \left( \left( \text{Ln} \left\{ \frac{(E_F + \hbar\omega_p)^{\frac{1}{2}} - E_F^{\frac{1}{2}}}{E_0^{\frac{1}{2}} - (E_0 - \hbar\omega_p)^{\frac{1}{2}}} \right\} \right) \right)^{-1}, \quad \text{Eq. 3-6}$$

where  $\hbar\omega_p$  is the plasmon energy,

$E_0$  is the primary electron energy,

$E_F$  is the Fermi energy of the solid,

$A_0$  is the Bohr radius.

### 3.3.1 Plasmons

The collection of loosely bound electrons together with the ion cores in a solid, form a plasma of high density. These electrons are capable of collective oscillation with a high eigenfrequency of energy  $\sim 10$  eV. This oscillation is a longitudinal density fluctuation and the quanta of this oscillation is called a plasmon. Now for a free electron gas of density  $N$  per unit volume the plasmon energy has been calculated to be<sup>91,92</sup>

$$\hbar\omega_p = \hbar \left( \frac{Ne^2}{m\epsilon_0} \right)^{\frac{1}{2}}, \quad \text{Eq. 3-5}$$

where  $m$  is the electron mass,

$\epsilon_0$  is the permittivity of free space,

$\hbar$  is Planck's constant/ $2\pi$ ,

and  $N$  is the density of electrons.

The study of plasmons is important for XPS and AES as some of the satellite structure appearing on the low energy side of the major peaks can be attributed to electrons from the major peaks having lost a characteristic amount of energy by exciting a plasmon while exiting from the solid.

Electron impact is one of the best methods of studying plasmon behaviour in solids. It has been shown theoretically by Quinn<sup>93</sup> that the mean free path  $\lambda$  for plasmon excitation in a free electron gas is given by

$$\lambda = \frac{2A_0 E_0}{\hbar\omega_p} \left( \left\{ \ln \left( \frac{(E_F + \hbar\omega_p)^{\frac{1}{2}} - E_F^{\frac{1}{2}}}{E_0^{\frac{1}{2}} - (E_0 - \hbar\omega_p)^{\frac{1}{2}}} \right) \right\} \right)^{-1}, \quad \text{Eq. 3-6}$$

where  $\hbar\omega_p$  is the plasmon energy,

$E_0$  is the primary electron energy,

$E_F$  is the Fermi energy of the solid,

$A_0$  is the Bohr radius.

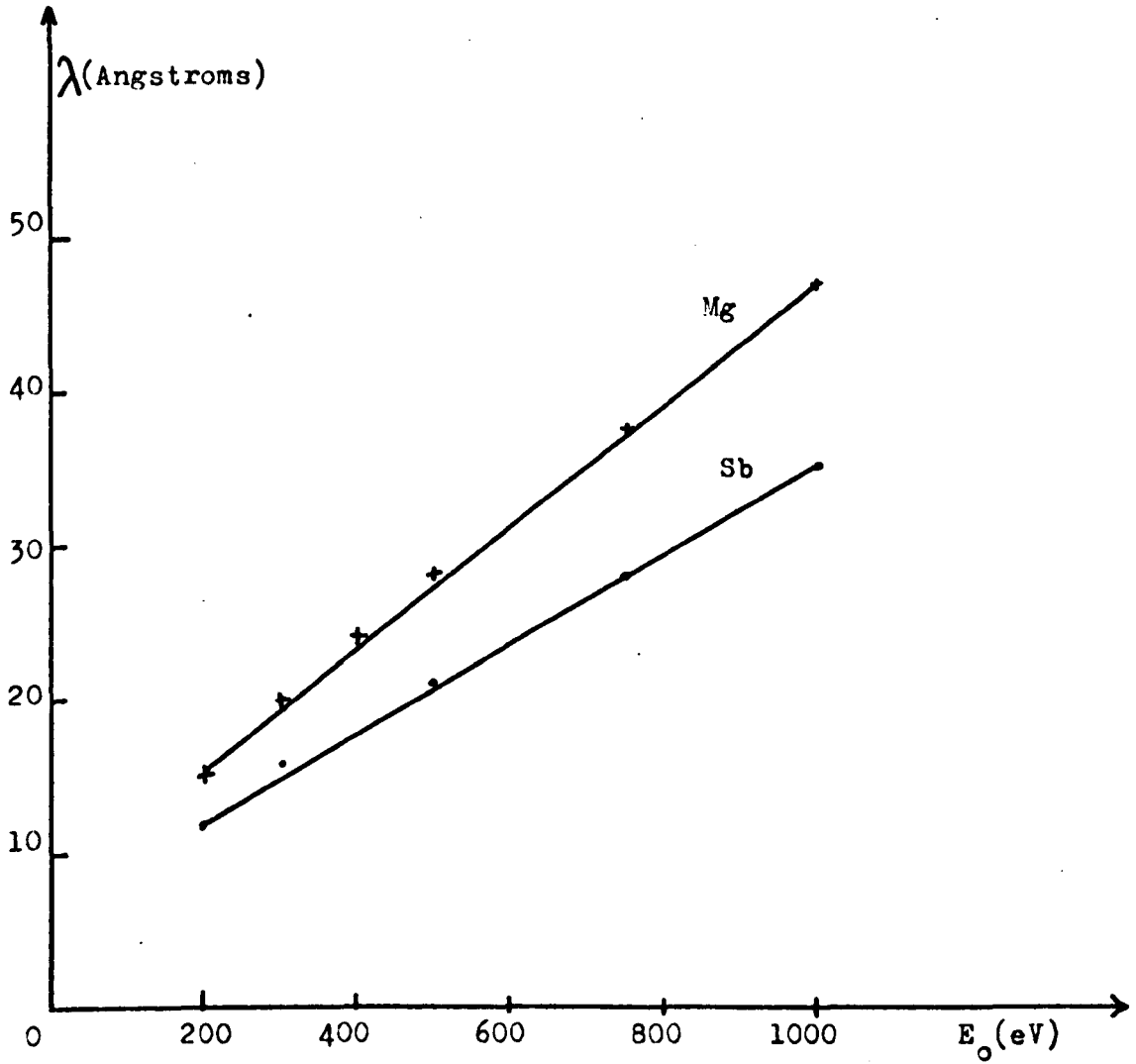


Fig. 3-2. The mean free path for plasmon excitation in Mg and Sb at different primary energies  $E_0$  .

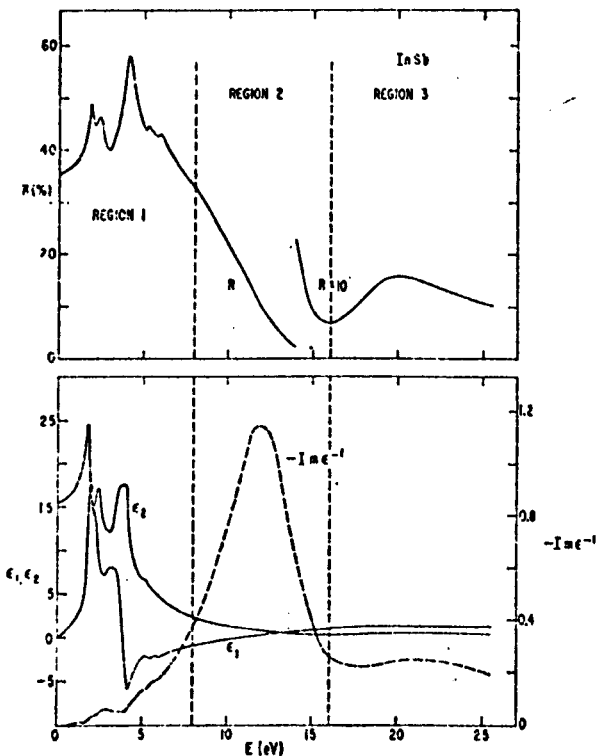


Fig.3-3. The Optical Properties of InSb, Showing the Real ( $\epsilon_1$ ) and Imaginary( $\epsilon_2$ ) Parts of the Dielectric Constant and the Bulk Loss Function  $\text{Im}(\frac{-1}{\epsilon})$ , from Phillip and Ehrenreich (1963)<sup>95</sup>.

Fig. 3-2 shows a plot of this expression as a function of the primary electron energy for the elements Mg and Sb. It is clear that the probability for plasmon excitation by electron impact is quite high.

Referring to Eq. 3-1 it can be seen that the dielectric constant of a free electron gas is strongly dependent on the plasmon frequency  $\omega_p$ . Also Pines<sup>92</sup> has shown that the loss function  $-\text{Im} \left[ \frac{1}{\epsilon} \right]$  of a system has a broad maxima at the plasmon frequency of its electrons so that optical measurements may be used to predict the plasmon oscillation energy of solids. Although maxima in  $-\text{Im} \left[ \frac{1}{\epsilon} \right]$  can also occur due to interband transitions (see subsection 3.3.3)<sup>94</sup>, at a plasmon frequency  $\epsilon_1(\omega) = 0$  and is changing from negative to positive values and  $\epsilon_2(\omega)$  is decreasing. This is illustrated by Fig. 3-3 reproduced from the work of Phillip and Ehrenreich (1963)<sup>95</sup>. The data obtained is from reflectivity measurements and the broad maxima in  $-\text{Im} \left[ \frac{1}{\epsilon} \right]$  at 12.0 eV occurs in the region where  $\epsilon_1 = 0$  and  $\epsilon_2$  is decreasing. The maxima in the loss function agrees well with the calculated value of 12.0 eV, which is the plasmon energy if the valence electrons of InSb are regarded as behaving like a free electron gas.

### 3.3.2 Surface Plasmons

The plasmons discussed in Section 3.3.1 are called volume plasmons, where the electron gas in which the excitations occur has three dimensional symmetry. Charge density oscillations can also occur at the surface of a solid giving rise to the concept of surface plasmons. These were originally proposed by Ritchie (1957)<sup>96</sup> with an additional contribution by Stern and Ferrell (1960)<sup>97</sup>. In the bulk of a material the real part of the dielectric constant has a continuous value  $\epsilon_1$  throughout. At the solid surface this quantity changes abruptly to that of the adjoining medium  $\epsilon_1'$ . Assuming that there is a

plasma oscillation in the first medium, the necessary continuity of the normal component of the electric displacement requires that

$$\epsilon_1 = -\epsilon'_1,$$

for a charge oscillation at the surface. Then for a free electron gas with surface plasmon frequency,  $\omega_s$

$$1 - \frac{\omega_p^2}{\omega_s^2} = -\epsilon'_1,$$

So that

$$\omega_s = \frac{\omega_p}{\sqrt{1 + \epsilon'_1}}$$

If the solid is in contact with vacuum then  $\epsilon'_1 = 1$  so that  $\omega_s = \frac{\omega_p}{\sqrt{2}}$ ,

is the relationship between the surface and volume plasmon frequencies for a free electron like solid.

Surface plasmons have been reviewed by Richie (1973)<sup>98</sup> and they are of importance because of the changes which can be produced in their energy and intensity by adsorbed layers. In the case of Si (III) the adsorption of a quarter of a monolayer of oxygen causes the surface plasmon peak to split into two peaks which increase in separation with increasing coverage<sup>99</sup>. These changes are as yet little understood. Surface plasmons are capable of quantitative exploitation as Wright<sup>53</sup> was able to use the shift in the surface plasmon energy of Mg with oxygen coverage to deduce the thickness of oxide layer formed.

Peaks have been assigned to surface plasmons oscillations in electron energy loss measurements by transmission and reflection of electrons. Experimental evidence for the existence of surface plasmons has come from Braudmeier et al (1975)<sup>100</sup> who was able to detect the radiation emitted from their decay in Ag films. Comparison with optical measurements is also possible as it has been shown that the probability of a fast electron losing energy to a surface exciton is proportional to  $\text{Im} \left( \frac{1}{1 + \epsilon} \right)$ <sup>101</sup>.

### 3.3.3 Inter- and Intra-band Transitions and Ionization Losses

These transitions are single particle excitations whereas volume and surface plasmons are a many particle phenomenon. In inter-band transitions electrons from lower bands are excited to some higher partially filled band, the primary electron losing the difference in energy between the two bands. An ionization loss is similar and involves the excitation of electrons from a core level to empty states near or above the Fermi level. Intra-band transitions have much lower energies and involve the excitation of electrons from the lower regions of a band to the upper regions of the same band. These excitations have only recently become of interest in energy loss spectroscopy, often the earlier work was interpreted in terms of multiples of the plasmon oscillations.

Strong interband transitions contribute to structure in the  $\epsilon_1$  and  $\epsilon_2$  components of the dielectric constant<sup>102,92</sup> and can strongly influence the energy at which the plasmon oscillation of the valence electrons is observed. Raether (1965)<sup>91</sup> has shown that the presence of a strong interband transition, whose energy is less than the calculated free electron like plasmon energy, shifts the observed value to higher energies, whereas a strong interband transition of energy greater than the calculated plasmon energy has the opposite effect. This is a simplified picture as normally several interband transitions can be excited in solid and the situation is particularly confusing for the noble elements in which strong interband transitions are excited with an energy close to the plasmon energy. The low energy ( $\approx 5$  eV) structure in  $\epsilon_1$  and  $\epsilon_2$  shown in Fig. 3-3, is probably due to the excitation of interband transition.

1	2	← Transition Metals →										2	3	4	5	6
—	Be												—	—	—	—
Na	Mg											Al	—	—	—	—
K	Ca	—	Ti	V	Cr	Mn	Fe	Co	Ni	Cu	Zn	Ga	Ge	As	Se	
—	—	—	Zr	—	—	—	—	—	Pd	<u>Ag</u>	<u>Cd</u>	In	Sn	Sb	Te	
—	Ba	—	—	—	—	—	—	—	<u>Pt</u>	<u>Au</u>	—	Tl	Pb	Bi	—	

The numbers at the top of the columns indicate the number of outer s and p electrons.

Fig. 3-4. The Elements whose Characteristic Energy Losses have been Studied by Powell<sup>103</sup> and co-workers.

### 3.4 Plasmon Excitations in Solids

Characteristic energy loss experiments have been performed on pure elements, alloys and compounds and plasmon oscillations identified in these solids.

#### 3.4.1 Elements

Plasmon excitations in most of the elements have been identified and in general there is good agreement between the observed energy and the plasmon energy calculated by assuming that the valence electrons of the solid behave as a free-electron like gas. Fig. 3-4 summarises the elements studied by Powell (1962)<sup>103</sup> and his group, the elements for which agreement between the calculated and experimental plasmon energies is not so good are underlined, and for these elements the plasmon peaks in the observed loss spectra are difficult to identify. The results of Powell are regarded as reasonably accurate although their experiments were performed in ordinary vacuum ( $\sim 10^{-6}$  Torr.) on surfaces not characterized by AES. Most subsequently workers have tended to confirm the results obtained by Powell, for the elements shown in Fig. 3-4. Other elements have been more recently studied.

#### 3.4.2 Alloys

Table 3-1 summarises some of the alloy systems in which plasma oscillations have been identified. For alloys of free electron like metals, for instance Al - Mg system, the observed plasmon energy is in good agreement with the value calculated from the relative concentrations of the two elements, but a system involving one of the elements underlined in Fig. 3-4, usually has considerable structure so that plasmon identification is difficult.

TABLE 3-1

<u>Alloys</u>	<u>Reference</u>
Al - Mg, Cd - Mg, Cu - Ni	Hartley and Swan (1970) <sup>104</sup>
Ti - Al, Co - Al, V - Al, Ni - Al	Bakalin et al (1972) <sup>105</sup>
Se - As (glasses)	Rechtin & Averbach (1974) <sup>106</sup>
Al - Ag	Porter et al (1974) <sup>107</sup>

### 3.4.3 Compounds

Plasmon oscillations have been identified in a number of chemical compounds and again for most materials studied so far there is good agreement between the calculated energy and the observed loss. Table 3-2 summarises the reported work of Best (1962)<sup>108</sup> for some alkali halides and Table 3-3 shows the identification of plasmon losses in some other compounds.

The calculated value of the plasmon oscillation energy is based on regarding the electrons involved in the bond formation of the compound behaving in a free electron like manner to sustain plasmons. For instance in sodium chloride it is the one outer electron of sodium and the seven outer electrons of chlorine which interact to form a NaCl molecule and it is these electrons which are regarded as undergoing plasmon oscillations. But there are some problems for instance poor agreement is obtained with the observed losses for the mercury chalcogenides<sup>112</sup>, the values calculated are on the basis of the 12 outer electrons of Hg and the 4 outer electrons of S participating in the oscillation. On the other hand, good agreement is obtained between the calculated and observed plasmon energies in the case of PbS, on the basis of all 6 outer electrons of S participating. In the case of AgGaS<sub>2</sub>, CuGaS<sub>2</sub> theoretical and experimental values agree on the basis of 22 electrons per molecule, (11 from Ag, 3 from Ga, 4 from S) contributing to the solid free electron gas. These results indicate that the number of electrons an atom contributes to the free electron like gas which undergoes plasmon oscillation may vary with the chemical environment of the atom.

**TABLE 3-2. The Results Of Best(1962)<sup>108</sup> For The Alkali Halides  
Showing Good Agreement Between Calculated And  
Experimental Plasmon Energies.**

**Table 6**  
**Comparison between the Theoretical Valence Electron Plasma Energies and Observed Energy Losses (in eV)**

	LiF	LiCl	NaF	NaCl	NaBr	NaI	KF	KCl	KBr	KI	RbCl	CsBr	CsI
<b>Observed energy loss</b>	24.9	16.1	20.9	15.5	13.9	12.3	17.1	13.8	12.5	11.2	13.1	11.1	9.8
<b>Theoretical valence electron plasma energy</b>	25.8	18.0	21.0	15.7	14.4	12.7	16.8	13.3	12.4	11.2	12.3	11.8	10.7

TABLE 3-3 Plasmons in Compounds

<u>Compound</u>	<u>Z</u>	<u><math>\hbar\omega_p</math> (eV)</u>	<u><math>\Delta E</math> (eV)</u>	<u>Reference</u>
ZnS	4	17	17	109
PbS	5	16	15	109
SbS <sub>3</sub>	5.6	18	19	109
MoS <sub>2</sub>	6	23	21	110
PbTe	5	14	15	109
PbSe	5	15	15	109
Mica	4.7	24	25	111
BeO	4	29	29	110
MgO	4	25	25	110
Li <sub>2</sub> CO <sub>3</sub>	4	24	24	110
Ca(OH) <sub>2</sub>	3.2	21	22	110
MoO <sub>3</sub>	6	24	25	110
SiO <sub>2</sub>	5.3	25	25	110
Al <sub>2</sub> O <sub>3</sub>	4.8	27	25	110
TeO <sub>2</sub>	6	23	23	110
SnO <sub>2</sub>	4	26	18	109
KBr	4	13	20	110
KCl	4	14	13	109
NaCl	4	16	16	109
GaP	4	16.3	16.9	95
GaAs	4	12.3	14.7	95
InSb	4	11.5	12.0	95
HgS	8	21.5	20.8	112
HgSe	8	19.8	17.2	112
HgTe	8	18.1	14.7	112
AgGaS <sub>2</sub>	5.5	18.9	18.5	113
CuGaS <sub>2</sub>	5.5	19.9	19.0	113

TABLE 3-3 Plasmons in Compounds

KEY:

- $Z$  = number of valence electrons per atom involved in plasma oscillations.
- $\hbar\omega_p$  = calculated value of the plasmon energy.
- $\Delta E$  = observed value of the loss.

### 3.5 Recent Developments in CELS

We conclude our survey of electron energy loss spectroscopy by outlining some recent investigations using this technique. Apart from continuing progress in the study of elements, alloys and compounds there is an increasing application of CELS to the study of semi conductor surfaces using primary electron beams of energy  $\approx 100$  eV. These low energy electrons are particularly surface sensitive as the inelastic escape depth at these energies is  $\sim 3 - 4\text{\AA}$ , (Fig. 2-1). Structure has been observed in the CELS of the Si (111) face which has been assigned to surface states<sup>99</sup>, and the effect of oxygen adsorption on the characteristic losses of GaAs (110) has been studied by Luth and Russel (1974)<sup>114</sup>, surface features being strongly influenced by oxygen adsorption. Studies have also been carried out to probe the empty conduction band states by exciting core level electrons with a primary beam. Ludeke and Esabi (1974)<sup>115</sup> have excited the 3d electrons of Ge and Ga (in GaAs) to probe the empty conduction band states of these solids. Also a similar study on Ge (111) has been carried out by Rowe (1974)<sup>116</sup>.

This concludes the survey of the background literature relevant to the techniques of AES and CELS. The next chapter describes the construction of a suitable apparatus in which AES and CELS studies can be performed on solid targets.

### 3.5 Recent Developments in CELS

We conclude our survey of electron energy loss spectroscopy by outlining some recent investigations using this technique. Apart from continuing progress in the study of elements, alloys and compounds there is an increasing application of CELS to the study of semi conductor surfaces using primary electron beams of energy  $\approx 100$  eV. These low energy electrons are particularly surface sensitive as the inelastic escape depth at these energies is  $\sim 3 - 4\text{\AA}$ , (Fig. 2-1). Structure has been observed in the CELS of the Si (111) face which has been assigned to surface states<sup>99</sup>, and the effect of oxygen adsorption on the characteristic losses of GaAs (110) has been studied by Luth and Russel (1974)<sup>114</sup>, surface features being strongly influenced by oxygen adsorption. Studies have also been carried out to probe the empty conduction band states by exciting core level electrons with a primary beam. Ludeke and Esabi (1974)<sup>115</sup> have excited the 3d electrons of Ge and Ga (in GaAs) to probe the empty conduction band states of these solids. Also a similar study on Ge (111) has been carried out by Rowe (1974)<sup>116</sup>.

This concludes the survey of the background literature relevant to the techniques of AES and CELS. The next chapter describes the construction of a suitable apparatus in which AES and CELS studies can be performed on solid targets.

## CHAPTER 4

### DESIGN, CONSTRUCTION AND OPERATION OF THE APPARATUS

#### 4.1 Introduction

Our basic need was to construct an apparatus for the purposes of studying solid surfaces by using electron beam spectroscopy. For any kind of meaningful results, experiments have to be performed in an ultra high vacuum. This is because a "clean" metal surface exposed to an ambient pressure of  $10^{-6}$  Torr of an active gas (Co, H<sub>2</sub>, O<sub>2</sub> etc.) will become covered by adsorbed atoms in a matter of seconds. Consequently an apparatus for realising a pressure of  $10^{-9}$  -  $10^{-10}$  Torr is needed for sufficient time to be available for measurements. In addition a good resolution electron spectrometer, which is capable of use as an Auger and characteristic energy loss spectrometer, is required. The apparatus must also incorporate in-situ specimen surface cleaning facilities, as well as a gas inlet system by means of which pure gases can be admitted, at a controlled rate, into the vacuum chamber to allow adsorption studies to be performed.

In this chapter the construction of such an apparatus is described. The design and the majority of the construction work was carried out at the University of Keele, with the assistance of the technical staff. Consequently the apparatus constructed is of a much lower cost than commercially available systems of equivalent performance. The design, construction and operation of the apparatus is considered to form a major part of the Ph.D. programme.

## 4.2 The Vacuum Chamber

To obtain a system of realising such low pressures ( $<10^{-8}$  Torr), the vacuum chamber was constructed from 18 gauge (1/16th ins. thick) EN58E stainless steel sheet. This has the advantage of high tensile strength and can be cyclically baked up to  $450^{\circ}\text{C}$  without degradation, such treatment being necessary as the chamber has to be outgassed at a high temperature to achieve UHV pressures. All the joints were sealed by argon arc welding. The chamber has a cylindrical shape entrance in to which was provided by a number of ports ranging in size from standard  $2\frac{1}{4}$  ins. flanges to 8 ins. flanges. These flanges can be vacuum sealed by copper gaskets sitting on a knife edge. A schematic diagram of the main chamber is shown in Fig. 4-1 and the proposed uses for the various parts are labelled, a photograph of the main chamber in actual use is shown in Plate 1.

### 4.2.1 The Initial Pumping Scheme

The internal surface area of the vacuum chamber was estimated to be  $\approx 12,000$  sq. cms. The outgassing rate of stainless steel after vacuum bake out is  $\sim 2 \times 10^{-12}$  Torr litres  $\text{Sec}^{-1}$   $\text{cms}^{-2}$ , so that in the absence of any leaks, a pumping speed of  $100$  litres  $\text{sec}^{-1}$  would produce a vacuum  $\approx 2 \times 10^{-10}$  Torr. Using this figure as a guide suitable vacuum pumps required to produce UHV were selected and in the initial pumping arrangement a total of four pumps were attached to the stainless steel chamber. These were:

a) A sorption pump, (Ferranti type FCD 23)<sup>117</sup>, using a molecular sieve type 5A. This is capable of roughing the chamber from atmosphere to a pressure of  $\sim 10^{-3}$  Torr.

b) A Ferranti<sup>117</sup> RJD 50 titanium diode sputter ion pump (nominal pumping speed  $50$  litres  $\text{sec}^{-1}$ ),

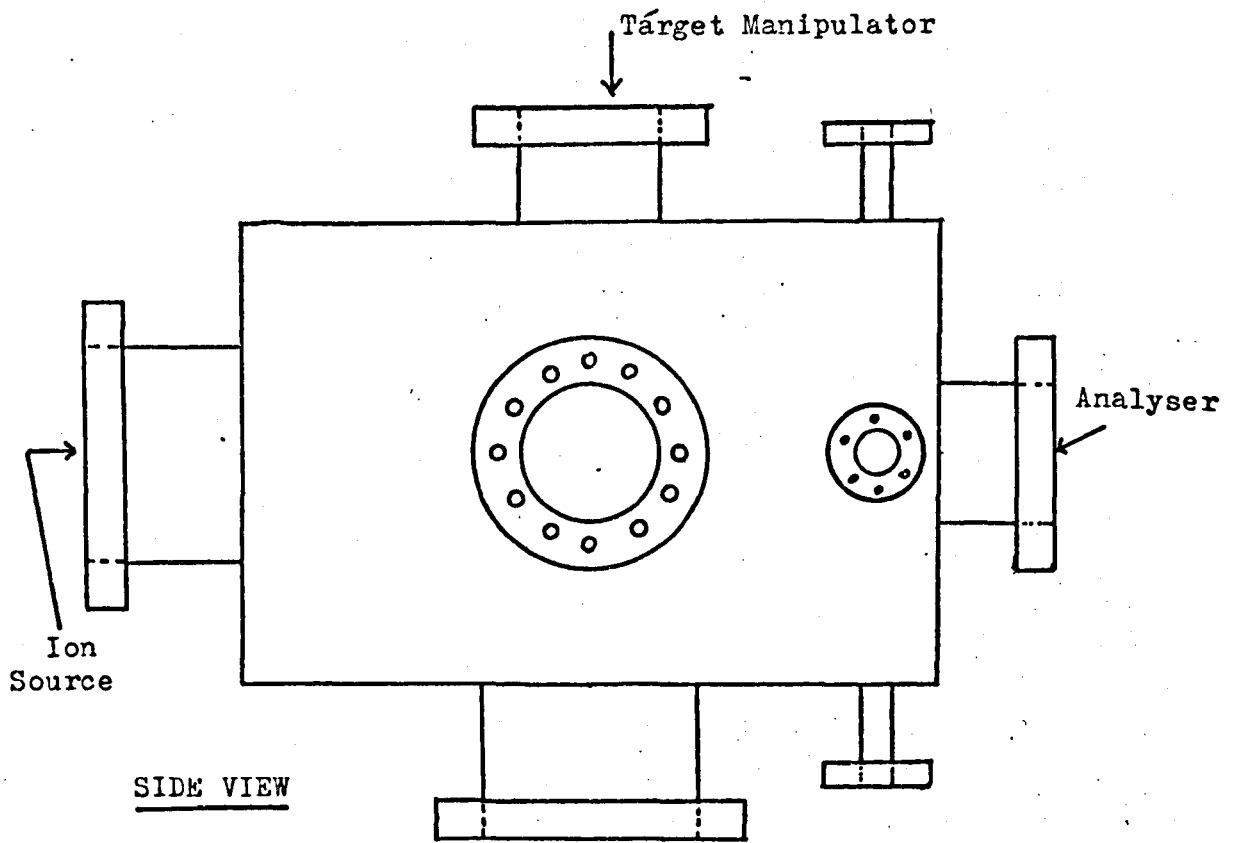
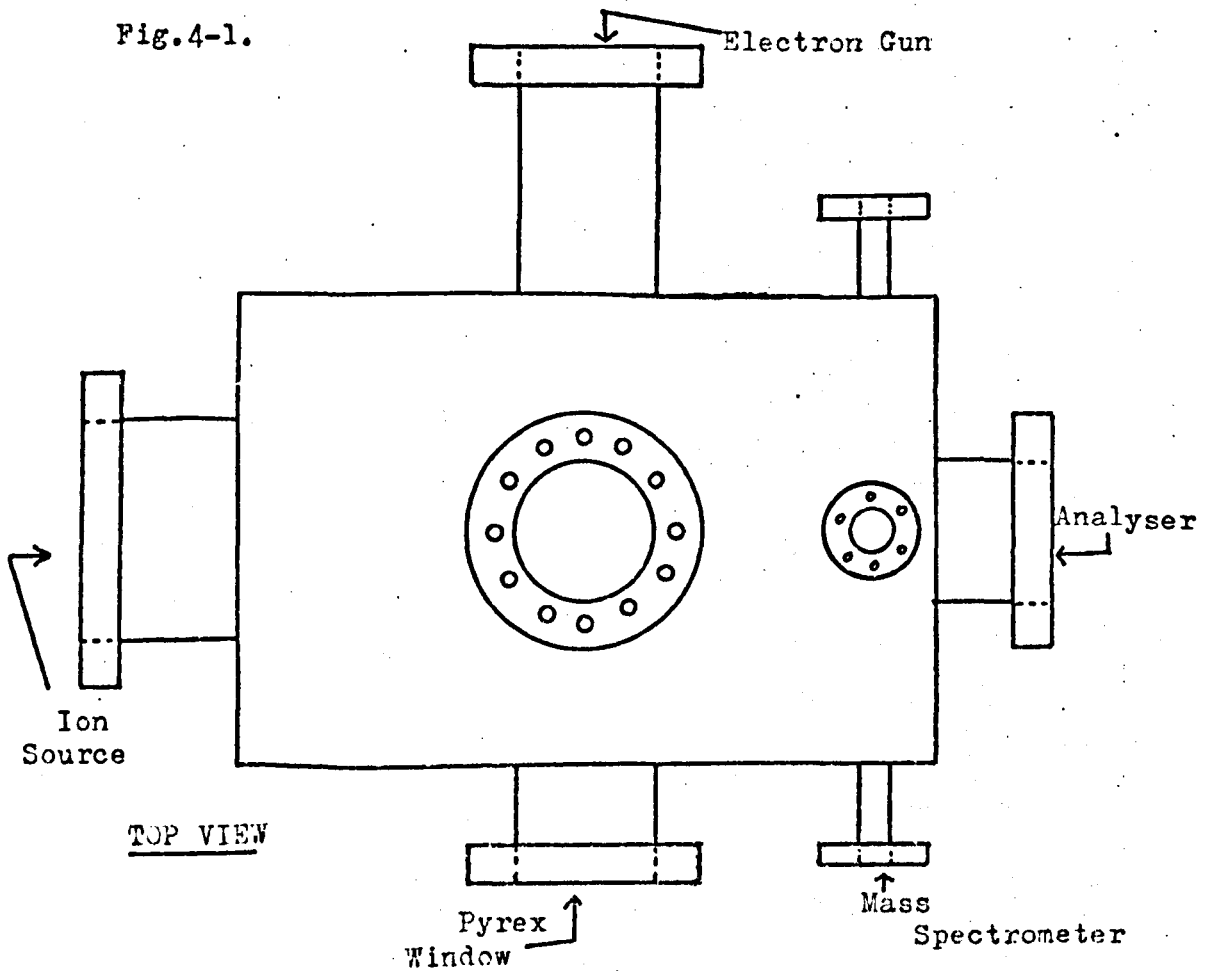


Fig.4-1.



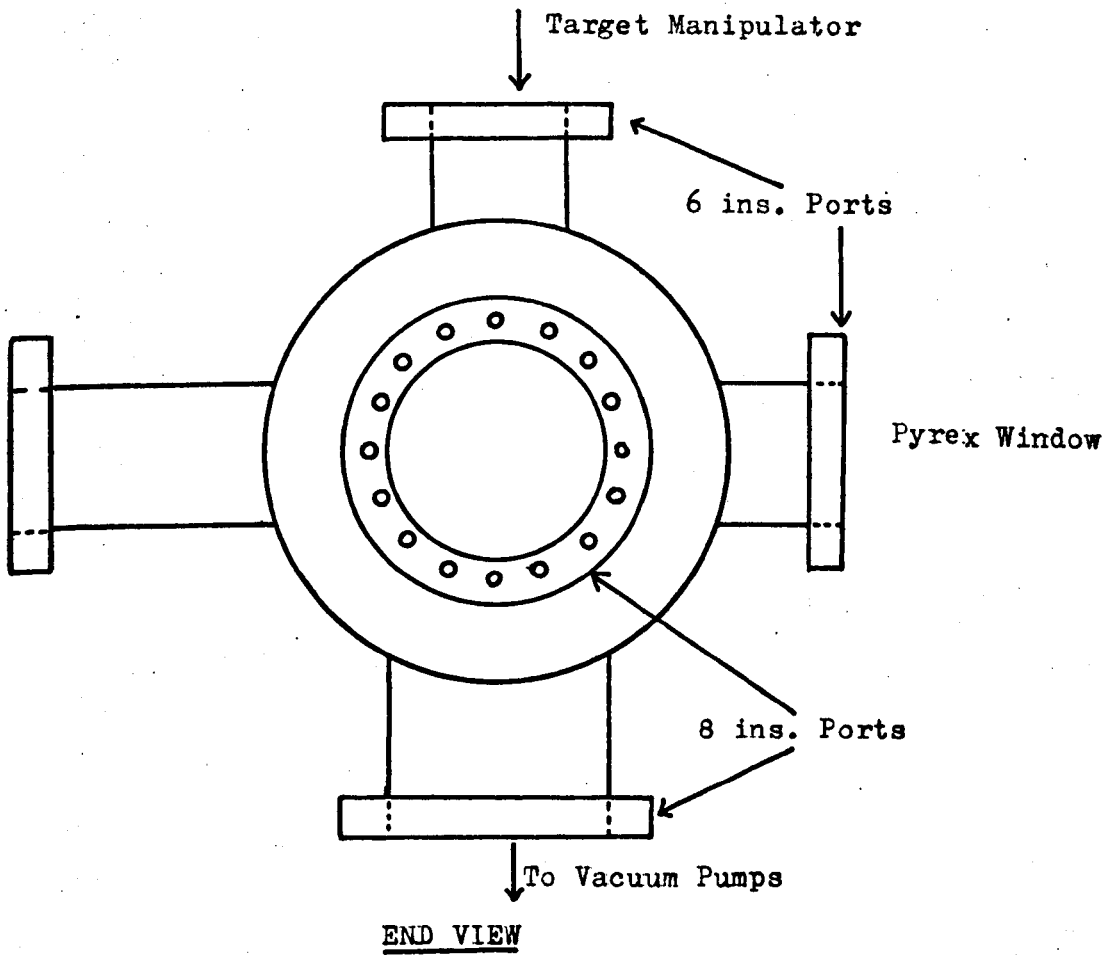


Fig.4-1. A Schematic Diagram of the Main Chamber, Showing the Uses of The Various Ports.

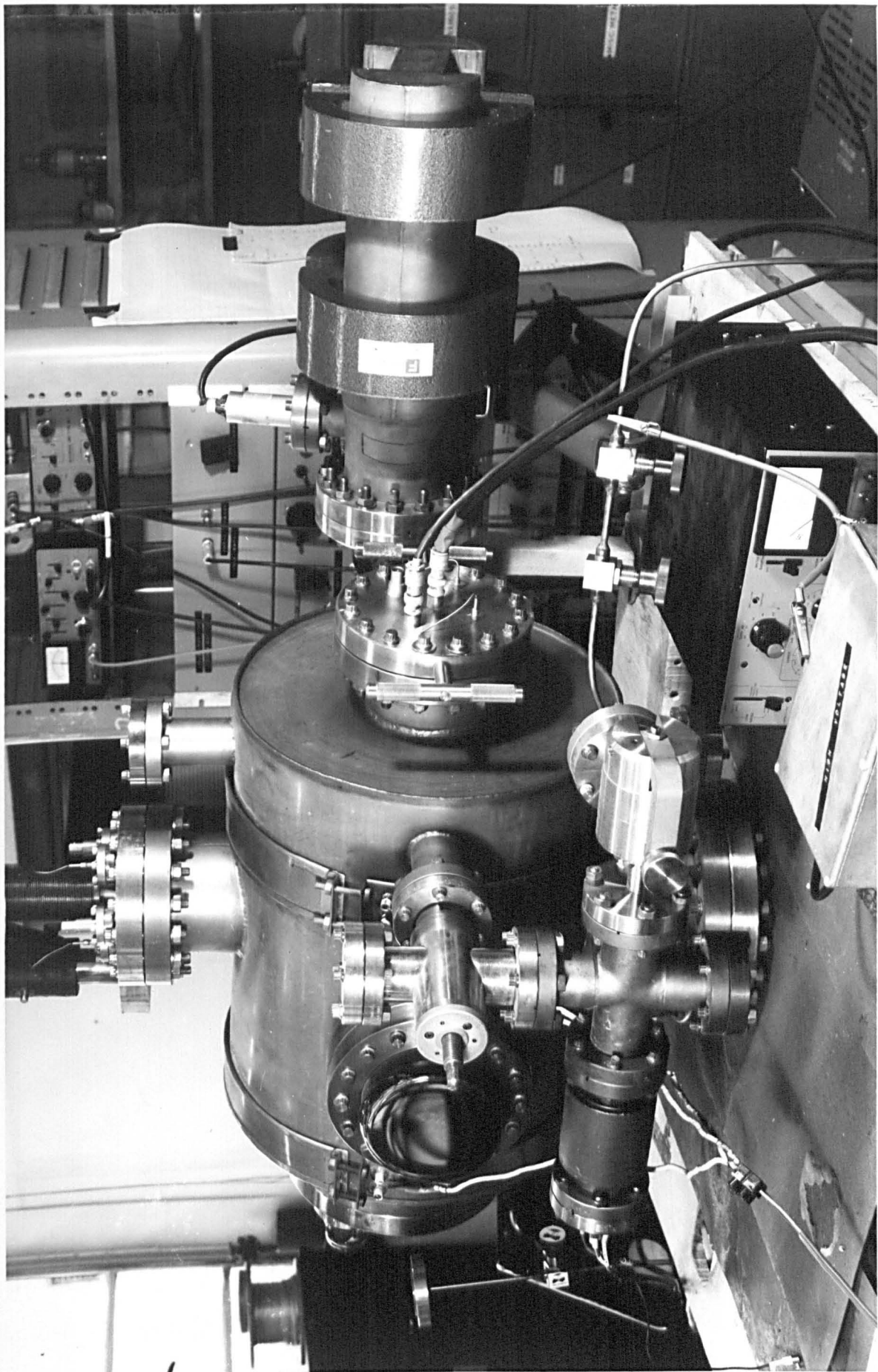


PLATE 1

c) An A.E.I. triode electrostatic getter ion pump, type 120 (nominal pumping speed 120 litres sec<sup>-1</sup>).

d) A S.A.E.S. SORB-AC cartridge pump. This is another type of getter pump using a zirconium alloy as the gettering element (nominal pumping speed  $\sim$  200 litres sec<sup>-1</sup>).

These are shown attached to the vacuum chamber in Fig. 4-2.

The sorption pump (a) was needed to reduce the pressure within the chamber sufficiently for the high vacuum pumps to start operating. The Ferranti pump was a standby measure because it had been found to be so reliable in the past but the ultimate aim was to pump the chamber to U.H.V. using the triode electrostatic and S.A.E.S. getter pumps only, because these two pumps did not require a magnetic field for their operation. We wanted to avoid using pumps which depended for their operation on magnetic fields due to the influence these would have on the electron optics of the energy analyser.

Using these pumps we attempted to evacuate the chamber. It was found that while the Ferranti pump was operating normally, the triode and SAES getter pumps were liberating gases into the vacuum chamber, that is the pressure in the chamber would decrease when these pumps were switched off. The manufacturers recommended activation procedure was tried on the SAES getter pump element without any detectable improvement in its pumping speed. It is believed that the hot elements inside the pumps were acting as a source for the production of methane (CH<sub>4</sub>) gas by reacting with the active gases within the vacuum chamber. The manufacturers recommended procedures for operating these pumps were repeated a number of times without any improvement in the vacuum obtained. Eventually it was concluded that the triode and SAES getter pumps would not evacuate an unbaked chamber.

Before proceeding any further a Varian quadruple mass analyser

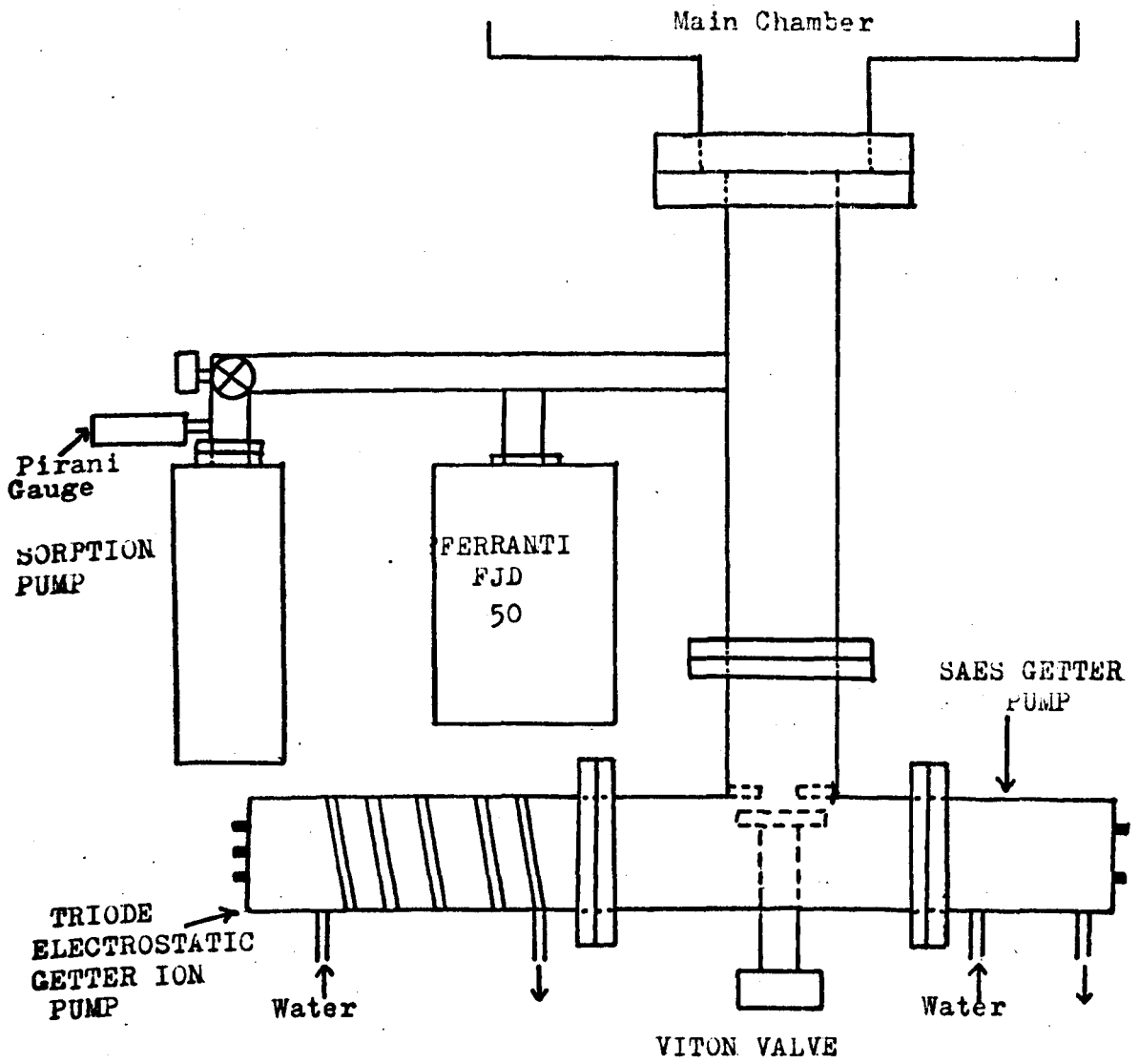


Fig.4-2. The Initial Pumping Arrangement Using Getter Pumps

(see section 4.3.3) was attached to the vacuum chamber and a thorough leak-testing procedure carried out to exclude the possibility of an inlet of gas preventing the operation of these pumps. The chamber was pumped by the Ferranti FJD 50 during the leak testing. This was the second time the chamber and ancillary equipment were leak tested, as a testing procedure was carried out during the welding and construction stage with a 20th Century<sup>119</sup> leak detector. No leaks could be detected by the mass spectrometer.

The system was then baked, while being evacuated, to a temperature of 350° - 400°C by placing a specially constructed ceramic wool oven over the main chamber, for a period of 24 hours. This is the normal outgassing procedure for obtaining UHV pressures. During the baking the chamber was initially pumped by the sorption pump until the pressure was low enough for the Ferranti ion pump to be started. The triode and SAES getter were not operated during the baking stage.

After baking the pressure, as registered by the leakage current on the FJD 50 ion pump, was measured to be  $2 \times 10^{-8}$  Torr. An improvement in the pressure was now attempted by operating the getter pumps. The manufacturers instructions were explicitly followed but again the effect of operating the triode and SAES getter pumps was to increase the pressure inside the chamber. The pumps were left switched on for a few days without any improvement in performance. The leak testing procedure was repeated, using the Varian quadruple mass analyser without discovering any undesired inlets of gas.

As activation procedures for the pump elements did not appear to be having any effect, it was decided at this stage to change the element of the SAES getter pump. The baking cycle was then repeated but again on operating the Triode and SAES getter pumps no improvement in the vacuum was obtained. In fact when the Ferranti ion pump was

switched off, with the getter pumps operating, the pressure in the chamber would rise to  $\approx 10^{-6}$  Torr from an initial value of  $\approx 1 \times 10^{-8}$  Torr.

Because of the poor performance of these getter pumps it was eventually decided to abandon them in favour of an alternative pumping scheme.

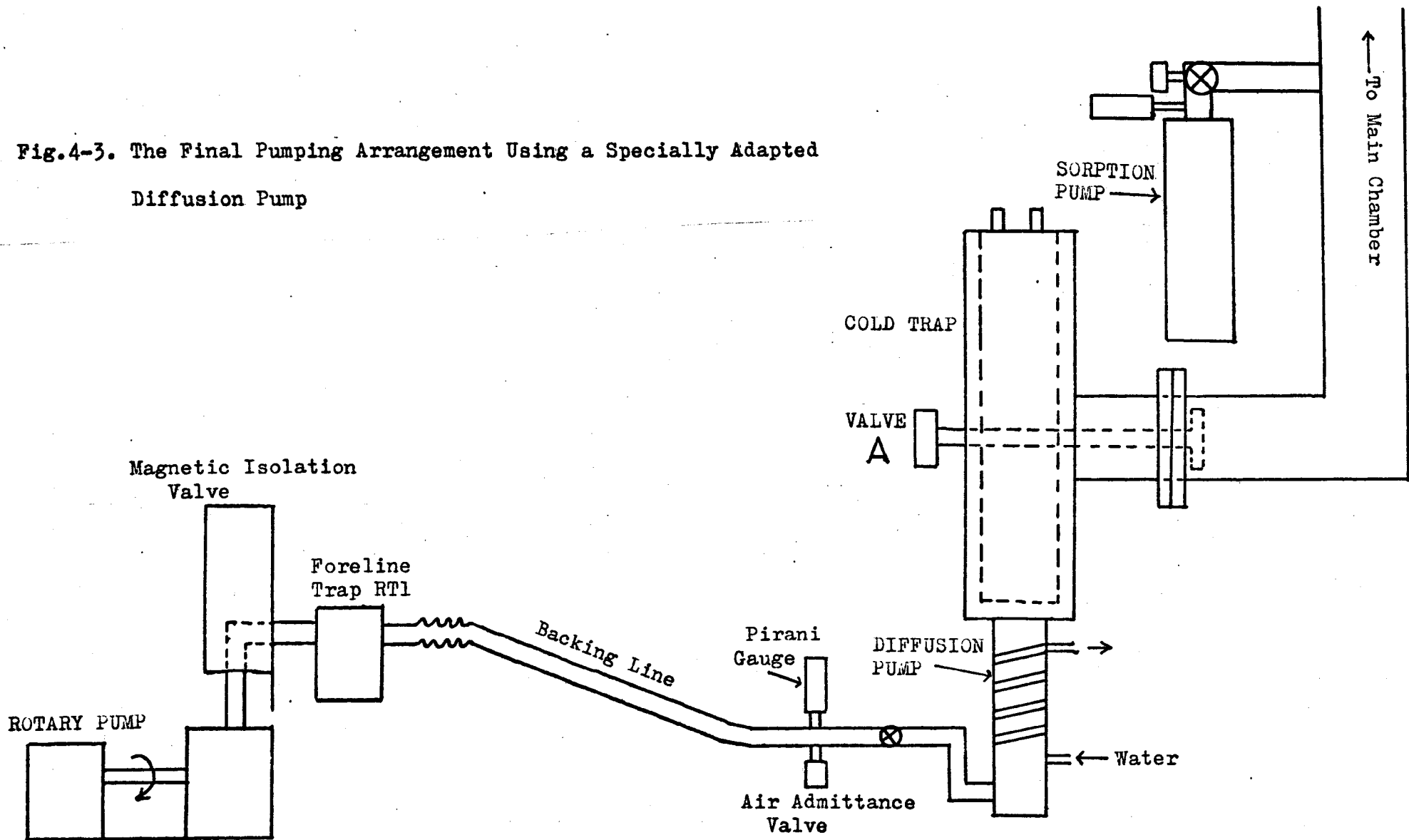
The possibility was considered of using a number of Ferranti ion pumps to evacuate the chamber, but these require large magnets for their operation whose effect would be undesirable on the electron spectrometer. At this stage of the project the electron spectrometer had been constructed and attempts were made to operate the electron gun and spectrometer with the chamber being pumped by the Ferranti ion pump, the getter pumps were isolated by the viton valve. The magnet was shielded by layers of "netic" material supplied by the Perfection Mica Co.<sup>120</sup>. Due to the stray fields, which could not be entirely eliminated, very poor signal to noise ratios for the Auger spectra were obtained as well as spurious peaks being present and frequently the analyser performance was so poor that Auger peaks could not even be detected.

Eventually it was decided to evacuate the chamber with a specially trapped Edwards diffusion pump, marketed by Vacuum Generators Limited. The specifications of this pump stated that it was capable of evacuating to UHV pressures. This pumping scheme is described in the next section.

#### 4.2.2 The Final Pumping Scheme

This is shown in Fig. 4-3. A diffusion pump has the great advantages for electron spectroscopy work that it operates without a magnetic field and pumps all gases, whereas ion or getter pumps have

Fig.4-3. The Final Pumping Arrangement Using a Specially Adapted Diffusion Pump



preferential pumping speeds for the active gases. The great disadvantage of diffusion pumps is that backstreaming of the working fluid can occur into the main chamber where it may contaminate the target under investigation. The diffusion pump we used attempts to minimise this disadvantage by incorporating a special cold trap between the pump and the chamber. The diffusion pump used was an Edwards EO2 Vapour Diffusion pump having a pumping speed of 150 litres  $\text{sec}^{-1}$ . The pump was fitted with a OCT 50 liquid air cold trap by Vacuum Generators Ltd. (V.G.). The unit was available complete from V.G. and by using "Santovac 5" as the working fluid of the diffusion pump the arrangement had the capability to pump to UHV pressures. This "Santovac" 5 is a polyphenyl ether with a low vapour pressure and a low tendency to backstream.

The backing line of the diffusion pump is also shown in Fig. 4-3. This consists of 1 ins diameter copper piping to which has been fitted a Pirani gauge, for measuring the backing line pressure, and an air admittance valve. The pressure in the backing line was maintained by a Metrovac rotary vacuum pump. A valve operated by a spring loaded solenoid was mounted next to the rotary pump as a safety factor. We used a V.G. RT1 foreline trap, containing molecular sieve type 13X to reduce the possibility of organic contamination, by the rotary pump oil, from reaching the chamber via the diffusion pump. A safety feature incorporated into the electrical connections was to operate the magnetic valve and the diffusion pump heater from one of the terminals of the three phase rotary pump motor electricity supply. Then any interruption of the electricity supply which switches off the rotary pump would also terminate the power to the diffusion pump heater and isolate the rotary pump by closing the magnetic valve, thus minimising any possible damage. The diffusion pump is additionally protected

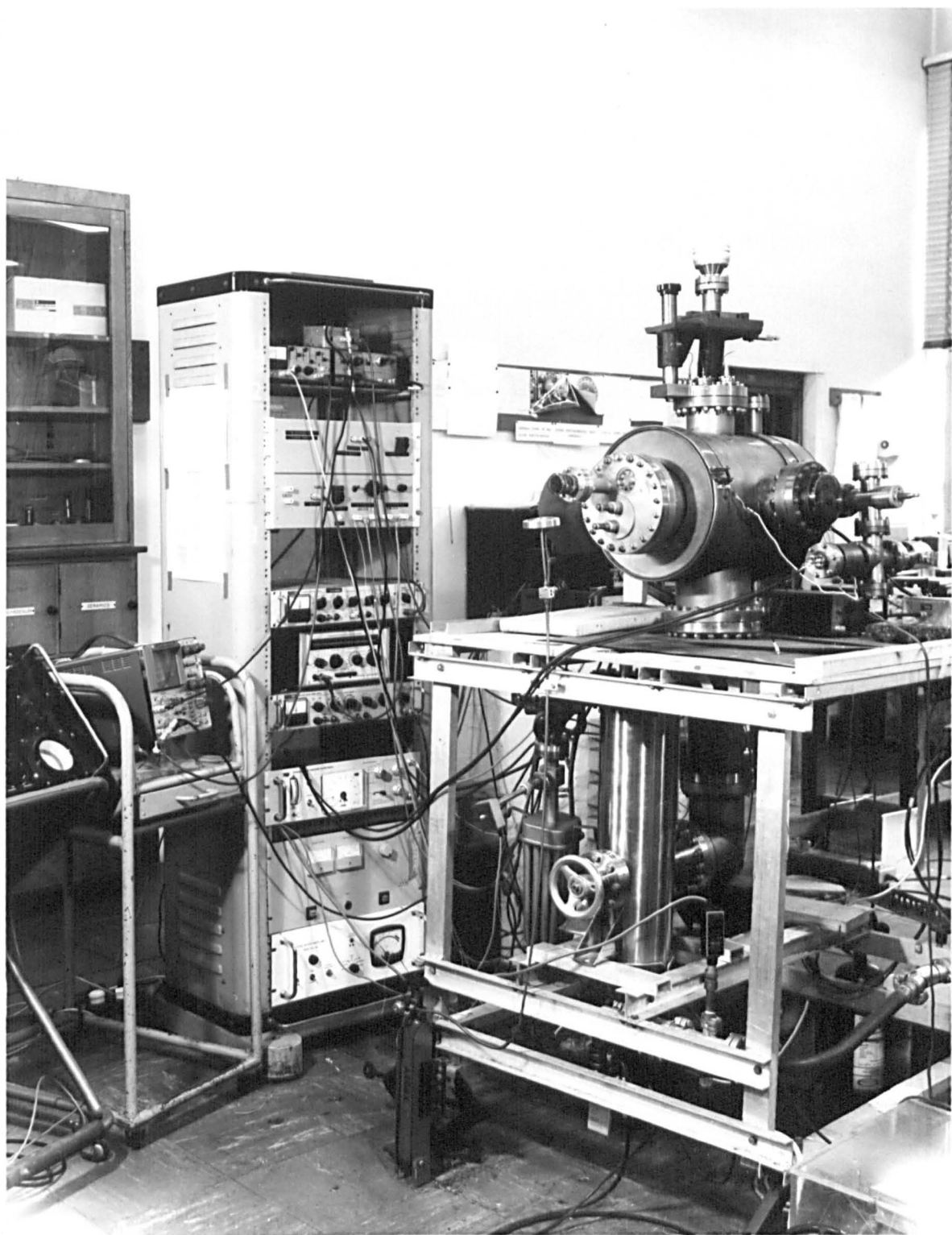


PLATE 2

from over-heating by a thermal cut out which switches off the heater electricity supply when the pump walls exceed 40°C in temperature.

The vacuum chamber is still rough pumped by the sorption pump to pressures of  $10^{-3}$  Torr before the diffusion pump isolation valve (A in Fig. 4-3) is opened. The Ferranti FJD 50 ion pump which has a removable magnet was still kept attached to the system, to assist in the pumping down of the chamber and also to maintain a low pressure within the chamber during periods when the diffusion pump had to be switched off, as for example at weekends. Diffusion pumped systems need careful attention because of their complexity and also to maintain the level of liquid air coolant in the cold trap for efficient operation whereas ion and getter pumps can be left unattended for long periods, once switched on. Plate 2 shows an overall view of the vacuum apparatus as pumped by the diffusion pump.

After pumping the vacuum chamber with the diffusion pump for a period of 72 hours a mass spectra of the gasses within the chamber was recorded with the quadruple mass analyser, and this is shown in Fig. 4.4. No hydrocarbon contamination could be detected, the gases within the chamber being predominantly carbon monoxide, carbon dioxide and oxygen. A small peak due to water vapour was also identified. The vacuum chamber, while being pumped by the diffusion pump, was then given a mild bake at a temperature of 150 - 200°C for 5 days. After turning off the heaters and further pumping for 3 days, the pressure inside the chamber was measured to be  $1 \times 10^{-9}$  Torr. (by the quadruple mass analyser) and the mass spectra of the gases within the chamber is shown in Fig. 4-5. The baking appears to have removed the oxygen and water vapour from the chamber leaving CO and CO<sub>2</sub> as the major contaminant gases. No heavy hydrocarbon molecules could be detected and subsequent baking and evacuating cycles failed to introduce such molecules into the

↑ Arb.  
Units

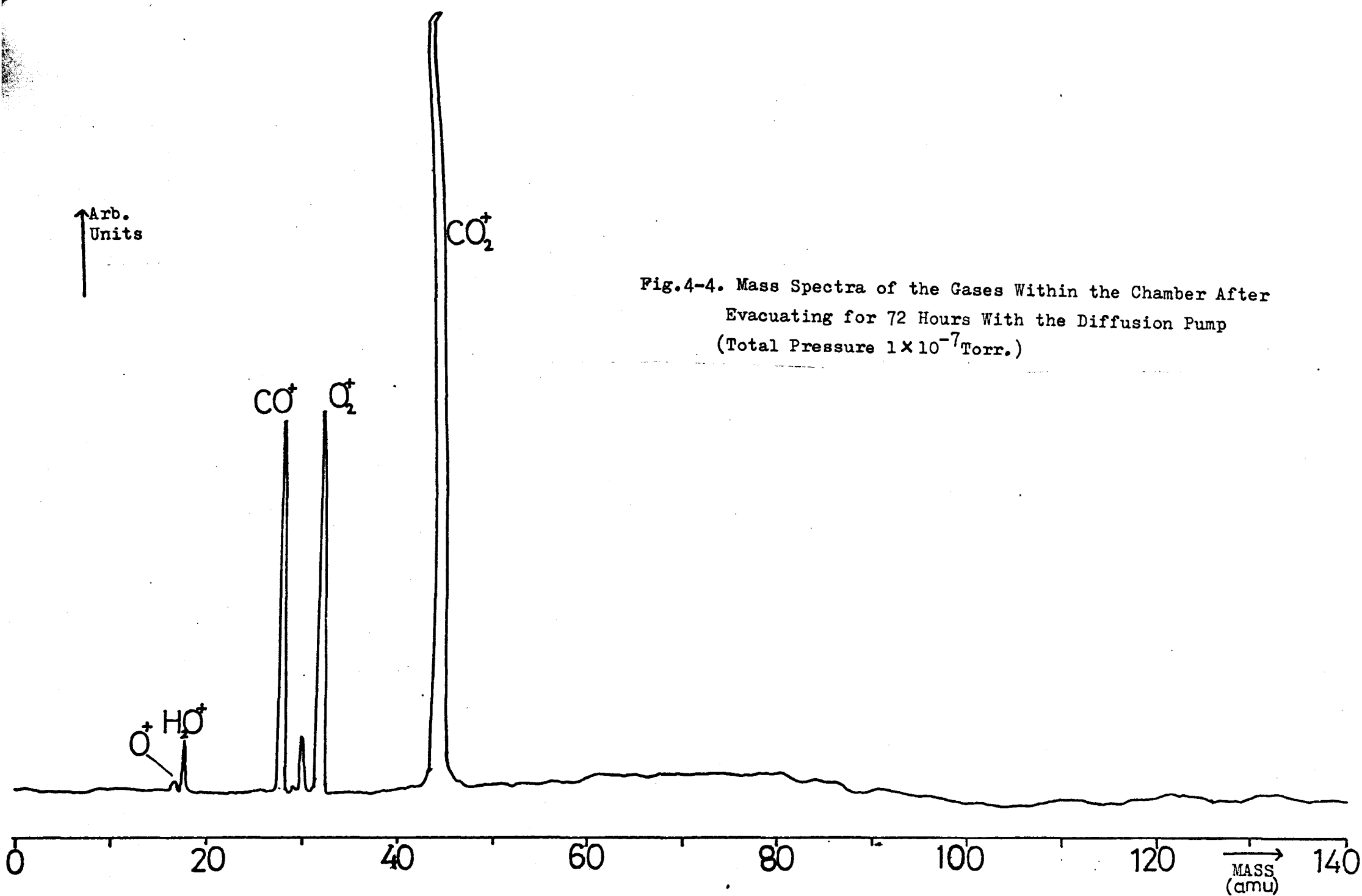
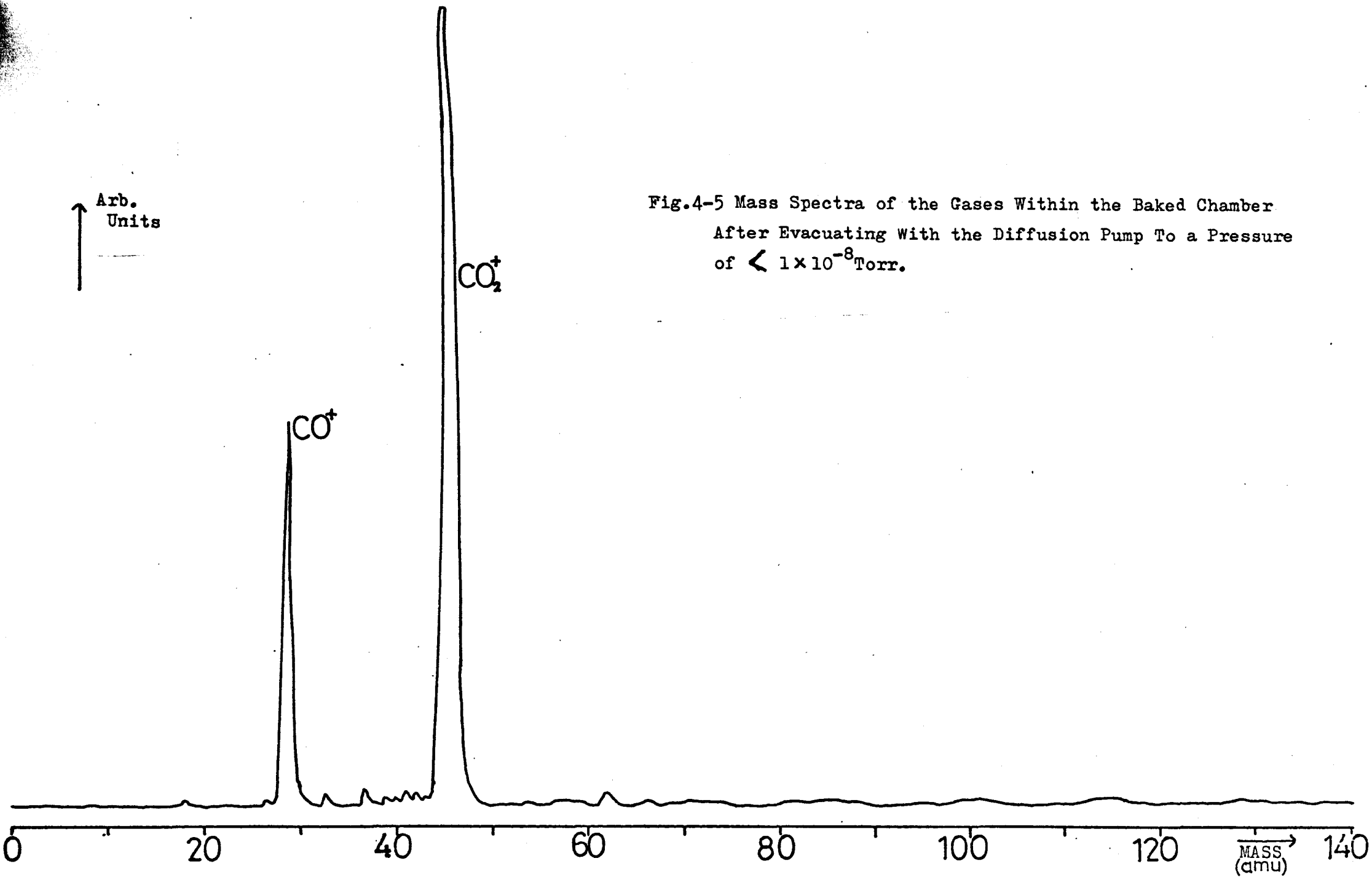


Fig.4-4. Mass Spectra of the Gases Within the Chamber After  
Evacuating for 72 Hours With the Diffusion Pump  
(Total Pressure  $1 \times 10^{-7}$  Torr.)

↑  
Arb.  
Units

Fig.4-5 Mass Spectra of the Gases Within the Baked Chamber  
After Evacuating with the Diffusion Pump To a Pressure  
of  $< 1 \times 10^{-8}$  Torr.



chamber indicating that as far as the mass spectrometer could detect a negligible amount of backstreaming was occurring from the diffusion pump working fluid.

In conclusion we can say that as far as the quadruple mass spectrometer can detect the diffusion pump provides a successful pumping arrangement for the vacuum chamber, free of hydrocarbon contaminants. The lowest pressure so far achieved has been measured to be  $5 \times 10^{-10}$  Torr and at these UHV pressures the ambient gases within the vacuum chamber are CO and CO<sub>2</sub>. During the operation of the electron spectrometer, the ion pump was switched off and the magnet removed a safe distance away. No consequent increase of the pressure within the chamber could be detected, probably because the pumping speed of the RJD 50 decreases rapidly for pressures below  $1 \times 10^{-8}$  Torr so that switching it OFF has an insignificant effect on the total pumping speed.

### 4.3 General Features

#### 4.3.1 The Universal Motion Target Manipulator

We needed a target manipulator capable of allowing horizontal, vertical and rotary motion of the specimen so that the target could be accurately positioned for energy analysis, surface cleaning operations and thin film evaporation.

Such a manipulator is shown in Plate 3. It consisted of three brass plates. One of these plates was free to slide on a pillar mounted vertically on the flange attaching the manipulator to the system. A screw arrangement ran through the centre of the pillar to which this plate was attached so that by turning the knob at the end, the plate could move vertically. Mounted on top of this plate

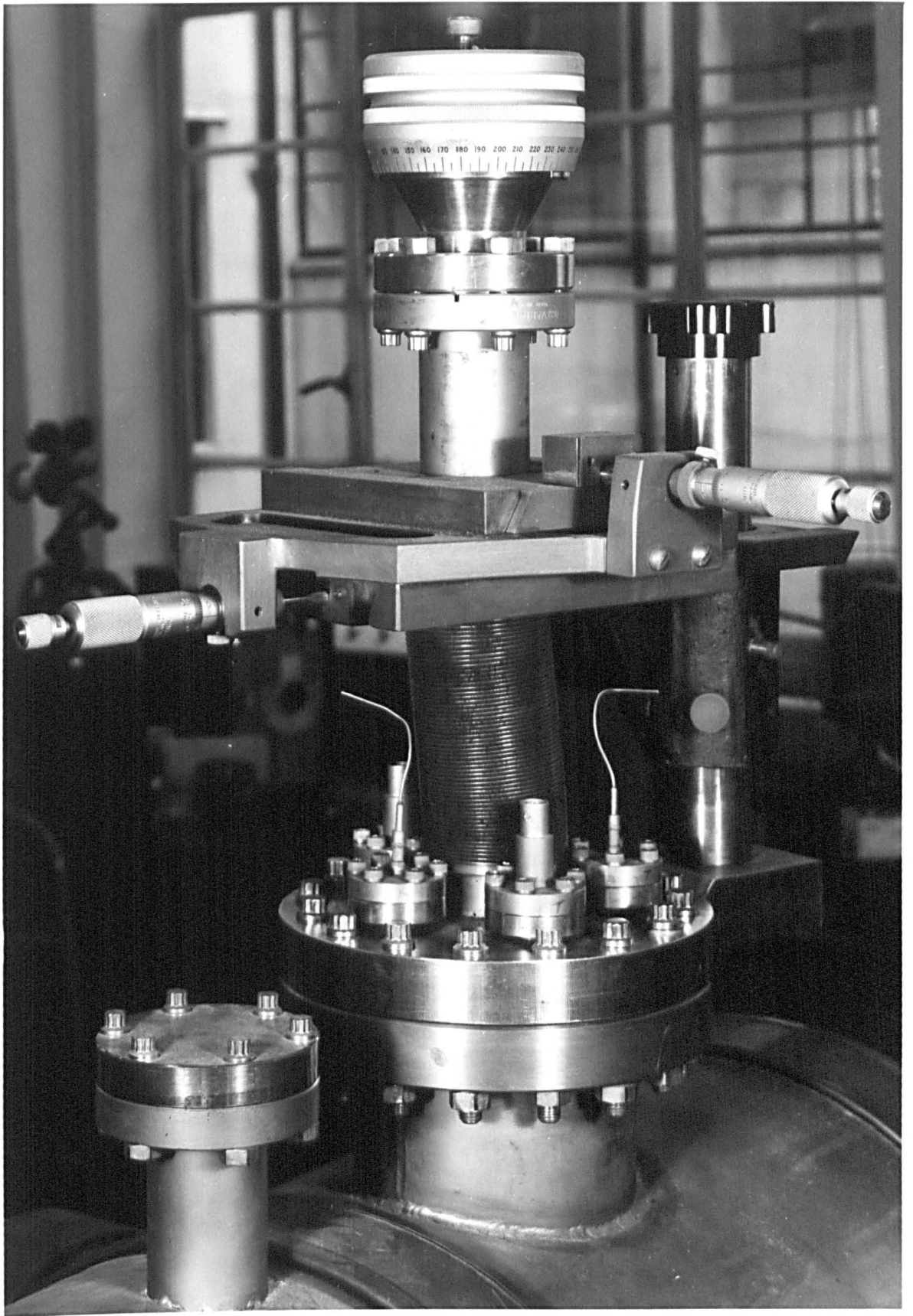


PLATE 3

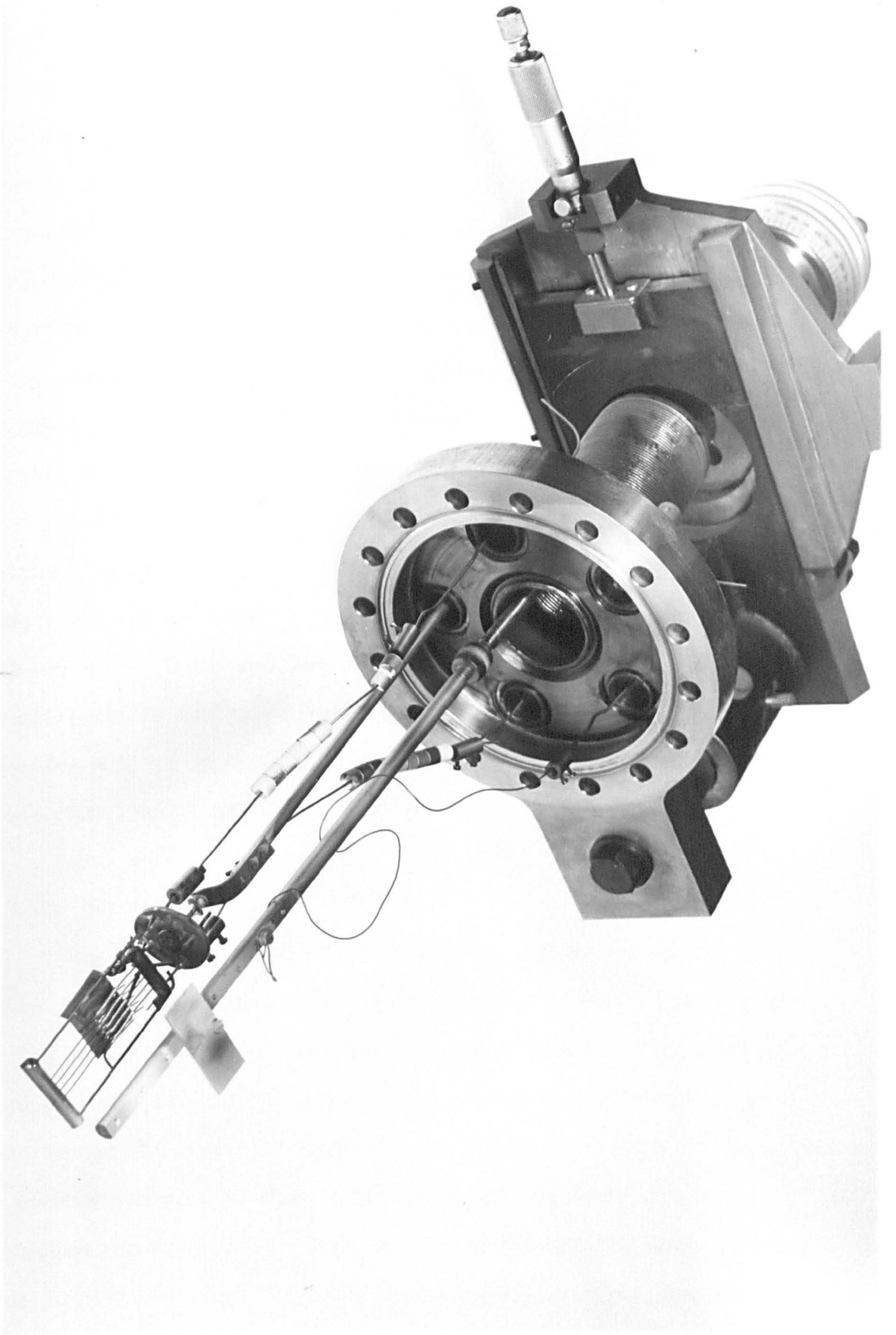


PLATE 4

were the other two brass plates which were capable of sliding in the x and y directions. One of these plates grips a linear bellows which accommodates the z motion of approximately 7 cms. The target was attached by means of a rod to an externally rotatable feed through so that by using this arrangement target movement in the x, y and z directions as well as rotation was possible. The constructional work for the manipulator was carried out in the University workshops resulting in considerable savings in costs.

Mounted on the target manipulator flange were five mini conflat. These were used to provide electrical feedthroughs into the vacuum chamber. At one stage of instrument operation, of the five feedthroughs, two were used to provide power to a projection lamp filament heater, two were used to provide connections for a thermocouple and one was used to provide contact to the target. The target rod consisted of two sections separated by an insulator so that the target could be earthed or used to measure the beam current from the electron gun, as necessary. Details of the target mounting and projection lamp filament are shown in Plate 4.

#### 4.3.2. The Electron Gun

The electron beam used to excite the transitions within the solid surfaces originated from a modified SE - 3K/5U<sup>121</sup> electron gun having electrostatic focusing and deflection plates. The original gun used a heated tungsten filament as the source of electrons but we experienced difficulty in aligning the filament relative to the grid to produce emission so that it was eventually replaced with a strontium oxide cathode. This has the advantage of a large emitting area for the electrons and lower operating temperatures than tungsten filaments but such cathodes are more easily poisoned and require

frequent replacement.

The rated maximum working voltage of the electron gun was 2.7 Kev, but we have used the SE - 3K up to 3.1 Kev and typically worked with primary electron voltages of 2.5 - 2.9 Kev for recording the Auger spectra. Typically electron beam currents of 100  $\mu$ A could be easily obtained from the gun for primary voltage exceeding 2 Kev. The electron beam current was measured by allowing the beam to strike the target, which was biased at 90 v + ve., the leakage current to earth was then measured with an Edwards D.C. Amplifier.

The electron gun was shielded with netic and conetic material to prevent interference from stray magnetic fields.

#### 4.3.3 Pressure Measurement

The pressure inside the chamber could be estimated by using the quadruple mass analyser, the ion gauge or the leakage current on the FJD 50 ion pump. The mass spectrometer was a Varian Associates Quadrupole Residual Gas Analyser model 974-0004 operated with an electron multiplier, at its output stage, to increase its sensitivity. This instrument could be used to measure the total pressure or the partial pressures of the ambient gases inside the vacuum chamber.

The ion gauge, supplied by V.G., was a Bayard-Alpert type model VG 10 operated by a IGP 3 control unit. This was capable of measuring pressures as low as  $2 \times 10^{-11}$  torr. Additionally a calibration curve was available for the leakage current in the ion pump versus the pressure, allowing pressures as low as  $5 \times 10^{-10}$  Torr to be estimated.

#### 4.3.4 Gas Admittance System

Two gas inlet systems had to be constructed to admit research grade purity gases into the vacuum chamber at a controlled rate. Argon

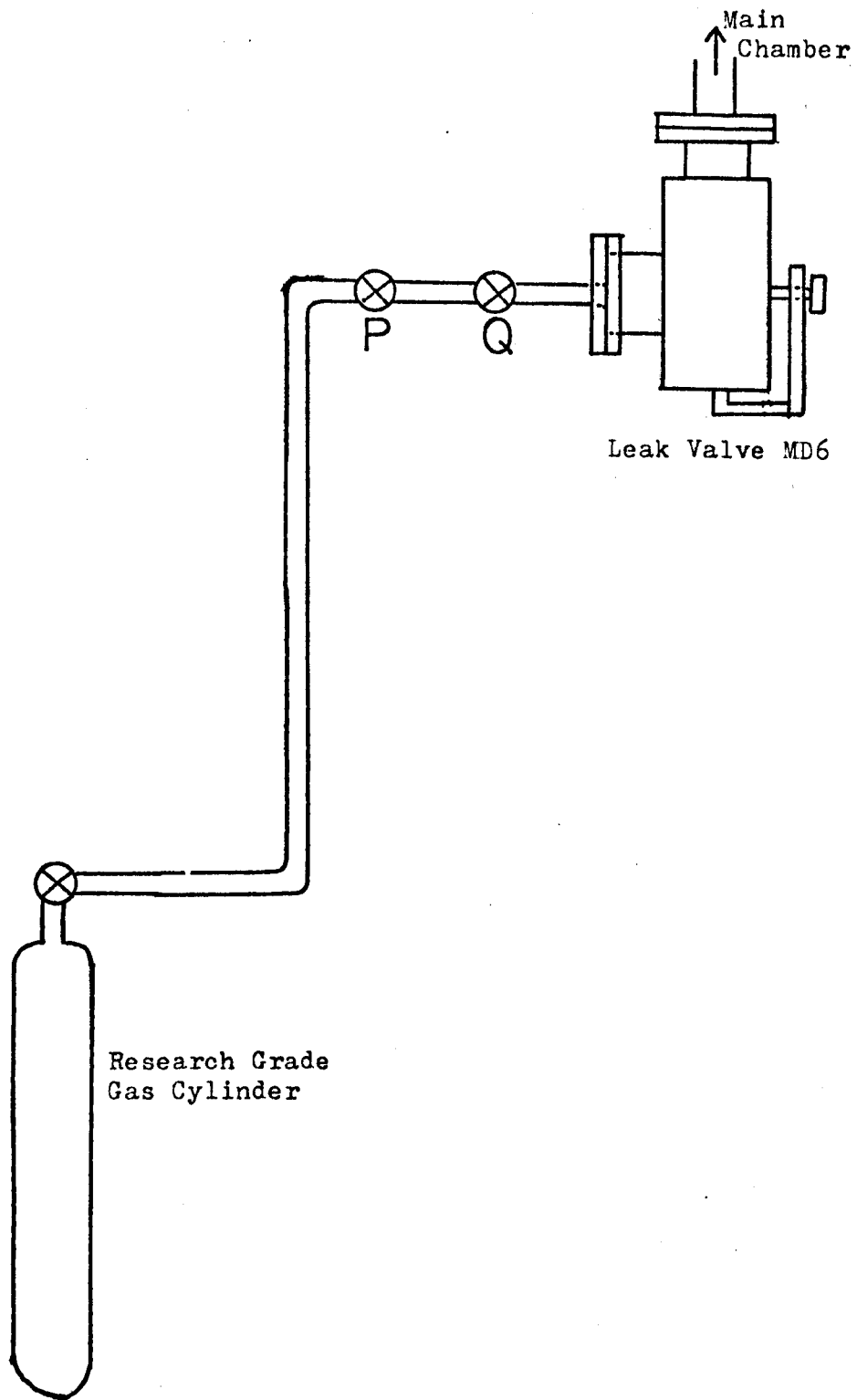


Fig.4-6. The Gas Admittance System.

needed to be admitted into the saddle field ion source (described in Section 4.4) to produce argon ions for the etching of surfaces and additionally an oxygen admittance system was needed to perform adsorption studies.

The oxygen gas admittance system is shown in Fig. 4-6. The cylinder containing the gas (supplied by Air Products at a purity of 99.995%) was connected by means of a  $\frac{1}{4}$  inch diameter stainless steel tube to two Nupro coarse leak valves<sup>122</sup>, labelled P and Q in Fig. 4-6. Connection was then made via another piece of  $\frac{1}{4}$  inch stainless steel tube to a fine control leak valve type MD6 (Vacuum Generators), which was attached to the vacuum chamber by a  $2\frac{3}{4}$  ins. flange. The argon gas admittance system was of a similar design.

To admit a pure gas into the chamber, the connecting tubes needed to be flushed clean of any impurity gases. The flushing was carried out, when the chamber had been pumped to a rough vacuum, by fully opening valves P, Q and MD6, and then partially opening the main valve, on the gas cylinder, a number of times for a few seconds. Then gas leaks from the cylinder through the tubes into the main chamber, effectively flushing out the impurity gases. All the valves were then closed and the vacuum chamber pumped to UHV pressures as normal. Typically in an experiment gas can be admitted into the chamber, at a controlled rate, by slowly opening MD6 and using the valves P and Q to regulate the gas pressure.

Fig. 4.7 shows the mass spectrum recorded during a controlled oxygen leak into the vacuum chamber. The initial mass spectrum was similar to Fig. 4-5 and the ion gauge was switched on during these measurements, it is thought that some of the oxygen is being converted into CO and CO<sub>2</sub> by the hot filament of the ion gauge. Fig. 4-8 supports this hypothesis as this mass spectrum was also recorded with

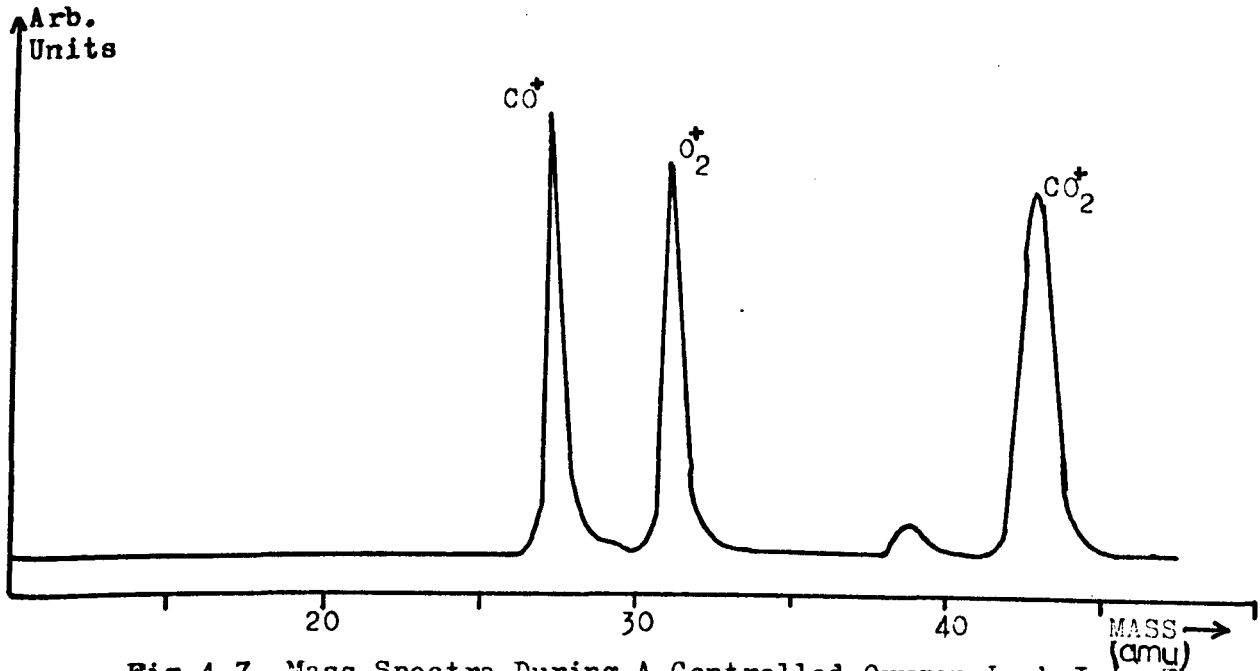


Fig.4-7. Mass Spectra During A Controlled Oxygen Leak Into The Chamber With The Ion Gauge SWITCHED ON

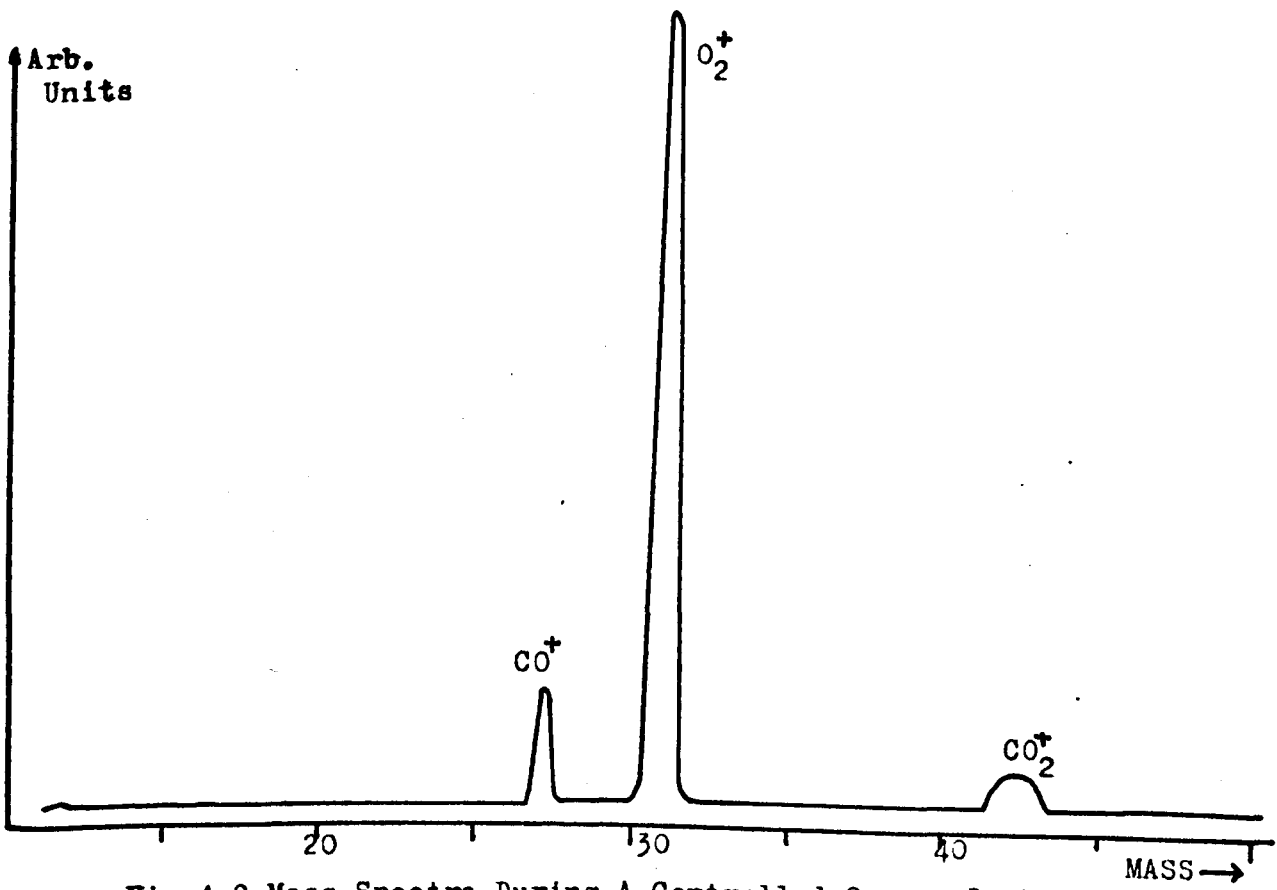


Fig.4-8 Mass Spectra During A Controlled Oxygen Leak Into The Chamber With The Ion Gauge SWITCHED OFF.

a controlled oxygen leak but with the ion gauge switched off. The pressure inside the chamber increased to  $6 \times 10^{-8}$  Torr during the oxygen leak (measured with the quadruple mass analyser) and the mass scan shows that now approximately 80% of the gas inside the chamber is oxygen at this leak rate.

#### 4.4 Surface Cleaning Facilities

A specimen in an ultra high vacuum environment does not necessarily have a "clean" surface so that in-situ specimen surface cleaning facilities had to be incorporated into the apparatus. A 1kw. projection lamp filament was mounted on the target flange (Plate 4) to allow specimen heating and an argon ion source was constructed to allow specimen etching, to generate a "clean" surface.

##### 4.4.1 Specimen Heating By Electron Bombardment

Target heating in the apparatus was accomplished by rotating the specimen and adjusting its height until it was directly opposite the projection lamp filament mentioned in 4.3.1. The filament was heated until electron emission occurs and by putting a +ve H.T. voltage on the target, the specimen surface was bombarded with electrons. The temperature to which the target became heated was measured with a chromel-alumel thermocouple and for the higher temperatures an optical pyrometer was used. Typically a target bombarded with a 100mA current of electrons of energy 10 kev would reach a temperature of about 2000<sup>o</sup>K. The target becomes "clean" by thermal desorption of the surface layers and impurities. Although specimen heating may cause other effects such as the diffusion of bulk impurities to the surface which may

limit the usefulness of this technique for surface cleaning.

The normal operational procedure was to firstly degas the projection lamp filament heater by slowly raising its temperature keeping the pressure in the chamber  $< 10^{-8}$  torr. When electron emission has started to occur, the target temperature was slowly raised again keeping pressure in the vacuum chamber below  $1 \times 10^{-8}$  torr until the required target temperature was reached. Targets could either be kept at a fixed temperature for long periods or flashed to a high temperature by quickly turning on the electrical power. This latter method is useful if there is a possibility of surface segregation occurring.

#### 4.4.2 The Argon Ion Source<sup>123</sup>

This device cleans a surface by etching away the top layers by high energy argon ion bombardment, any changes in surface structure produced can be subsequently restored by annealing. The device we constructed has the advantages that it is electrostatic and operates at a low argon gas pressure. The rate of removal of the surface atoms can be controlled so that the device can be used for depth profiling in combination with AES. Argon ion sputtering is a destructive technique and this disadvantage may limit its usefulness.

The construction of the sputterer was based on the papers of Fitch et al (1970, 1971)<sup>124, 125</sup>. The device consisted of a cylindrical cathode made of stainless steel tube, 6 cms. in diameter and 11.5 cms long. The ends of the tube were sealed with stainless steel discs, which also supported a pair of electrically isolated, loosely fitting anodes, as shown in Fig. 4-9. These anodes were two tungsten wires 12 cms. in length, 1.7 mm. diameter and placed 6 mm apart. These values were chosen from the papers of Fitch to maximise the

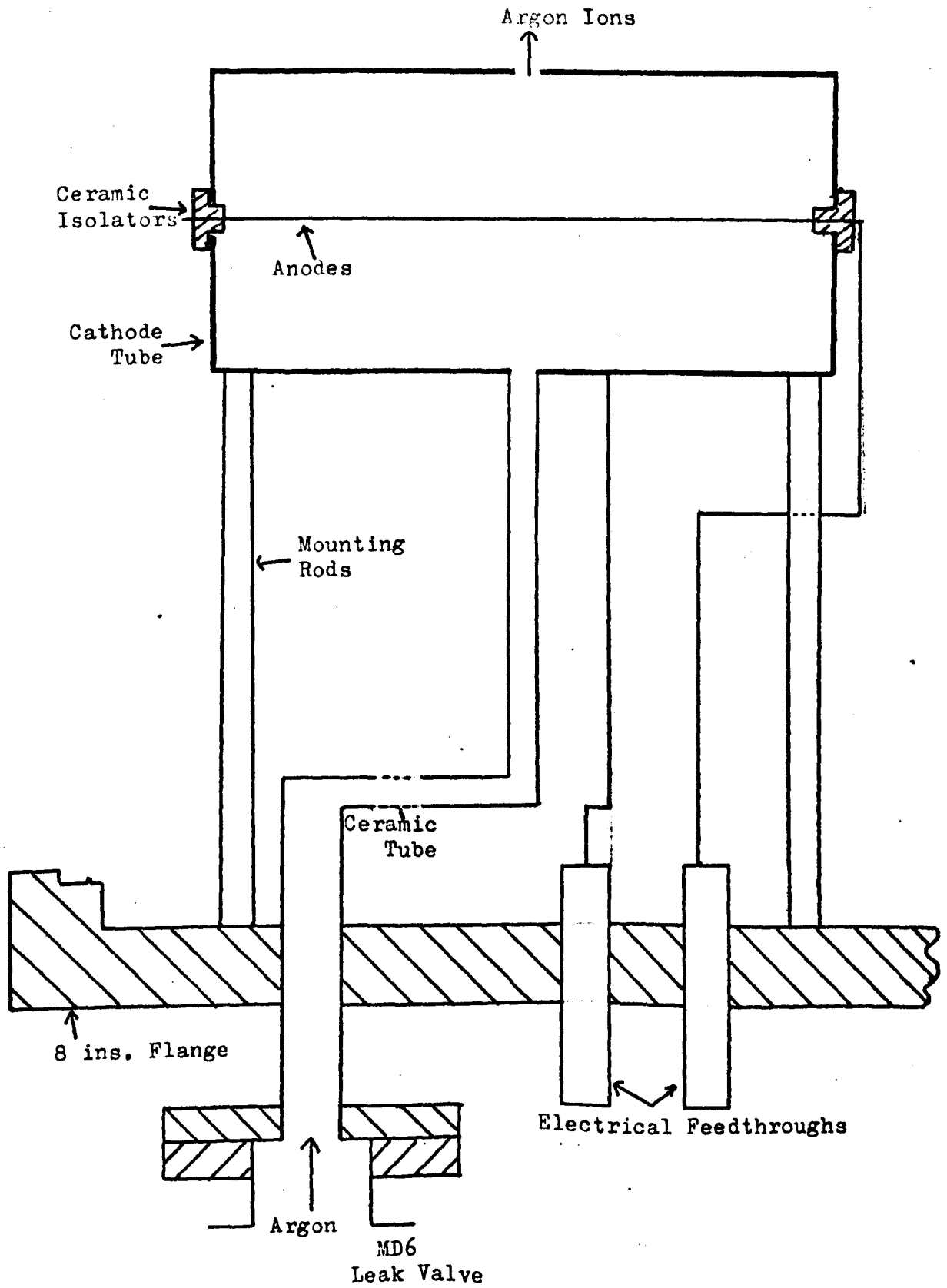


Fig.4-9. The Argon Ion Source.

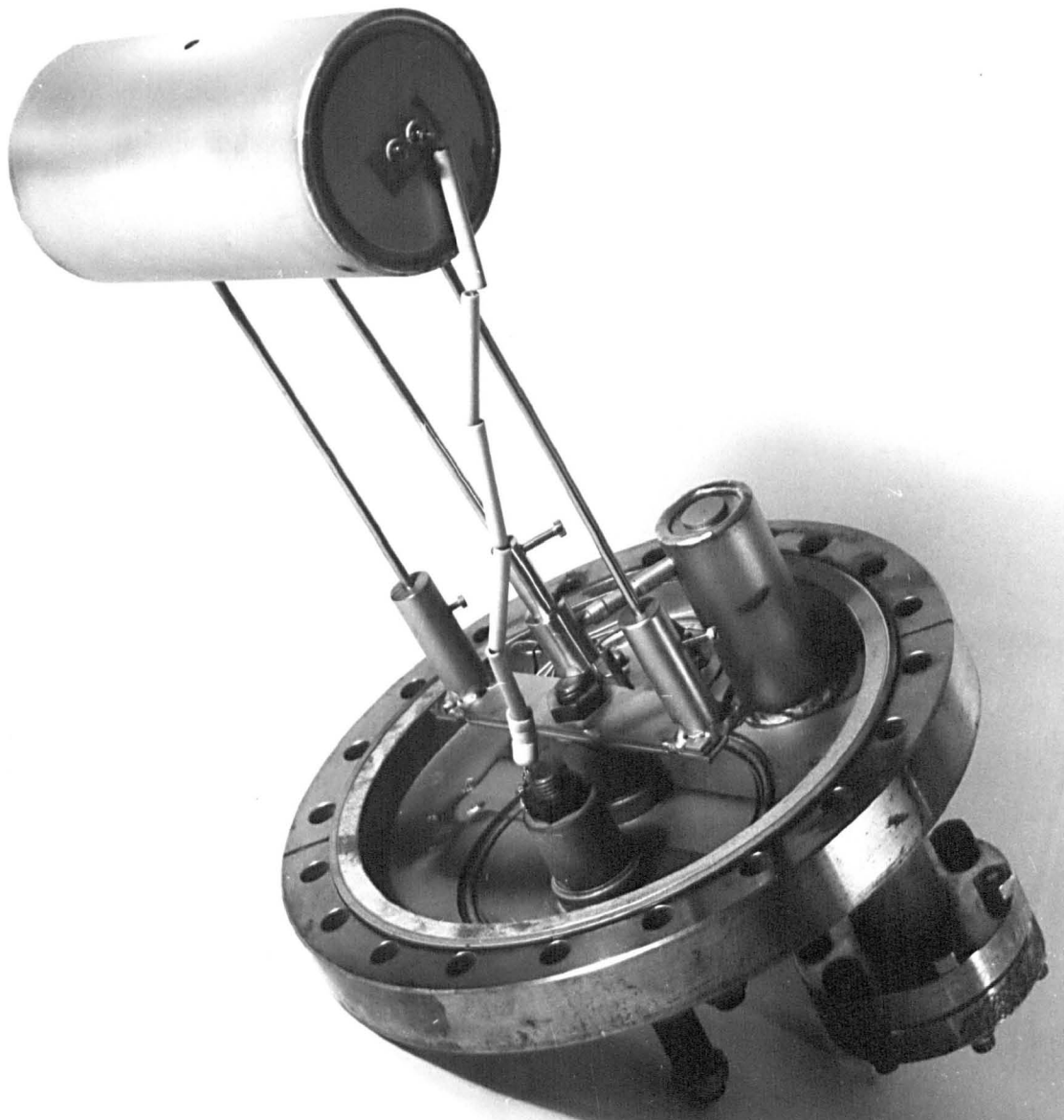


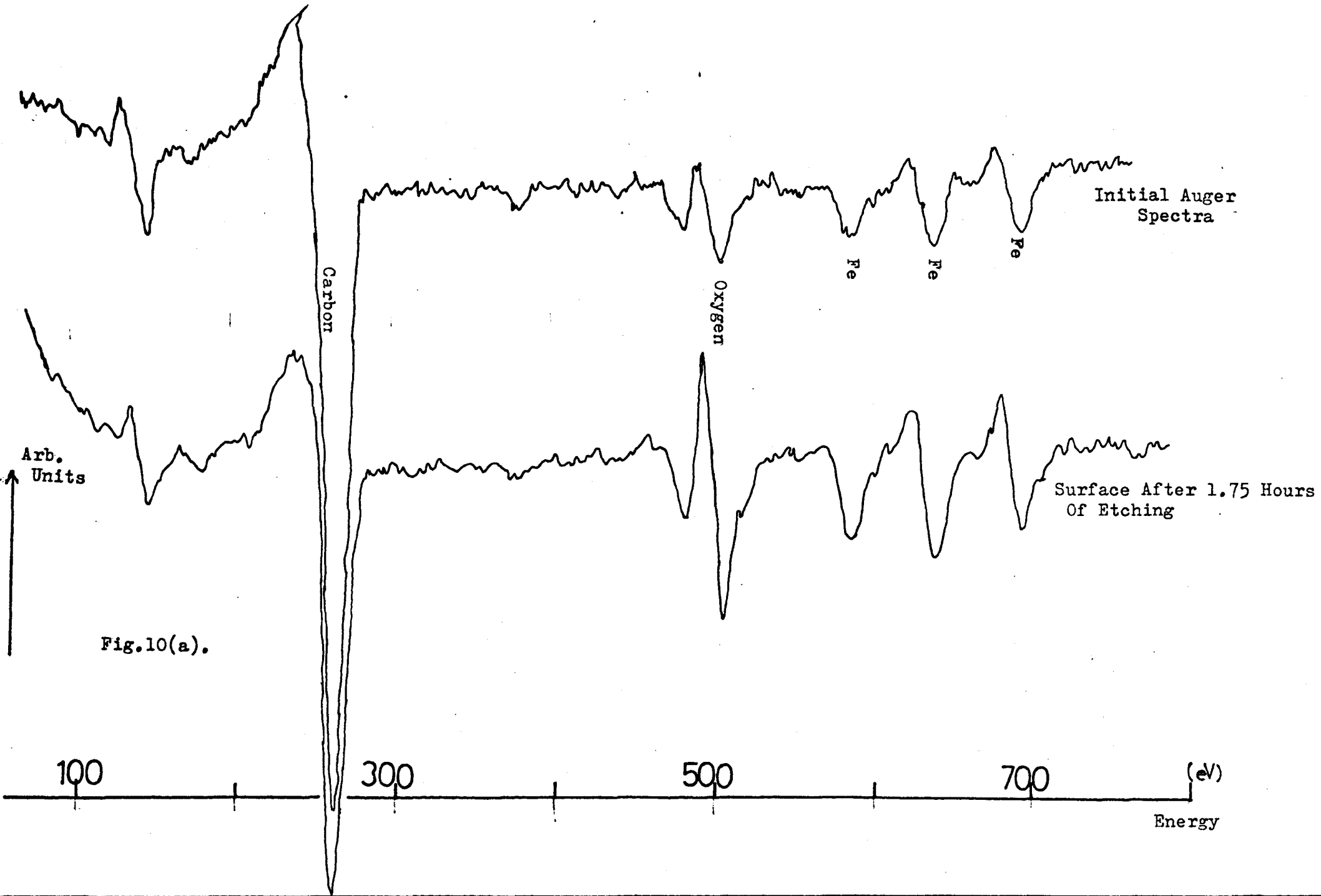
PLATE 5

current between anode and cathode for optimum performance. The argon gas was admitted into the cathode tube by means of a stainless steel tube coupled to a MD6 leak valve such that the gas was only admitted into the cathode tube and not into the whole chamber. The gas inlet system was similar to that described for oxygen in Section 4.3. When in operation the ions generated in the discharge escaped from an aperture 4 mm diameter in the cathode tube (Plate 5), in front of which the target to be etched was placed. The whole arrangement was mounted on an 8 ins. flange, as shown in Plate 5.

The operation of the ion source is based on the discovery that the electrons describe long oscillating paths in the electrostatic field configuration of the above electrode arrangement. As a result the probability of ionizing any gas atoms present in the source is greatly increased so that a discharge can be sustained at considerably lower pressures than conventional cold cathode discharge tubes. The positive ions created are accelerated towards the cathode and emerge with a range of velocities out of the aperture.

The ion source constructed by Fitch operated for argon pressures of  $10^{-4}$  -  $10^{-6}$  torr, however, during the operation of our device we were unable to monitor the pressure inside the cathode tube, but the pressure inside the main chamber was  $\approx 10^{-6}$  Torr so that pressures inside the tube were probably similar to those used by Fitch. The device was normally operated with 6 - 8 Kev anode voltage giving a tube current between the anode and cathode of 2 - 3 mA. The target current to earth for these conditions was between 15 - 30  $\mu$ A, with an estimated current density of about  $100 \mu\text{A cm}^{-2}$ . These values were similar to those obtained by Fitch et al.

Some results obtained from a stainless steel target, illustrating the cleaning action of the ion source, are shown in Fig. 4-10 (a) and (b).



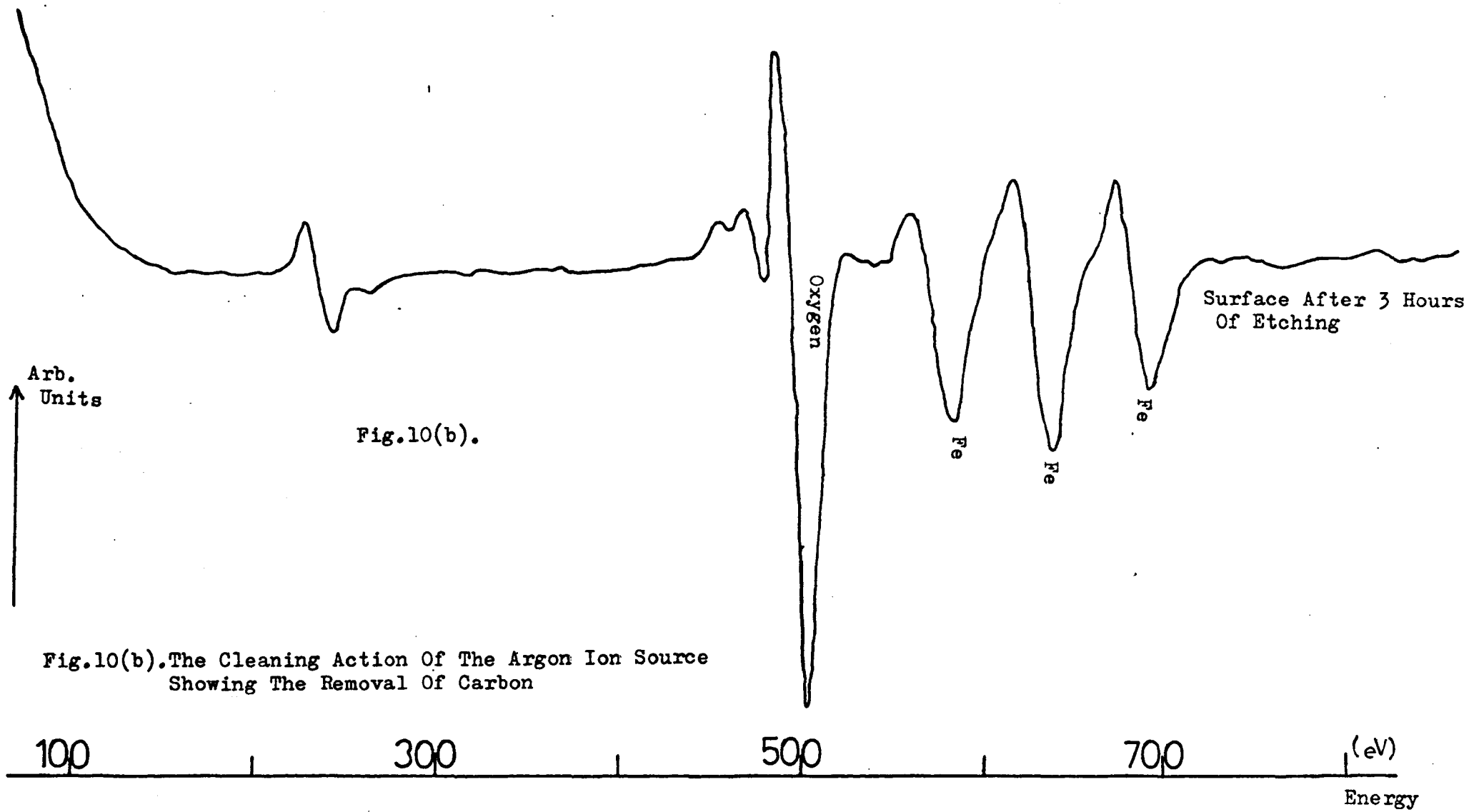


Fig.10(b). The Cleaning Action Of The Argon Ion Source Showing The Removal Of Carbon

A.E.S. The figure shows the removal of carbon contaminant from the surface to reveal the characteristic iron peaks expected from stainless steel. By weighing a stainless steel target before and after ion bombardment, under known conditions, a removal rate of 3 atoms per ion was calculated in good agreement with Fitch who obtained a yield of 4 atoms per ion from a copper surface. For bombardment of a surface by 6KeV, 30  $\mu$ A ions from the source a removal rate of approx. 4 atom layers per minute is estimated.

#### 4.4.3 Cold Cathode Inert Gas Sputtering

This is a less well controlled method of surface cleaning than the electrostatic ion source, although the principle of etching by ion bombardment is similar. The procedure adopted was to allow argon gas (any inert gas is suitable) into the vacuum chamber, from which the vacuum pumps had been isolated, to a pressure  $\sim$  1 torr. Then a glow discharge was struck between a positive electrode, and the target, which was at earth potential. Thus the surface of the target was effectively bombarded with argon ions. This method was often found to be suitable for the first stage of the surface cleaning process, so as to reveal a moderately clean surface which could then be improved upon by using one of the other techniques.

The cleaning action by this method is illustrated in Fig. 4-11, which shows the Auger spectra from a stainless steel target after 30 minutes and 120 minutes of cold cathode inert gas sputtering respectively. It may be seen that the carbon Auger peak has been reduced in intensity by the sputtering action and the iron peaks increased as the surface contaminants were removed.

This technique has limited use because the chamber has still to be evacuated to U.H.V. pressures and as this involves baking some

The composition of the surface under ion bombardment was monitored with A.E.S. The figure shows the removal of carbon contaminant from the surface to reveal the characteristic iron peaks expected from stainless steel. By weighing a stainless steel target before and after ion bombardment, under known conditions, a removal rate of 3 atoms per ion was calculated in good agreement with Fitch who obtained a yield of 4 atoms per ion from a copper surface. For bombardment of a surface by 6KeV, 30  $\mu$ A ions from the source a removal rate of approx. 4 atom layers per minute is estimated.

#### 4.4.3 Cold Cathode Inert Gas Sputtering

This is a less well controlled method of surface cleaning than the electrostatic ion source, although the principle of etching by ion bombardment is similar. The procedure adopted was to allow argon gas (any inert gas is suitable) into the vacuum chamber, from which the vacuum pumps had been isolated, to a pressure  $\sim$  1 torr. Then a glow discharge was struck between a positive electrode, and the target, which was at earth potential. Thus the surface of the target was effectively bombarded with argon ions. This method was often found to be suitable for the first stage of the surface cleaning process, so as to reveal a moderately clean surface which could then be improved upon by using one of the other techniques.

The cleaning action by this method is illustrated in Fig. 4-11, which shows the Auger spectra from a stainless steel target after 30 minutes and 120 minutes of cold cathode inert gas sputtering respectively. It may be seen that the carbon Auger peak has been reduced in intensity by the sputtering action and the iron peaks increased as the surface contaminants were removed.

This technique has limited use because the chamber has still to be evacuated to U.H.V. pressures and as this involves baking some

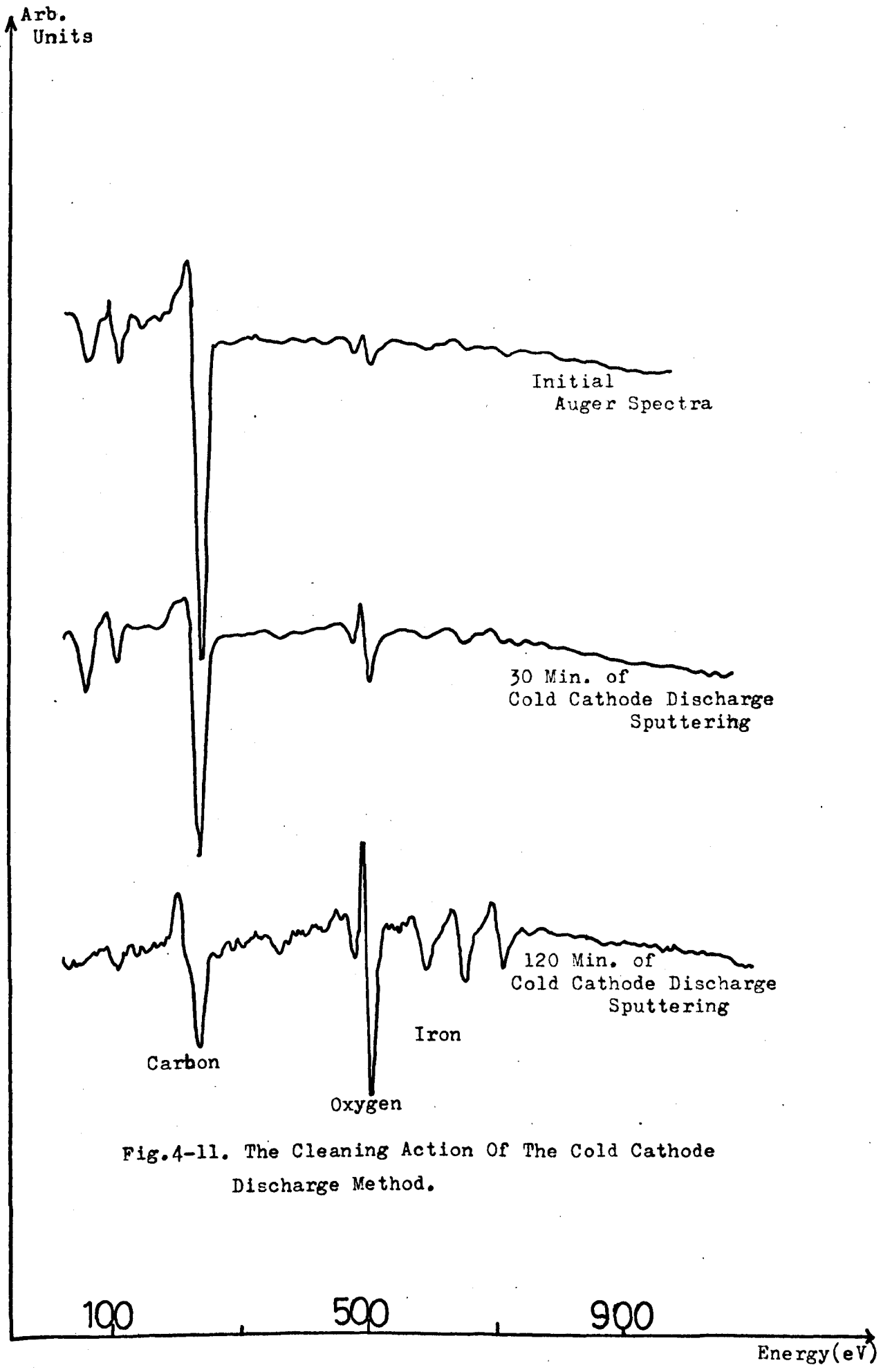


Fig.4-11. The Cleaning Action Of The Cold Cathode Discharge Method.

contamination may be re-introduced on to the target surface. The results shown in Fig. 4-11 were recorded by evacuating to pressures  $\sim 10^{-8}$  torr, without baking the chamber, after cold cathode inert gas sputtering.

#### 4.4.4 Thin Film Evaporation

By evaporating a material from an outgassed filament or an evaporation boat, in a U.H.V. environment, onto a suitable substrate a clean surface characteristic of that material can be produced. Such a facility was provided in the present apparatus and was used in the investigation of several compounds and the element bismuth.

### 4.5 Design of a Cylindrical Mirror Analyser

#### 4.5.1 Introduction

The theory of the cylindrical mirror analyser (CMA), (also sometimes referred to as the cylindrical capacitor) has been available for some time, but experimental arrangements involving the energy analysis of charged particles by such an analyser is a comparatively recent development. The CMA was first described by Blauth (1957)<sup>126</sup>, but it was Palmberg, Bohn and Tracy (1969)<sup>20</sup> who first realised its potential as an Auger electron spectrometer. Nowadays it is generally accepted that the CMA is perhaps the best analyser for AES both from a constructional and performance standpoint. It has the advantage of a high transmission (up to 10%) for a dispersive type of analyser as well as a superior signal/noise ratio (by as much as a factor 100) than a retarding field type of analyser.

In the present work a CMA was designed and constructed, and

subsequently used to perform AES and CELS investigations on selected surfaces. In the following sections the theory, construction and performance of such an analyser are described.

#### 4.5.2 Theory of the CMA

The theory of the cylindrical capacitor as an energy analyser has been thoroughly treated by Sar-El (1967)<sup>127</sup> and by Zashkvara et al (1966)<sup>128</sup>. Their main results, upon which the construction of our CMA was based, are briefly summarized in this section.

The cylindrical capacitor analyser consists of two co-axial cylinders with a radial electric field in between, usually produced by a voltage on the outer cylinder with the inner cylinder at earth potential. Fig. 4.12 shows a cross section through the cylindrical analyser. The hollow inner cylinder has two slots cut around its periphery in such a way that the plane determined by them is normal to the common axis of the cylinders. The theory is usually developed for electrons originating from a source S located on the co-axis of the two cylinders. The source is assumed to be at ground potential, like the inner cylinder, so that the electrons follow straight line trajectories while inside the inner cylinder. Those electrons emitted about the angle  $\theta$  enter the electric field region, between the cylinders, through the first slot. Then by a suitable adjustment of the voltage on the outer cylinder, mono-energetic electrons are deflected back to the inner cylinder through the second slot to be focussed at I.

In principle  $\theta$  can have any value between 0 and  $\pi/2$  with the exception of both limiting values. Each angle will determine three main interdependent parameters for the CMA, (i) the source to image distance on the common axis of the cylinders, (ii) the corresponding deflection voltage for particles of a given energy, (iii) the ratio

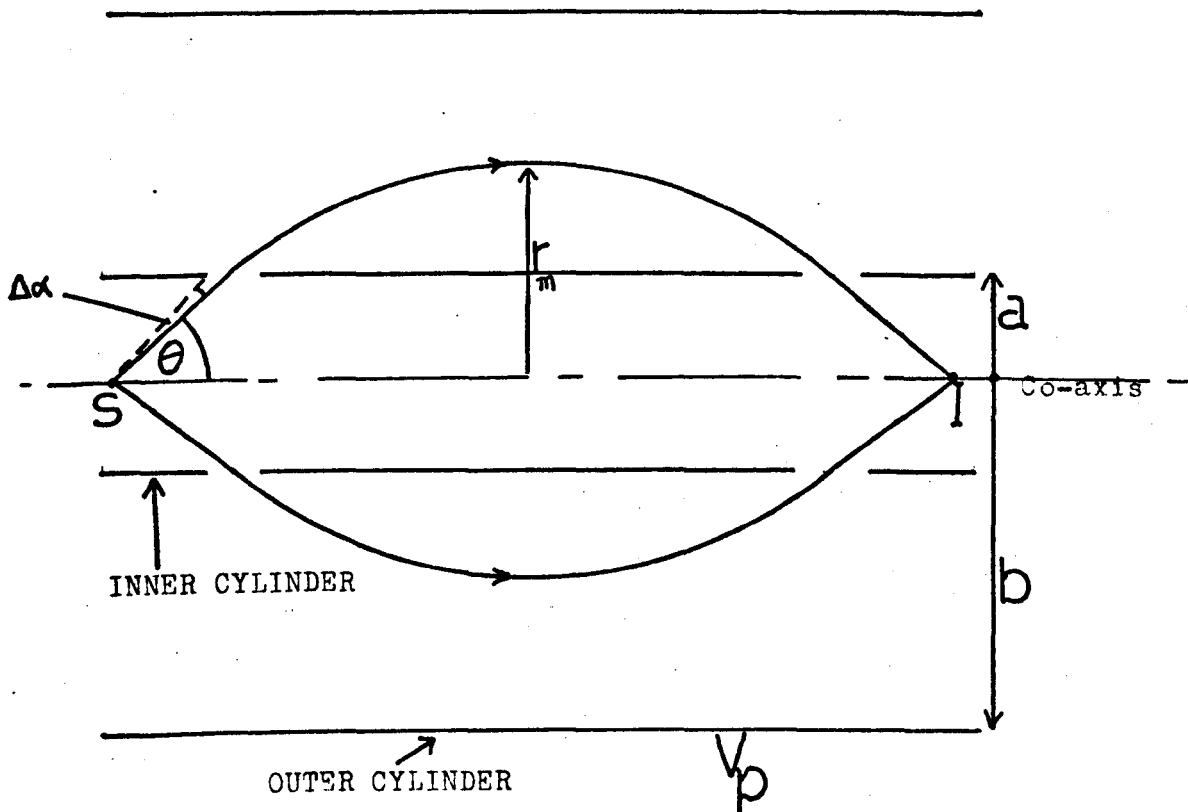


Fig.4-12. Schematic Diagram Of The Cylindrical Mirror Analyser Showing Particles From Source S Being Focussed At I By A Voltage  $V_p$  On The Outer Cylinder.

between the radii of the cylinders.

Particles of a given energy entering the electric field region between the cylinders have an angular divergence  $\theta \pm \Delta\alpha$ . Because this divergence is small the distance between the source and image  $L$ , can be expanded as a Taylor series:

$$L = L_0 + \frac{dL}{d\theta} (\Delta\alpha) + \frac{1}{2!} \frac{d^2L}{d\theta^2} \cdot (\Delta\alpha)^2 \dots\dots\dots$$

The condition for first order focussing requires that  $\frac{dL}{d\theta} = 0$ . The theoretical work of Sar-El and Zashkavara showed that for a particular value of  $\theta = 42^\circ 18'$ , the second order focusing term is also zero and then the linear dispersion in the focused image at  $I$  is at a minimum. Thus we designed our instrument to have  $\theta = \theta_0 = 42^\circ 18'$ , the optimum angle for the electrons to enter the electric field region for minimum linear dispersion.

Then for the optimum focusing condition the relationship between the radii of the cylinders and the voltage  $V_p$  on the outer cylinder needed to focus electrons of energy  $V_e$ , is given by

$$\frac{V_e}{V_p} = 1.3098 \text{ Log } \left(\frac{b}{a}\right) \quad \text{Sar-El (1967)} \quad \text{Eq. 4-1}$$

Where  $a$  = radius of the inner cylinder

and  $b$  = radius of the outer cylinder.

The distance between the source and image is then given by;

$$L = 2a \text{ Cot } \theta_0 \left( 1 + k e^{-\frac{1}{2}k^2} \int_0^k e^{-u^2/2} du \right) \quad \text{Eq. 4-2.}$$

where  $k^2 = 2.6198 \text{ Sin}^2 \theta_0$ .

The transmission  $T$  of the analyser can be shown to be given by

$$T = \Delta\alpha \text{ Sin} \theta_0. \quad \text{Eq. 4-3}$$

Sar-El has shown that the base resolution of an ideal instrument operating at the optimum focusing condition for electrons originating

from a point source is given by

$$R' \approx 21 T^3 \quad \text{Eq. 4-4}$$

For a finite source of radius P and length S located on the central axis, Sar-El has derived the effect on the base resolution of the analyser to be given by

$$R = \frac{S + 1.1P}{5.6a} + 21T^3 \quad \text{Eq. 4-5}$$

(Zashkvara derives the effect on the resolution to be  $\frac{0.5P}{a}$  ).

Using the equations 4-1 to 4-5 a suitable instrument for Auger electron spectroscopy can be designed.

In a single stage CMA, having only one focus, a finite source of electrons will cause a distortion of the image due to the presence of non-axial rays. These non-axial rays can be eliminated by using multiple focusing of the analysed beam, with an aperture at each focus to intercept the non-axial rays. Zashkavara has considered the effect of multiple focusing of the analysed beam and shows that for a two-stage analyser (with double focusing) the transmission is nearly halved while the resolution is increased by factor of approximately two.

### 4.5.3 Design

The theory so far described was used to construct a suitable energy analyser compatible with the vacuum chamber and of sufficient resolution (< 1%) for Auger analysis. At the time of the initial design only single stage cylindrical mirror analysers had been used in AES, Palmberg et al (1969)<sup>20</sup>. But the single stage instrument has certain experimental limitations in that the target has to be carefully positioned so as to allow the electrons to enter the analyser at the optimum angle  $\theta_0$ , in addition with different target positions the source to image distance changes, thus the ratio  $V_e/V_p$  changes so that calibration is necessary for each target position. Also in a single stage

CMA non-axial rays from a finite source will cause a distortion of the focused image.

To overcome these disadvantages of the single stage CMA we decided to construct a two stage analyser, as shown in Fig. 4.13. The second stage of such an analyser defines a virtual image of the source from which the electrons originate, so that when the target is not at the optimum position as for example at position 2 or 3 in Fig. 4.13, there is some loss of sensitivity, but the electrons still enter analyser at the optimum angle as if originating from the source S. The other advantages of a two stage CMA are that an aperture can be placed at the first focus to intercept the non-axial rays and the ratio  $V_e/V_p$  remains constant, independent of target position.

Other features taken into consideration when designing the CMA were:

(a) Resolution

For a point source the resolution of an analyser is determined by the semi angular aperture  $\Delta\alpha$ . The angular aperture should be as large as possible to give the maximum transmission, but with an acceptable resolution. We decided on a value of  $\pm 6^\circ$  for  $\Delta\alpha$  as used by Palmberg et al<sup>20</sup> for a single stage CMA. Such a value gives an optimum resolution of 0.5% according to equation 4-4. For two such analysers in tandem the resolution is expected to be about 0.3% for a point source, with a transmission of about 3 - 4%.

(b) Overall Dimensions

It was intended to mount the CMA in a 3.5 ins. diameter port (6 ins. flange) of the vacuum chamber. This was a constraint on the radii of the inner and outer cylinders which could be used. The values eventually decided upon were,

$$a = 0.5 \text{ ins.}$$

$$b = 1.153 \text{ ins.}$$

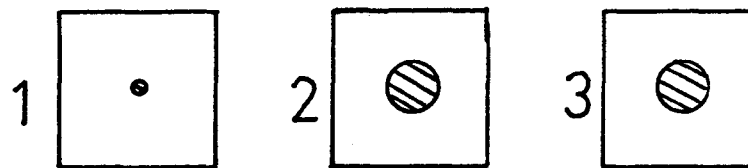
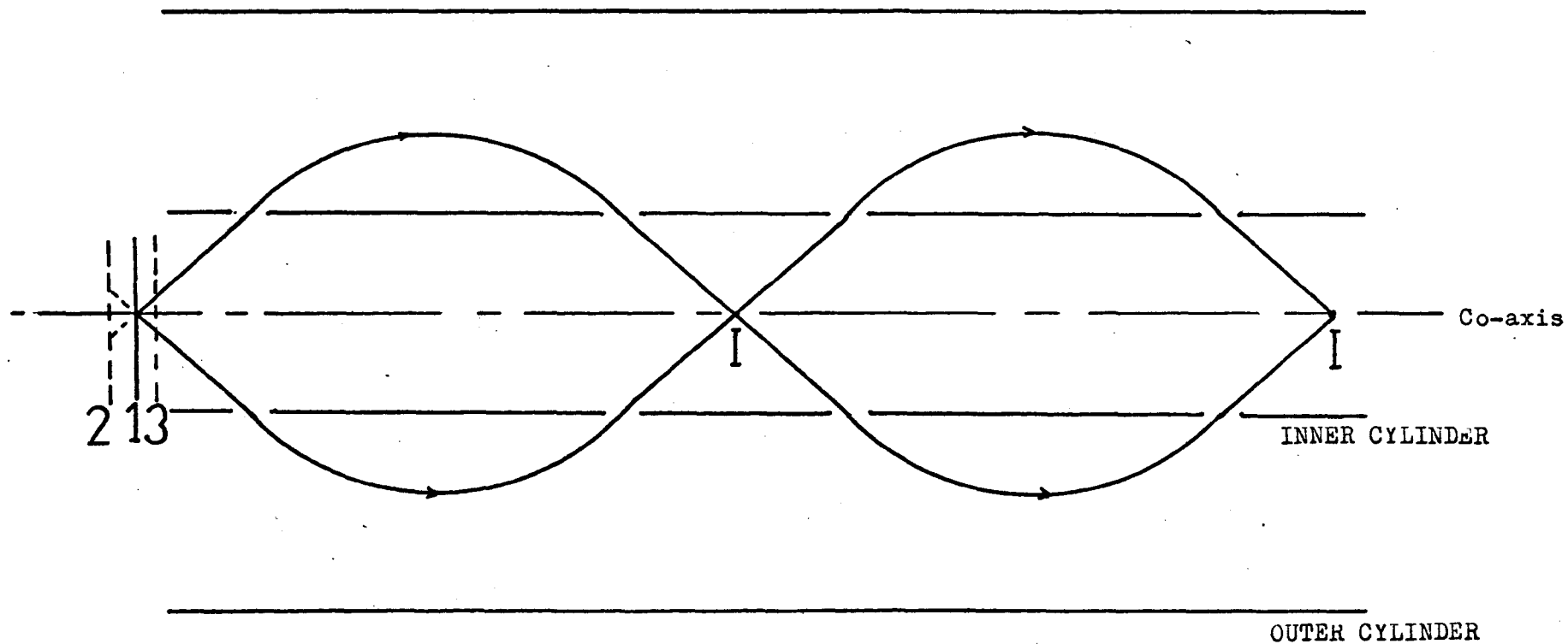


Fig.4-13. Schematic Diagram Of The 2-Stage CMA Showing  
The Source Area For Target Positions 1,2 and 3.

Then the relationship between the voltage on the outer cylinder and the energy of the focused particles is,

$$V_e = 1.565 V_p.$$

B was chosen to be greater than  $\gamma_m^{\lambda}$ , the maximum distance from the cylindrical axis of the electron trajectory, given by Sar-El's equation:

$$\begin{aligned}\gamma_m^{\lambda} &= a \exp.(1.31 \sin^2 \theta_0), \\ &= 0.8989 \text{ ins. for our analyser.}\end{aligned}$$

With the chosen values of the radii of the two cylinders, the source to image distance was calculated from Eq. 4-2 to be

$$L = 3.064 \text{ ins.}$$

#### 4.6 Construction of the OMA

The theory and calculations summarised in Section 4.5 provided a sufficient basis to produce constructional diagrams for the various components of the analyser. Fig. 4-14 shows the design of the inner cylinder which was machined out of stainless steel. Along its length were milled four slots through which the electrons can describe trajectories as shown in Fig. 4-13. The dimensions were chosen to make  $\Delta\alpha = 6^\circ$ ,  $\theta = 42^\circ 18'$  and the source to image distance, 3.064 ins. Additional consideration which had to be borne in mind were that a channel electron multiplier had to be mounted at the exit of the electrons, and that the cylinders should be as close as possible to the target so as to minimise the distortion of the electric field between the cylinders by the "end effects". A photograph of the machined cylinder is shown in Plate 6.

To eliminate the non-axial electron trajectories two apertures

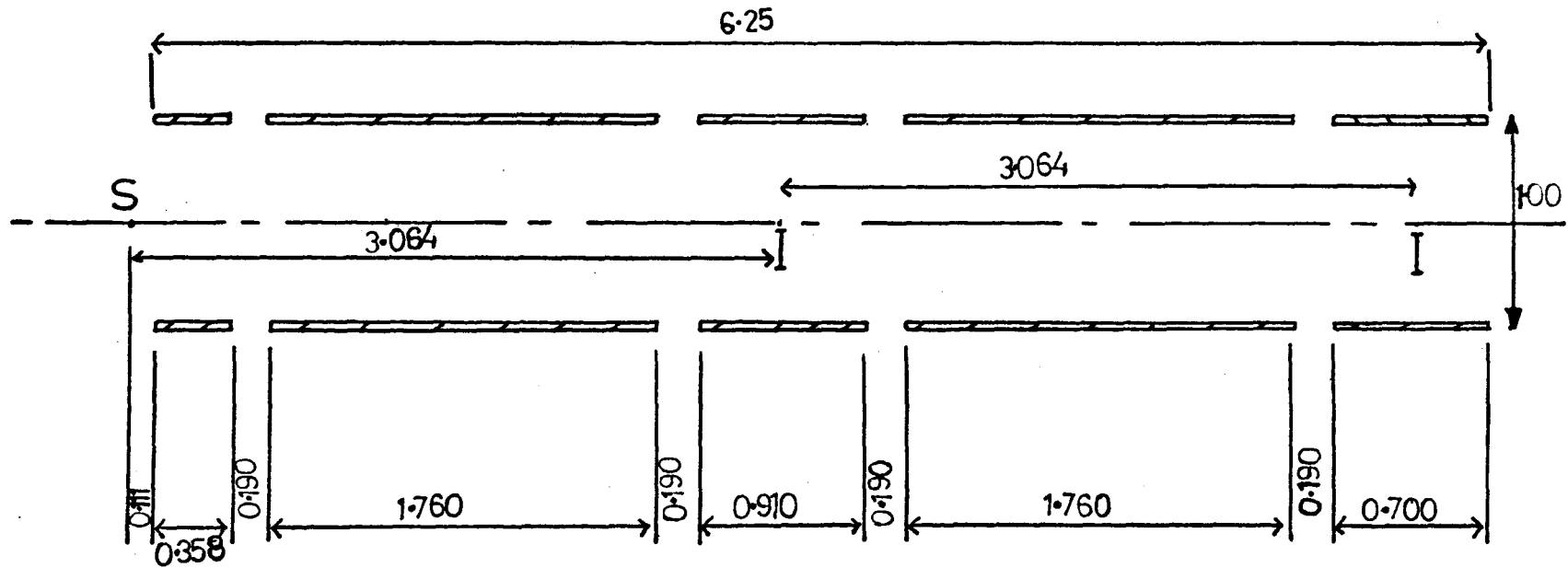


Fig.4-14. The Design Of The Inner Cylinder, All Dimensions  
 Are In Inches.



PLATE 6

were designed to push fit inside the inner cylinder at the two focii of the analysed electrons. Their design and positioning is shown in Fig. 4-15. The radius of the central hole of the aperture at  $I_1$ , effectively determines the resolution of the analyser as this hole acts as an object for the second stage of the instrument. The distance  $X$  which also influences the resolution of the instrument can be varied by turning the screw A in Fig. 4-15.

The outer cylinder of the CMA was 5.510 ins. long and it was machined out of aluminium tube so as to be of uniform bore throughout. It was made as long as practicable to reduce distortions of the electric field by the "end effects". The inside of the outer cylinder was initially a mirror finish but it was coated with gold black prior to assembly. This gold black is a polycrystalline gold film evaporated in an inert gas atmosphere whose effect is to reduce the secondary electron yield coefficient, Thomas and Pattinson (1970)<sup>169</sup>, and so possibly improve the signal to noise ratio of the instrument.

#### 4.6.1 Assembly

The individual constructed pieces of the analyser had to be fitted together. The most critical aspect of the analyser design was the accurate concentric mounting of the cylinders and the positioning of the apertures. To assemble the inner and outer cylinder concentrically two end plates, of stainless steel, were constructed, Fig. 4-16. These were identical except for an extra hole in one of them to make an electrical connection to the outer cylinder.

These end plates made a push fit on to the inner cylinder, the outer cylinder was concentrically clamped between these end plates and electrically isolated from them by means of 8 spherical ruby balls of diameter 2.5 mm. These ruby balls rested in hollows grooved out of the

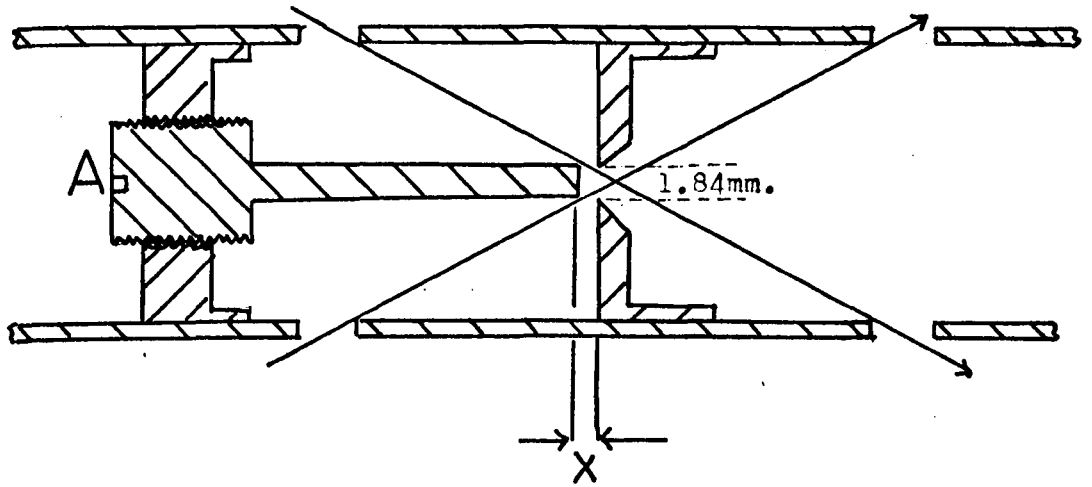


**Fig.4-15.** Aperture Design Showing The Central Aperture In Position, By Turning Screw A Distance X Can Be Varied

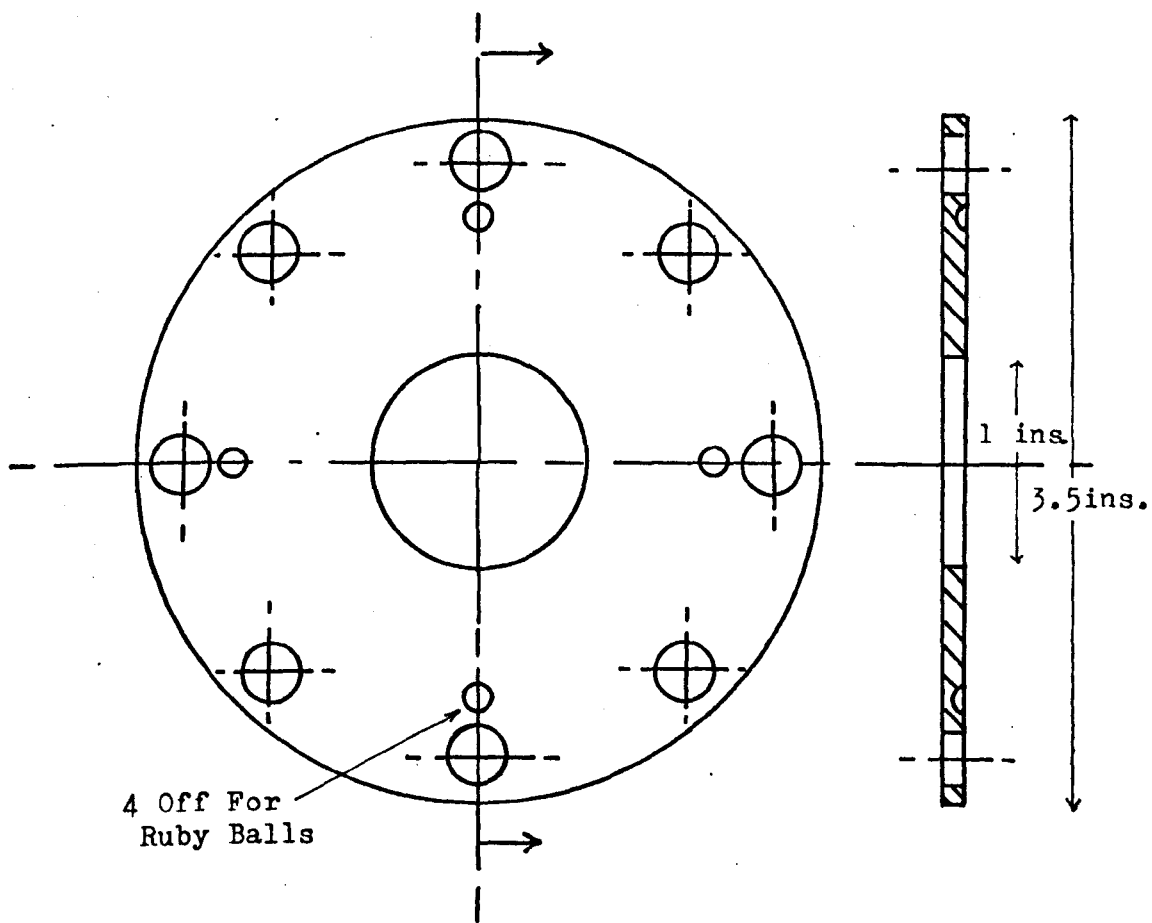


Fig.4-16. The Design Of The End Plates.

end plates and the outer cylinder was gripped between them by 4 clamping rods with screwed ends, as shown in Fig. 4-17. The slots on the inner cylinder were covered with a fine tungsten mesh, of 88% transmission, to reduce any distortion their presence may introduce on the electric field between the cylinders.

When the analyser is in operation, the metal end plates are at earth potential so that they inevitably introduce a distortion of the radial electrostatic field. To reduce field distortions at the ends an attempt was made to use ceramic end plates on whose inside surface was evaporated a thin resistive film. The outer cylinder was then clamped directly between the ceramic plates. It was intended that, when in operation, the voltage on the outer cylinder would cause a current to flow through the thin film setting up a potential gradient and thus reducing the distortion of the electric field between the cylinders. With such an arrangement we obtained unusually poor signal to noise ratios in operation, probably due to inhomogeneities in the resistance of the evaporated film causing distortions in the electrostatic field whose effect was worse than the uniform symmetric distortion produced by the metal end plates.

Behind the exit aperture of the analyser a channel electron multiplier (CEM) was mounted by using a specially constructed collar. The multiplier was a type B4/9AL/01, supplied by the Mullard Company<sup>129</sup>, and is UHV compatible being bakeable up to 250°C. This device has a gain  $\approx 10^8$  when operating at the maximum voltage, but this figure is thought to vary with the energy of the incident electrons.

The entire assembled analyser was mounted on a 6 ins. flange by means of 4 rods, as shown in Fig. 4-18. Electrical connections were made to the outer cylinder and the channel electron multiplier by

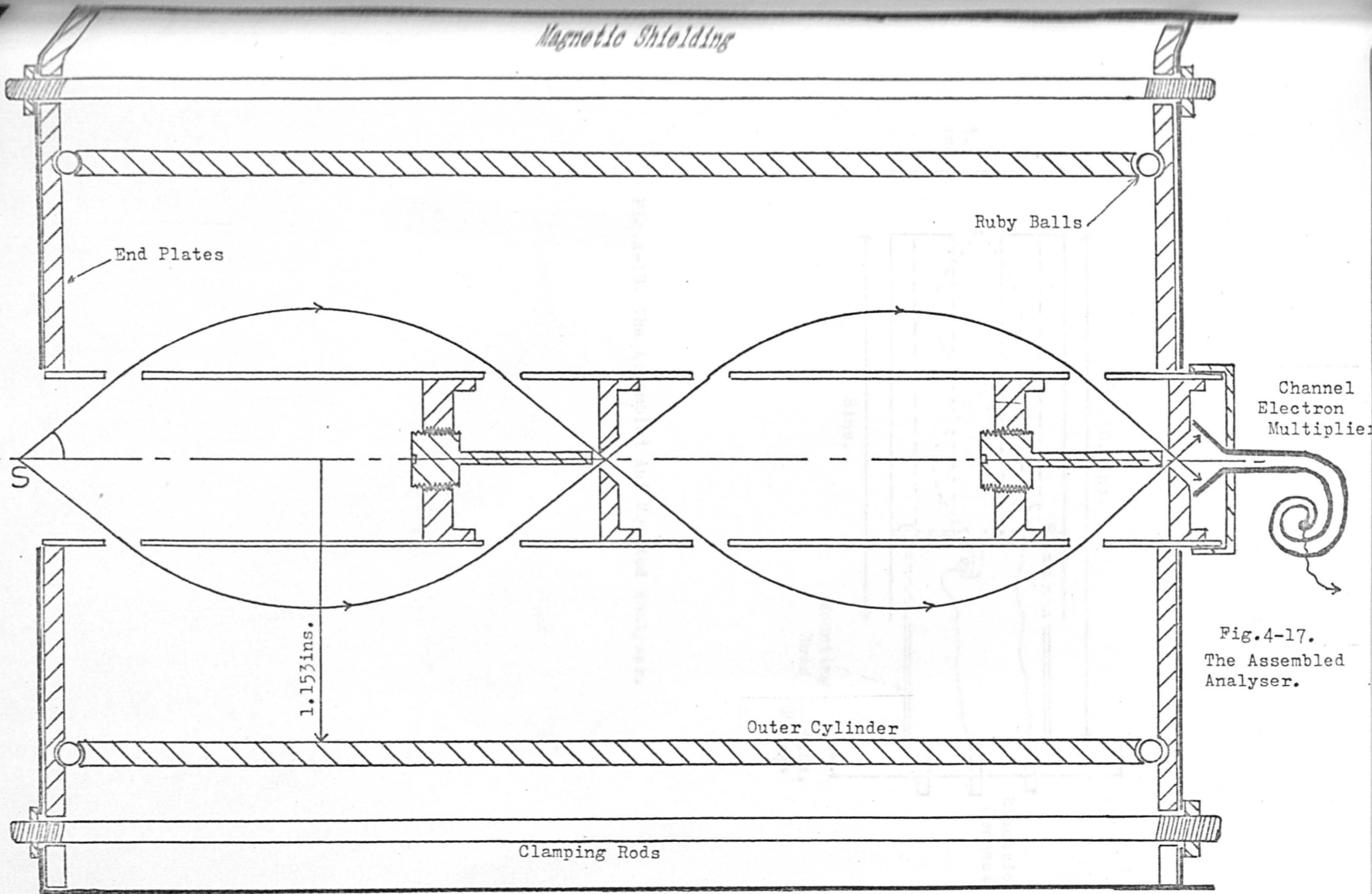


Fig.4-17.  
The Assembled Analyser.

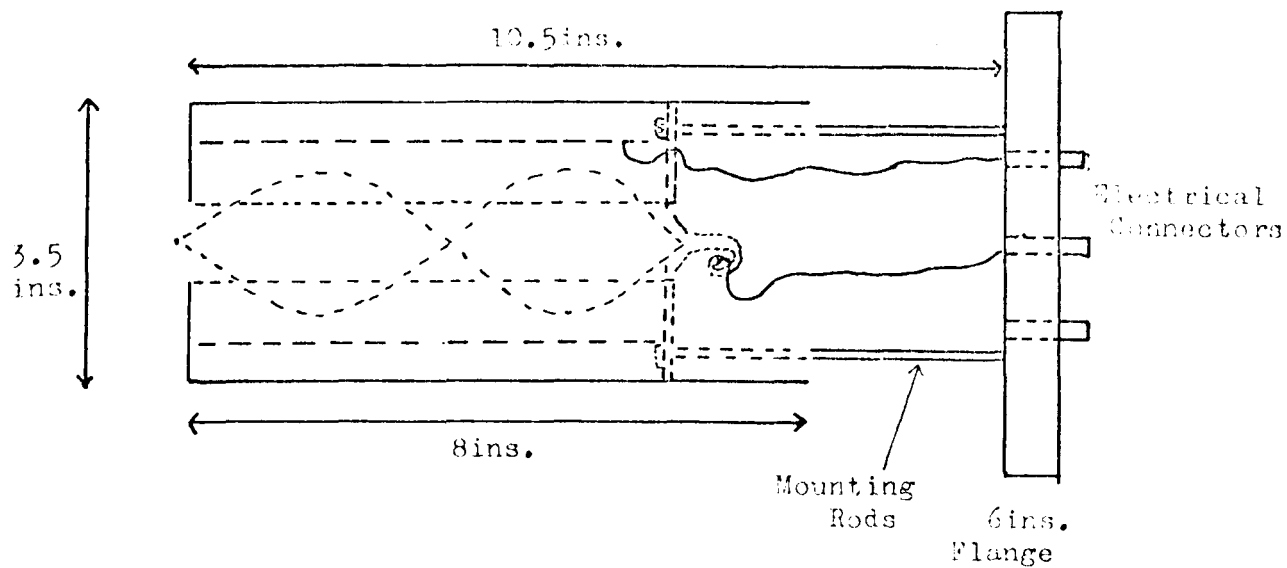


Fig.4-18. The Assembled And Mounted Analyser.

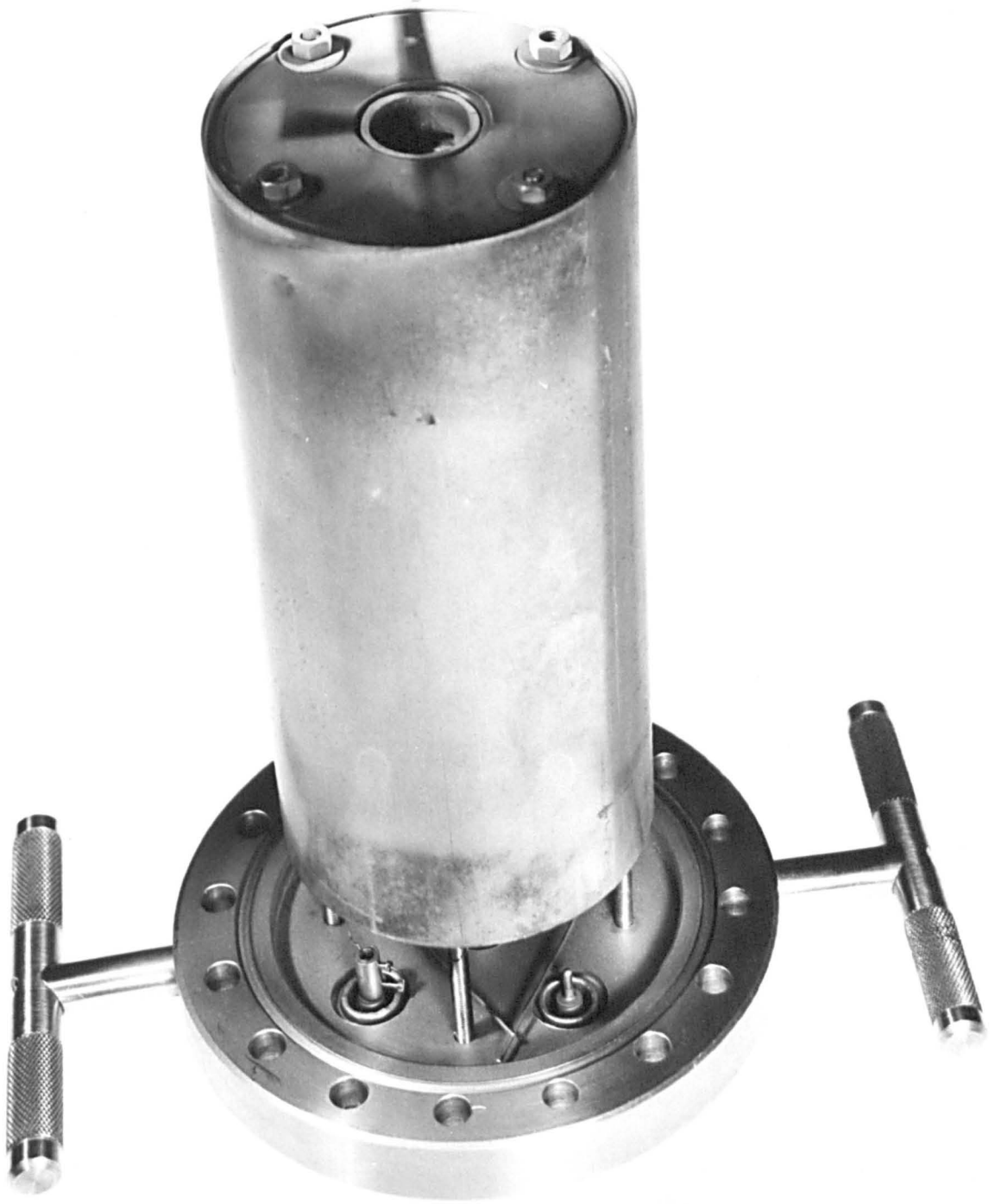


PLATE 7

"ceramseal", BNC type of feethroughs, welded to the mounting flange. The assembled and mounted CNA is shown in Plate 7.

#### 4.6.2 Magnetic Shielding

Since the presence of magnetic fields degrades the performance of the Analyser shielding was provided. The effect of a weak uniform field along the axis of the analyser will tend to cancel out over the whole trajectory, but the performance will be most affected by transverse magnetic fields. Consequently the CMA was enclosed in an cylindrical shield made of 'co-netic' alloy<sup>120</sup>. The thickness used was capable of attenuating a normally incident magnetic flux by 25 db. Due to the presence of large magnets, for the operation of ion pumps, in our laboratory environment additional shielding with netic material (high flux shielding) was found to improve the performance of the analyser. A layer of conetic and netic material was also placed on the outside of the end plates thus providing a completely shielded analyser.

#### 4.7 Operation of the CMA

The theory and construction of the CMA have so far been summarised in this chapter. We now proceed to describe the operation of the instrument in electron beam spectroscopy particularly to the study of electron stimulated emission from solid surfaces. The analyser can be used to obtain either the energy distribution of the SEE spectrum  $N(E)$ , the first derivitive  $dN/dE$  of the energy spectrum or the second derivative  $d^2N/dE^2$  by the use of suitable detection circuits. In this section we briefly summarise the theory of CMA operation as well as describing the

electronic detection circuits used.

When the analyser is in operation electrons from the target, stimulated by a primary beam, are entering the instrument. At a particular pass energy  $E$ , the current collected  $I_c$  at the exit aperture of the CMA is given by

$$I_c = I_p K E N(E) , \quad \text{Eq. 4-6}$$

Where  $I_p$  is the primary beam current,

$N(E)$  is SEE distribution at energy  $E$

and  $K$  is a constant for the analyser.

Consider an expansion of this equation in a Taylor series about an energy  $E_0$ .

Then,

$$I_c(E) = I_c(E_0) + (E-E_0) (I_c'(E_0)) + \frac{(E-E_0)^2}{2!} (I_c''(E_0)) \dots$$

So

$$I_c(E) - I_c(E_0) = (E-E_0) \left[ E_0 \frac{dN}{dE} \Big|_{E_0} + N(E_0) \right] K I_p \\ + \frac{(E-E_0)^2}{2!} \left[ 2 \frac{dN}{dE} \Big|_{E_0} + E_0 \frac{d^2N}{dE^2} \Big|_{E_0} \right] K I_p \dots$$

Eq. 4-7

If we now apply a small a.c. modulation to the pass energy such that

$$E - E_0 = k \sin \omega t.,$$

Then

$$I_c(E) - I_c(E_0) = \sin \omega t \left[ E_0 \frac{dN}{dE} \Big|_{E_0} + N(E_0) \right] k K I_p \\ + (1 - \cos 2\omega t) \left[ 2 \frac{dN}{dE} \Big|_{E_0} + E_0 \frac{d^2N}{dE^2} \Big|_{E_0} \right] \frac{k^2 K I_p}{4} \quad \text{Eq. 4-8}$$

The first harmonic of the collector current is

$$I_c(\omega, E) = \left[ E \frac{dN}{dE} + N(E) \right] k K I_p$$

In this expression, because of the E factor, the term  $E \frac{dN}{dE}$  is dominant so that if the pass energy of the electrons can be modulated by a frequency  $w$  then the component of the collector current with frequency  $w$  is proportional to  $E \frac{dN}{dE}$ , the first derivative of the SEE spectrum.

#### 4.7.1 Detection Circuit for $\frac{dN}{dE}$

To obtain the first derivative of the SEE spectrum an electronic circuit was designed to measure  $I_c(w,E)$ , as shown in Fig. 4-19. A sinusoidal modulation was applied to the voltage on the outer cylinder of the CMA, by way of the isolation transformer, effectively modulating the energy of the electrons collected at the channel multiplier. The circuit incorporated a H.T. supply voltage for the C.E.M., then the current from the CEM needed to be de-coupled to ground potential before it could be passed into the lock-in amplifier. The isolating capacitor was rated to breakdown at 4 KeV and its value was chosen so that its impedance  $Z_c \ll R_a$  at the modulation frequency.

The deflecting voltage on the outer cylinder of the CMA was supplied by a programmeable 'Kepco OPS 2000' negative voltage supply. The programmer was a Kepco FG 100/A instrument, which also supplied the X input of the chart recorder. Then as the voltage on the outer cylinder is ramped bringing different energy electrons into focus on to the CFM, the recording pen sweeps horizontally in proportion. This arrangement allowed the voltage on the outer cylinder to be swept at various speeds.

The modulation to the outer cylinder was supplied by a low distortion signal generator feeding the low voltage primary of a ferrite pot core 1:1 ratio isolation transformer. The signal generator also supplied the same frequency directly to the reference unit of the lock-in amplifier. The frequency and amplitude of modulation were variable

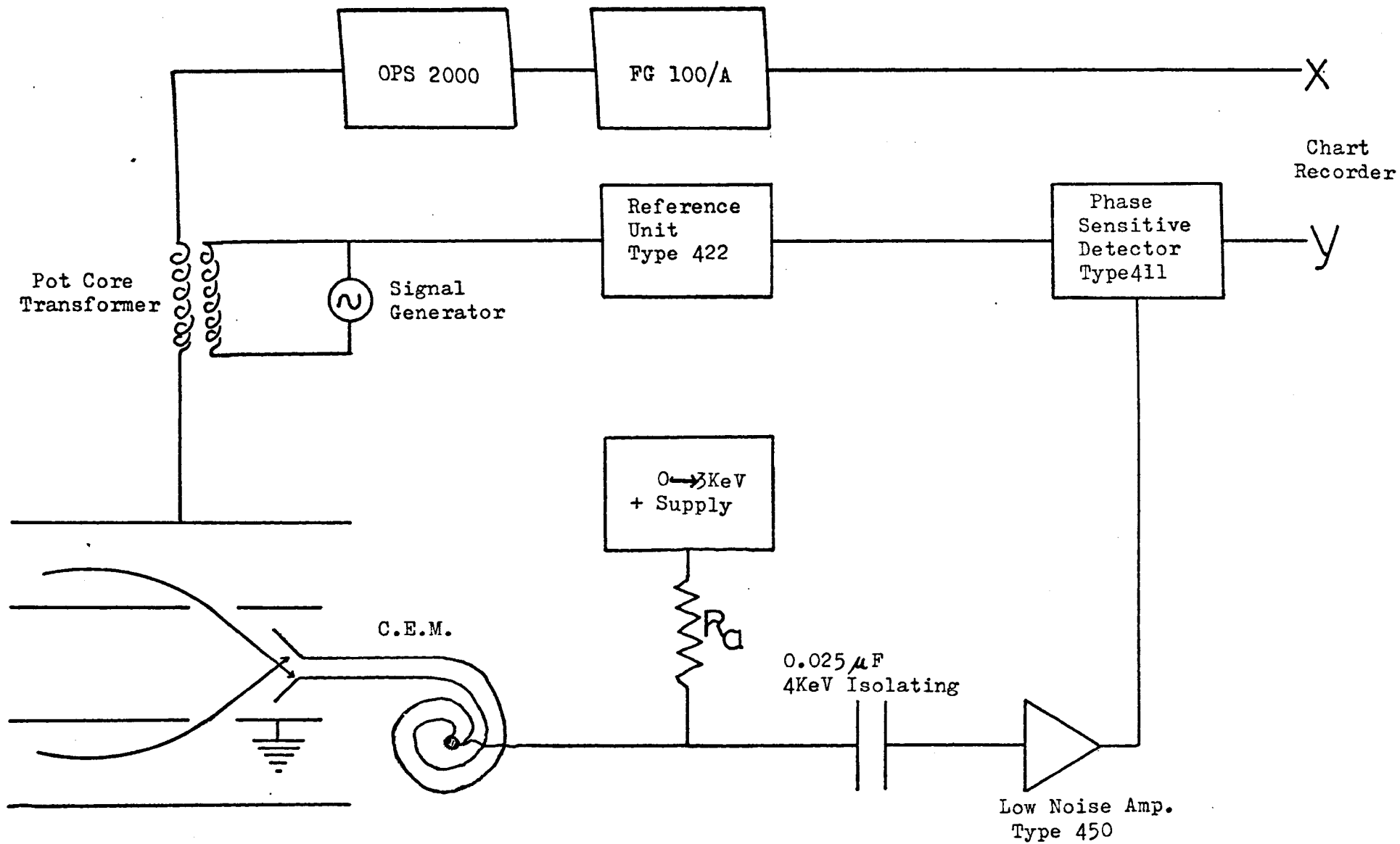


Fig.4-19. Detection Circuit For  $\frac{dN(E)}{dE}$ .

from the signal generator typically in normal operation frequencies of 2000 Hz and modulation amplitudes of 1-12v/bk-nk were used although the transformer was capable of dealing with frequencies of up to 40 KHz for possible fast scanning applications.

The lock-in amplifier used was manufactured by Brookdeal Electronics and consisted of a reference unit (Type 422) a phase sensitive detector (Type 411) and a low noise amplifier (Type 450). It amplified and detected the signal from the CEM at the modulation frequency so that its output was proportional to the first harmonic of the collector current (Eq. 4-8) and hence the first derivative of the SEE spectrum. The output of the lock-in amplifier was supplied directly to the Y input of the chart recorder so that with an appropriate sweep speed the  $E \frac{dN}{dE}$  vE spectrum of the specimen under investigation was traced out revealing the small features such as the Auger peaks.

This is the normal mode of operation of the CMA to obtain the first derivative of the secondary electron emission spectrum, almost invariably used by all workers having such an instrument.

#### 4.7.2 Detection Circuit for $\frac{d^2N}{dE^2}$

From equation 4-8 it is clear that the component of the collector current at  $2\omega$ ,  $I_c(2\omega, E)$  is proportional to  $(2 \frac{dN}{dE} + E \frac{d^2N}{dE^2})$ . In this expression the second derivative of the energy spectrum is the dominant term and if we could measure  $I_c(2\omega, E)$ , then we could obtain a signal proportional to  $d^2N/dE^2$ . Now  $I_c(2\omega, E) \ll I_c(\omega, E)$  because of the convergent nature of the Taylor series and also because in the practical situation  $I_c(\omega, E)$  is compounded by capacitance pick up from the modulation on the outer cylinder. So that when the circuit of Fig. 4-19 was used to detect the component  $I_c(2\omega, E)$  the PSD became

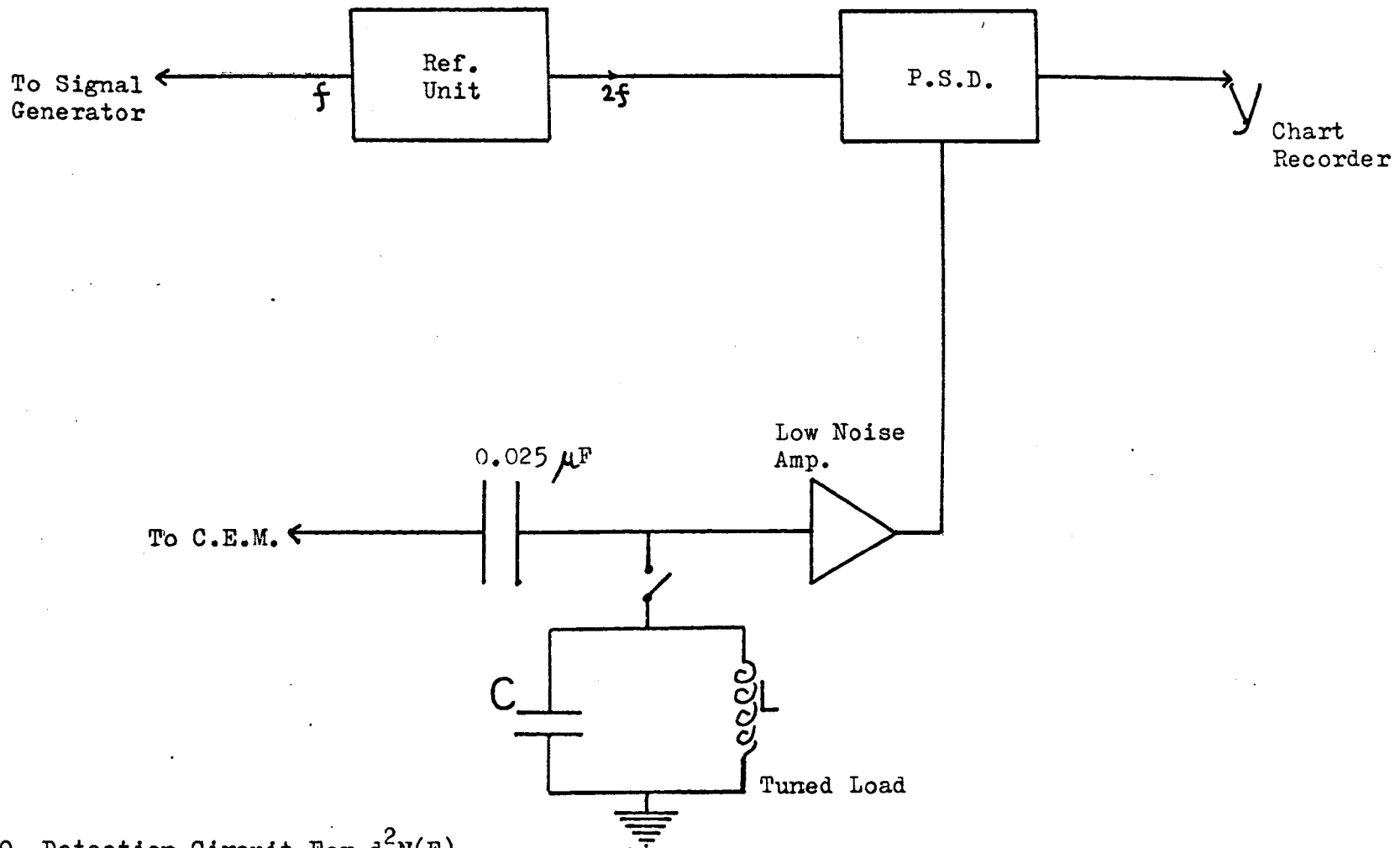


Fig.4-20. Detection Circuit For  $\frac{d^2N(E)}{dE^2}$  .

overloaded with the component  $I_c(w,E)$ . Consequently it was decided to modify the circuit of Fig. 4-19 slightly by constructing a tuned load, which would filter out all frequencies except the pass frequency. The tuned load was designed to have a resonance at 1000 Hz so by modulating the outer cylinder at 500 Hz, only the component  $I_c(1000,E)$  would be detected by the lock-in amplifier, Fig. 4-20. The output of the PSD is then proportional to  $E \frac{d^2N}{dE^2}$ .

The recording of spectra in the second derivative mode has certain advantages in that some structure in the  $\frac{dN}{dE}$  spectrum can be easily resolved also the location of the maxima of the peak in the  $\frac{d^2N}{dE^2}$  spectrum occurs at the same energy as the peak in the  $N(E)$  spectrum, whereas in the first derivative of a spectrum the energy of a feature has to be estimated from the mid position of the peak-peak height. We found the  $\frac{d^2N}{dE^2}$  mode of operation particularly useful for the characteristic energy loss measurements although the signal to noise ratio was not as good as detection in the  $dN/dE$  mode consequently the weaker peaks in energy loss spectroscopy were detected in the first derivative mode. In the literature the operation of CMA's in the second derivative mode for energy loss measurements appears to be increasing in popularity eg. Rowe<sup>99,116</sup> and Ludeke et al<sup>115</sup> record their energy loss spectra with a CMA operating in this mode.

#### 4.7.3 Detection Circuit for $N(E)$

As already mentioned (Equation 4-6), the collector current at the exit aperture of the CMA is

$$I_c = K E N(E) I_p.$$

Now supposing we modulate the intensity of the primary electron beam by a sinusoidal wave  $k \sin wt$ .

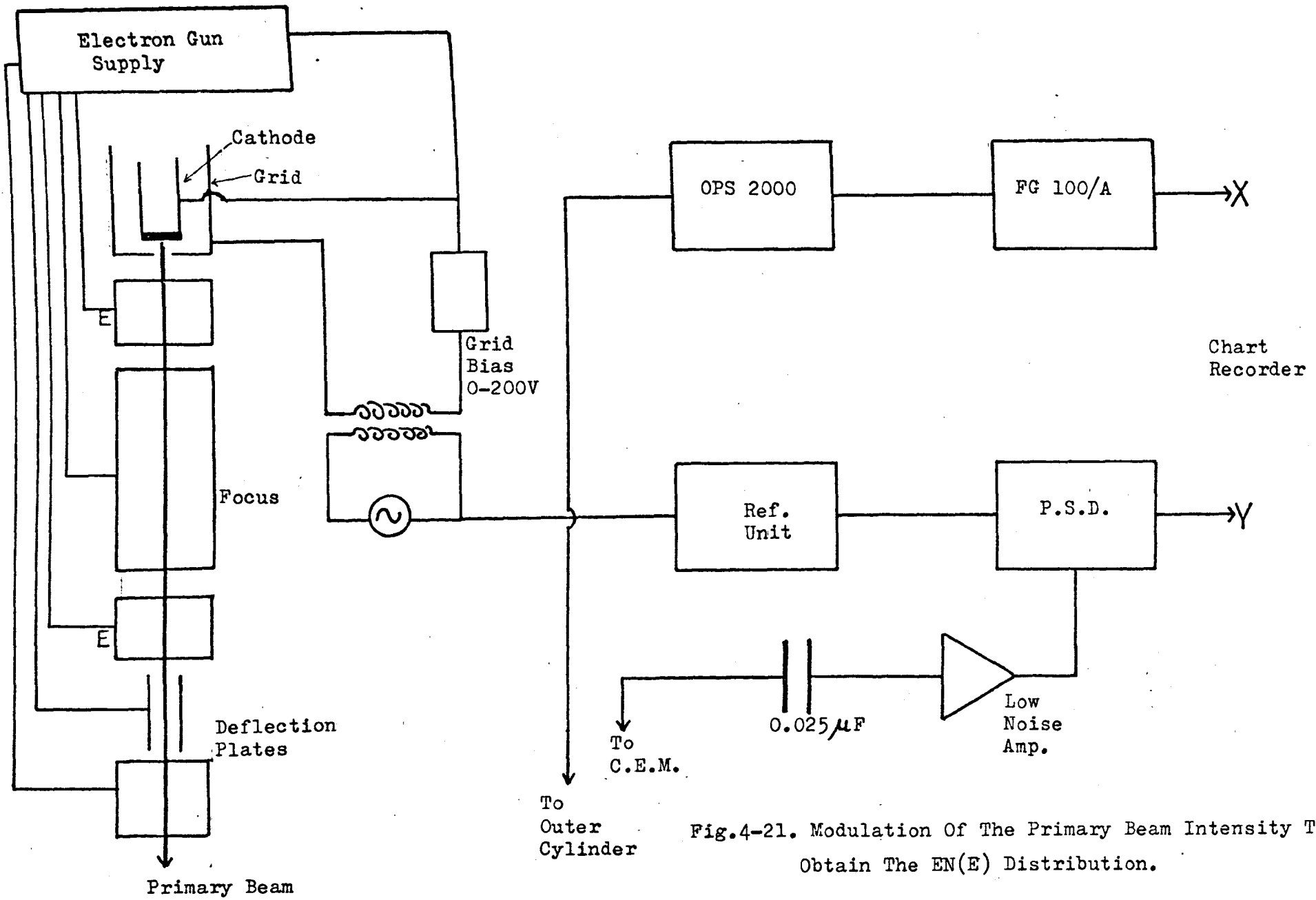


Fig.4-21. Modulation Of The Primary Beam Intensity To Obtain The EN(E) Distribution.

$$\text{Then } I_c = K E N (E) (I_0 + k' \sin \omega t),$$

so that the collector current consists of a d c term and a sinusoidal term  $I_c' (\omega, E) = k' K E N (E) \sin \omega t$ .

Then by detecting the component of the collector current at the frequency  $\omega$  the output of the lock in amplifier is proportional to  $E N (E)$ .

It is well known that the electron beam current is controlled by the grid voltage so that by modulating this voltage the intensity of the primary beam can be modulated by a frequency  $\omega$ . The circuit used for intensity modulation and subsequent detection of  $I_c' (\omega, E)$  is shown in Fig. 4-21. The detection circuit was similar to that used for obtaining the first derivative (c.f. Fig. 4-19), with the modification that the voltage from the OPS 2000 supply was now applied directly to the outer cylinder with the ferrite pot core transformer removed. An output from the lock-in amplifier proportional to the  $E N (E)$  distribution of the emitted electrons could thus be obtained.

It may be wondered why the direct d.c. output of the CEM was not used to obtain  $N (E)$ . The reason is that the output of the multiplier is at a H.T. voltage so that it needs to be decoupled to ground potential and additionally stray currents are picked up in the multiplier making this an unsatisfactory method for obtaining  $N (E)$ .

With the instrument in operation to obtain the  $N (E)$  distribution typical modulation voltages of 12 - 15 volts peak-peak at 1000 Hz were used as well as high electron beam currents  $\approx 100\mu\text{A}$ . Fig. 4.22 shows the spectra recorded, on the same scale, from a molybdenum sample in the  $\frac{dN}{dE}$  and  $E N (E)$  mode of analyser operation. The Auger peaks are clearly detectible although they are on a large sloping background in the  $E N (E)$  spectra.

This mode of operation for a CMA has not been widely used and in

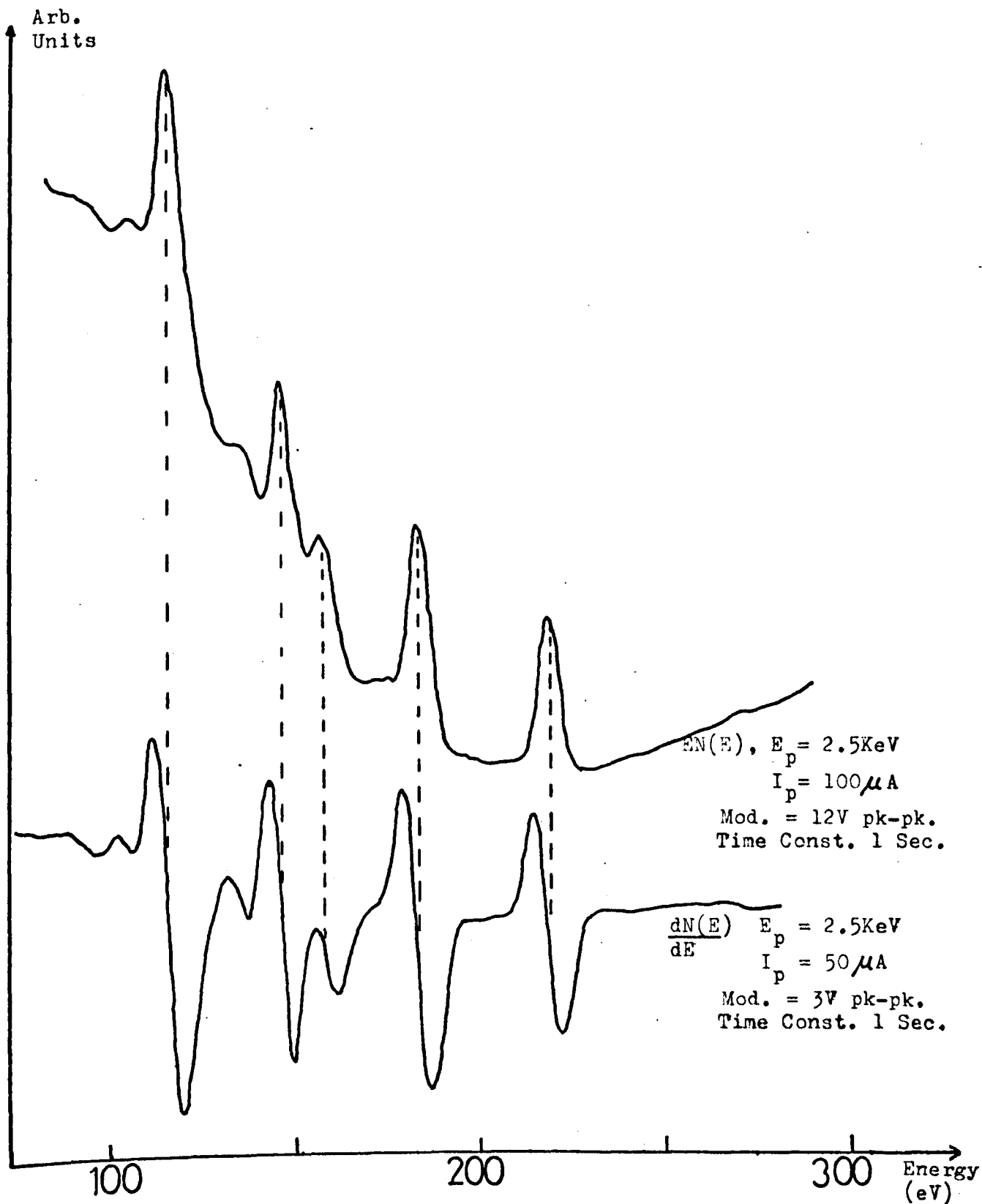


Fig.4-22. The Auger Spectrum Of Mo Plotted In The EN(E) And  $\frac{dN(E)}{dE}$  Mode Of Analyser Operation.

fact in the literature only one previous study, by Seah<sup>131</sup>, using this technique has been reported. We found that Auger peaks were normally on large sloping backgrounds and weak features were difficult to identify so that this mode of operation was not used in our experiments.

#### 4.8 Experimental Properties of the CMA

In this section some experimental results concerning the fundamental instrumental properties of the analyser are presented. As these results were recorded when attempts were still being made to improve the performance of the analyser, they are of necessity, brief.

##### 4.8.1. Resolution

The first results recorded on the instrument were to determine and optimise its resolution. Although the theoretical resolution of the instrument was  $\approx 0.3\%$  there were a number of experimental considerations which prevented the achievement of this value. In particular it was found difficult to reduce the size of the electron beam to obtain a point source and additionally the size of the central aperture meant that the second stage of the instrument was focusing electrons from a finite source.

The resolution was obtained by measuring the peak-peak width  $\Delta E$  of the elastic peak in the first derivative form. The width was assumed to be equal to the half width of the elastic peak in the  $N(E)$  form. The primary electrons were assumed to be monoenergetic so that the observed elastic peak width was entirely instrumental. Then the resolution was calculated from  $R = \frac{\Delta E}{E_p}$ , where  $E_p$  was the energy of the primary electrons.

The effect of the aperture size on the resolution is summarised in Table 4-1. The diameter of the apertures remains constant, in this experiment the resolution has been recorded as a function of the distance  $X$ , in Fig. 4-15. The resolution was measured using a primary beam of 2 KeV and a modulation of 1.5v peak-peak. It was found that with setting (3) in Table 4-1 the signal to noise ratio became so poor, when recording the Auger spectra, that  $X$ , of the end aperture was increased to 0.007 ins., and this was the final setting used to record all subsequent results. The experimentally measured resolution of the CMA for this setting of the apertures was 0.7 - 0.8%.

It has already been mentioned that the source size also influences the resolution of the instrument. Sar-EI (Eq. 4-5) and Zashkvara<sup>128</sup> had predicted the effect, on the resolution, of finite sources and an investigation was carried out to experimentally test the theory. The source size was estimated by allowing the electron beam to strike a fluorescent screen placed just beyond the target, different sized sources could be obtained by varying the focusing voltage in the electron gun. The resolution was estimated by recording the 1200 eV primary beam with 1v pk-pk modulation in the first derivative mode of operation. The results obtained, although of an approximate nature, are summarised in Table 4-2, together with the theoretically predicted values of Sar-EI and Zashkvara. The longitudinal dimension of the source was small in comparison with its diameter so it was neglected in the calculations. These results of Table 4-2 are approximate because the source diameter on the fluorescent screen had to be estimated, nevertheless the experimental values indicate a confirmation of Sar-EI's formula for the resolution of an analyser with a finite source whereas the values predicted by Zashkvara are too high. The results show an increase in resolution with decreasing spot size as expected.

TABLE 4-1

<u>Central Aperture</u>	<u>End Aperture</u>	<u>Resolution</u>
1) 0.010 ins.	0.010 ins.	1.2%
2) 0.005 ins.	0.010 ins.	0.8%
3) 0.005 ins.	0.005 ins.	0.5%

TABLE 4-2

The Effect of Source Size on the Resolution

<u>Source Size (mm.)</u>	<u>Resolution (Sar-E1)<sup>127</sup></u>	<u>Resolution (Zashk vara)<sup>128</sup></u>	<u>Resolution (Experimental)</u>
1	1.8%	4%	1.6%
$\frac{3}{4}$	1.4%	3%	1.2%
$\frac{1}{2}$	1.1%	2%	1.1%
$\frac{1}{4}$	0.7%	1%	0.6%

#### 4.8.2 Effect of the Amplitude of Modulation

In AES and CELS the modulation technique is normally used to obtain the first derivative of the secondary electron emission spectrum, consequently it is important to understand the role the amplitude of modulation plays in the recorded derivative peak heights and additionally how to interpret the peak heights in quantitative AES. In this section some results obtained with our analyser operating in the first derivative mode are presented.

In Fig. 4-23 the change in the observed peak height with amplitude of modulation  $V_m$  is shown for two elastic peaks. The height of the recorded elastic peak increases to a maxima and then slowly starts to decrease with further increase in  $V_m$ . The amplitude of modulation at which the maxima occurred was found to be approximately equal to  $RE_p$ , that is the energy window of the analyser. This result suggests that for maximum instrumental sensitivity to a peak at energy  $E$  an amplitude of modulation =  $R \times E$  must be used, with larger values of  $V_m$  not only does the sensitivity decrease but the resolution also deteriorates. During the course of these results it was found that for small amplitude modulation the peak width was approximately equal to the energy window of the analyser.

In quantitative AES frequently the heights of two peaks at different energies needs to be compared. To gain some insight into the instrumental response some results were recorded on the elastic peaks at 300, 400, 500, 600 eV with amplitudes of modulation: 1, 2, 3, 4, 6 and 8 volts. The observed elastic peak height in the first derivative spectrum is plotted as a function of peak energy, for different amplitudes of modulation in Fig. 4-24. All other parameters were kept constant during these measurements. From Fig. 4-24 it is clear that if  $h_A$  is the height of the elastic peak at energy  $E_A$ ,  $h_B$  is the height of the elastic peak at energy  $E_B$  then the ratio  $h_A/h_B$

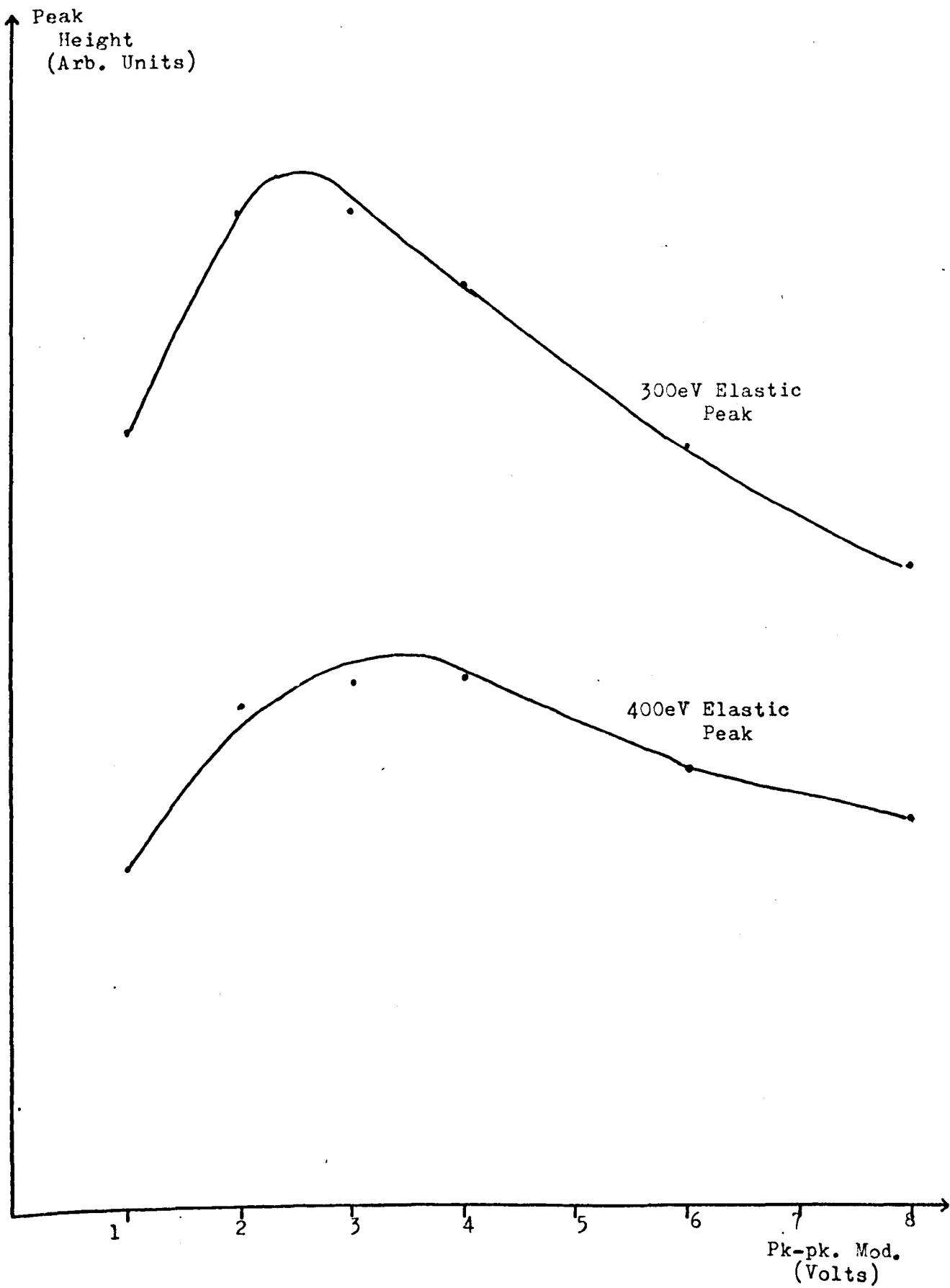


Fig.4-23. The Effect Of The Amplitude Of Modulation On The Observed Peak Height For The 300eV and 400eV Elastic Peaks.

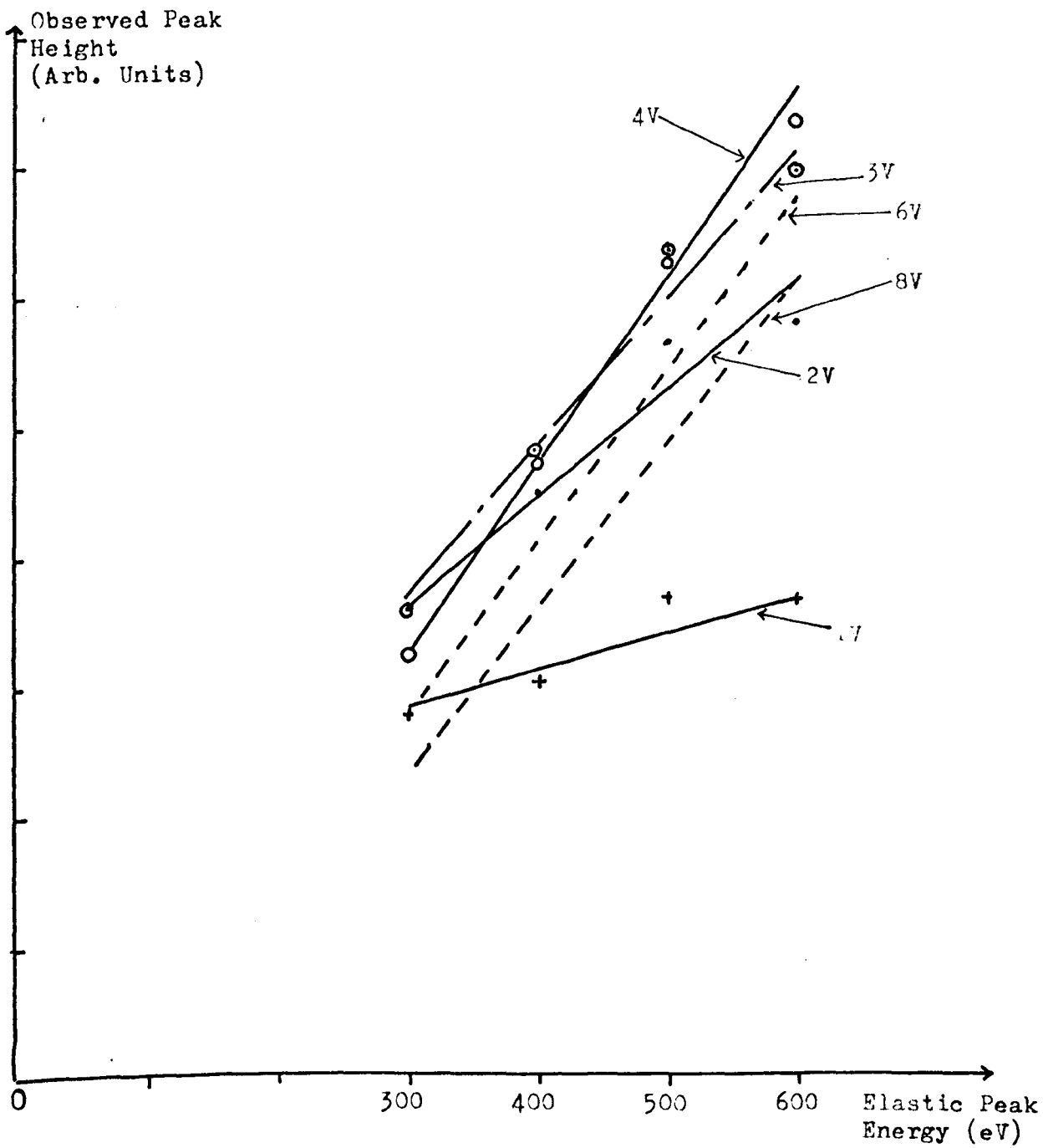


Fig.4-24. The Observed Peak Height v Energy For Different Amplitudes Of Modulation(pk-pk).

depends on the modulation used. This result suggests that care needs to be taken when comparing two Auger peak heights at different energies.

The results so far suggest that the observed height of an elastic peak is a complex interaction of the energy window of the analyser and the modulation amplitude. The question arises as to how the peak heights at different energies are related when recorded by a modulation amplitude  $V_m = \Delta E$ , the energy window of the analyser at that energy. Results were recorded to answer this question and they are plotted in Fig. 4.25. A resolution of 0.8% was assumed for the analyser, then the elastic peak, due to 300 eV electrons would be focused by a voltage of approximately 200 on the outer cylinder, so in these results it is recorded with a modulation amplitude of 0.8% of 200 = 1.6 volts pk-pk, similarly for all the other peaks. All other parameters were kept constant ( $I_p = 3\mu A$  for each energy). A direct proportionality between the energy and peak height is now observed so that  $h_A/h_B = E_A/E_B$ .

These results obtained for the elastic peaks can be used as a guide to compare Auger Peaks at different energies. Auger peaks are generally much more complex having different shapes and widths, but to a first approximation these differences can be neglected and the heights of two Auger peaks at different energies compared by recording them with an appropriate modulation equal to the energy window of the analyser. Then amongst other factors the height of the Auger peak will be proportional to its energy. This result is later used in the adsorption of oxygen on a molybdenum surface.

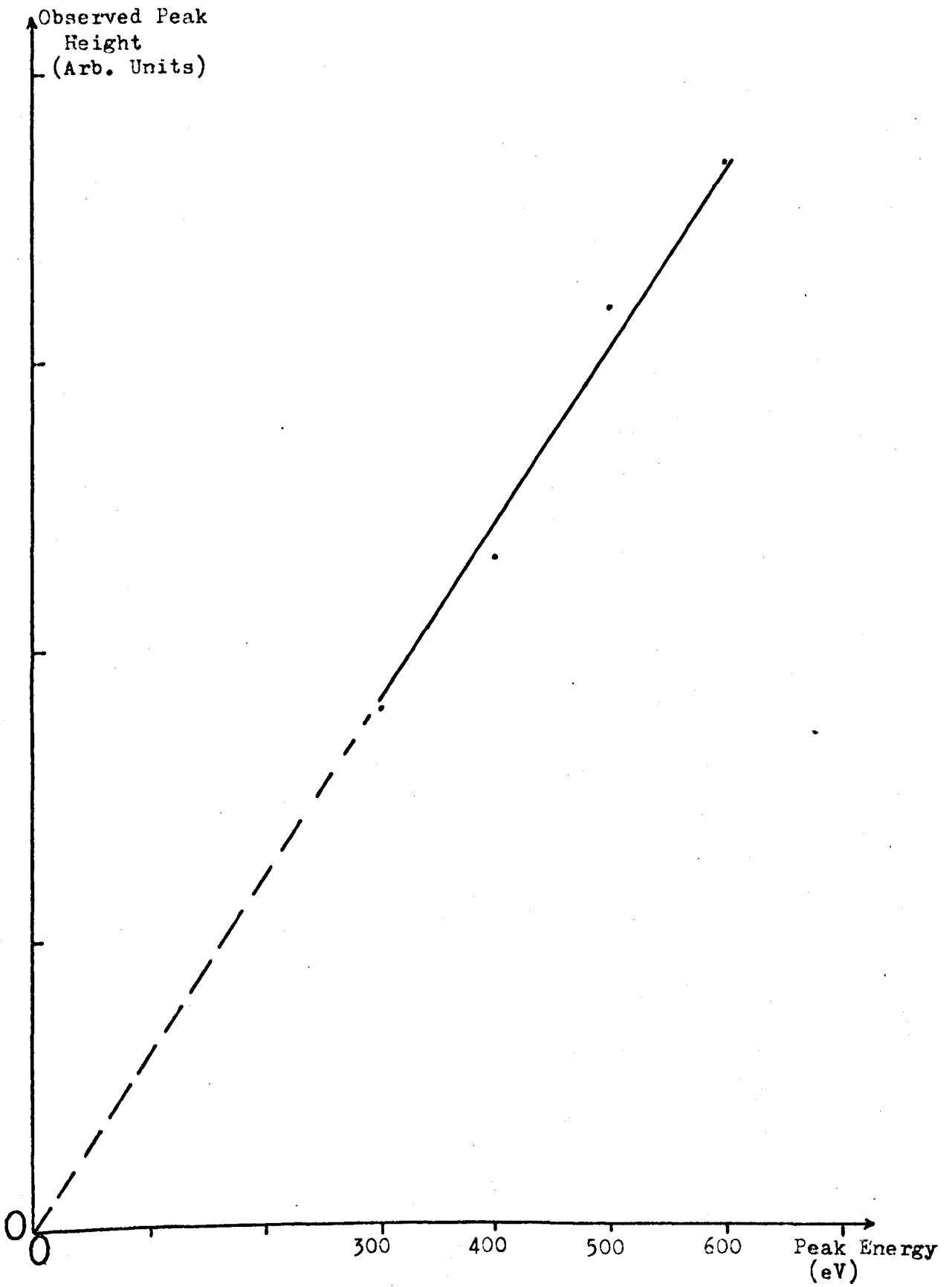


Fig.4-25. The Peak Height v Energy When Recorded With A Modulation Equal To the Energy Window (RX E) Of The Analyser.

#### 4.9 Comparison with other Analysers

There has been no report in the literature describing the construction of a double focusing cylindrical mirror analyser since the commencement of this work although the construction of a single stage instrument has been described by Arnott et al (1972)<sup>132</sup> and by Bishop et al (1972/3)<sup>133</sup>. The double focusing analyser has now become commercially available from P.E.I.<sup>56</sup> (model 15-255) with a minimum resolution of 0.4%. It is thought that the P.E.I. instrument has a better resolution than ours because it uses a smaller central aperture diameter (1mm) than us (1.84mm, Fig. 4-15). There are several commercial organisations (P.E.I., VG, Varian) marketing single stage instruments with resolutions  $\approx$  1%.

The other analyser widely used in Auger spectroscopy is the retarding field (RFA). These instruments have been constructed with better resolutions, on the elastic peak, than the CMA described here, eg. Wright<sup>53</sup> measures a resolution of 0.01% on the 1 Kev elastic peak. But an RFA needs a large modulation amplitude ( 5 - 10 v pk-pk.) to detect the Auger peaks because of their poorer signal to noise ratio hence in practise the CMA is superior for Auger analysis.

#### 4.10 Summary and General Comments

This chapter has described the successful construction of an apparatus for surface studies. An ultra high vacuum ( $5 \times 10^{-10}$  torr) environment can be routinely obtained by mildly baking the chamber up to 200°C for a few days and then electronspectroscopy studies performed on a specimen. An electron energy analyser, suitable for Auger spectroscopy and characteristic energy loss spectroscopy, has

been constructed whose performance (resolution 0.7 - 0.8%) compares favourably with commercially available instruments of considerably higher cost.

The following chapters are devoted to presenting the results obtained, by using this apparatus to study selected materials. It must be stressed that not all the results presented in the following chapters were recorded with the apparatus at its optimum performance. In particular the measurements on stainless steel, gold and some of the molybdenum results were recorded when the apparatus was still at a development stage.

A large number of Auger spectra in the  $\frac{dN}{dE}$  mode were recorded in the course of the present work and in general, unless otherwise stated in the text, the instrument operating conditions were as follows:

Primary beam energy - 2.7 - 2.9 Kev.

Primary beam current - 50-70 $\mu$ A, lower if beam induced effects present.

Primary beam strikes target at a glancing angle of 20-25 $^{\circ}$ .

Modulation frequency - 2000 Hz.

Modulation amplitude - 1 - 12v. pk-pk.

Time constant on phase sensitive detector -

normally 1 sec, although 3 secs. and 10 sec. also sometimes used.

Sweep rate - normally 1eV/sec, but slower for more accurate work.

Prior to recording the Auger spectra, the output signal from the PSD was maximised by adjusting the X and Y deflection plates in the electron gun. The spectra were recorded as a function of the voltage  $V_p$  on the outer cylinder of the CMA and then calibrated by measuring the

voltage necessary to focus electrons of a known primary energy, without altering the target position. Although the theoretical ratio between the energy of the particles  $V_e$  and the focusing voltage  $V_p$  on the outer cylinder was 1.565 in practise slightly lower values (1.530 - 1.550) were measured, possibly due to the influence of "end effects".

## CHAPTER 5

### AUGER ELECTRON SPECTROSCOPY OF STAINLESS STEEL (EN58E)

#### 5.1 Introduction

Stainless steel is a widely used material whose surface properties are of considerable practical interest. The Auger spectrum of stainless steel was initially studied because it contains a number of elements having peaks over a wide energy range, so that the detection of these peaks would confirm the successful operation of the energy analyser. Additionally a specimen of stainless steel could be easily obtained and was of a known composition so that the sensitivity of the instrument could be qualitatively estimated.

Previous surface studies have been carried out on stainless steel using Auger electron spectroscopy. In particular Stein et al (1969)<sup>135</sup> has used AES to confirm the segregation of atoms to grain boundaries during temper embrittlement of low alloy steels. Depth profiles of the oxide films on stainless steel surfaces have been carried out by Betz et al (1974)<sup>136</sup> and by Coad et al (1974)<sup>137</sup> using AES in conjunction with sputter etching.

#### 5.2 Experimental

The specimen studied was cut from a 1/16th inch thick sheet of EN58E stainless steel (Type 304). This was the same grade which was used in the construction of the vacuum chamber. One face of the target, of dimensions (1 cms. x 2 cms.) was polished on wet grinding paper, different grades were used and the final polish was carried out on a 15 $\mu$

(grit size) paper. The target was then polished with grade A diamond paste<sup>138</sup> to give the surface a mirror finish. Before insertion into the vacuum chamber the target was ultrasonically cleaned in acetone and distilled water.

The chamber was then evacuated to a pressure of  $1 \times 10^{-9}$  Torr after several days of pumping and baking. The subsequent Auger spectra recorded were normally excited with glancing incident electron beam ( $20 - 25^\circ$ ) of 2.9 KeV energy and 50 $\mu$ A current.

### 5.3 Results and Discussion

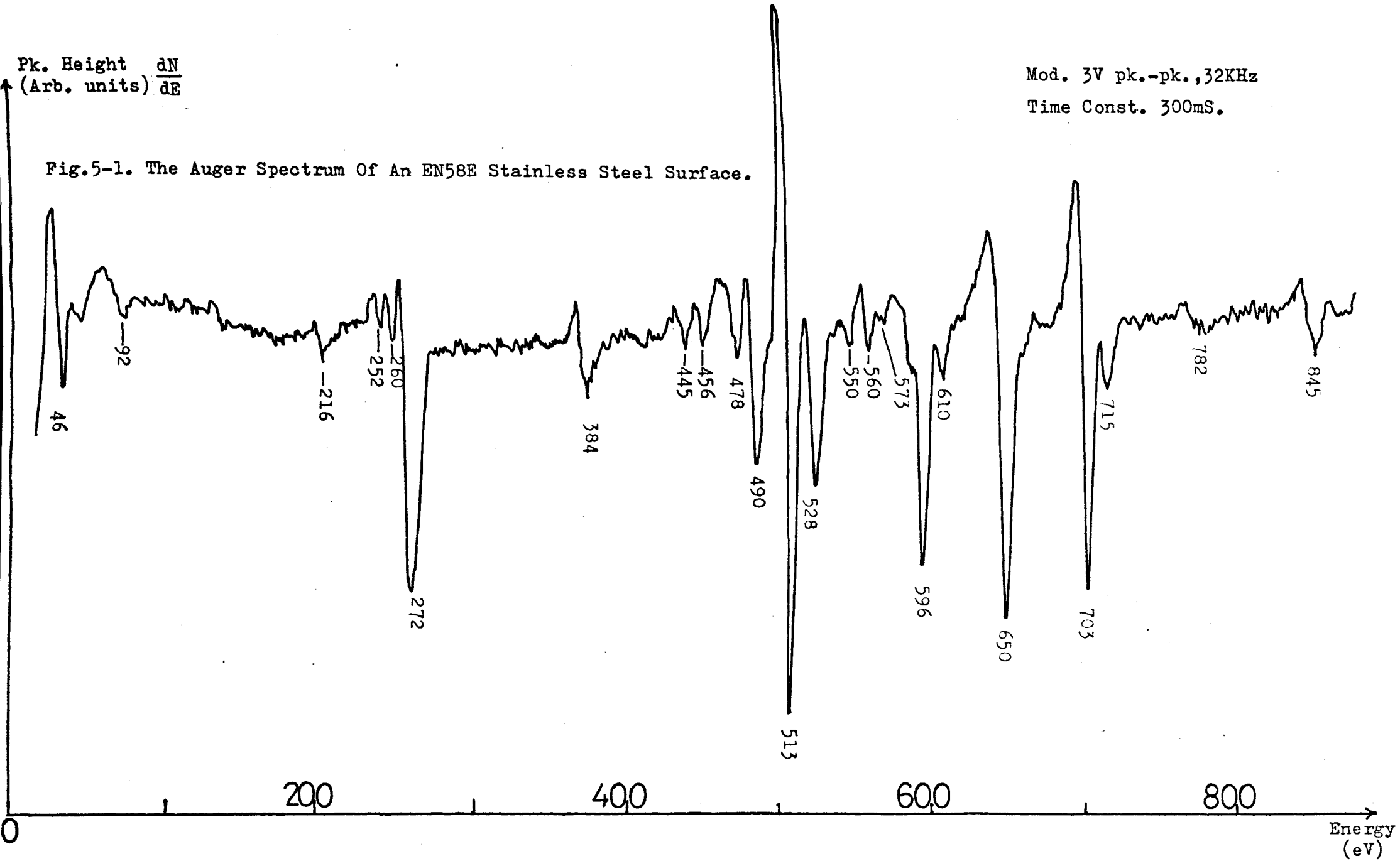
The initial Auger spectra of the specimen surface detected the Carbon KLL peak at  $\approx 270$ eV only. The top layer of the target surface thus needed to be removed and this was attempted by using the cold cathode glow discharge method, described in sub-section 4.4.3. A cleaning action similar to that shown in Fig. 4-11 was observed to take place, but the C could not be completely removed. Further cleaning of the surface was carried out using the argon ion source described in sub-section 4.4.2, eventually when an estimated 2000A<sup>0</sup> of the surface layers had been removed, an Auger spectra characteristic of the sample was recorded and this is shown in Fig. 5-1. Further removal of the surface layers did not produce any detectable change in the observed Auger spectra.

Due to the inlet of gases for specimen sputtering the pressure inside the chamber deteriorated and the Auger spectra of Fig. 5-1 was recorded in a vacuum of  $1 \times 10^{-8}$  Torr and as the gases inside the chamber are mainly CO, and CO<sub>2</sub> this probably accounts for the large carbon and oxygen peaks detected on the surface at 270 and 513 eV respectively.

Pk. Height  $\frac{dN}{dE}$   
(Arb. units)

Mod. 3V pk.-pk., 32KHz  
Time Const. 300mS.

Fig.5-1. The Auger Spectrum Of An EN58E Stainless Steel Surface.



The composition of a piece of EN58E stainless steel had been determined by the suppliers<sup>139</sup> and is summarised in Table 5-1.

TABLE 5-1

Composition of EN58E Stainless Steel

C	0.05%
Si	0.62%
Mn	0.99%
S	0.015%
P	0.034%
Ni	9.26 %
Cr	18.0 %

The remainder being Fe

The energies of the observed Auger peaks were determined and are summarised in Table 5-2. From a knowledge of the composition of the sample and using the P.E.I. Handbook of Auger Electron Spectroscopy<sup>140</sup> for comparison, the elements from which the observed peaks originate are identified and transitions assigned to them from the tables of Coghlan and Clausing<sup>36</sup>, Table 5-2.

There is some uncertainty as to the origin of the two peaks at 445 and 456 eV. No element, of which the steel is composed, has strong peaks at these energies, a possibility is that they may arise due to the interaction of the oxygen with the surface to form an oxide. No peaks were observed due to the elements sulphur or phosphorus, as

TABLE 5-2

Observed Auger Peaks from Stainless Steel (EN58E)

<u>Observed Energy (eV)</u>	<u>Element</u>	<u>PEI Energy (eV)<sup>140</sup></u>	<u>Transition<sup>36</sup></u>
46	Fe	47	$M_{2/3}M_{4/5}M_{4/5}$
92	Si	92	$L_3M_{2/3}M_{2/3}$
216	Ar	215	$L_3 M_{2/3}M_{2/3}$
252			
260			
272	C	272	$K L_{2/3}L_{2/3}$
384	N	381	$K L_{2/3}L_{2/3}$
445			
456			
478	O <sub>2</sub>	475	$K L_1L_1$
490	O <sub>2</sub> , Cr	490,489	$L_3M_{2/3}M_{2/3}$ (Cr) $K L_1L_{2/3}$ (O <sub>2</sub> )
513	O <sub>2</sub>	510	$K L_{2/3}L_{2/3}$
528	Cr	529	$L_3M_{2/3}M_{4/5}$
550	Fe	550	$L_3 M_1 M_{2/3}$
560	Fe	562	$L_2 M_1 M_{2/3}$
573	Cr	571	$L_3 M_{4/5}M_{4/5}$
596	Fe	598	$L_3 M_{2/3}M_{2/3}$
610	Fe	610	$L_2 M_{2/3}M_{2/3}$
650	Fe	651	$L_3 M_{2/3}M_{4/5}$
703	Fe	703	$L_3 M_{4/5}M_{4/5}$
715	NiFe	716,716	$L_2 M_{4/5}M_{4/5}$ (Fe) $L_3 M_{2/3}M_{2/3}$ (Ni)
782	Ni	783	$L_3 M_{2/3}M_{4/5}$
845	Ni	848	$L_3 M_{4/5}M_{4/5}$

expected, due to their small concentrations. The 92eV peak is identified as the Si,  $L_3 M_{2/3} M_{2/3}$  transition implying an instrumental sensitivity of less than 1% for Si. This peak could not be associated with any of the other elements present in the sample so that it originates wholly from Si atoms and its detection gives us a rough estimate of the instrumental sensitivity. The strong peaks of manganese occur at 542 and 589 eV (P.E.I. energy), but these could not be detected because of the low concentration of this element and the presence of strong Fe and Cr peaks in this energy range. A peak at 216 eV is identified as originating from argon and the one at 384 eV as being from nitrogen, these elements are thought to have been embedded into the surface during the ion bombardment stage of specimen treatment.

The intensity of the observed carbon peak at 272 eV is larger than expected from the carbon concentration of the sample. Additionally the shape of the observed peak and particularly the features at 252 eV, 260 eV suggest that the C is present in the form of a carbide. The C (KLL) Auger peak is known to have a distinct shape depending on its chemical environment<sup>64</sup>. Coad and Riviere (1970)<sup>141</sup> have observed structure and overall shape similar to this in the carbon peak from nickel carbide  $Ni_3C$  and the energies of their peaks: 270, 259, 250 eV agree well with our values suggesting that possibly the C present on our stainless steel specimen is bonded to the nickel atoms. The general shape of the C Auger peak in Fig. 5-1 is different from its shape when recorded from a molybdenum surface as shown in Chapter 7 and the measured energies of the features are also different.

The large C signal and the large oxygen signal at 513 eV probably originated from the poor vacuum conditions in which the specimen was studied. The residual gases inside the chamber are carbon monoxide

and carbon dioxide and these are probably dissociating on the specimen surface under the impact of the electron beam, with the carbon atoms forming a carbide and the oxygen atoms combining with one of the other elements present in stainless steel to form an oxide. Betz et al (1974)<sup>136</sup> have studied the formation of oxide films on stainless steel surfaces and they have shown that chromium oxide formation is favoured at all temperatures, in preference to NiO, or the iron oxides, thus we are inclined to associate the oxygen atoms as bonding with the chromium atoms present on the surface. Other evidence to support this argument comes from the work of Ueda and Shimizu (1974)<sup>142</sup> who have shown that on the formation of an iron oxide the 46 eV Auger peak of iron is split into two peaks at approximately 41 and 49 eV. We observed no such splitting of our 46 eV Auger peak in Fig. 5-1.

Of the major Auger peaks from pure chromium at 489, 529, 571 eV<sup>140</sup> only the  $L_3 M_{2/3} M_{4/5}$  transition at 528 eV could be clearly identified due to the presence of a strong oxygen signal in this energy range. By taking the peak to peak height in the derivative spectrum as a measure of the intensity of a transition, the relative intensity of the 490 eV peak to the 513 eV ( $O_2$ , KLL) peak in Fig. 5-1 is larger by 25% than the relative intensity of these two peaks obtained from the oxygen spectrum of P.E.I., indicating a contribution to the 490 eV peak due to the chromium  $L_3 M_{2/3} M_{2/3}$  transition. The 573 eV peak identified as the  $L_3 M_{4/5} M_{4/5}$  transition is considerably reduced in intensity relative to the  $L_3 M_{2/3} M_{4/5}$  transition than in pure chromium.

The major LMM series of iron Auger peaks can all be identified and this portion of the spectrum in Fig. 5-1 compares well with Fe Auger spectrum of P.E.I.<sup>140</sup> although minor differences are observed. The 591 eV peak of P.E.I. is only observed as a shoulder in our spectrum and the 650 eV peak appears to have broader low energy tail than the same peak

in the pure element.

The three principal nickel peaks were also detected although their intensity is weak due to its low concentration. The Ni  $L_3 M_{2/3}$  is expected to make only a small contribution to the 715 eV peak which is thought to be primarily an iron transition. Thus all the major elements of which the stainless steel was composed of were identified on the surface.

#### 5.4 Summary

At this stage of the apparatus performance an Auger spectra had been successfully obtained from a EN58E stainless steel sample validating the design and correct operation of the energy analyser as an Auger electron spectrometer in the energy range 0 - 900 eV. The results also confirmed the usefulness of the argon ion source as a surface cleaning tool. The major elements of which the steel was thought to be composed of were identified from the Auger spectra and silicon with a concentration of < 1% was detected indicating a rough estimate for the sensitivity of the instrument.

## CHAPTER 6

### THE AUGER AND CHARACTERISTIC ENERGY LOSS SPECTROSCOPY OF GOLD

#### 6.1 Auger Spectroscopy of Gold

##### 6.1.1. Introduction

Gold is a comparatively inert noble element, and for this reason it was chosen for study in the early stages of operation of the equipment when a UHV environment could not be easily obtained. The element is widely used in pure and alloy form and this study is a contribution to the Auger electron spectroscopy of gold surfaces. There have been several previous studies of the Auger spectra of Au, <sup>143,144,145,140,82</sup> but the only complete spectra published has been by P.E.I.<sup>140</sup>. In general the published spectra are in broad agreement with each other and with the spectra of Suleman (1971)<sup>51</sup> and Wright (1974)<sup>53</sup>, recorded in our own laboratory, using a retarding field type of analyser.

##### 6.1.2 Experimental

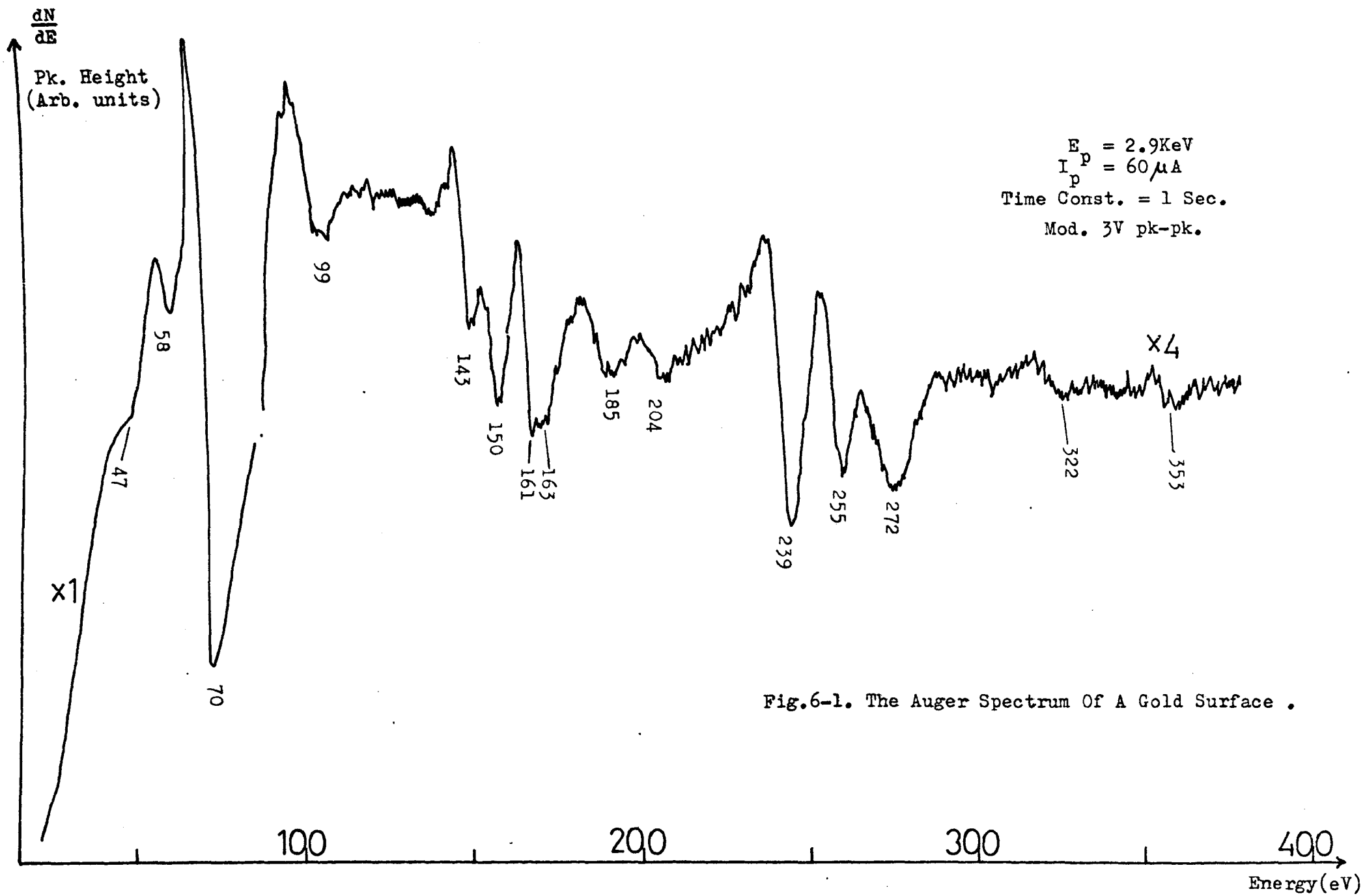
A target of 1.5 cms x 0.8 cms. dimensions was cut from a sheet of polycrystalline gold of spectroscopic purity, supplied by the Johnson Matthey Company<sup>146</sup>. One face of the target was polished with grade A diamond paste and then ultrasonically cleaned in acetone and distilled water before inserting the specimen into the chamber. The chamber was then evacuated and baked up to a temperature of 200°C, for several days to obtain a pressure  $\sim 10^{-9}$  Torr. Auger spectra were then excited by a glancing incidence electron beam of 2.7 - 2.9 KeV energy and up to 70 $\mu$ A beam current.

### 6.1.3 Results and Discussion

The initial Auger spectra of the target revealed a strong peak at 272 eV due to carbon. Gold was known to have strong peaks in the energy range 66 - 70 eV, and although these peaks were detected they were of approximately the same intensity as the C peak, additionally the signal to noise ratio in the Auger spectra for such a surface was very poor being only about 5:1. The shape of the carbon peak suggested that it was present on the surface in the form of a graphite layer and not as a carbide. A small peak due to oxygen could also be detected at 510 eV about 1/20th the size of the main C peak.

Attempts were made to remove the carbon contamination from the surface by argon ion bombardment using the sputterer, but although some reduction in the size of the carbon Auger peak occurred, it could not be eliminated. Attempts were then made to reduce the contamination by heating the specimen to near its melting point (1336<sup>o</sup>k), by electron bombardment for short intervals. This was found to further reduce the carbon Auger signal but it could not be completely removed. Joyner et al (1973)<sup>82</sup> also found that carbon could not be completely removed from a gold surface by simply heating the specimen. Possibly there is some segregation of carbon occurring from the bulk to the surface of the target during heating eventually reaching an equilibrium situation when the amount of carbon removed from the surface equals the amount which segregates from the bulk. It was noted that as the carbon contamination decreased the signal to noise ratio improved.

With the carbon peak at a minimum and no detectable oxygen peak, the low energy Auger spectrum of gold is shown in Fig. 6-1. The overall appearance of the spectra is in good agreement with the work of other authors. Fig. 6-1 was recorded with a modulation amplitude of 3v pk-pk and a strong peak in the Auger spectra was observed at 65 - 70 eV. Fine structure in this peak was detected when 1 volt



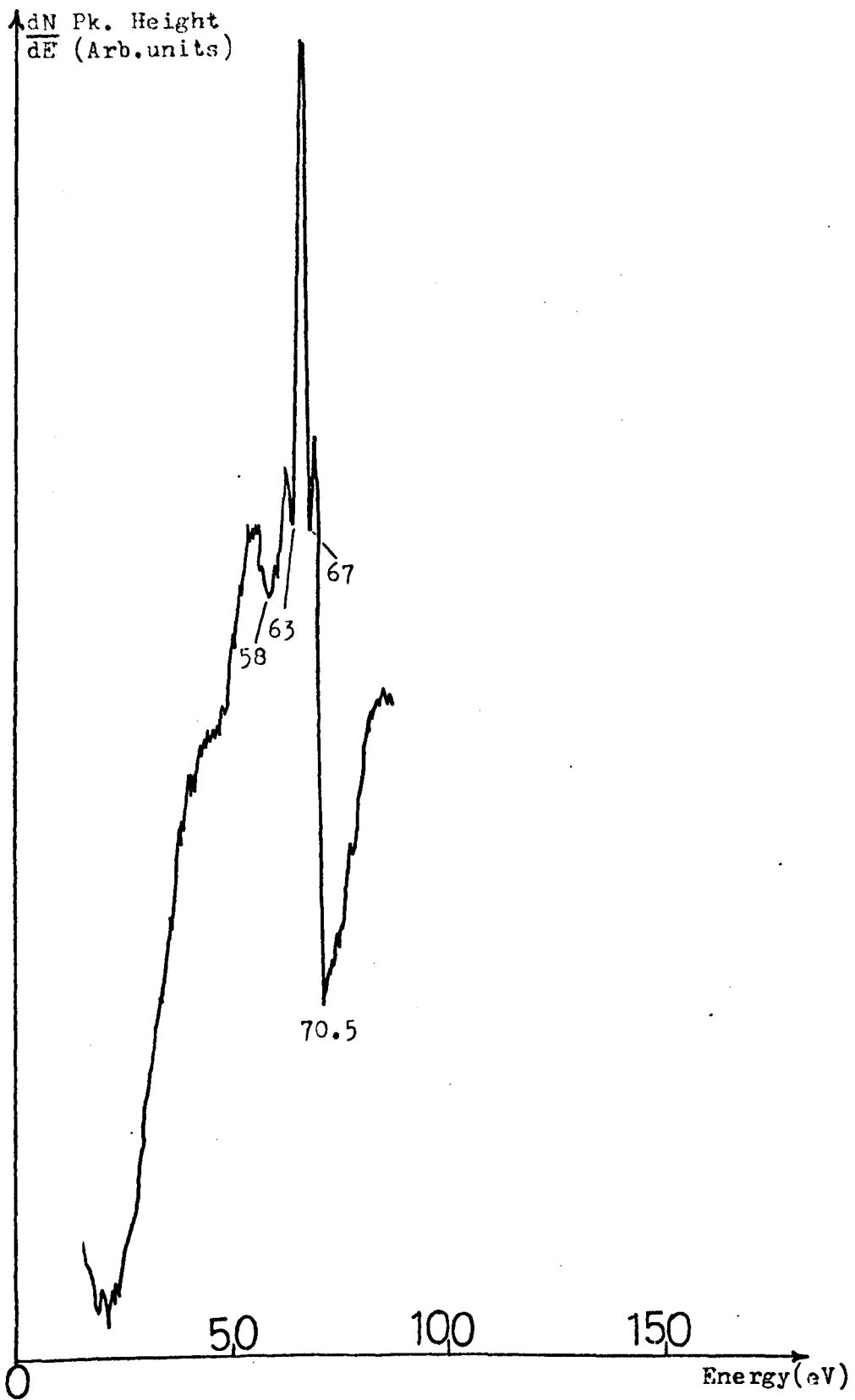


Fig.6-2. The Major Gold Auger Peak Recorded With 1V Pk-Pk Modulation.

TABLE 6-1

Energies of Observed Peaks (eV) of Gold

<u>Present Work</u>	<u>PEI<sup>140</sup> (1972)</u>	<u>Joyner and Roberts (1973)<sup>82</sup></u>	<u>Haas et al (1970)<sup>143</sup></u>
47	43		44
58	56		
63			
67	66	66	
70.5	69	68	
99			
143	141	136	144
150	150	146	
161	160	158	156
163	165	163	164
185	184	180	
204	200	196	
	216		
239	239	233	
255	255	248	
272			
322	323		
353	351/356		

pk-pk modulation was used, as shown in Fig. 6-2. The high energy peaks reported by P.E.I. at about 2000 eV could not be detected with our instrument at this stage of its development.

The energies of the observed peaks are summarised in Table 6-1 together with the values obtained by other workers. Our energy value of a peak is the position of its maximum negative excursion. Transitions were assigned to the observed peaks using the tables of Coghlan and Clausing and these are summarised in Table 6-2. The energy of the primary electrons is such that only the N and O levels are ionized. In Table 6-2 only the strongest transitions, on the basis of the multiplicity, having an energy close to the observed energy are summarised and in many cases a single transition cannot be assigned to an observed peak.

No transition could be satisfactorily assigned to the 58 eV peak possibly it is a plasmon loss of the  $N_6, N_7$  W electrons, as the strongest peaks in the spectra were identified as due to  $N_6, N_7$  W transitions. Most of the peaks having energies above 100 eV were identified as Coster Kronig type transitions, whose influence is particularly apparent when the intensity of the  $N_6$  W transition is compared with the intensity of the  $N_5$  W transition. On the basis of the multiplicity these transitions should have equal intensity but the observed value of the ratio of the peak heights is approximately 8 : 1, in favour of the  $N_6$  W transition and even this value must be regarded as a minimum due to the poorer C.E.M. gain at the  $N_6$  W electron energy. Vacancies in the  $N_4, N_5$  subshells are being filled by Coster Kronig transitions of type  $N_4 N_6 N_7, N_5 N_6 N_7$  etc. effectively enhancing the vacancy distribution in the  $N_6, N_7$  subshells contributing to their observed high relative intensity. The 272 eV peak was assigned to a carbon K  $L_{2/3} L_{2/3}$  transition with some contribution from the gold

$N_5 O_3 V$  transition.

It is interesting to note that the peaks identified as the  $N_6$ ,  $N_7$   $VV$  transitions are very narrow, whereas the valence band of gold has been measured to be approximately 7 eV wide by photoemission<sup>147,148</sup>. As mentioned in Chapter 2, authors have suggested that an Auger peak of type  $NW$  will contain the convolution of the valence band density of states, but the narrowness of our observed  $N_6$ ,  $N_7$   $VV$  peaks, estimated width  $\approx 3$  eV, suggests that a comparatively small part of the valence band of gold is available for an Auger emission process. These peaks appear to have more of a quasi-atomic nature than solid state character possibly the results reflect a variation of the transition probability across the width of the valence band or the operation of a selection rule as suggested by Joyner et al (1973)<sup>82</sup>, with whom our results are in broad agreement. These results are also in agreement with the observations on the  $L_{2/3}$   $VV$  Auger transition of  $Cu^{72}$ , and the  $M_{4/5}$   $VV$  transition of  $Ag^{149}$  which display no valence band influences either.

## 6.2 Energy Loss Spectroscopy of Gold

### 6.2.1 Introduction

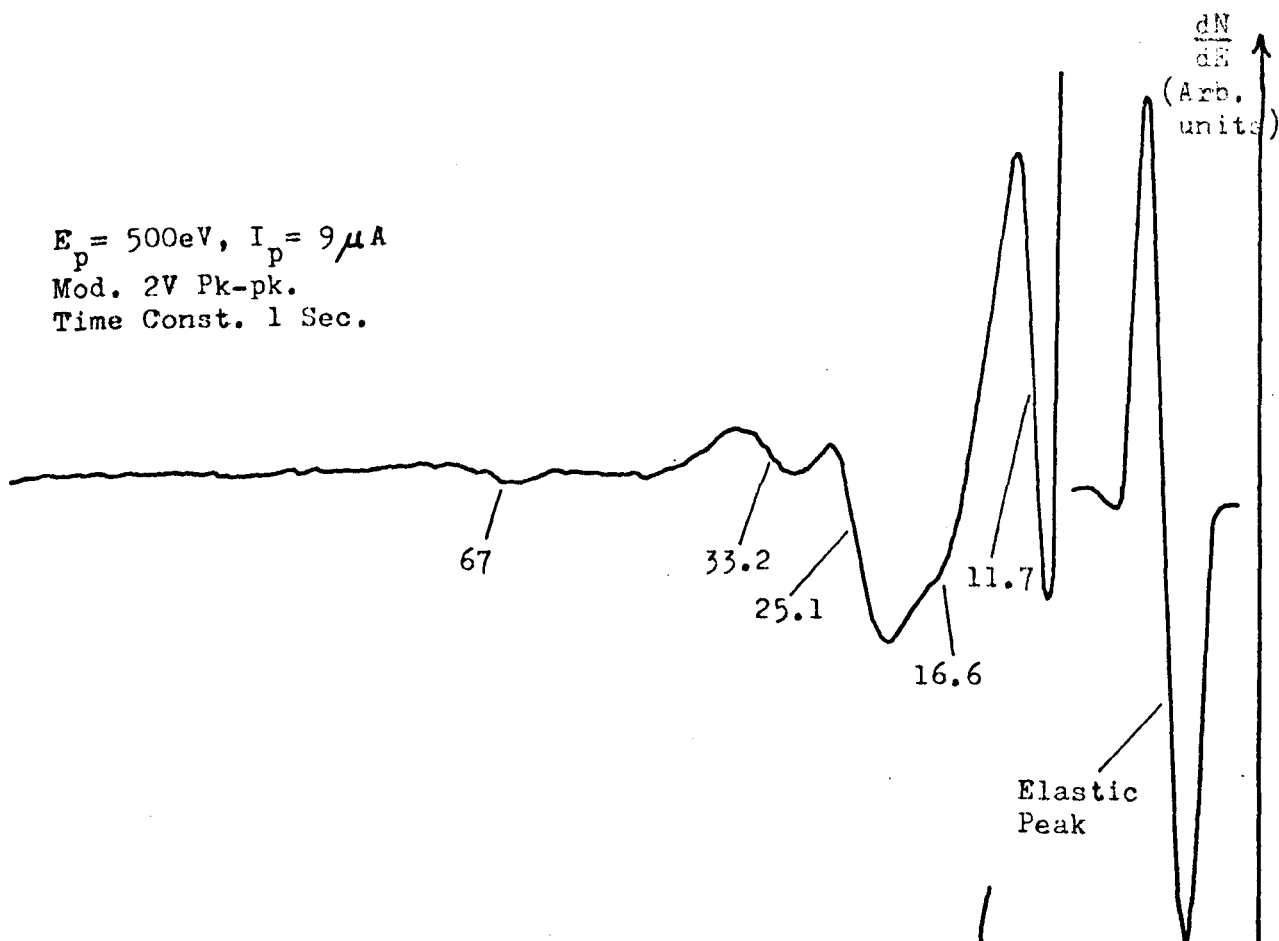
The instrument could easily be adapted to obtain the characteristic energy losses of a material, so that after recording the Auger spectra of gold its characteristic losses were studied. There have been several previous measurements of the characteristic energy loss spectra of gold, Robins (1961)<sup>150</sup> and Powell (1968)<sup>151</sup> are considered the most useful. Powell (1968) has reviewed the previous studies of the energy losses and indicates that there is some controversy as to the position and intensity of the observed losses when measured under identical conditions probably due to differences in surface topography and the presence of surface contaminants as some of the results were recorded in poor vacuum. Thus it would be interesting to study the Au losses on an A.E.S. characterized surface, the only previous such study being by Suleman (1971)<sup>51</sup>.

### 6.2.2 Experimental

The energy losses of gold were recorded on a surface characterized by AES. Auger spectra similar to Fig. 6-1 were obtained before and after recording each loss spectra, particular attention was given to detecting any increase in the contaminants C, S and O. Sulphur and oxygen were not detected on the initial or final Auger spectra and no change in the 272 eV peak due to carbon could be found over the time scale of recording the loss spectra.

The losses were recorded with the electron beam incident at a glancing angle of 20 - 25°. The energy of the primary electrons were measured with a digital voltmeter (DVM) and the voltage on the outer cylinder of the analyser needed to focus these electrons was also

$E_p = 500\text{eV}$ ,  $I_p = 9\mu\text{A}$   
Mod. 2V Pk-pk.  
Time Const. 1 Sec.



$E_p = 900\text{eV}$ ,  $I_p = 15\mu\text{A}$   
Mod. 4V Pk-pk.  
Time Const. 1Sec.

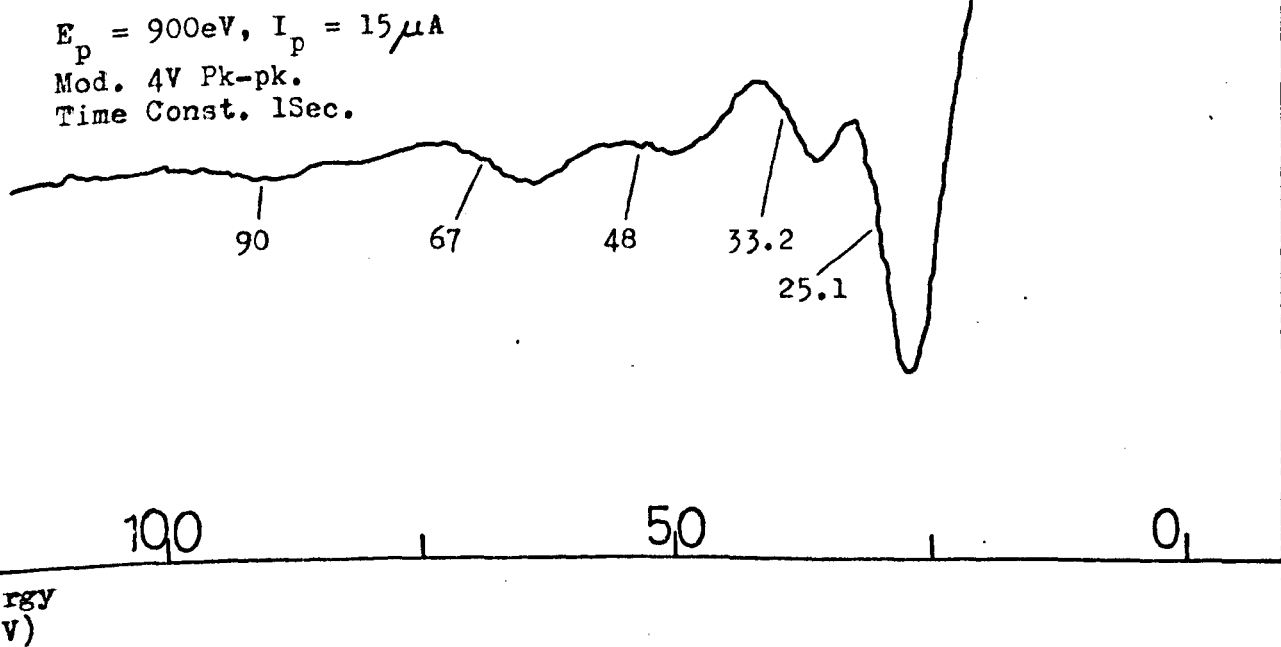


Fig.6-3. The Characteristic Loss Spectra Of Gold Excited With 500eV And 900eV Primary Electrons.

TABLE 6-3

Characteristic Losses of Gold at Different  
Primary Energies

<u>Primary Electron Energy (eV)</u>	<u>Observed Losses (eV)</u>						
500	11.6	16.8	22.2	31.4	45.9	62.9	
500	12.0	16.5	23.0	30.0	41.5		
700	11.5		25.2	34.3	50.4	67.3	90
700			25.2	32.0	48.1	66.5	
900			25.4	34.6	47.7	67	87.6
1000			29.8	36.2	51.2	69.6	91
Mean	11.7	16.6	25.1	33.2	47.5	66.9	89.5

TABLE 6-4

Comparison of the Au Losses

<u>Present Work (eV)</u>	<u>Suleman (1971)<sup>51</sup></u>	<u>Powell (1968)<sup>151</sup></u>	<u>Robins (1961)<sup>150</sup></u>	<u>Cranfield (1964)<sup>153</sup></u>
	7	6.2	6.3	6.7
11.7		10.8		
16.6		16.3	16	16.3
25.1	25.6	24.8	25.8	25.8
33.2	33.4	33.2	32.6	32.6
48				
67	62			
90				

measured with a DVM to provide an accurate calibration of the energy scale. The losses were recorded in the  $\frac{dN}{dE}$  mode of operation of the analyser at different primary electron energies.

### 6.2.3 Results and Discussion

The characteristic energy losses measured using different energy primary electrons are summarised in Table 6-3 and the mean values obtained. Typical loss spectra recorded with 500 eV, and 900 eV primary electrons are shown in Fig. 6-3. The losses obtained from Table 6-3 are labelled on these spectra. The low energy losses are not detected with the 900 eV primary electrons due to the poor instrumental resolution at these energies but the high energy losses are detected due to the higher beam currents increasing the instrumental sensitivity.

The losses identified are compared with some of the values available in the literature in Table 6-4. The low energy loss observed at about 6 - 7 eV by various workers was not detected in our spectra possibly due to poor resolution. Cranfield et al (1964)<sup>153</sup> identified the losses from optical measurements on gold thin films, whereas the other values quoted in Table 6-4 are from electron spectroscopy. The high energy losses detected in our spectra have not been previously reported.

The losses of gold are complicated in comparison with the losses of a free electron metal, eg. aluminium. The presence of strong interband transitions and collective oscillations makes identification of the losses difficult. Discussion of our observed losses is based on the optical properties of gold summarised by Cooper et al (1965)<sup>152</sup>, Fig. 6-4 and the binding energies of the outer electrons, shown in Fig. 6-5, as obtained by Beardon and Burr<sup>30</sup>. The valence band structure from photoemission measurements<sup>147</sup> is also shown in Fig. 6-5.

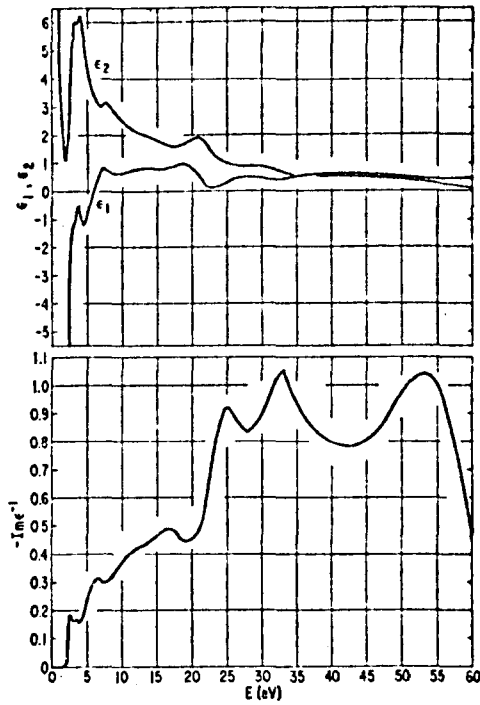


Fig6-4. The Real ( $\epsilon_1$ ) And Imaginary ( $\epsilon_2$ ) Parts Of The Dielectric Constant And The Bulk Loss Function  $-\text{Im}(\frac{1}{\epsilon})$  For Gold.<sup>152</sup>

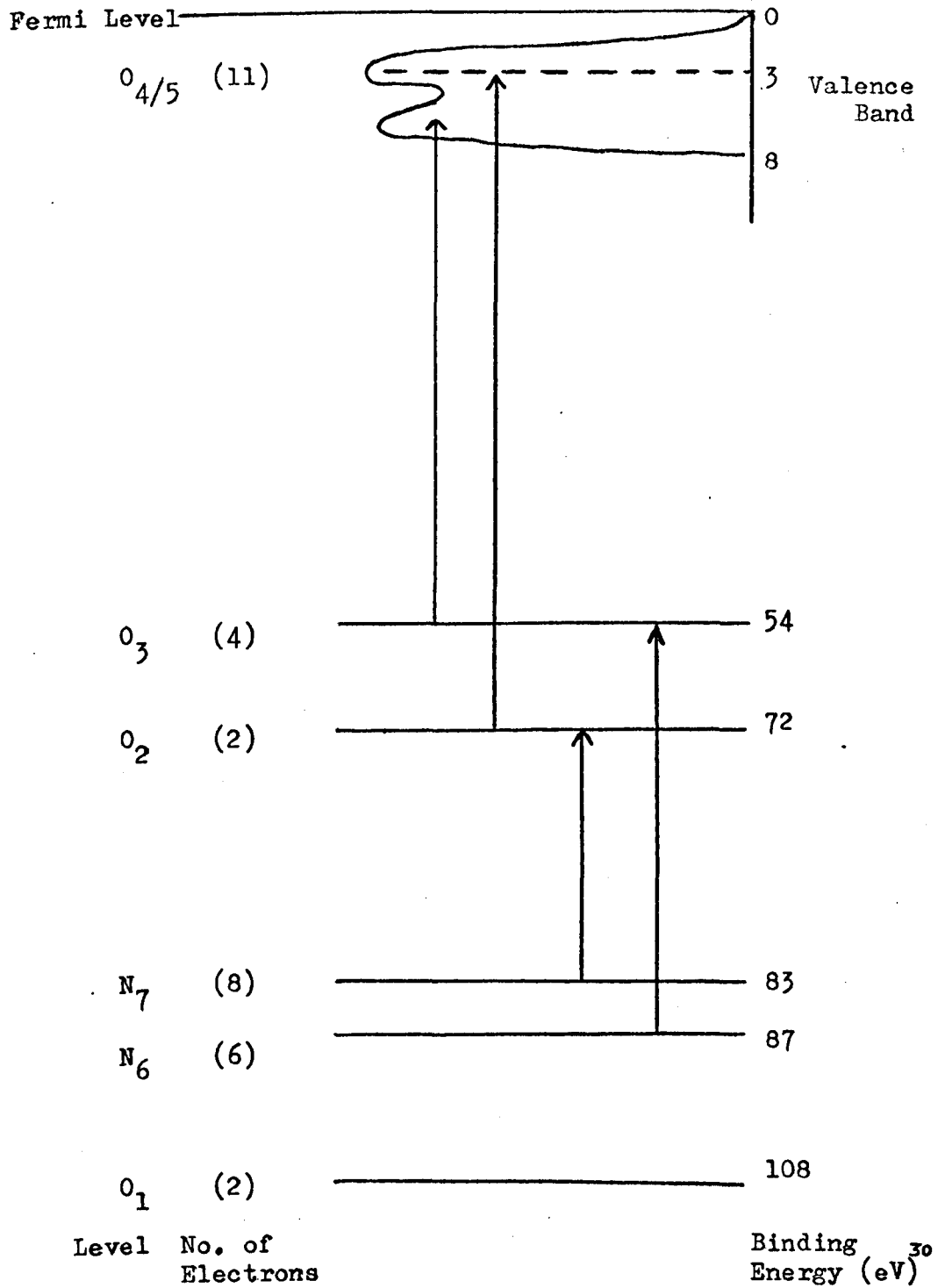


Fig.6-5. The Valence Band And Outer Electronic Levels Of Gold. Possible Characteristic Losse Are Identified On This Diagram.

The 11.7 eV is the strongest loss observed in the spectra excited by the 500 eV primary electrons but it does not correspond to  $\epsilon_1 = 0$ , or to a maxima in  $-\text{Im} \left( \frac{1}{\epsilon} \right)$  in Fig. 6-4. Additionally it is not suspected to be a surface loss as  $\epsilon_1 \neq -1$  in this region. Powell has speculated that this loss is a plasmon oscillation although another possibility is that it is due to the excitation of electrons from the  $N_7$  to the  $O_2$  subshell, Fig. 6-5. This transition has an energy = 11 eV in reasonable agreement with the energy of the observed loss.

The 16.6 eV loss is much weaker in intensity, in Fig. 6-3. but it can be associated with a feature in the loss function  $-\text{Im} \left( \frac{1}{\epsilon} \right)$ . The identification of this loss as a surface plasmon with the 25.1 eV loss as a volume plasmon seems reasonable as they satisfy the  $\frac{\hbar\omega_p}{\hbar\omega_s} = \sqrt{Z}$  relationship. Additionally  $\epsilon_1$  is close to zero and there is a strong maxima in  $-\text{Im} \left( \frac{1}{\epsilon} \right)$  at about 25 eV giving further support to the identification of the 25.1 eV as a volume plasmon loss. On the basis of 11 electrons/atom in the valence band of gold ( $5d^{10}6s^1$ ) the plasmon energy for free electron oscillations can be calculated to be 29.7 eV. The discrepancy may be explained as being due to the presence of strong interband transitions at higher energies.

The 33.2 eV loss has been interpreted as a volume plasmon by Cooper et al and by Powell, but another possibility is that it is due to the  $N_6 - O_3$  interband transition, labelled in Fig. 6-5, whose energy is in good agreement with the observed loss. The 48 eV and the 67 eV losses are interpreted as excitations of the  $O_3$  and  $O_2$  electrons to states in the valence band and the 90 eV loss as the excitation of  $N_6$  electrons to empty states above the Fermi level of the solid.

### 6.3 Summary

The Auger peaks of gold have been identified in the energy range 0 - 350 eV and transitions assigned to them. The spectra is apparently strongly influenced by Coster-Kronig type transitions and the observed width of the peaks involving the valence band indicates that only a narrow portion of the valence band participates in the Auger process.

The characteristic energy losses of gold have been determined from an A.E.S. characterized surface. Explanation of the losses have been tentatively suggested in terms of interband transitions and volume and surface plasmons, by comparison with optical measurements.

## CHAPTER 7

### MOLYBDENUM

#### 7.1 Introduction

Molybdenum is a widely used 4d refractory transition metal, having a b.c.c. crystal structure. The effect of small concentrations of the element on the corrosion resistance of stainless steel is well established<sup>154</sup> and the refractory properties make Mo suitable for use in electronic valves. Additionally molybdenum dioxide is used as a catalyst in the manufacture of ammonia so that a surface study of Mo is of practical importance.

Auger spectroscopy has been used in a number of experiments to characterise clean and contaminated Mo surfaces,<sup>155, 156, 157, 158</sup> mostly in connection with the deposition of thin metal films on to a molybdenum surface, for potential use as thermionic emitters. Studies, using AES, have also been carried out on the adsorption of common gases O<sub>2</sub>, N<sub>2</sub>, CO on to clean and contaminated Mo surfaces<sup>159, 160</sup>. Although the Auger spectra of Mo is well established, transitions have only been assigned to the major peaks, by Haas et al (1970)<sup>143</sup>. Additionally although the loss spectra have been reported by a number of authors there have been no studies on a Mo surface characterised by AES.

In this chapter a more complete Auger spectra than obtained previously is reported together with the characteristic energy losses from a "clean" surface. Additionally work on the initial sticking coefficient of adsorbed oxygen on to a clean and contaminated Mo surface is presented.

## 7.2 Auger Spectroscopy of Molybdenum

### 7.2.1 Experimental

The target used was a flat molybdenum plate of unknown purity having dimensions 1 cms. x 2 cms. x 0.1 cms. and polycrystalline structure. It was supplied by the Murex Company<sup>164</sup>. One face of the target was polished to a mirror finish with the usual metallographic techniques described in Chapter 5 for the stainless steel specimen, and ultrasonically cleaned in acetone and distilled water before insertion into the chamber. The chamber was then evacuated and baked up to 200°C for several days achieving a base pressure  $\sim 10^{-10}$  Torr.

Auger spectra were then obtained with the analyser operating to record the first derivative of the secondary electron emission excited by a glancing incidence electron beam.

### 7.2.2 Results and Discussion

Initial Auger spectra of the target revealed strong peaks due to the contaminants sulphur ( at 150 eV,  $L_{2/3} M_{2/3} M_{2/3}$ ), carbon (at 270 eV,  $K L_{2/3} K_{2/3}$ ) and oxygen ( at 510 eV,  $K L_{2/3} L_{2/3}$ ). The peaks characteristic of Mo were only weakly observed. To remove these contaminants the molybdenum target was heated in-situ by means of electron bombardment from the projection lamp filament. The temperature of the target, estimated with an optical pyrometer, was gradually raised keeping the pressure in the vacuum chamber below  $1 \times 10^{-6}$  Torr. Auger spectra from the surface were recorded periodically and it was found that the target needed to be raised to a temperature  $\sim 1400-1500^\circ\text{C}$  before C and O contaminants began to be removed from the surface, although the S peak height remained unchanged. As the carbon and oxygen atoms were removed from the surface, the intensity of the

molybdenum Auger peaks increased until eventually the strong molybdenum peaks were about the same intensity as the sulphur 150 eV peak. Eventually the C peak could not be reduced any further although the oxygen signal was reduced to below the detection limit of the instrument. It is possible that S and C atoms were segregating to the surface from the bulk in the hot target, certainly S segregation has been reported by Kunimori et al (1974)<sup>165</sup> in his study on molybdenum ribbon although the carbon may be present due to an interaction with the ambient gases in the vacuum chamber (mainly CO<sub>2</sub>, CO).

It had been indicated in the literature<sup>155</sup> that flashing the target to a temperature ~1800°C removes S contamination from a molybdenum surface. With the target heated by the maximum available power of about 120 watts, this temperature could be achieved and a reduction of the S Auger peak was observed. Flashing was continued until the S,150 eV peak was at a minimum.

A typical Auger spectrum taken within 30 minutes of flashing the molybdenum target to about 1800°C is shown in Fig. 7-1 and the low energy Auger peaks are shown in Fig. 7-2. Some carbon contamination is still present as indicated by the peak at ~270 eV and possibly some S contamination. The level of sulphur contamination is difficult to estimate because the S peak coincides with a molybdenum Auger peak at 149 eV. The spectra of Fig. 7-1 was recorded after flashing the target until the 150 eV peak was a minimum relative to the 161 eV. A small oxygen peak (smaller than the C peak in Fig. 7-1) was also detected, probably due to the dissociation of CO or CO<sub>2</sub> on to the Mo surface by the primary electron beam.

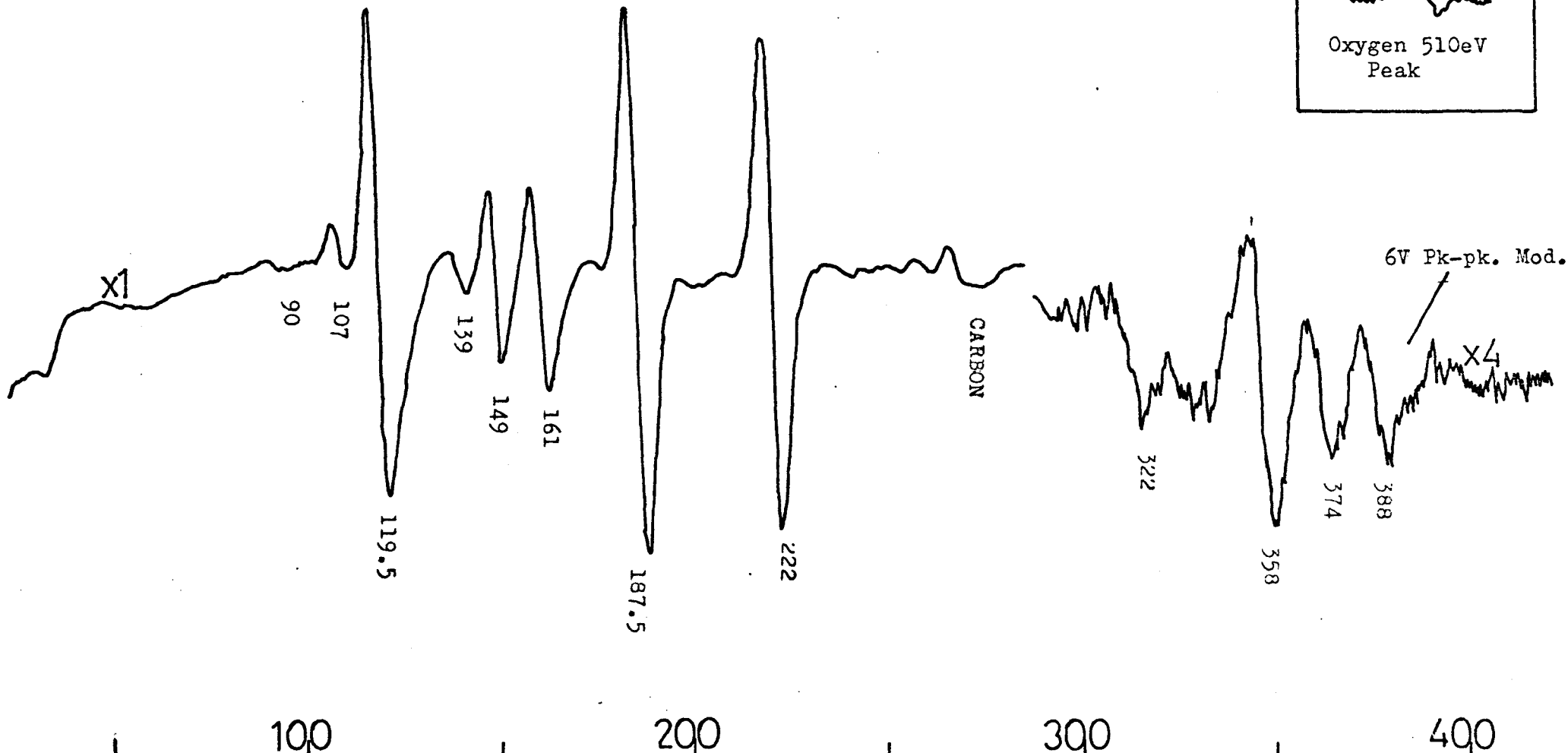
The peak energies as measured by the negative excursion in the derivative spectrum are summarised in Table 7-1 together with the values obtained by other authors. The overall spectra is in broad agreement

$\frac{dN}{dE}$  Pk. Height  
(Arb. units)

Fig.7-1. The Auger Spectrum Of Molybdenum.

$E_p = 2.9 \text{ KeV}$   
 $I_p = 40 \mu\text{A}$   
Mod. = 3V Pk-pk.  
Time Const. 1 Sec.

X1  
Oxygen 510eV  
Peak



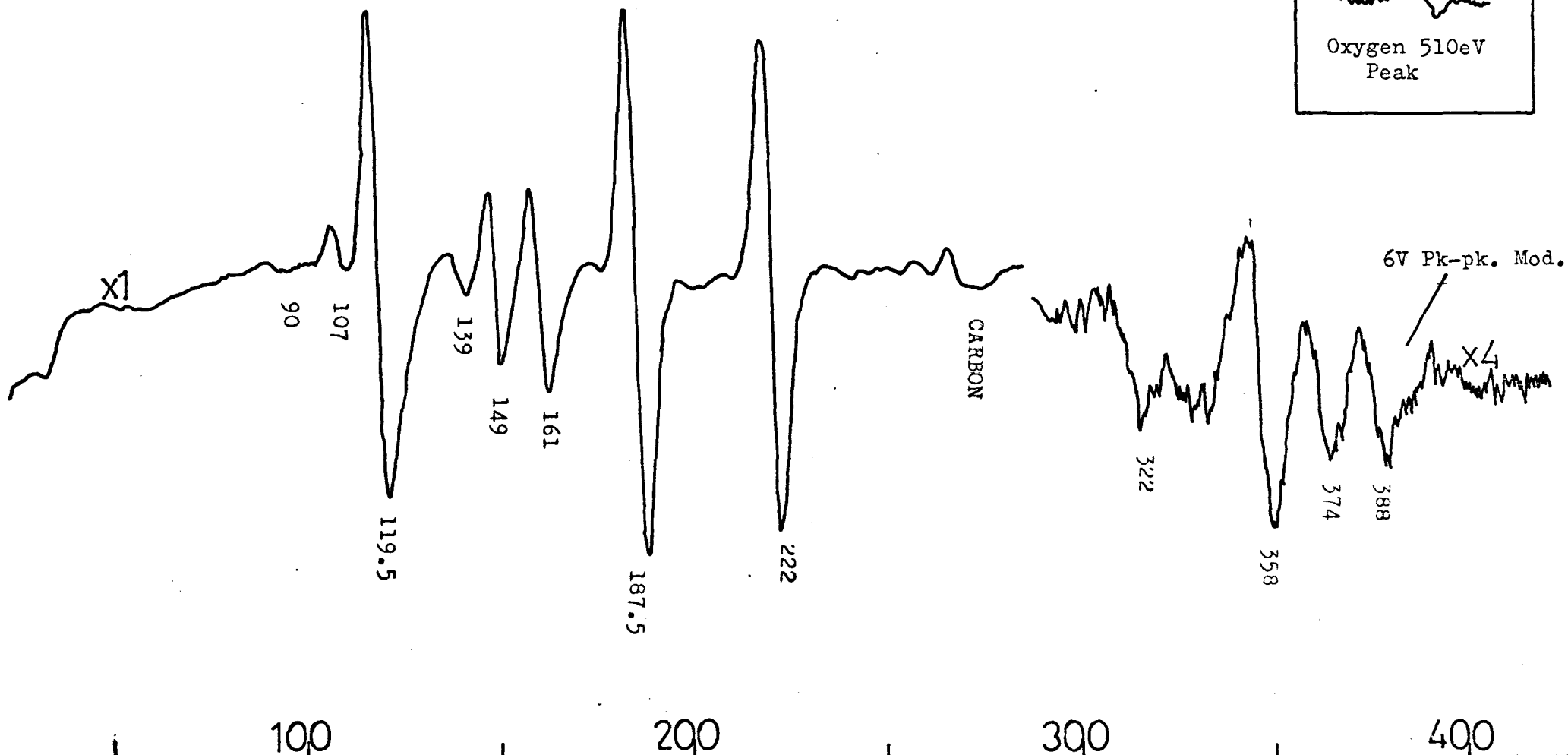
Energy (eV)

$\frac{dN}{dE}$  Pk. Height  
(Arb. units)

Fig.7-1. The Auger Spectrum Of Molybdenum.

$E_p = 2.9 \text{ KeV}$   
 $I_p = 40 \mu\text{A}$   
Mod. = 3V Pk-pk.  
Time Const. 1 Sec.

X1  
Oxygen 510eV  
Peak



Energy  
(eV)

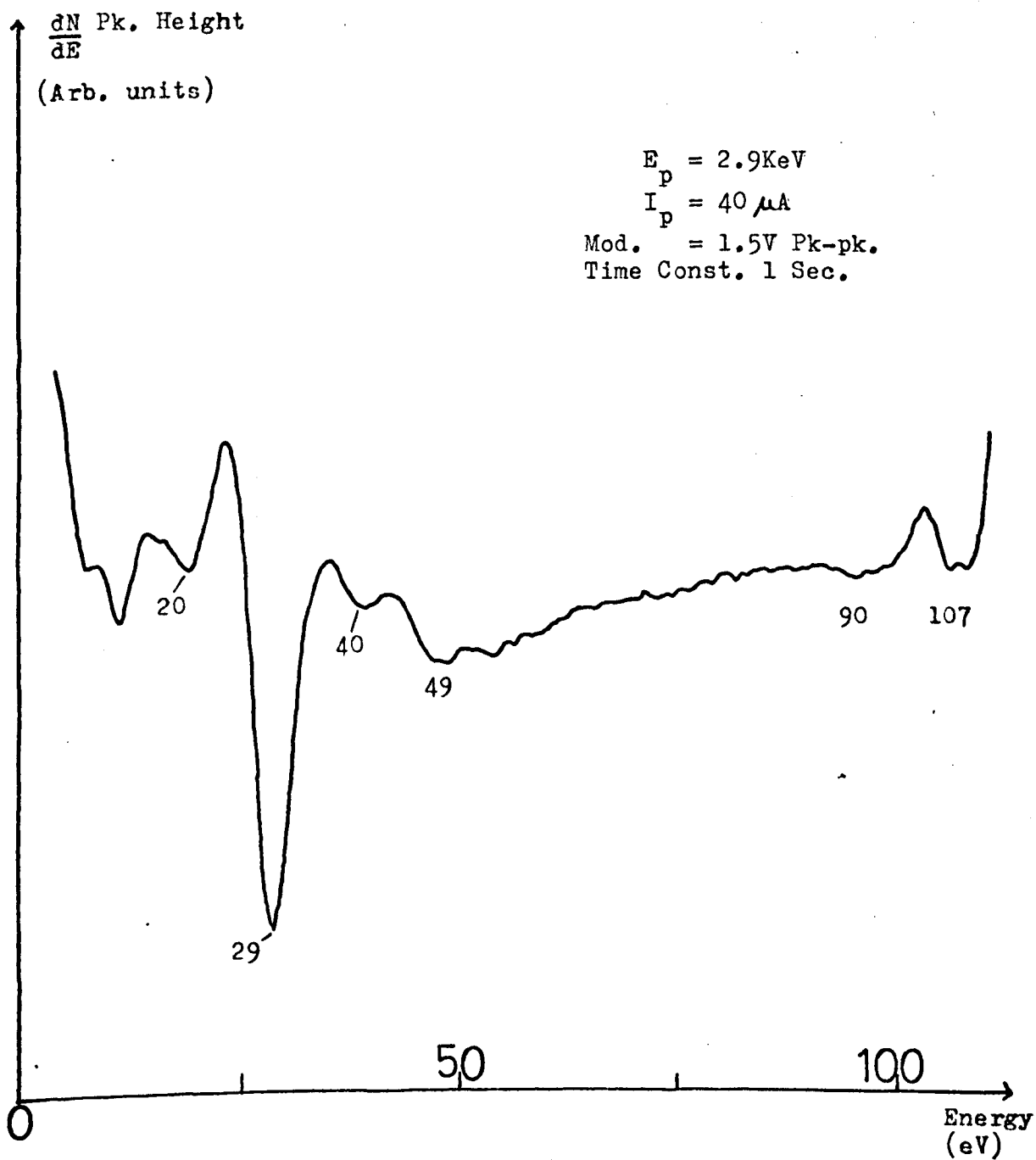


Fig.7-2. The Low Energy Auger Spectrum Of Molybdenum.

TABLE 7-1

ENERGIES OF AUGER PEAKS OF Mo (eV)

<u>Present Work</u>	<u>P.E.I.<sup>140</sup></u>	<u>Haas et al (1970)<sup>143</sup></u>	<u>Kunimori et al (1974)<sup>167</sup></u>	<u>Ignatiev et al(1975)<sup>204</sup></u>
20				21
29	28	28		31
40				42
49				
90	96			98
107				
119.5	120,125	125	124.2	123, 127
139	139		142.6	141
149	148	153	152.2,155	151
161	161	166	163.5	163
187.5	186	192	187	188
222	221	226	222.4	223
322				
358	354			
374				
388				

with the published work but there are a number of features which do not appear to have been previously reported. The results reported here are an average of a number of measurements and an accuracy of  $\pm 1$  eV is estimated for the values summarised in Table 7-1.

Published spectra of molybdenum indicate that the ratio of the 161 eV peak height to the 149 eV peak height is 2 : 1. In our spectra this ratio is approximately equal so that there is probably some S contamination as well as C contamination present on the surface. The additional features observed in the spectra are not thought to be due to the presence of these impurities and P.E.I.'s spectra does show structure similar to ours in the region of their 354 eV peak, to which they have not assigned energy values.

The observed peaks are assigned transitions using the tables of Clausing and Coghlan<sup>36</sup> on the basis of the strongest transition from multiplicity values close to the observed energy. The assignments are summarised in Table 7.2. Several transitions had to be assigned to some features particularly the 149, 161 eV peaks as there are several transition close to these energies having a high multiplicity.

Although the  $M_4$  and  $M_5$  levels differ in energy by 3 eV, no splitting of the  $M_{4/5}$  VV, (222 eV) peak could be observed even when a low modulation voltage of 1 v pk-pk was used to record the spectra. The valence band width of molybdenum is  $\approx 4$  eV from photo emission measurements<sup>165</sup>, but the observed width of the 222 eV Auger peak is  $\approx 2$  eV suggesting no strong influence of the valence band on the peak shape. The  $M_4$  VV contribution to the intensity of the 222 eV is weak probably due to Coster Kronig transitions of the type  $M_4M_5V$ . The  $M_3$  W transition at 388 eV is also thought to be weak due to relaxation of these holes by Coster Kronig processes such as  $M_3M_4V$ ,  $M_3M_5V$ . The effect of these Coster-Kronig transitions would be to enhance the vacancy distribution

TABLE 7-2

AUGER PEAK ASSIGNMENTS FOR Mo

<u>Energy</u>	<u>Transition</u>	<u>Calculated Energy</u> <sup>36</sup>	<u>Multiplicity</u>
20	M <sub>1</sub> M <sub>5</sub> M <sub>5</sub> ) N <sub>1</sub> N <sub>2/3</sub> V )	25 23	33 33
29	N <sub>2/3</sub> V V	31	100
40	M <sub>1</sub> M <sub>2</sub> N <sub>23</sub>	40	11
49	N <sub>1</sub> V V	58	33
90	M <sub>1</sub> M <sub>3</sub> V	94	22
107	M <sub>3</sub> M <sub>4</sub> N <sub>23</sub>	112.5	44
119.5	M <sub>3</sub> M <sub>5</sub> N <sub>23</sub> ) M <sub>5</sub> N <sub>1</sub> N <sub>23</sub> )	116 125	66 33
139	M <sub>2</sub> M <sub>5</sub> N <sub>23</sub> ) M <sub>3</sub> M <sub>4</sub> V )	133 147.5	33 44
149	M <sub>3</sub> M <sub>5</sub> V	151	66
161	M <sub>5</sub> N <sub>23</sub> N <sub>23</sub>	153	100
	M <sub>4</sub> N <sub>2/3</sub> N <sub>23</sub>	156	66
	M <sub>5</sub> N <sub>1</sub> V	160	33
187.5	M <sub>5</sub> N <sub>23</sub> V ) M <sub>4</sub> N <sub>23</sub> V )	188 191	100 66
222	M <sub>5</sub> V V ) M <sub>4</sub> V V )	223 226	100 66
322	M <sub>3</sub> N <sub>2/3</sub> N <sub>2/3</sub>	319	66
358	M <sub>3</sub> N <sub>2/3</sub> V	354	66
374	M <sub>2</sub> N <sub>2/3</sub> N <sub>2/3</sub>	371	33
388	M <sub>3</sub> V V	389	66

in the  $M_5$  subshell so that the 222 eV peak is dominated by the transition  $M_5W$ . The other effect of Coster-Kronig transitions is that peaks like  $M_1W$  expected at about 501 eV and  $M_2W$  expected at about 406 eV are not observed.

The assignments are in agreement with those made by Haas et al (1970) for their peaks although we differ slightly in recorded energy as shown in Table 7-1. The energy difference between the 388 eV and 222 eV peaks agrees with the energy difference between the  $M_5$  and  $M_3$  subshells and the same is true of the 222 eV peak and the 29 eV peak ( $M_5$ ,  $N_{2/3}$  subshells) so that the assignments for these energies, at least, are probably correct.

### 7.3 The Effect of Contaminants on the Auger Spectra of Mo

The spectra shown in Fig. 7-1 and 7-2 were recorded from a surface with the minimum of contamination possible using the available cleaning techniques. The effect of selected surface contaminants: carbon, sulphur and oxygen on the Auger spectra is now examined.

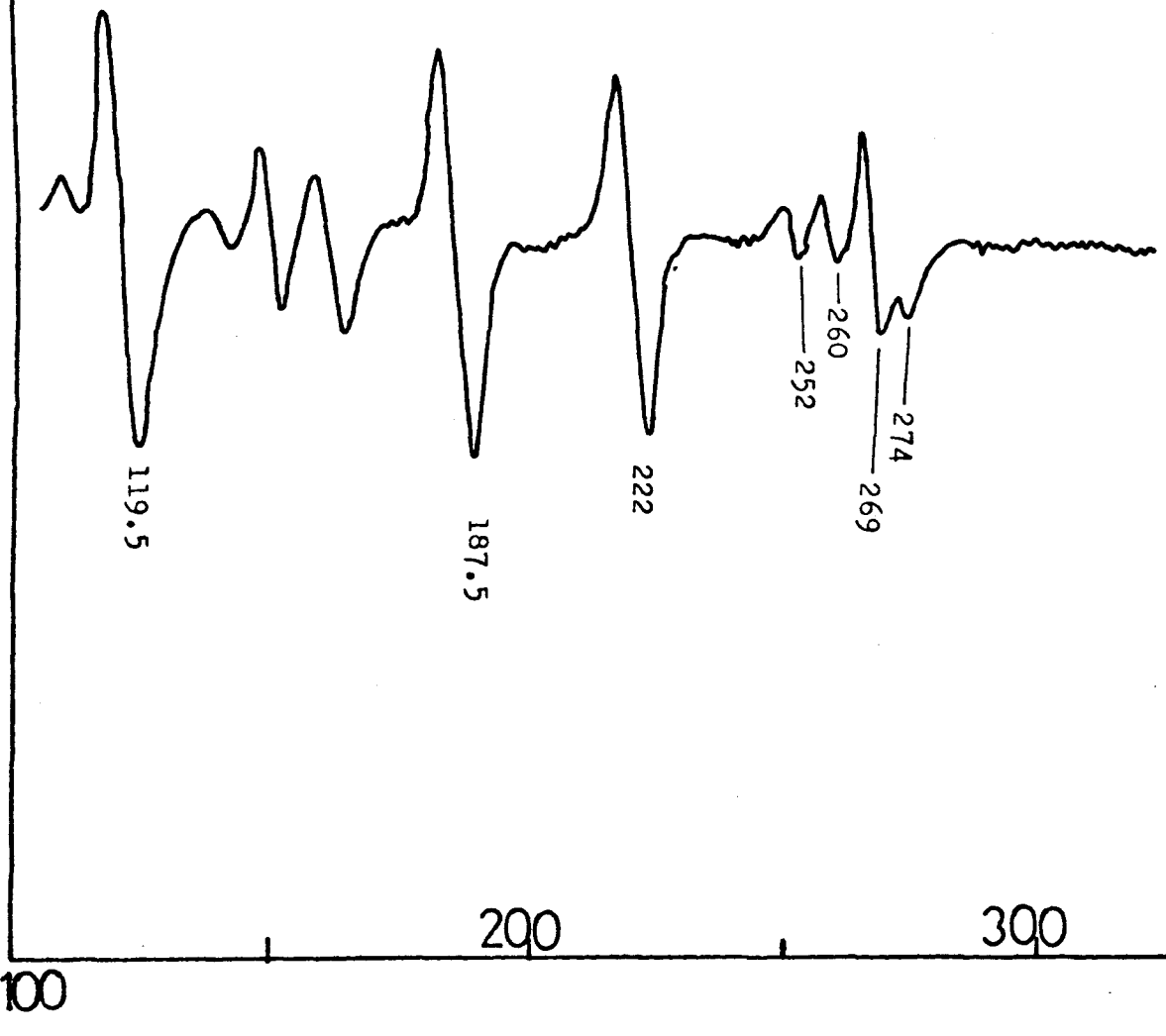
#### 7.3.1 Carbon Contamination

Carbon contamination was induced onto an initially clean Mo surface by bombarding the surface with a 25 $\mu$ A electron beam for a few hours. The electron beam cracks the molecules of gases such as CO, CO<sub>2</sub> present in the vacuum chamber on to the target, the C atoms remain on the surface whereas the oxygen is believed to be desorbed. The Auger spectra of a C contaminated Mo surface is shown in Fig. 7-3, a small peak due to oxygen can also be detected.

$\frac{dN}{dE}$  Pk. Height  
(Arb. units)

Fig.7-3. Carbon Contaminated Molybdenum Surface.

$E_p = 2.9\text{KeV}$   
Mod. 2V Pk-pk.  
Time Const. 1 Sec.



Oxygen 510eV  
Peak

The shape of the C peak in Fig. 7-3 at  $\sim 270$  eV differs considerably from its shape in Chapter 4, where the C was thought to be present in a graphitic form. The difference in the shapes is thought to be a chemical effect due to the C atoms combining with the molybdenum atoms to form a molybdenum carbide  $\text{Mo}_2\text{C}$ . Changes in the carbon KLL Auger peak shape with chemical composition have been reported recently by Ducros et al (1976)<sup>166</sup> and the Auger spectra of  $\text{Mo}_2\text{C}$  has been published previously by Haas, Grant and Dooley (1972)<sup>163</sup>. Their shape, obtained by the absorption of CO on molybdenum, is very similar to ours and the energies of the features in their spectra are compared with ours in Table 7-3, together with the possible assignments.

Whereas the carbon Auger peak has changed drastically in shape the molybdenum peaks appear unaffected. Additionally it is to be noted how the appearance of the C Auger peak in Fig. 7-3 is different from the shape recorded from the stainless steel surface in Chapter 5. These changes in shape can only be due to the chemical bond formation which will cause a re-arrangement of the outer electrons.

TABLE 7-3

Carbon Auger Peak Features from Molybdenum Carbide

<u>Present Work (eV)</u>		<u>Haas et al (1972)<sup>163</sup></u>
274	275	$\text{KL}_2\text{L}_2, \text{KL}_2\text{L}_3, \text{KL}_3\text{L}_3$
269	272	$\text{KL}_1\text{L}_2, \text{KL}_1\text{L}_3$
260	262	$\text{KL}_1\text{L}_2$
252	254	$\text{KL}_1\text{L}_1$

### 7.3.2 Sulphur Contamination

The molybdenum surface was contaminated with sulphur impurity by heating the target with electron bombardment to a temperature  $\approx 1500^{\circ}\text{C}$ . The peak-peak height of the S Auger Signal at 150 eV slowly increased due to the build up of contamination. The changes produced in the Auger spectra of the specimen are shown in Fig. 7-4. No carbon or oxygen contamination could be detected. Comparing with Fig. 7-1 it is clear that the most significant effect of the increase of S contamination is on the 119.5 eV peak. This peak is considerably reduced in intensity relative to the Mo peaks at 187.5 and 222 eV and in Fig. 7-4 two peaks can be identified at 119 eV and 126 eV as labelled. The 187.5 and the 227 eV peaks appear to remain unchanged in shape on S contamination.

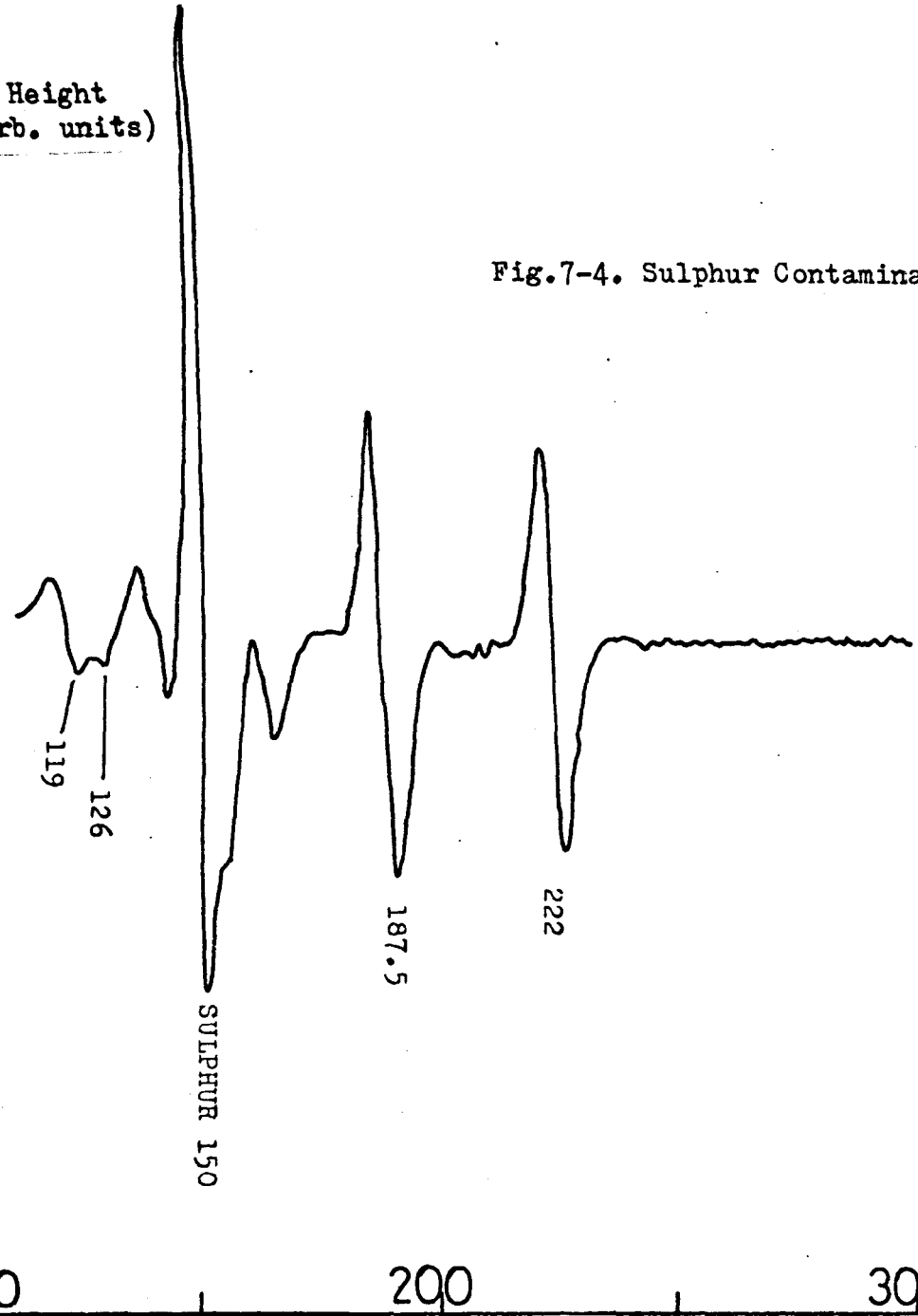
Evidence is presented by Kunimori et al (1974)<sup>167</sup> which indicates that the S has formed a compound  $\text{MoS}_2$  on the surface. The transference of electronic charges involved in the formation of the chemical bond has probably resulted in a change of transition probability for the transitions contributing to the 119.5 eV peak. P.E.I. and Ignatiev et al<sup>204</sup> resolved two peaks at about the energy in the Auger spectra from clean molybdenum (Table 7-1), whereas we only resolve two peaks after S contamination.

The small feature on the high energy side of the S peak, in Fig. 7-4, is probably due to the Mo, 149 eV transition. The low energy Auger spectrum (0 - 100 eV) was also investigated with the large S contamination of Fig. 7-4, and although some changes appear to have been produced, they could not be conclusively identified. Measurements were made of the energies of the Auger peaks of Mo with the S contamination such that the height of the sulphur 150 eV peak was equal to the height of the Mo, 222 eV peak, but no chemical shift of the peak positions

$\frac{dN}{dE}$   
Pk. Height  
(Arb. units)

Fig.7-4. Sulphur Contaminated Molybdenum Surface.

$E_p = 2.9\text{KeV}$   
Mod. 1.5V Pk-pk.  
Time Const. 1 Sec.



Oxygen 510eV  
Peak

100 200 300

Energy  
(eV)

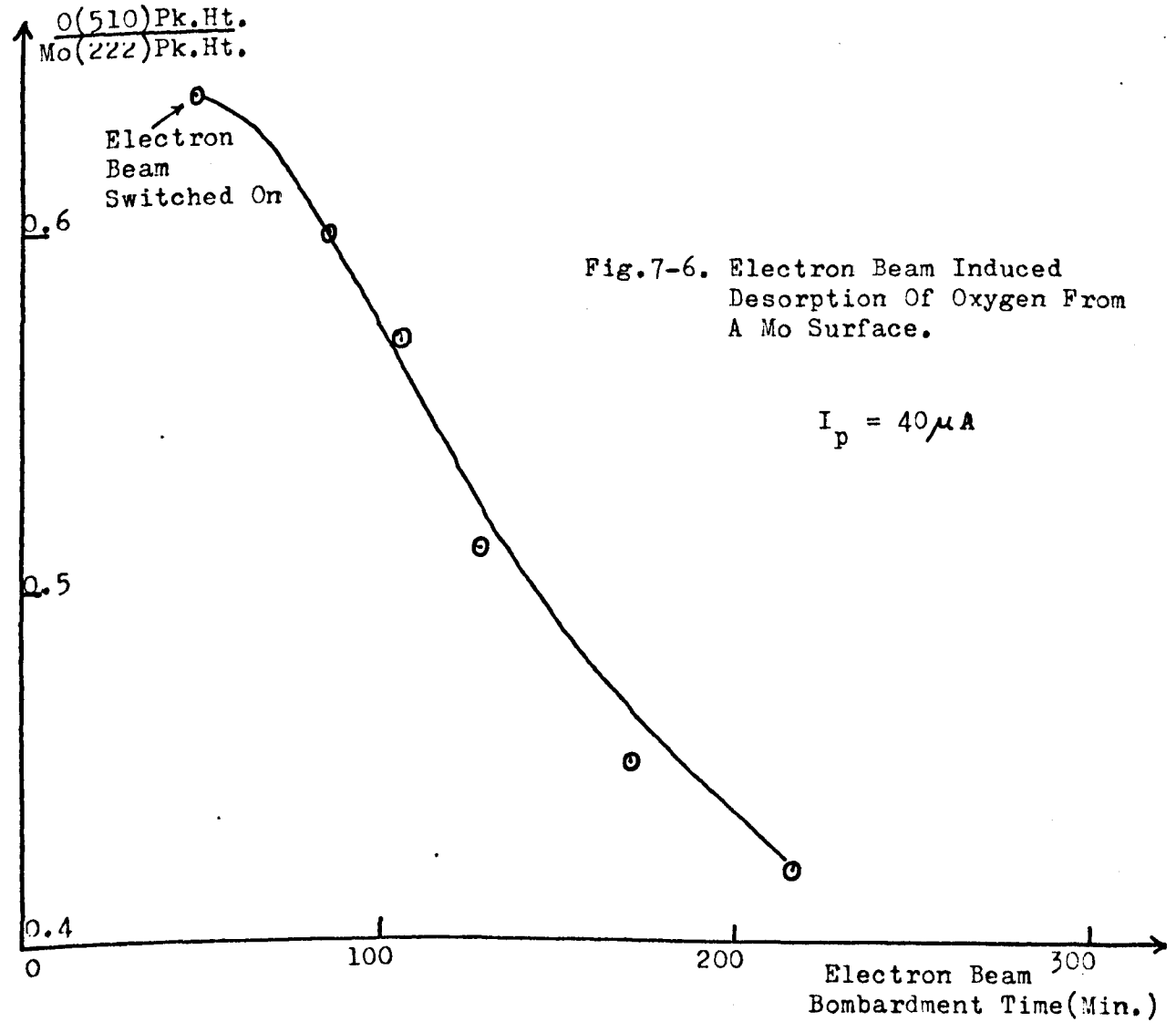
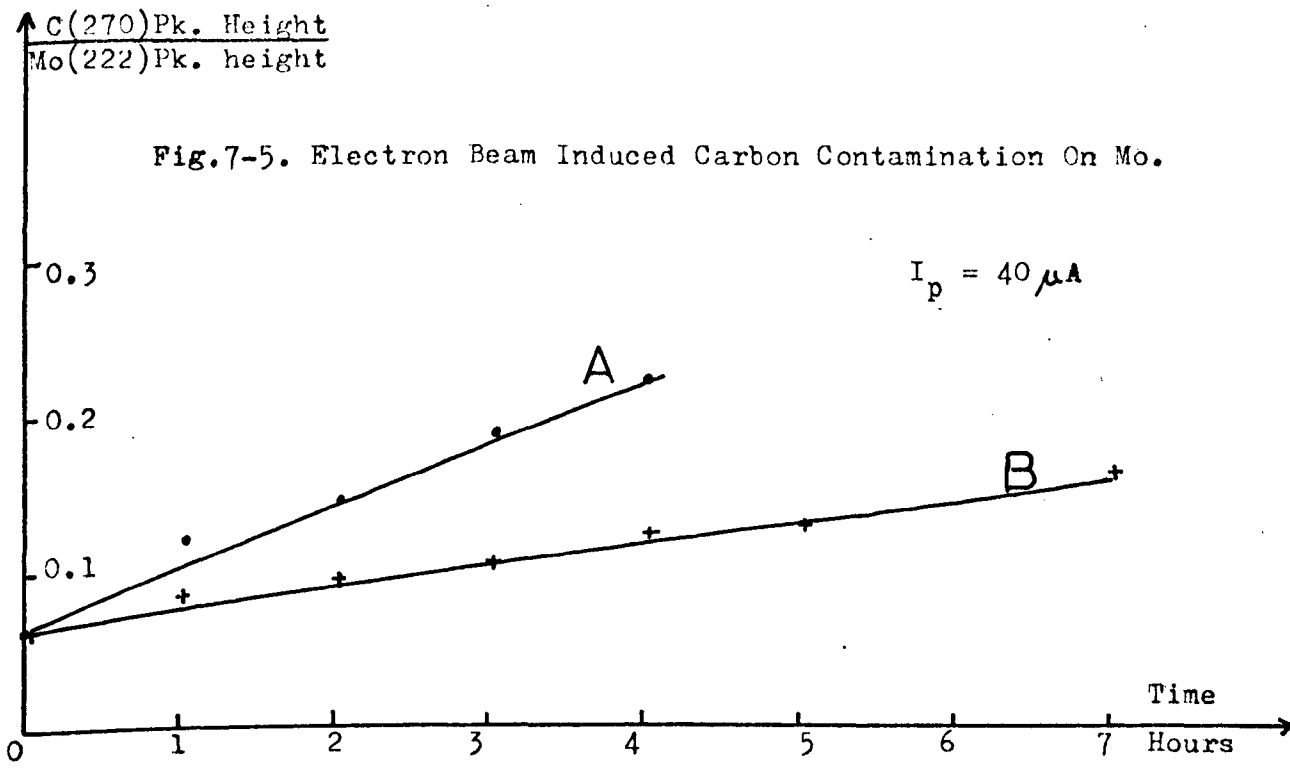
could be detected.

### 7.3.3 Oxygen Contamination

A clean molybdenum surface was exposed to oxygen gas at low pressure and the  $O_2$  Auger signal at 510 eV monitored with time. It was found to increase very slowly until its height was 0.4 of the 222 eV peak height (see adsorption studies in Section 7.5). No changes were detected either in the shape of the Mo Auger spectra in the energy range 110 - 230 eV or in the positions of the Auger peaks. Since these results were recorded a paper has been published by Hooker et al (1975)<sup>168</sup> on the chemical shifts of the  $M_{4/5}$  NN Auger peaks with oxygen adsorption. They detected peak shifts  $\approx 0.5$  eV or less as well as some changes in the shape of the  $M_{4/5}$  WV peak, as we used much higher modulation amplitudes than these authors such changes would not have been detected in our spectra.

## 7.4 Electron Beam Effects

The impact of the primary electrons on a surface can induce effects which may be undesirable. The changes produced on the initially clean molybdenum surface by electron impact were monitored by recording the Auger spectra with the time of exposure to the electron beam. The results were recorded in a vacuum of  $1 \times 10^{-8}$  Torr and as mentioned previously the main gases inside the chamber were CO and  $CO_2$  so that an increase in contamination due to C was expected. The change in the level of carbon contamination of the surface was monitored by the ratio of the C, KLL peak height to the Mo,  $M_{4/5}$  WV peak height. This ratio is plotted as function of beam exposure in Fig. 7-5. Two



sets of results were recorded starting from the same set of initial conditions, in one set the electron beam was left switched ON all the time (A in Fig. 7-5) and in a second set (B in Fig. 7-5) the beam was only switched on to record the surface species all other conditions being kept constant. Then results B measure the increase in C contamination due to the interaction of the ambient gases with the molybdenum surface, whereas results A contain an electron beam induced contribution.

For the set of results B, the electron beam is switched on for about 5 minutes every hour to record the Auger spectra. It would appear from the results that some dissociation of the ambient gases is occurring at the Mo surface even without the impact of the electron beam, but the electron beam does enhance this effect.

In view of these effects Auger spectra from molybdenum surfaces need to be recorded in UHV pressures and with the minimum time elapsing between flashing the target and recording the Auger spectra.

The influence of electron bombardment on adsorbed oxygen was then investigated. Initial Auger spectra of the molybdenum surface revealed small S contamination such that the ratio of the S (150 eV) peak height to the Mo (222 eV) peak height was  $\approx 1$ . No carbon contamination was present on the surface. Research grade oxygen gas was admitted into the chamber via the leak valve and the pressure allowed to rise to  $8 \times 10^{-8}$  torr. The surface was exposed to this pressure for several hours. Then after pumping to UHV, Auger spectra were recorded as a function of the exposure to the electron beam. The change in the oxygen concentration of the surface was monitored by the ratio of the oxygen KLL peak height to the molybdenum 222 eV peak height and this ratio is plotted in Fig. 7-6 as a function of the time of exposure to the electron beam. Clearly oxygen is being desorbed from the surface by the action of the electron beam.

## 7.5 Adsorption of Oxygen on to Polycrystalline Molybdenum

### 7.5.1 Introduction

There have been a number of studies<sup>170,171</sup> carried out on the adsorption of oxygen ( $O_2$ ) on to single crystal molybdenum surfaces using LEED and AES. The present experiment has been performed on a polycrystalline surface at room temperature using AES to obtain information about the initial sticking coefficient of oxygen on molybdenum and the effect of sulphur impurity on the initial sticking coefficient.

### 7.5.2 Experimental

The experiment performed was to monitor the Mo, 222 eV peak and the O, 510 eV peak as a function of the exposure to oxygen gas. These two peaks were chosen because the 510 eV is the strongest oxygen peak and the Mo, 222 eV peak is sufficiently separated from the other molybdenum Auger peaks to be unaffected. Additionally the energies of these peaks are such that they are thought to be on the flat portion of the channel electron multiplier gain v electron energy graph<sup>140</sup>, so that quantitative comparisons are possible. The peaks were recorded with different modulation amplitudes compatible with the energy window of the analyser, as outlined in Chapter 4. The 222 eV peak was recorded with a modulation amplitude of 2 v pk-pk and the 510 eV peak was recorded with 4 v pk-pk modulation.

Oxygen gas can be admitted into the chamber at a controlled rate by the leak valve MD6. The partial pressure of the oxygen was determined by using the quadrupole mass spectrometer to calibrate the leakage current on a FJD8 ion pump (nominal pumping speed 8 litres sec<sup>-1</sup>). This pump was attached to the chamber at the time of the experiment due to its lower pumping speed. The ion gauge was not used to monitor the

pressure because it reacted with the oxygen to produce CO and CO<sub>2</sub> so that during the measurements it was switched off. From the calibrated ion pump leakage current the total pressure in the chamber could be estimated and the peak heights of the individual gases recorded by the quadrupole mass analyser indicated that approximately 80% of the total pressure inside the chamber was due to oxygen gas.

During an experiment the diffusion pump valve to the chamber was partially closed and the oxygen gas leak rate periodically adjusted to maintain a steady pressure inside the chamber. Typically oxygen partial pressures of  $10^{-7}$  -  $10^{-8}$  torr were used in the adsorption experiments. The Auger peaks of interest, Mo, 222 eV and O<sub>2</sub>, 510 eV were then recorded from the Mo surface as a function of time, all other conditions (E<sub>p</sub>, I<sub>p</sub>, sweep rate, time constant, etc.) were maintained constant during an experiment and the build up of oxygen concentration under the impact of the electron beam monitored.

### 7.5.3 Results

The adsorption experiments performed on an initially clean molybdenum surface was repeated once but only one adsorption experiment was performed on a sulphur contaminated Mo surface. The change in the ratio of the oxygen (510 eV) peak height to the molybdenum (222 eV) peak height with exposure is plotted in Fig. 7-7. The exposure in Langmuirs was estimated from the oxygen partial pressure and the time for which the surface was exposed, as 1 Langmuir =  $10^{-6}$  torr-sec. The results on the contaminated surface were obtained with the S (150 eV)/Mo (222 eV), peak height ratio equal to 1.3 and in this experiment the target was exposed to an oxygen partial pressure of  $1 \times 10^{-8}$  torr. The results on the clean surface were obtained by exposing the target to an oxygen partial pressure of  $1 \times 10^{-7}$  Torr. The general trend of the adsorption results was indicated by preliminary experiments on the

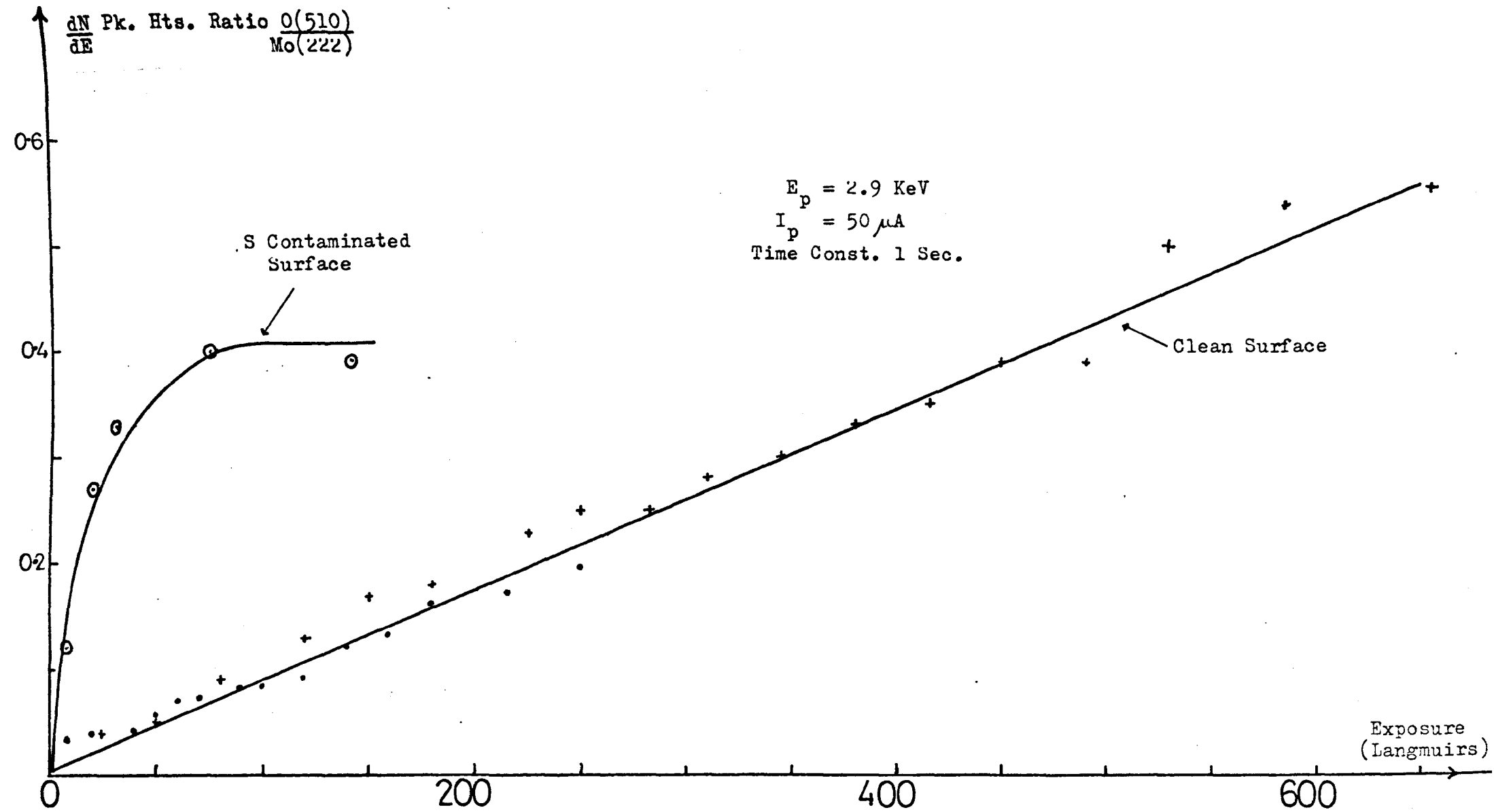


Fig.7-7. Oxygen Adsorption On A Clean And Sulphur Contaminated Molybdenum Surface.

surface and subsequently we proceeded to record the data plotted in Fig. 7-7 under strictly controlled experimental conditions.

The results of Fig. 7-7 show that there is a considerable difference between adsorption on a clean Mo surface and adsorption on a sulphur contaminated Mo surface. During adsorption on the contaminated surface, the S peak remained uncharged in shape and the ratio of its height to the Mo 222 eV peak height also remained at 1.3 (the initial value) suggesting that S was not removed from the surface by the adsorbing molecules.

#### 7.5.4 The Initial Sticking Coefficient

Using the adsorption results of Fig. 7-7, the initial sticking coefficient of oxygen on molybdenum was estimated by developing a simple model relating the ratio of the Auger peak heights to the sticking coefficient.

##### Theory

Bishop and Riviere (1969)<sup>172</sup> derive the formula for the Auger current  $I_A$  from a monolayer as

$$I_A = I_p N \frac{\Omega}{4\pi} (1-w) r \text{Cosec } \phi \phi(E, E_A) \quad \text{Eq. 7-1.}$$

Where  $N$  = Number of atoms per sq.cms,

$w$  = Fluorescence yield = 0 for low energy transitions,

$\phi(E, E_A)$  = Cross-section for ionization of an electron in energy level  $E_A$  by electrons of energy  $E$ ,

$r$  = Backscattering factor,

$\phi$  = Angle of Incidence of the primary beam,

$\Omega$  = Solid angle of collection of the analyser.

By making the assumptions (i) the Auger current originates predominantly from the first monolayer, and (ii) the Auger current is proportional to the peak-peak height of the signal in the first derivative spectrum. Then the observed heights can be related to the

Auger currents. These assumptions have been made by a number of authors, eg. Meyer and Vrakking (1974)<sup>77</sup>.

We have also shown in Chapter 4 for a CMA that when a peak is recorded with a modulation amplitude equal to the energy window of the analyser then the peak height is proportional to the energy. So that if

$H_M$  is the height of the molybdenum Auger peak at energy  $E_M$ ,  
and  $H_O$  is the height of the oxygen Auger peak at Energy  $E_O$ ,

Then in Eq. 7-1

$$H_M \propto I_p N_M r \text{ Cosec } \phi \frac{\Omega}{4\pi} \phi_M(E_p, E'_M) \times E_M \quad \text{Eq. 7-2}$$

and

$$H_O \propto I_p N_O r \text{ Cosec } \phi \frac{\Omega}{4\pi} \phi_O(E_p, E'_O) \times E_O \quad \text{Eq. 7-3}$$

where  $E'_M$ ,  $E'_O$  are the binding energies of the initial vacancies.

As we are concerned with the first monolayer, the backscattering contribution  $r$  will be approximately equal.

Gryzinski (1959, 1965)<sup>173,174</sup> has shown that the ionization cross-section has the general form

$$\phi(E, E_A) = \frac{\Sigma}{E_A^2} f(u) \quad \text{where } f(u) \approx \text{constant} \\ \text{for } u > 5 \quad \text{Eq. 7-4}$$

$$U \text{ is the reduced energy } = \frac{E}{E_A}$$

We are concerned with the  $M_{4/5}$  W transition at 222 eV ( $E_M$ ) for which  $E'_M = 227$  eV, and the oxygen KLL peak at 510 eV ( $E_O$ ) for which  $E'_O = 532$  eV. As a primary electron excitation energy of 2.7 KeV was used to record spectra in Fig. 7-7 then the condition  $U > 5$  is satisfied in Eq. 7-4, so that

$$\frac{\phi(E_p, E'_O)}{\phi(E_p, E'_M)} = \left[ \frac{E'_M}{E'_O} \right]^2 = \frac{1}{5.5},$$

and from equations 7-2 and 7-3

$$\frac{H_O}{H_M} = \frac{N_O}{2.30N_M}$$

Eq. 7-5

If the initial sticking coefficient of oxygen on to the surface is  $S_0$ , then after an exposure of  $E$  Langmuirs

$$N_0 = S_0 E \times \text{number of oxygen molecules striking the surface per unit area per sec at a pressure of } 1 \times 10^{-6} \text{ Torr.}$$

From the kinetic theory of gases, the number of molecules  $v$  incident per unit area per sec, at room temperature is given by

$$v = P(2\pi mkT)^{-\frac{1}{2}}$$

The symbols having their usual meaning. Then,

$$N_0 = S_0 E \cdot 3.57 \times 10^{18}.$$

In Eq. 7-5

$$\frac{H_0}{N_M} = \frac{S_0 \cdot 1.55 \times 10^{18}}{N_M} E \quad \text{Eq. 7-6}$$

Thus from the initial gradient of the curves plotted in Fig. 7-7 the initial sticking coefficient can be obtained. Using a value of  $N_M = 1.62 \times 10^{19} \text{ m}^{-2}$  a value of  $S_0 \sim 1/100$  is deduced for the clean surface and a value of  $S_0 \sim 1$  for the sulphur contaminated surface. A value of  $S_0 = 1/3$  has been obtained for the adsorption of oxygen on clean (111) Mo surface by Lambert et al (1971)<sup>175</sup> whereas Miura et al<sup>171</sup> obtains an initial value of  $S_0 = 1/100$  on a (110) surface. Other studies carried out in pre-AES days indicated  $S_0$  values of unity on single crystal and polycrystalline surfaces<sup>176,177</sup>.

Although the method of obtaining the sticking coefficient is restricted by a number of assumptions, the results do indicate that the presence of sulphur contaminant increases the adsorption of oxygen by a factor of about 100 and this is perhaps the important deduction from the data of Fig. 7-7. Additionally it should be remembered that the adsorption of oxygen was carried out under electron beam bombardment, which will also have an influence on the adsorption properties of the surface.

## 7.6 Energy Loss Spectroscopy of Molybdenum

### 7.6.1 Introduction

As a part of the program of investigating the clean molybdenum surface, the characteristic energy losses were also obtained. There have been several previous studies of the characteristic losses<sup>178,179,180</sup>, but none, as far as we could discover in a UHV atmosphere on an AES characterised surface. Kawai et al (1974)<sup>181</sup> has studied the losses from an AES, characterised surface, but the pressure used,  $10^{-7}$  Torr, and the contaminants detected on his surface introduce doubts about their results. Also there is still some confusion as to the position of the losses and the physical processes from which they originate so that a loss study of molybdenum would be worthwhile.

### 7.6.2 Experimental

The measurements were made at different primary electron energies on an AES characterised clean surface in a UHV environment. The method of obtaining the molybdenum loss spectra was the same as used to obtain the gold results, but in this case spectra were recorded in the  $\frac{d^2N}{dE^2}$  mode of operation as well as the  $\frac{dN}{dE}$  mode of operation of the analyser. No contamination problems were encountered, the Auger spectra taken before and after recording the losses were similar to that shown in Fig. 7-1, but without a detectable carbon peak. These results were recorded when the target had been in the vacuum chamber a number of weeks and the pressure attained normally improved with pumping so that the electron beam effects became insignificant over the time scale of recording the loss spectra.

### 7.6.3 Results and Discussion

The loss spectra recorded with 300 eV primary electron energy and

$\frac{dN}{dE}$  Spectra, 2V Pk-pk Mod.  
 $I_p = 5 \mu A$   
 Time Const. (T.C.)

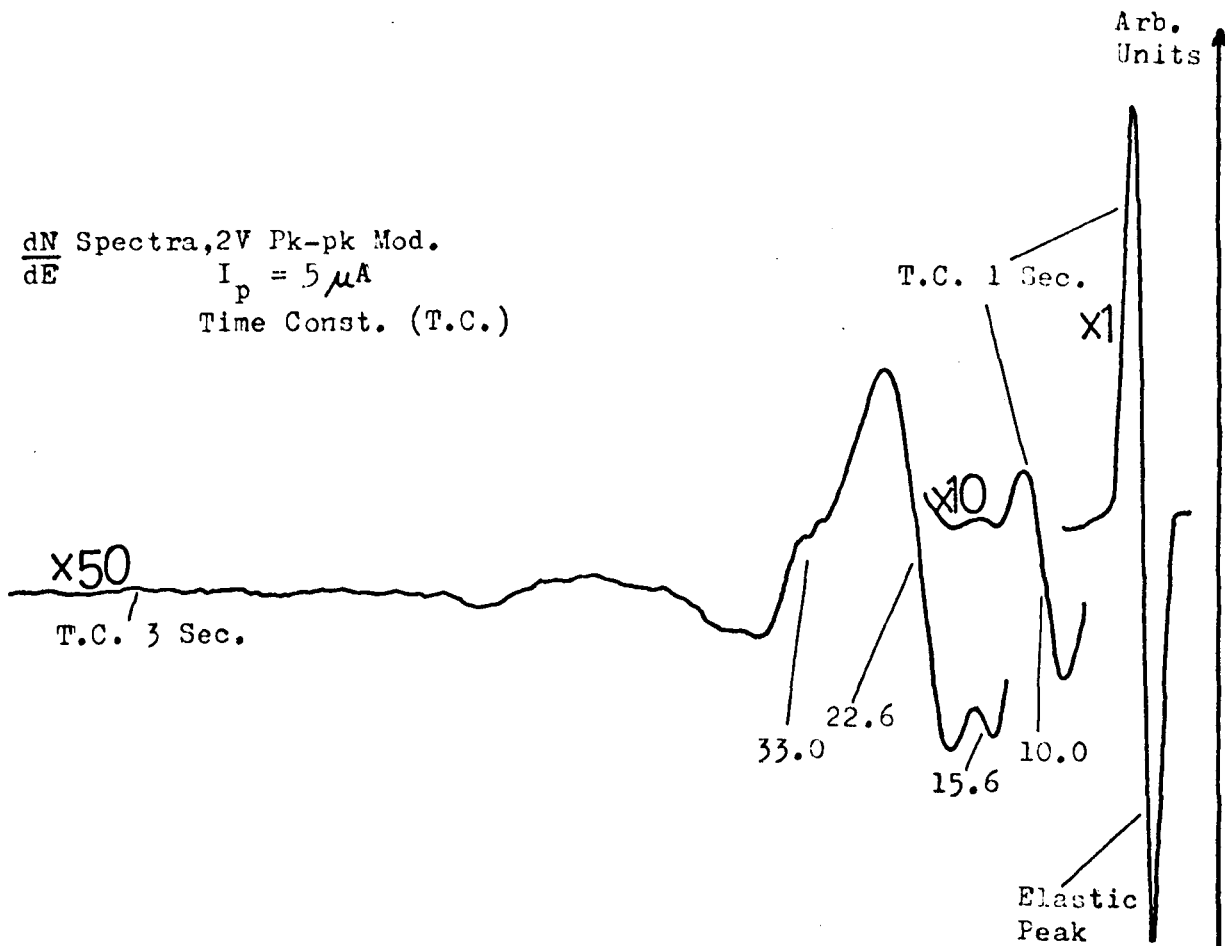
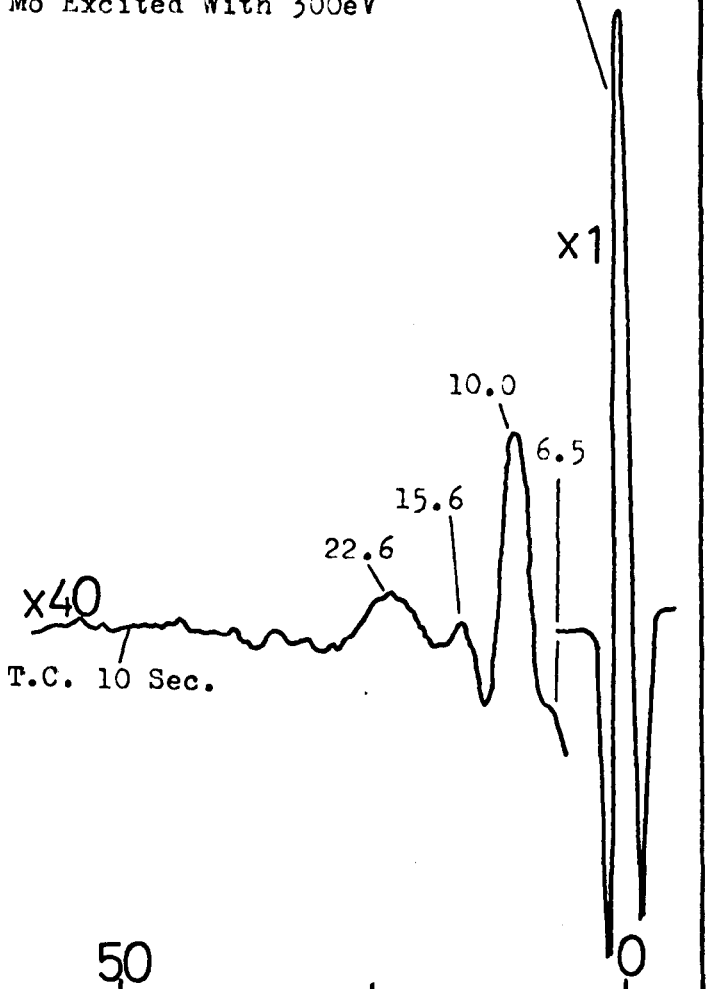


Fig.7-8. The Loss Spectra Of Mo Excited With 300eV Electrons.

$\frac{d^2N}{dE^2}$  Spectra, 2V Pk-pk. Mod.



Energy (eV)  
 100 50 0

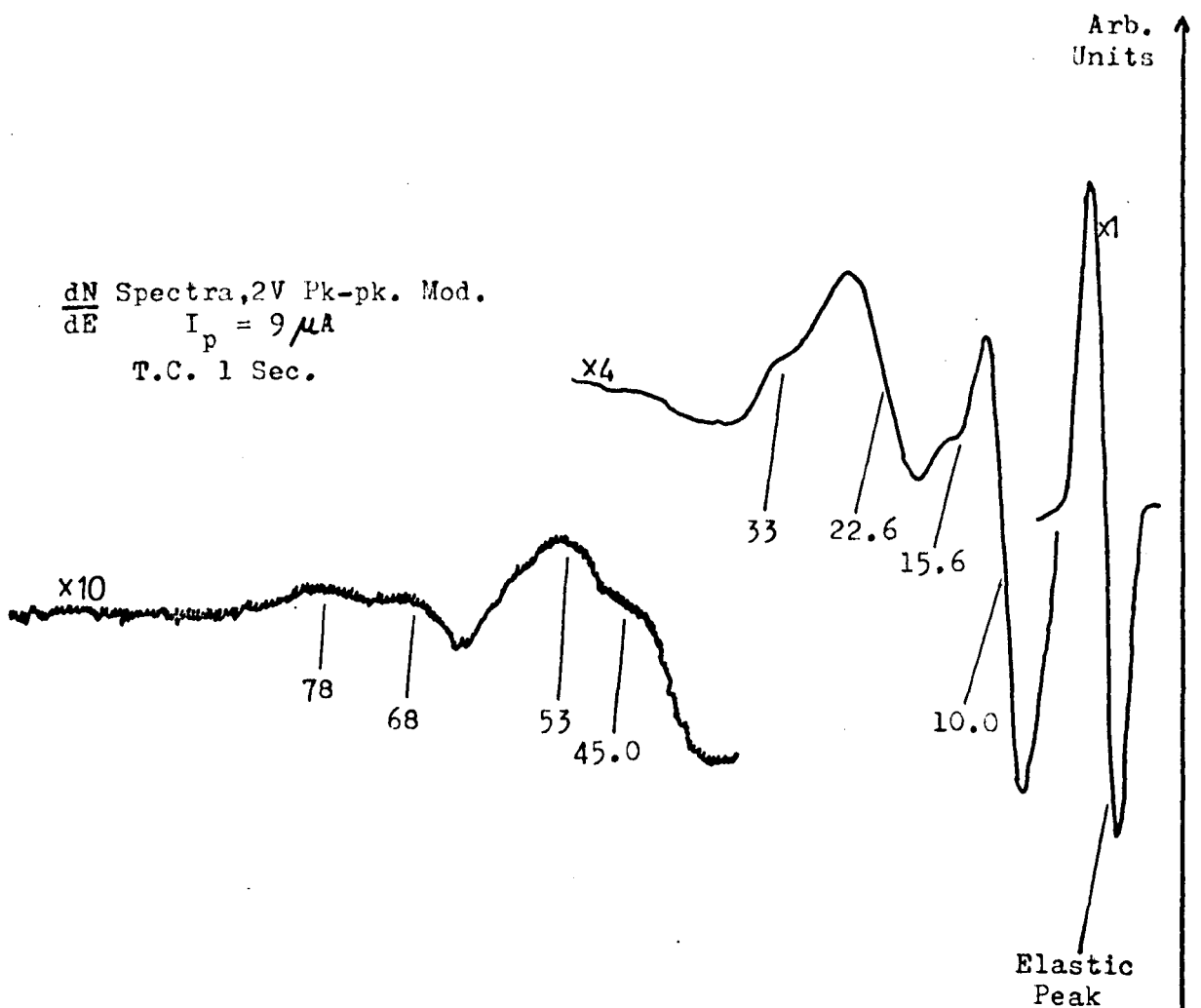


Fig.7-9. The Loss Spectra Of Mo Excited With 500eV Electrons.

$\frac{d^2N}{dE^2}$  Spectra, 2V Pk-pk. Mod.

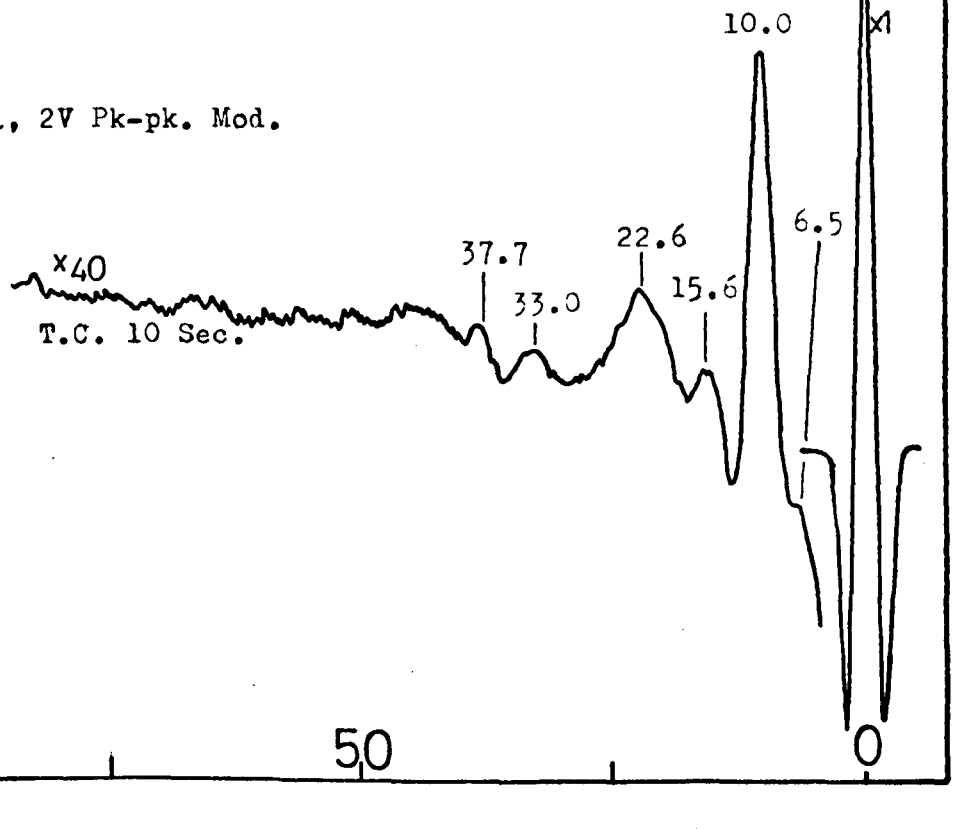


TABLE 7-4

CHARACTERISTIC LOSSES OF  $M_0$  AT DIFFERENT PRIMARY ENERGIES

<u>Primary Energy (eV)</u>	<u>Analyser Operation mode</u>										
300	$\frac{d^2N}{dE^2}$	6.3	9.8	16.0	22.2	32.8					
500			10.3	15.0	23.4	33.4		44.1			
500	"		9.5	15.6	22.5	32.4					
300			9.7	15.7	22.7	32.7	38.1				
750	"		9.9		22.9			45.0	51.9	67	
500		6.6	10.4	15.3	21.9	32.7	37.3	43.4			
500	"		10.1	16.1	22.5	34.0					
300		6.5	10.0	15.2	22.3						
500			10.9	16.3	23.4	33.0					
300			10.0	15.2	22.0						
500	$\frac{dN}{dE}$							44.7	53.1	68.4	77.6
								46	53.7	68.1	79
Mean Value		6.5	10.0	15.6	22.6	33.0	37.7	45.0	52.6	67.8	78
			$\pm 0.2$	$\pm 0.2$	$\pm 0.2$	$\pm 0.3$		$\pm 0.5$			

500 eV primary electron energy are shown in Figures 7-8 and 7-9. Higher excitation energies were used but as the instrumental resolution deteriorates with energy so features close to the elastic peak were not detected. The loss features in 7-8 and 7-9 are labelled and the values are the mean of several measurements at each energy. The losses detected at each energy are summarised in Table 7-4 and the values obtained are compared with published values from the literature in Table 7-5. The error bars quoted in Table 7-4 have a confidence level of 66%.

Considerably more losses than previously reported were detected, due to the better instrumental sensitivity. The overall appearance of the loss spectra in Figs. 7-8 and 7-9, indicates that the strongest loss features are at 10.0eV and 22.6 eV. The higher energy losses (>50 eV) were only detected in the more sensitive first derivative mode of operation of the analyser.

The losses are explained by comparison with the optical properties measured by Juenker et al (1968) and Weaver et al (1974)<sup>183</sup>, who used synchrotron radiation. The optical properties of these authors are in good agreement and considered to be reliable, Juenker had obtained values from molybdenum targets flashed to 2000<sup>o</sup>K in a UHV atmosphere, and although Weaver removed the top layers before experimentation he does concede that there may be a thin oxide film covering his samples. The dielectric functions of molybdenum and the volume and surface loss functions as deduced by Weaver et al are shown in Fig. 7-10.

The 6.5 eV loss has not been previously reported in energy loss studies of molybdenum and it is tentatively assigned as being due to an interband transition (IB). There is some structure in the dielectric functions  $\epsilon_1$  and  $\epsilon_2$  of Fig. 7-10 at about this energy and the band structure calculation of Petroff and Viswanathan (1971)<sup>184</sup> predict a

TABLE 7-5

COMPARISON OF THE  $M_0$  LOSSES AND THEIR ASSIGNMENT

<u>Present Work (eV)</u>	<u>Zash k vara (1973) <sup>178</sup></u>	<u>Kawai (1974) <sup>181</sup></u>	<u>Harrower (1956) <sup>180</sup></u>	<u>Assignment</u>
1) 6.5				1B
2) 10.0	10	10	11.6	$VL_1$
3) 15.6				SL
4) 22.6	20.2-23.5	23	24.7	$VL_2$
5) 33.0				$VL_1 + VL_2$
6) 37.7				$N_{2/3} \rightarrow \text{Fermi}$
7) 45.0				$2VL_1 + VL_2$
8) 53			53.2	$3VL_1 + 2VL_2$
9) 68				$3VL_2$
10) 78.			76.9	$VL_1 + 3VL_2$

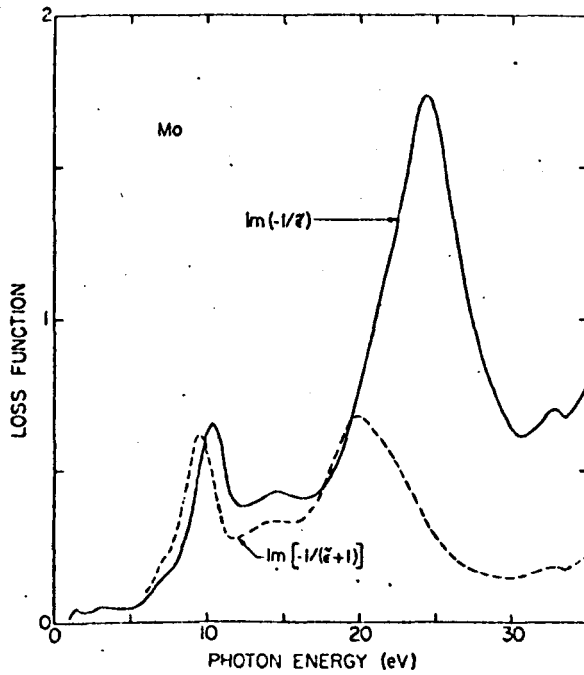
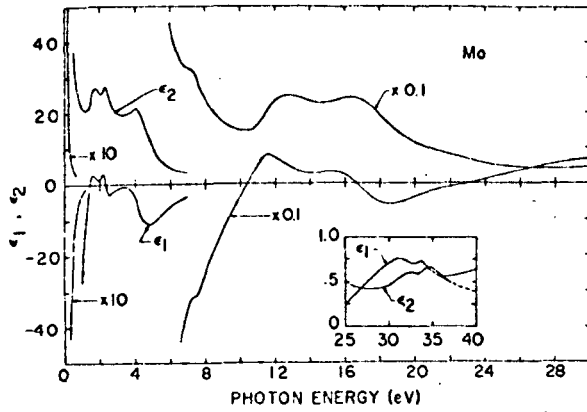


Fig.7-10. The Real( $\epsilon_1$ ) And Imaginary( $\epsilon_2$ ) Parts Of The Dielectric Constant And The Bulk And Surface Loss Functions For Molybdenum.<sup>183</sup>

high density of empty states just above the Fermi level, so that this loss can be explained as the excitation of electrons from the valence band to these empty states, Fig. 7-11.

The 10.0 eV loss has been regarded as a shifted surface plasmon by Kawai et al (1974)<sup>181</sup> and by Lecante (1971)<sup>185</sup>, who measures its energy to be 11.6 eV. Kawai obtained his results on a contaminated surface in poor vacuum while Lecante heated his samples to a temperature of 1300°C, which is likely to introduce surface contaminants due to segregation of bulk impurities additionally he did not characterise his surface with an element sensitive technique. Our results suggest that the 10.0 eV loss is a volume loss because it did not change in position when sulphur was segregated to the surface or when oxygen gas was adsorbed on to the Mo surface. The extent of sulphur segregation is shown in Fig. 7-4 and the oxygen adsorption was  $\sim 600$  Langmuirs, (see Fig. 7-7). Also its intensity relative to the known volume loss at 22.6 eV remains unchanged when the primary exciting electron energy is reduced from 500 to 300 eV, the lower energy is expected to be more surface sensitive. The optical measurements of Jaenker et al and Weaver et al show that  $\epsilon_1 = 0$ ,  $\epsilon_2$  is decreasing and the volume loss function  $\text{Im}(-\frac{1}{\epsilon})$  has a maximum at about 10 eV, Fig. 7-10, indicating that there is a volume plasmon oscillation in molybdenum at this energy. Thus the 10.0 eV loss in Table 7-5 is identified as a volume plasmon loss (VL<sub>1</sub>). Although the surface loss function in Fig. 7-10 also has a maximum at about 10 eV, its contribution to the intensity of the 10.0eV loss is thought to be small because no effects could be detected when the surface was contaminated by oxygen or sulphur.

The 22.6 eV loss is identified as a volume plasmon oscillation (VL<sub>2</sub>) being in good agreement with the plasmon energy of 21.9 eV calculated by regarding the  $4d^5 5s^1$  valence electrons of molybdenum as

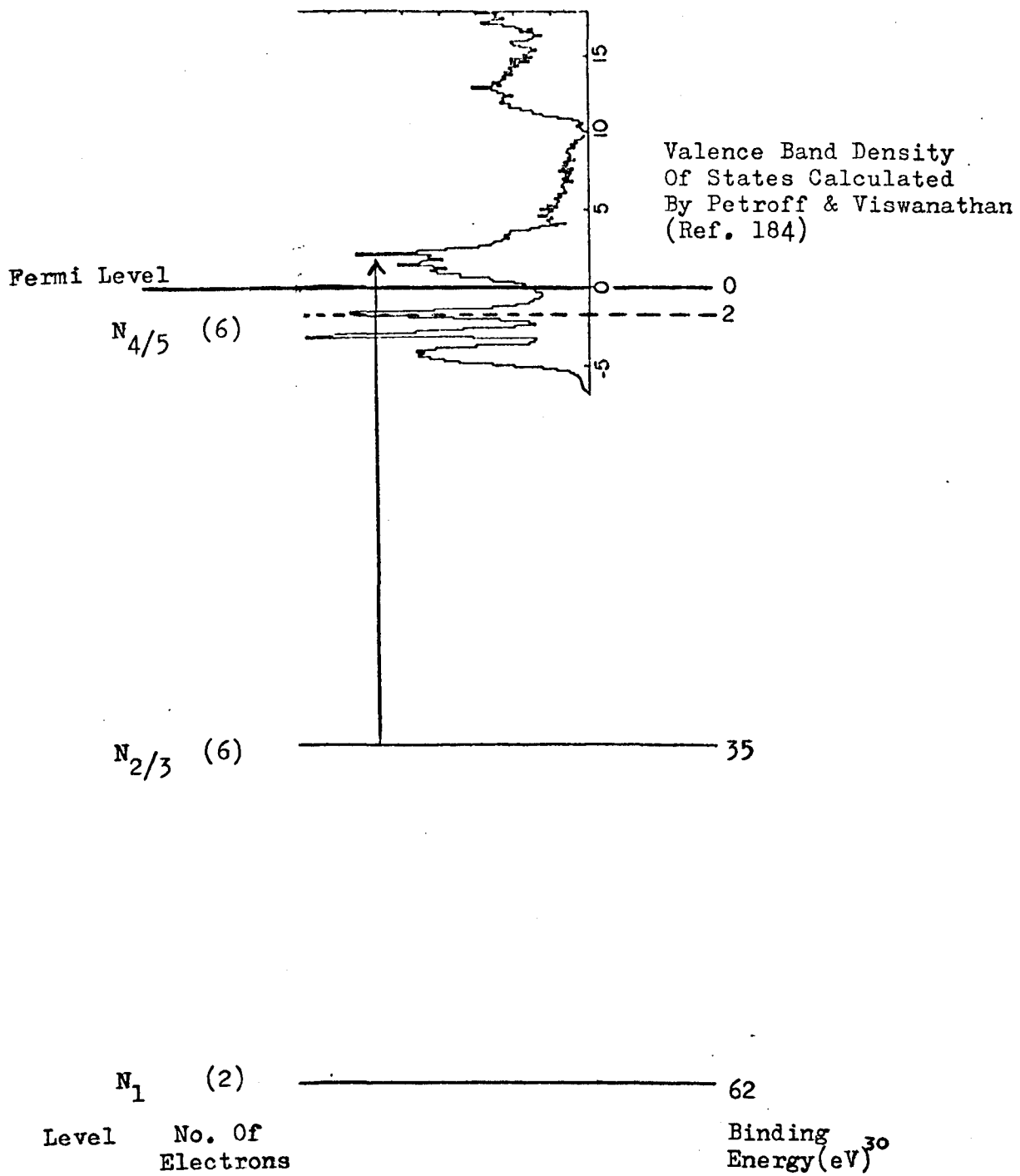


Fig.7-11. The Valence Band And Outer Electronic Levels Of Molybdenum.

forming a free electron like gas. Also from the optical measurements of Fig. 7-10,  $\epsilon_1 = 0$ ,  $\epsilon_2$  is decreasing and there is a broad maxima in the volume loss function  $\text{Im} \left( \frac{1}{\epsilon} \right)$  at about this energy. Thus in molybdenum two volume plasmons  $VL_1$  and  $VL_2$  are identified. Two plasma resonances have also been identified in graphitic carbon by Taft and Phillip (1965)<sup>186</sup>, one at 25 eV was identified with the plasmon in the gas formed by the 4 outer electrons from each atom and the other at 7 eV was identified with a plasmon resonance of the electrons forming the bond between the carbon layers. Similarly it is thought that in molybdenum the 22.6 eV loss is due to the oscillations of  $4d^5 5s^1$  electrons from each atom in the solid and the 10.0 eV loss is tentatively associated with a plasmon resonance of the  $5s^1$  electrons. These 5s electrons are of a different character from the  $4d^5$  electrons, because it is the  $5s^1$  electrons which are the ones actively involved in any chemical bond formation. The plasmon energy calculated on the basis of 1 electron per atom contributing to the electron gas is 8.9 eV in reasonable agreement with the observed value of 10.0 eV. Thus the 10.0 eV loss is tentatively identified with the plasmon of the  $5s^1$  electrons of molybdenum.

The 15.6 eV loss has not been previously reported in the literature and it is identified as a surface plasmon loss (SL) because its energy is approximately  $\frac{1}{\sqrt{2}}$  times the volume plasmon energy of 22.6 (Chapter 3). The surface loss function  $\text{Im} \left( \frac{-1}{1 + \epsilon} \right)$  also has a small maxima in the region of 15 eV, in Fig. 7-10. The detection of the 15.6 loss considerably aids the identification of the observed losses of Mo and refutes the suggestion made by Kawai et al and by Lecante that the 10.0 eV loss is a shifted surface plasmon. The observed intensity of the loss is small in comparison with the bulk losses at 10.0 eV and 22.6 eV in Figs. 7-8 and 7-9. Molybdenum is expected to have properties

similar to tungsten and it is interesting to note that the surface plasmon loss in tungsten is also very much weaker than the volume loss and it was only with great difficulty that the 16 eV surface plasmon loss of W, corresponding to its 22 eV bulk loss, was detected<sup>187</sup>.

The 37.7 eV loss is very weak and is tentatively identified with the excitation of  $N_{2/3}$  electrons to empty states just above the Fermi level, Fig. 7-11. No peak could be identified with the excitation of  $N_1$  electrons to these states. The remaining observed losses are identified as a combination of the volume losses  $VL_1$  and  $VL_2$ , i.e. the primary electron has suffered multiple inelastic collisions before emerging from the solid. The assignments are summarised in Table 7-5.

## 7.7 Summary

In this chapter the surface of a polished molybdenum specimen was studied. The main results obtained were:

(i) An Auger electron spectra characteristic of molybdenum was obtained and transitions assigned to the observed peaks. Contamination of the surface by sulphur, carbon or oxygen produced no detectible shift of the Mo Auger peaks although the C KLL peak was significantly influenced. Electron beam induced effects were also observed.

(ii) Adsorption of pure oxygen onto a clean and sulphur contaminated Mo surface (at room temperature) was carried out and a simple model developed which indicated that the initial sticking coefficient of oxygen was about a hundred times greater on the contaminated surface.

(iii) The characteristic energy losses from clean Mo were obtained and two previously unreported peaks detected at 6.5 eV and 15.6 eV. The losses were explained on the basis of two volume plasmons existing within the molybdenum, a surface plasmon oscillation and interband transitions. Multiple excitation losses were also identified.

AUGER ELECTRON AND ENERGY LOSS SPECTROSCOPY OF ANTIMONY,  
ANTIMONY OXIDE AND ANTIMONY SULPHIDE

8.1 Antimony

8.1.1 Introduction

Antimony is a group 5 semi-metal having an outer electron configuration of  $5s^2 5p^3$ . The group 5 semi metals arsenic, antimony and bismuth have resistivities higher than the transition metals, eg. the resistivity of antimony is  $39\mu\Omega$  cms in comparison with molybdenum  $5.2\mu\Omega$  cms. Although antimony is an important element in the electronic industry, being used in semi conducting materials such as InSb, AlSb and GaSb, its surface has not been thoroughly investigated. Ellis (1974)<sup>192</sup> has studied the arsenic surface, obtaining its Auger spectra and the characteristic energy losses, but as far as we can discover the Auger spectra of antimony has not been well investigated. The Sb spectra has been published in the P.E.I. handbook and in our own laboratory Wright (1974)<sup>53</sup> and Harris (1972)<sup>52</sup> have recorded the Auger spectra of antimony but only in the energy range 300 - 500 eV and some oxygen contamination was present on their thin film surfaces. In this chapter a more complete investigation of the Auger spectra is reported from a polycrystalline and a single crystal (100) surface.

The characteristic energy losses have been previously studied by Powell (1960)<sup>188</sup> and by Wright and Harris. The values reported here are from a clean single crystal surface uncontaminated by carbon, oxygen or sulphur, as detected by AES.

### 8.1.2 Experimental

Experiments were carried out on two antimony targets. One was a polycrystalline specimen of 2 cms diameter and 2mm. thick cut from a rod of 99.99% purity supplied by Metals Research Ltd.<sup>189</sup> One face of the disc was carefully ground on wet 15 $\mu$  abrasive paper and then polished with grade A diamond paste. After ultrasonically cleaning in acetone and distilled water the specimen was etched in a recommended solution of 30% hydrochloric acid in water with 5% hydrogen peroxide for 5 minutes<sup>190</sup>. The grain structure on the surface was thus revealed and the target again ultrasonically cleaned in distilled water before insertion into the chamber which was then evacuated to UHV pressures.

The other target was a single crystal disc of about 1 cms. diameter, 2 mm. thick and 99.99% purity. Antimony crystallises into a rhombohedral (trigonal) cell which can be described as pseudo-cubic with  $a = 6.22^{\circ}\text{A}$ ,  $\alpha = 87^{\circ}24'$ . The (100) face of this pseudo cubic structure accurate to  $\pm 2^{\circ}$  was obtained from Metals Research Ltd. The crystal face was gently polished with grade A diamond paste and then etched, in the solution described above for the polycrystalline sample, for 10 minutes followed by cleaning in distilled water before insertion into the vacuum chamber.

For both specimens the chamber was evacuated to a base pressure of  $5 \times 10^{-10}$  Torr, by the usual method. Auger spectra were recorded in the  $dN/dE$  mode with a glancing incident electron beam, and the loss spectra were recorded in the  $\frac{dN}{dE}$  and  $\frac{d^2N}{dE^2}$  mode on an AES characterised surface. Problems were encountered on locating the electron beam solely on to the crystal sample, because of its small size, but these were eventually overcome by careful adjustments of the target manipulator.

### 8.1.3 Results and Discussion of the Auger Spectra

The initial Auger spectra of antimony revealed no contamination due to sulphur, carbon, oxygen or any other element. This is probably due to the inert nature of the element and also it is thought that the exciting electron beam has a surface cleaning effect. The thermal conductivity of antimony is poor so that the bombarding electrons are thought to have created a localised hot spot and as antimony sublimes at a low temperature,  $883^{\circ}\text{K}$ , some removal of the surface layers probably occurs from the area under the electron beam bombardment. Thus no antimony specimen cleaning procedure was necessary and no electron beam induced contamination could be detected even for long exposures (several hours) with high currents ( $\sim 70\mu\text{A}$ ).

There was no detectable difference between the Auger spectra recorded from the polycrystalline and single crystal specimens, so that the results from the single crystal only are presented here. The overall Auger spectrum recorded from the (100) face of antimony is shown in Fig. 8-1. This is in good agreement with the published spectra of P.E.I. The finer details of this spectra are shown on an expanded scale in Figs. 8-2a and 8-2b.

The energies of the observed peaks are summarised in Table 8-1, together with the values observed by other authors. For the stronger observed features the energies shown in Table 8-1 are the mid points of the peak-peak heights in the derivative spectrum and the values in the energy range 330 - 500 eV are an average of six recordings of the Auger spectra. These six measurements were made on different days and for slightly different target positions and each spectra was calibrated after it was recorded. An accuracy of  $\pm 0.5$  eV is estimated in the energy of a peak as shown in Table 8-1. The energies of the peaks obtained from the polycrystalline target were in good agreement with the

Energy (eV)

800

700

600

500

400

300

200

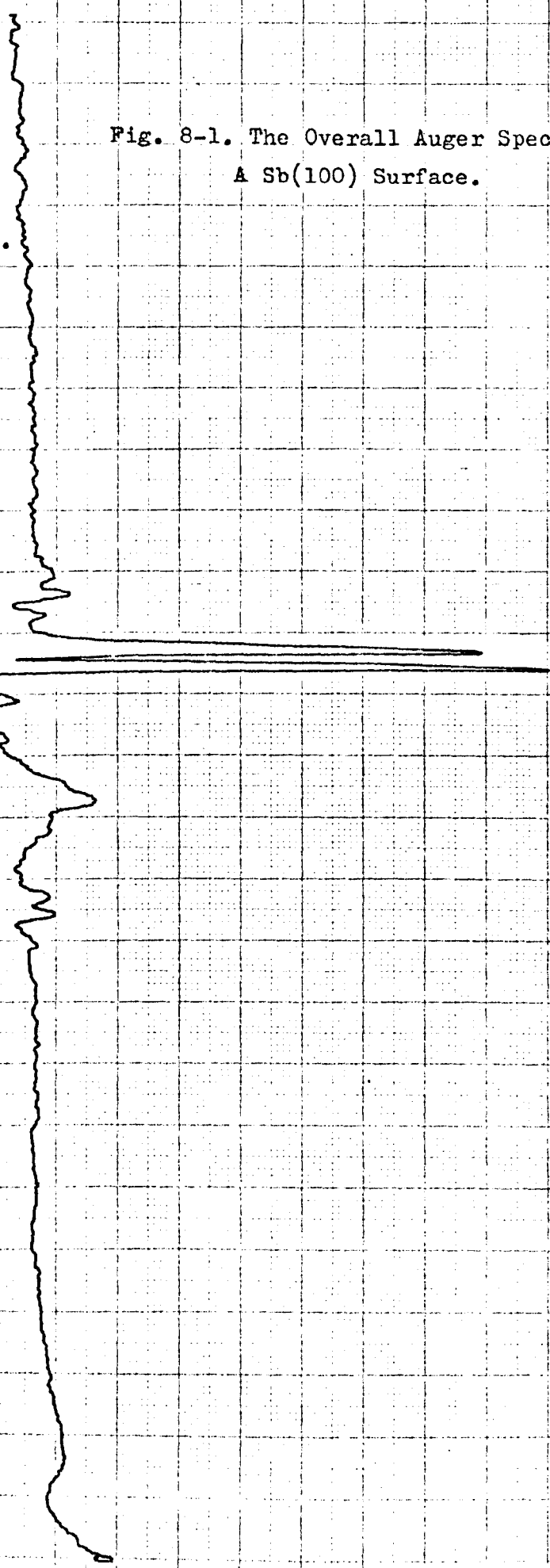
100

0

$E_p = 2.5 \text{ KeV}$   
 $I_p = 30 \mu\text{A}$   
Mod. 4V Pk-pk.  
Time Const. 1 Sec.

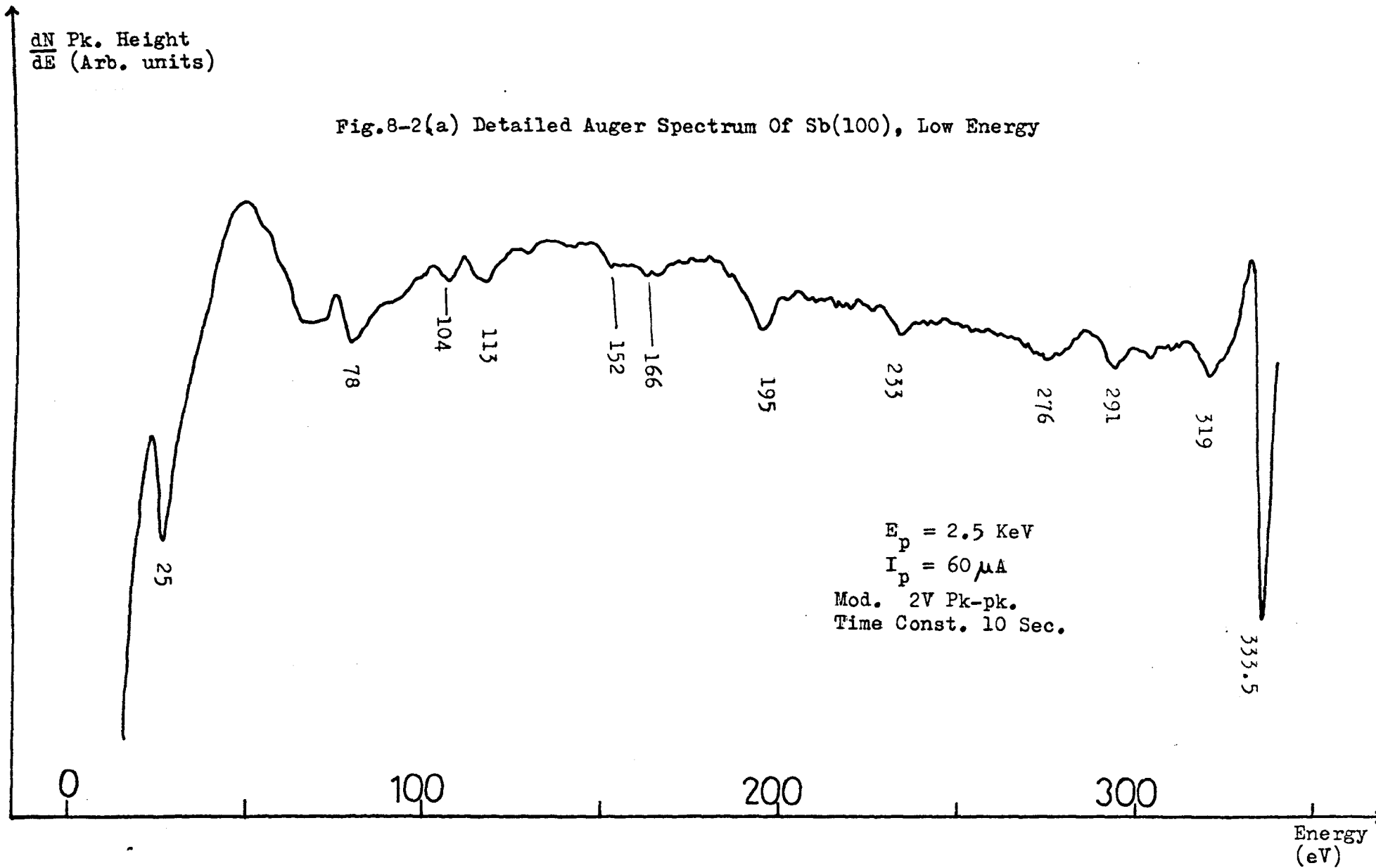
Fig. 8-1. The Overall Auger Spectrum Of  
A Sb(100) Surface.

$\frac{dN}{dE}$  Pk. Ht.



$\frac{dN}{dE}$  Pk. Height  
(Arb. units)

Fig.8-2(a) Detailed Auger Spectrum Of Sb(100), Low Energy



$\frac{dN}{dE}$  Pk. Height  
(Arb. units)

Fig.8-2(b). Detailed Auger Spectrum Of Sb(100),300- 500eV.

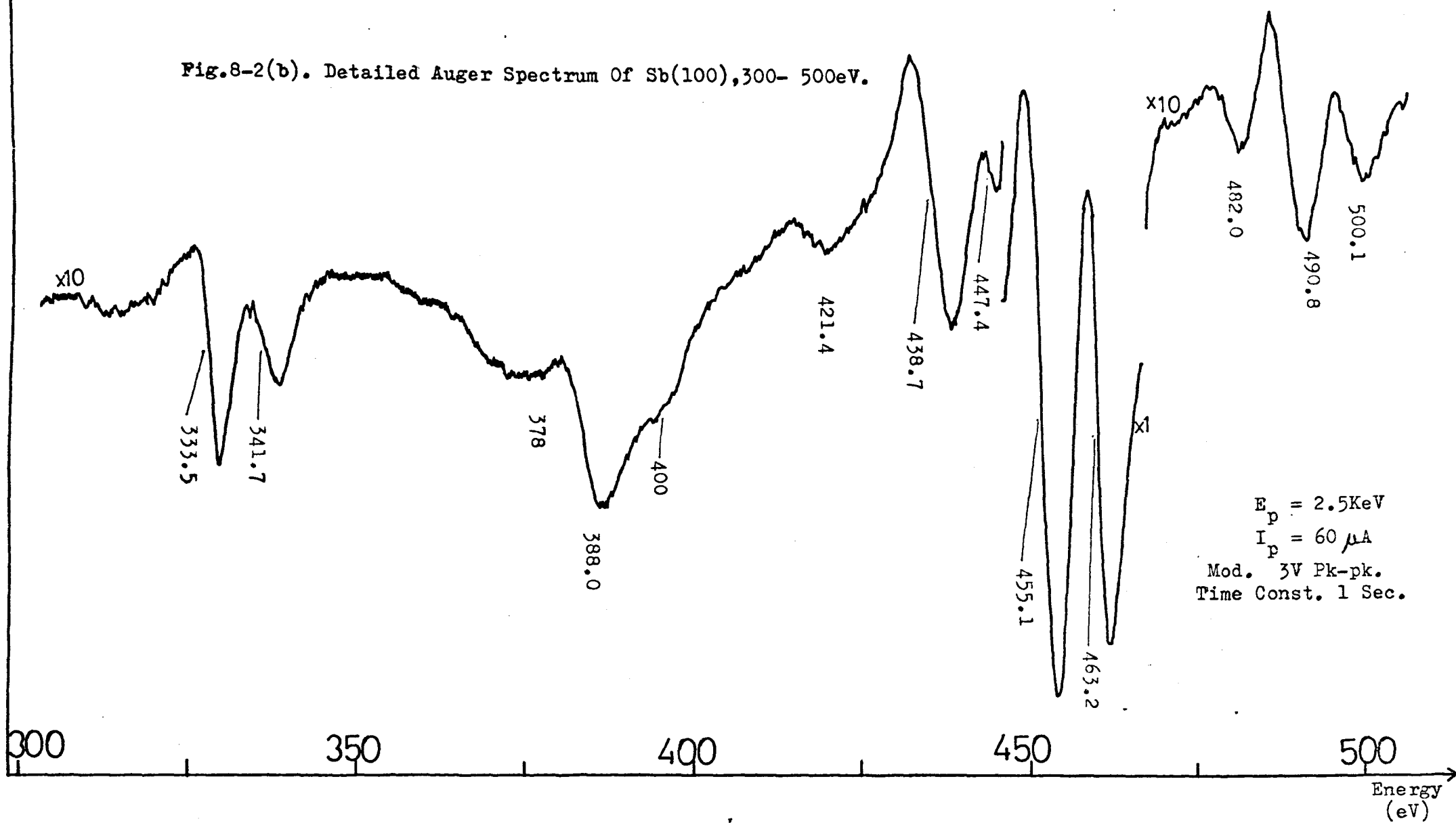


TABLE 8-1

OBSERVED PEAK ENERGIES (eV) FOR SB (100)

<u>Present Work</u>	<u>P.E.I.<sup>140</sup></u>	<u>B.W.<sup>53</sup></u> <u>(1974)</u>	<u>Harris<sup>52</sup></u> <u>(1972)</u>
25	26		
78			
104			
113			
152			
166			
195			
233			
276			
291			
319			
333.5 $\pm$ 0.5	334	335	332
341.7 $\pm$ 0.5	342	367	
378			370
388.0 $\pm$ 0.5	388	386	388
400			
421.4 $\pm$ 0.5			
438.7 $\pm$ 0.5	440	438	436
447.4 $\pm$ 0.5			450.5
455.1 $\pm$ 0.5	454	453	452.2
463.2 $\pm$ 0.5	462	462	459.5
482.0 $\pm$ 0.5			
490.8 $\pm$ 0.5	492	488	490
500.1 $\pm$ 0.5	499		

values of Table 8-1.

Transitions are assigned to the observed peaks, using the tables of Clausing and Coghlan<sup>36</sup>, and these are summarised in Table 8-2. The energy of the primary electrons was such that only the M,N and O levels were ionized. No transition could be identified with the feature at 378 eV, whose width in Fig. 8-2 suggests that it probably consists of several unresolved peaks. The 438.7 eV and 447.4 eV peaks are probably due to the  $M_{4/5}, N_{4/5}, N_{4/5}$  electrons (455.1, 463.2 eV) exciting a plasmon as they exit from the solid. The energy difference agrees well with the observed volume plasmon energy ( $\approx 16$  eV) of antimony and additionally no strong Auger transition could be identified with these (438.7, 447.4 eV) peaks.

Nearly all the observed peaks are assigned Auger transitions between core levels, the number of valence electrons (2 in the  $O_1$  and 3 in the  $O_{2/3}$  subshell) is small in comparison with the number of electrons in the  $N_{4/5}$  level (10), so that transitions involving the  $N_{4/5}$  level would be expected to be stronger and this is in fact found to be so as the strongest observed peaks at 455.1 eV and 463.2 eV are assigned the  $M_5, N_{4/5}, N_{4/5}; M_4, N_{4/5}, N_{4/5}$  transitions. For this pair of peaks the difference in energy between the Auger peaks, 8 eV, is in good agreement with the difference in binding energy of the  $M_5, M_4$  electrons, 9 eV as given by Bearden and Burr<sup>30</sup>.

The Auger spectra of antimony is influenced by Coster-Kronig transitions as the  $M_3, N_{4/5}, N_{4/5}$  transition at 694 eV, expected to be of the same intensity as the  $M_4, N_{4/5}, N_{4/5}$  transition on the basis of the number of electrons involved, was not observed. It is thought that vacancies created in the  $M_3$  subshell are filled by Coster Kronig transitions of type  $M_3, M_4 -$ ,  $M_3, M_5 -$ , and indeed peaks due to such transitions are observed at low energies as seen in Table 8-2. The

TABLE 8-2

AUGER PEAK ASSIGNMENTS FOR SB.

<u>Observed Energy (eV)</u>	<u>Transition</u>	<u>Calculated<sup>36</sup> Energy</u>	<u>Multiplicity</u>
25	$N_{2/3} N_{4/5} N_{4/5}$	27	100
78	$N_1 N_{4/5} N_{4/5}$	80	33
104	$M_3 M_4 N_{2/3}$	102	16
113	$M_3 M_5 N_{2/3}$	111.5	24
152	$M_2 M_5 N_{2/3}$	157.5	12
166	$M_3 M_4 N_{4/5}$	170.5	26
195	$M_3 M_5 N_{4/5}$	180	40
233	$M_2 M_5 N_{4/5}$	226	20
276	$M_4 N_1 N_{2/3}$	263	12
291	$M_5 N_1 N_{2/3}$	272	8
319	$M_5 N_{2/3} N_{2/3}$	319	36
	$M_4 N_{2/3} N_{2/3}$	328	24
333.3	$M_5 N_1 N_{4/5}$	332	20
341.7	$M_4 N_1 N_{4/5}$	341	13
378			
388.0	$M_5 N_{2/3} N_{4/5}$	387.5	60
400	$M_4 N_{2/3} N_{4/5}$	396.5	40
421.4	$M_5 N_{2/3} O_{2/3}$	421	18
438.7	$M_4 N_{2/3} O_{2/3}$	430.5	12
	{ Plasmon Loss of		
	$M_5 N_{4/5} N_{4/5}$		
447.4	Plasmon Loss of		
	$M_4 N_{4/5} N_{4/5}$		
455.1	$M_5 N_{4/5} N_{4/5}$	456.0	100
463.2	$M_4 N_{4/5} N_{4/5}$	465.0	66
482.0	$M_5 N_{4/5} O_1$	482.0	20
490.8	$M_5 N_{4/5} O_{2/3}$	490.0	30
500.1	$M_4 N_{4/5} O_{2/3}$	499	20

vacancy distribution in the  $M_4$ ,  $M_5$  subshells is thus enhanced increasing their relative intensity.

#### 8.1.4 Results and Discussion of the Energy loss Spectra

After characterising the Auger spectra of antimony, its characteristic energy losses were studied. The Auger spectra recorded before and after obtaining an energy loss spectra were identical indicating no change in the surface species. The loss spectra were recorded at different primary energies, and Figs. 8-3, 8-4 and 8-5 show the general appearance of the spectra recorded with 300 eV, 500 eV and 1000 eV primary electrons. The losses observed in the  $\frac{d^2N}{dE^2}$  spectra at different energies are summarised in Table 8-3 and the mean values obtained. The error bars in Table 8-3 have a confidence limit of 66%. These losses were also detected in the first derivative spectra, as shown in Figs. 8-3 and 8-4 and additional features at 49 eV, 66 eV and 80 eV could also be identified. In the 1000 eV  $dN/dE$  loss spectra in Fig. 8-5 only multiples of the 15.8 eV loss (identified as the volume plasmon energy) could be observed possibly the relative excitation probability of this loss has increased.

The energy of the losses observed from the polycrystalline antimony specimen were similar to the values observed from the single crystal target and also the general shape of the observed spectra, at the same primary energy, from the two targets were in good agreement. Several measurements were made on the loss spectra and the average energies of the observed losses from the polycrystalline Sb target were: 6.9, 11.0, 15.8, 26.9, 33.6, 50, 66, 80 eV. No importance is attached to the small energy differences with the values summarised in Table 8-3.

$\frac{dN}{dE}$  Spectra, Mod. 1V Pk.-pk.  
 $I_p = 2.5 \mu A$   
 Time Const. 1 Sec.

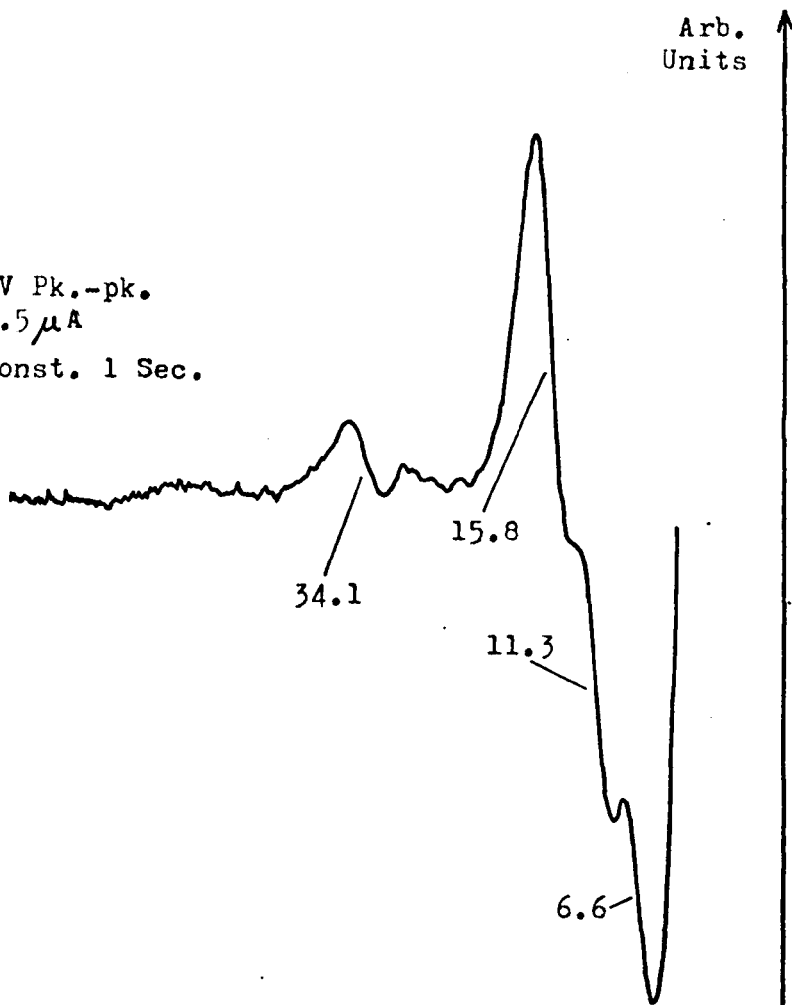
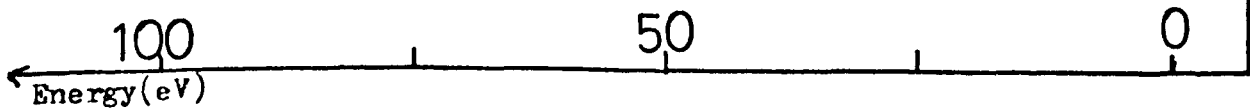
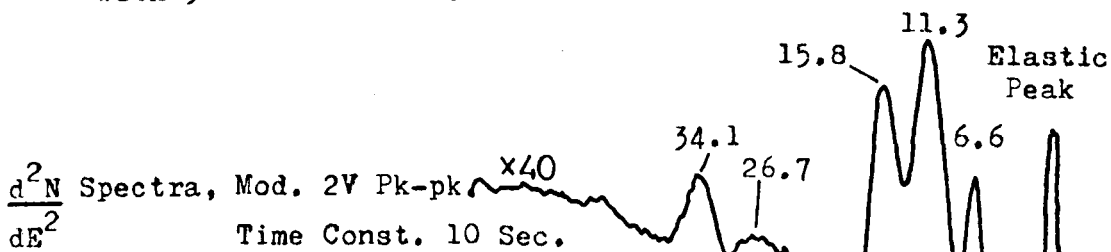


Fig.8-3. Energy Loss Spectra Of Antimony(100) Excited  
 With 300eV Electrons.



Arb. Units

$\frac{dN}{dE}$  Spectra, Mod. 2 V Pk-pk.  
 $I_p = 7.5 \mu A$   
Time Const. 1 Sec.

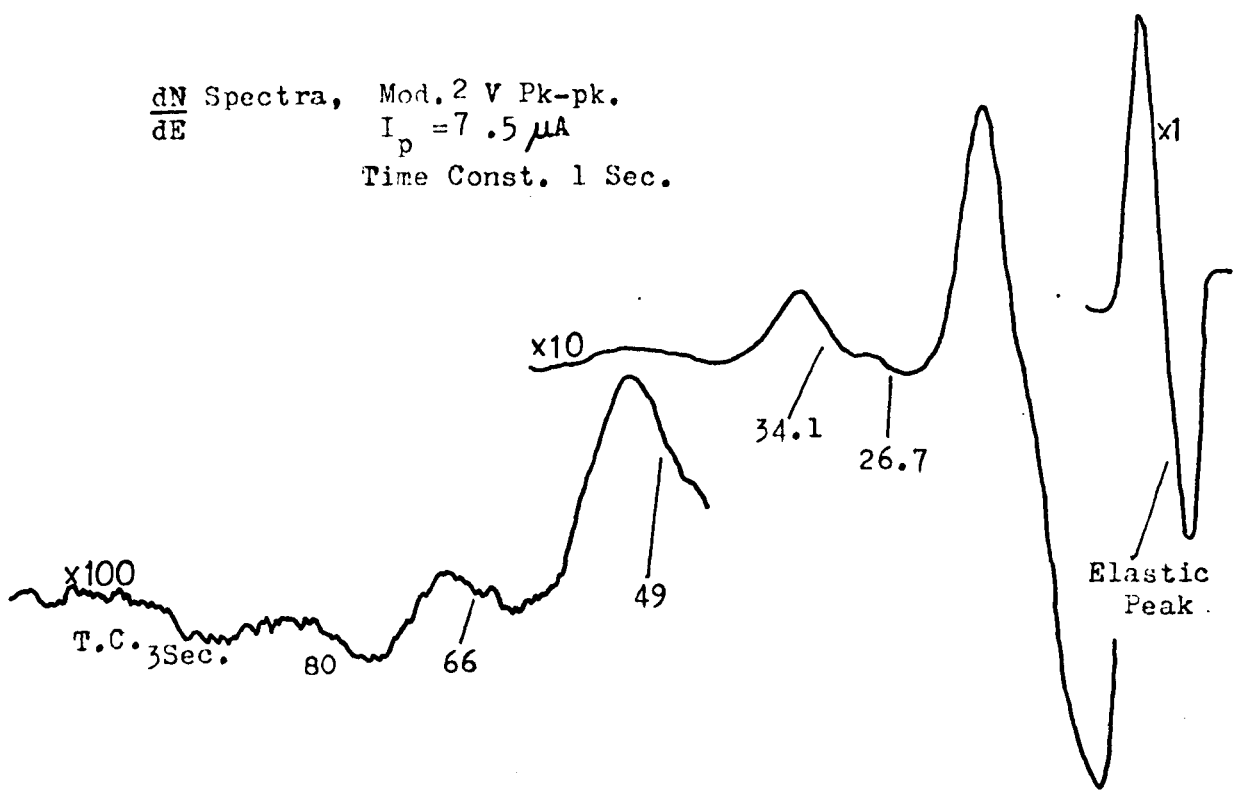
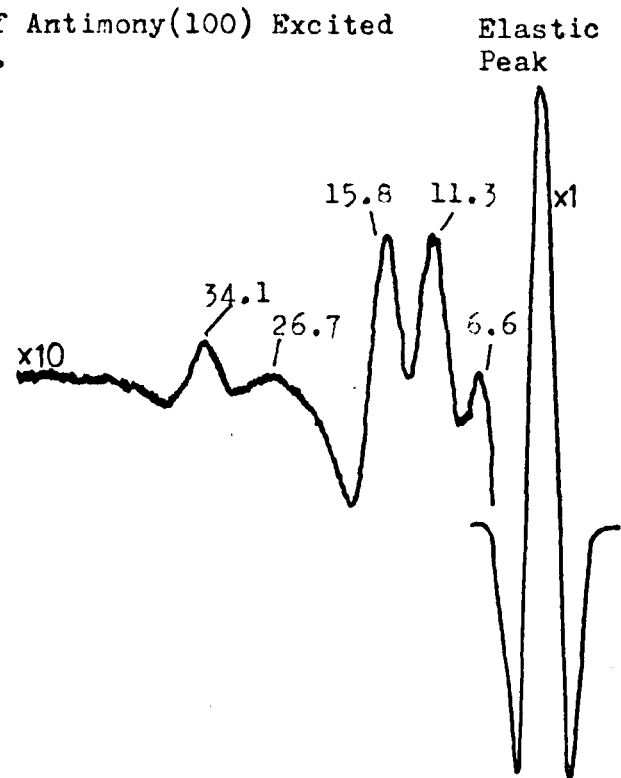


Fig.8-4. Energy Loss Spectra Of Antimony(100) Excited With 500 eV Electrons.

$\frac{d^2N}{dE^2}$  Spectra, Mod. 2.5V Pk-pk.  
Time Const. 1 Sec.



100  
Energy (eV)

50

0

$\frac{dNPk.Ht.}{dE}$   
(Arb. units)

Fig.8-5. Energy Loss Spectra Of Antimony(100)  
Excited With 1000eV Electrons.

x10

x1

$I_p = 13 \mu A$   
Mod. 5V Pk-pk.  
Time Const. 1 Sec.

100  
50  
0  
Energy(eV)

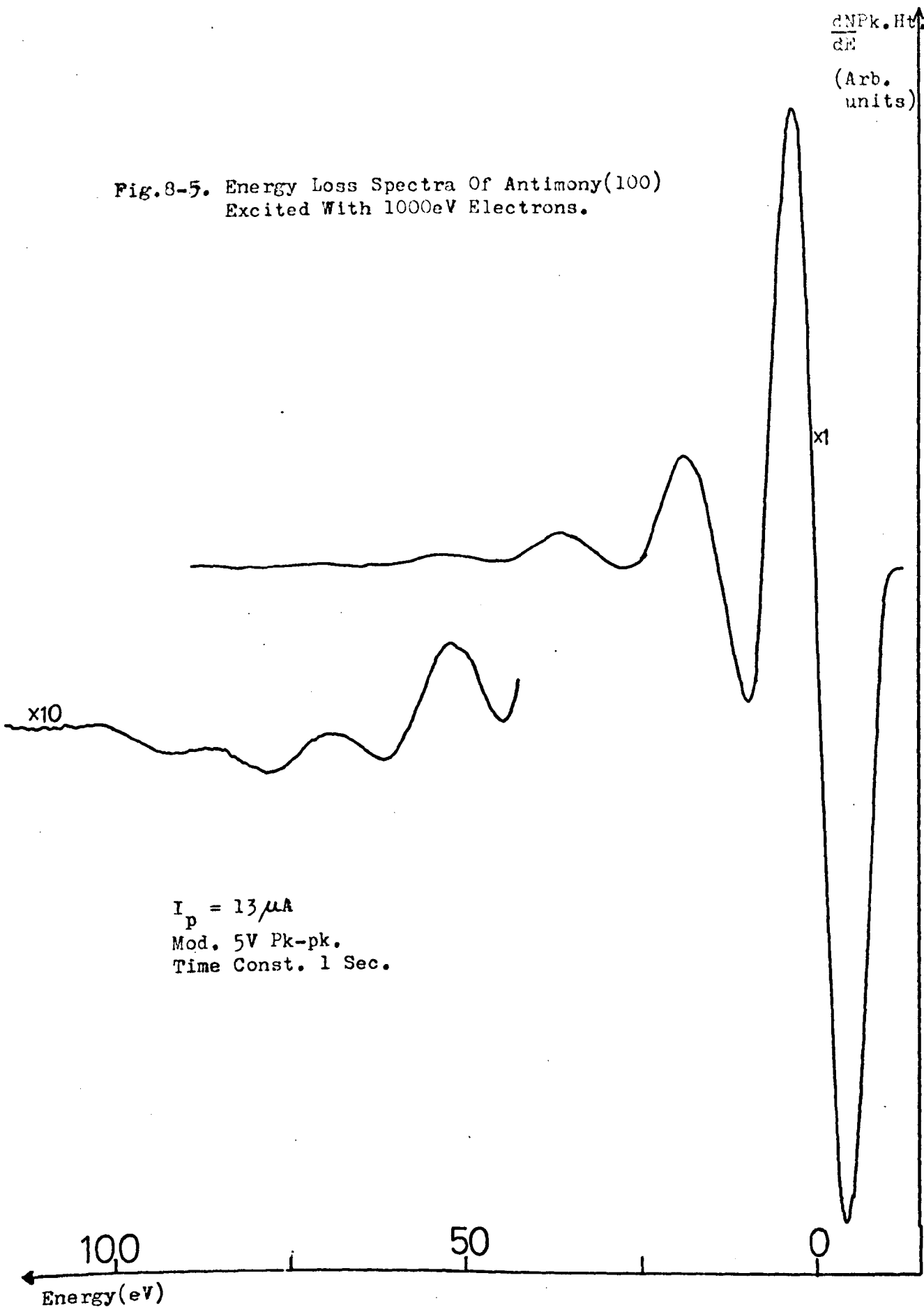


TABLE 8-3

SUMMARY OF CHARACTERISTIC LOSSES OBSERVED

AT DIFFERENT PRIMARY ENERGIES

<u>E<sub>p</sub> (eV)</u>	<u>Analyser Operation Mode</u>	<u>Observed Losses (eV)</u>				
750	$\frac{d^2N}{dE^2}$		11.1	16.1	28.8	34.9
			10.5	15.2	26.4	33.0
			11.9	15.7	27.3	34.2
500	$\frac{d^2N}{dE^2}$	6.4	10.5	15.7	27.7	33.5
		6.2	10.8	15.9	27.1	33.7
		5.6	11.0	15.6	24.7	34.2
		5.8	11.3	15.3	24.9	34.5
300	$\frac{d^2N}{dE^2}$	7.1	11.6	15.8	26.6	34.4
		7.1	12.0	16.5		34.4
		7.9	11.9	16.4	24.7	34.2
<hr/> Mean Value		6.6	11.3	15.8	26.7	34.1
		± 0.3	± 0.3	± 0.3	± 0.4	± 0.4

In Table 8-4, the energies of the losses observed from the crystal sample are compared with the values obtained by other authors. In general agreement is good, particularly with the values obtained by Powell (1960)<sup>188</sup>. Harris and Wright observe some additional features which we were unable to identify in our spectra, possibly the presence of oxygen on their surfaces contributed these peaks.

An explanation of the losses is offered by comparison with the optical measurements (0 - 16 eV) performed on Sb thin films, in UV, by Lemonier et al (1974)<sup>191</sup>. The 15.8 eV loss is thought to be a volume plasmon (VP) oscillation of the valence band electrons of Sb. On the basis of each Sb atom contributing five electrons ( $5s^2 5p^3$ ) to the valence band and these electrons behaving as a free-electron like gas for oscillation, a volume plasmon energy of 15.1 eV can be calculated in good agreement with the observed value. The small discrepancy between the observed and calculated values may be due to a low lying interband transition, Raether (1965)<sup>91</sup>. Additionally evidence comes from the optical measurements<sup>191</sup> which predict a volume plasma at 15.8 eV on the bases of  $\epsilon_1 = 0$ ,  $\epsilon_2$  decreasing and a broad maxima occurring in  $\text{Im} \left( \frac{-1}{\epsilon} \right)$ , the volume loss function, at about this energy.

The 11.3 eV loss is approximately  $\frac{1}{\sqrt{2}}$  of the volume plasmon energy and also Lemonier has shown that the surface loss function  $\text{Im} \left( \frac{-1}{1+\epsilon} \right)$  has a maximum in the vicinity of 11 eV so that this loss can be assigned to a surface plasmon (SP) oscillation.

The 6.6 eV loss is thought to be due to the excitation of the  $O_1$  electrons to states near the Fermi level, because the binding energy of these electrons is 6.7 eV, Servier (1972)<sup>31</sup>, and the optical measurements<sup>191</sup> show weak structure in  $\epsilon_1$ ,  $\epsilon_2$  and  $\text{Im} \left( \frac{-1}{\epsilon} \right)$  at about 7 eV. The 34.1 eV loss is similarly identified as an excitation of the  $N_{4/5}$  electrons to empty states close to the Fermi level of the solid. Because the binding energy of the  $N_{4/5}$  electron is estimated to be 32 eV (Servier)<sup>31</sup>

TABLE 8-4

CHARACTERISTIC ENERGY LOSSES OF SB (100)

<u>Present Work</u> (eV)	<u>Powell<sup>188</sup></u> (1960)	<u>Harris<sup>52</sup></u> (1972)	<u>Wright<sup>53</sup></u> (1974)	<u>Assignment</u>
6.6		6?	7	$O_1 \rightarrow$ Fermi level
11.3	11.3	11.5	11	SP
15.8	15.9	16	15	VP
26.7	26.5	28	28	VP + SP
34.1	32.3	34	32	$\left\{ \begin{array}{l} N_{4/5} \rightarrow \text{Fermi level} \\ 2VP \end{array} \right.$
49	48.3	43 49	47 52 59	
66		63	68	$\left\{ \begin{array}{l} N_{2/3} \rightarrow N_{4/5} \\ 4VP \end{array} \right.$
80		81	80	

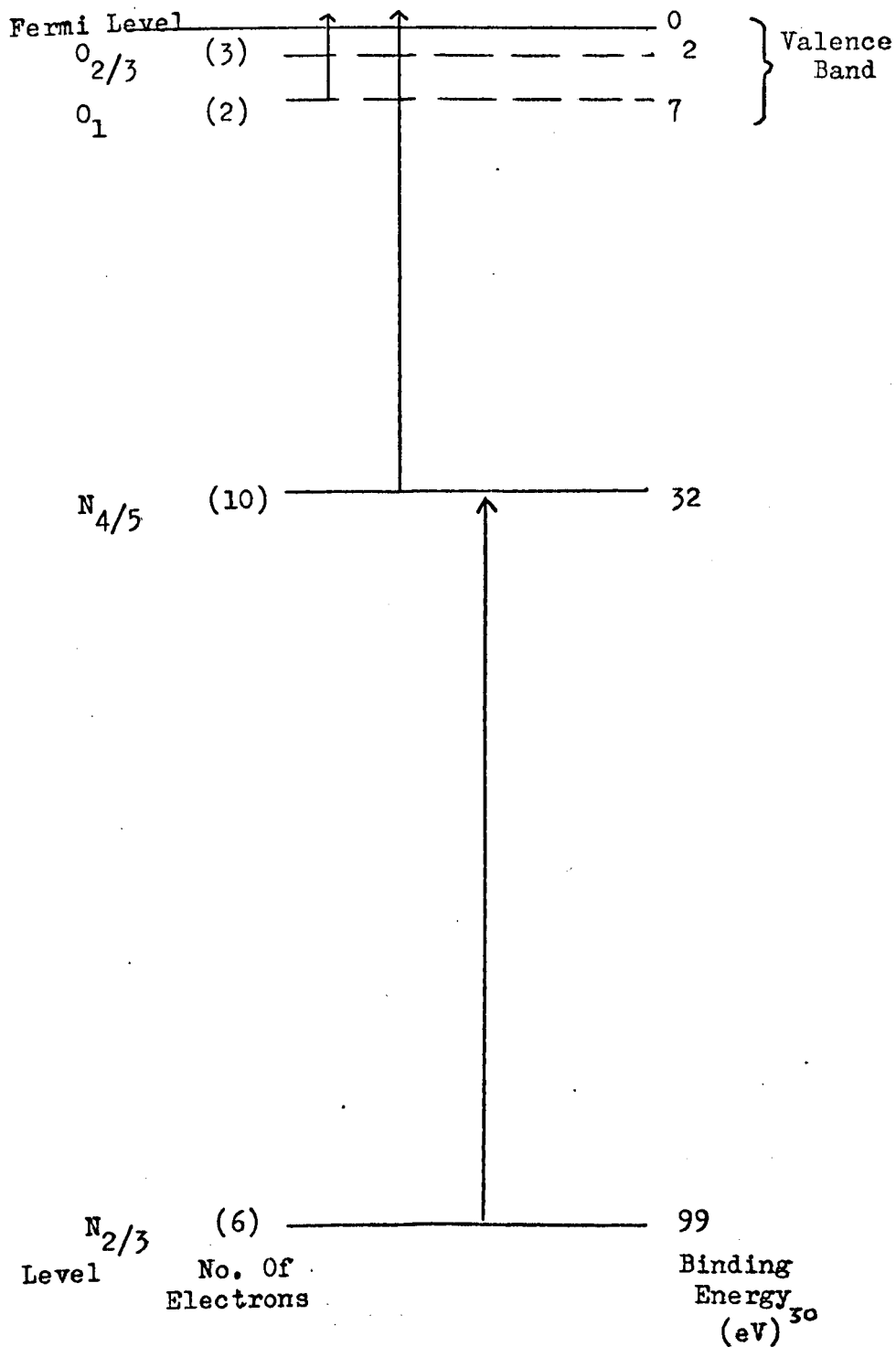


Fig.8-6. The Outer Electronic Levels Of Antimony Showing Possible Characteristic Losses.

excitation is possibly occurring to states just above the Fermi level. These excitations are summarised in Fig. 8-6. A contribution to the 34.1 eV loss peak is also expected from primary electrons which have excited two volume plasmons before exiting from the solid.

The remaining losses are identified as multiples of the surface and volume plasmons, and their assignments are summarised in Table 8-4, with the possibility of  $N_{2/3} \rightarrow N_{4/5}$  electron excitations contributing to the 66 eV peak.

As can be seen from Fig. 8-5, the losses of Sb contain strong plasmon features. It has been remarked by Wright (1974) that the losses of semi-metallic antimony are anomalous because they resemble the losses of a metal such as aluminium which has a free-electron like character. Wright has proposed an explanation for the free electron like behaviour of antimony and of other poor conductivity solids such as Si, which also has strong plasmon features. The explanation is based on a region of high electron density being produced, in poor conductivity materials, by the primary beam and then free electron like plasma oscillations occurring in this confined plasma. This explanation may be criticised because it does not explain why the plasmon energy calculated by regarding the valence electrons as undergoing free-electron like oscillations, agrees so well with the observed plasmon energy for a large number of solids. Also typical electron beam currents used to observe the characteristic losses are  $\approx 100 \mu\text{A}$  in a  $1 \text{ mm}^2$  spot (this figure is an upper limit). On this basis approximately  $10^{17}$  electrons are incident per sec per sq. cms. on to the solid, this number is considerably less than the densities of  $10^{22}$  electrons  $\text{cms}^{-3}$  required for plasmon oscillations of 10 - 20 eV energy, typically observed in solids.

The results indicate that the plasmons in Sb and other solids such as silicon are excited in the valence band electrons. These valence band

electrons appear to be behaving in a free electron like manner for the high frequency plasmon oscillations although they may not display a free electron like character for other properties, such as conduction. For the 1000 eV primary electrons loss spectra, shown in Fig. 8-5, five volume plasmon losses can be detected, probably because of the instrumental sensitivity and the greater depth of penetration of these electrons.

From the natural width of a plasmon loss peak the life time of an oscillation can be estimated by using the Uncertainty Principle  $\Delta E \Delta T = \hbar$ . The loss spectra recorded with 1000 eV primary electrons in Fig. 8-5 was used to estimate the width of the first plasmon loss peak and from it was subtracted the width of the elastic peak, which was regarded as the instrumental contribution to the plasmon peak width. From the natural peak width thus estimated the life time for an electron excited plasmon oscillation is calculated to be  $2 \times 10^{-15}$  secs. This value is to be compared with the figure  $1 \times 10^{-16}$  secs. obtained by Lemonier from optical measurements, who suggests that such low lifetimes indicate that the dominant mechanism of plasmon decay is probably electron-electron collisions.

#### 8.1.5 Adsorption of Oxygen on to the Sb (100) Face

An adsorption experiment similar to the one performed on the Mo surface was attempted. The crystal face was exposed to 2700 L of pure oxygen at controlled rate without the observation an oxygen peak in the Auger spectra of the surface. It was thought that antimony does not oxidise easily by this method, and possibly the sticking coefficient of oxygen on the crystal surface was very low. Due to the lack of detection of the oxygen signal further experimentation along this line of enquiry was not pursued.

## 8.2 Antimony Oxide ( $\text{Sb}_2\text{O}_3$ )

### 8.2.1 Introduction

It is of considerable current interest in AES to study the influence of chemical combination on the Auger spectra. So after studying pure antimony we proceeded to study the Auger spectra and characteristic losses of antimony oxide, one of the more simpler antimony compounds. The Auger spectra of  $\text{Sb}_2\text{O}_3$  is of practical importance because progress can then be made to understand the surface oxidation of useful semi-conducting materials such as InSb, by using AES.

### 8.2.2 Experimental

An antimony oxide surface was prepared by slowly subliming the material from a molybdenum boat, on to a molybdenum substrate at room temperature. The antimony oxide was obtained in tablet form from BDH<sup>193</sup> and ground to a powder before insertion into an previously out gassed molybdenum boat. Antimony oxide is a suitable material for vapor deposition and it sublimes at a low temperature of 400 - 500°C.

The molybdenum substrate surface was prepared, as described in Chapter 7, to a mirror finish and after pumping to UHV pressures, the substrate was flashed to a high temperature to remove any contaminants, as detected by AES. The target was then placed opposite the boat containing the antimony oxide and the material slowly evaporated keeping the pressure within the chamber below  $1 \times 10^{-7}$  torr. Periodically an Auger spectra of the surface was recorded which indicated a decreasing intensity of the Mo Auger peaks as the antimony and oxygen Auger peaks increased in intensity. Even when the Mo Auger peaks could not be detected, evaporation was continued until we were satisfied that there

were no substrate influences on the observed spectra, but care was taken not to evaporate too thick a film as surface charging effects then become apparent.

Initial experiments on the  $\text{Sb}_2\text{O}_3$  evaporated surface indicated the presence of electron beam artifacts in the recorded Auger spectra. With an electron beam current  $\approx 50\mu\text{A}$  these became significant after a bombardment time  $\approx 30$  minutes. Hence the Auger spectra were recorded only in the energy range 300 - 500 eV in a period of about 15 mins. and from a freshly evaporated film. On some occasions the target was moved so that the spectra was recorded from a freshly bombarded part of the film. Periodically checks were carried to detect the presence of contaminants carbon and sulphur and also for the substrate Auger peaks, but no such peaks were observed and the spectra presented are believed to be characteristic of  $\text{Sb}_2\text{O}_3$ . The lower energy weaker Auger peaks were not investigated because the long scanning times needed would introduce electron beam effects.

The characteristic energy losses of  $\text{Sb}_2\text{O}_3$  were also recorded from a fresh part of the surface with 300 eV and 500 eV primary electrons. Spectra were recorded in the  $\frac{dN}{dE}$  mode and the  $\frac{d^2N}{dE^2}$  mode of operation, from an AES characterised clean surface.

### 8.2.3 Results and Discussion of the Auger spectra of $\text{Sb}_2\text{O}_3$

A typical Auger spectra from an antimony oxide surface is shown in Fig. 8-7. A total of six spectra were recorded from freshly bombarded surfaces and the energies of the observed peaks determined, by following the same procedure as for Sb. The mean energies of the peaks observed from  $\text{Sb}_2\text{O}_3$  in the energy range 300 - 510 eV are summarised in Table 8-5. The energy of the same peak from Sb (100) crystal is also summarised in Table 8-5 and the peak shift deduced. The difference is

$\frac{dN}{dE}$  Pk. Height  
(Arb. units)

Fig.8-7. The Auger Spectrum Of Antimony Oxide.

$E_p = 2.5\text{KeV}$   
 $I_p = 50\mu\text{A}$   
Mod. 2.5V Pk.-pk.  
Time Const. 1 Sec.

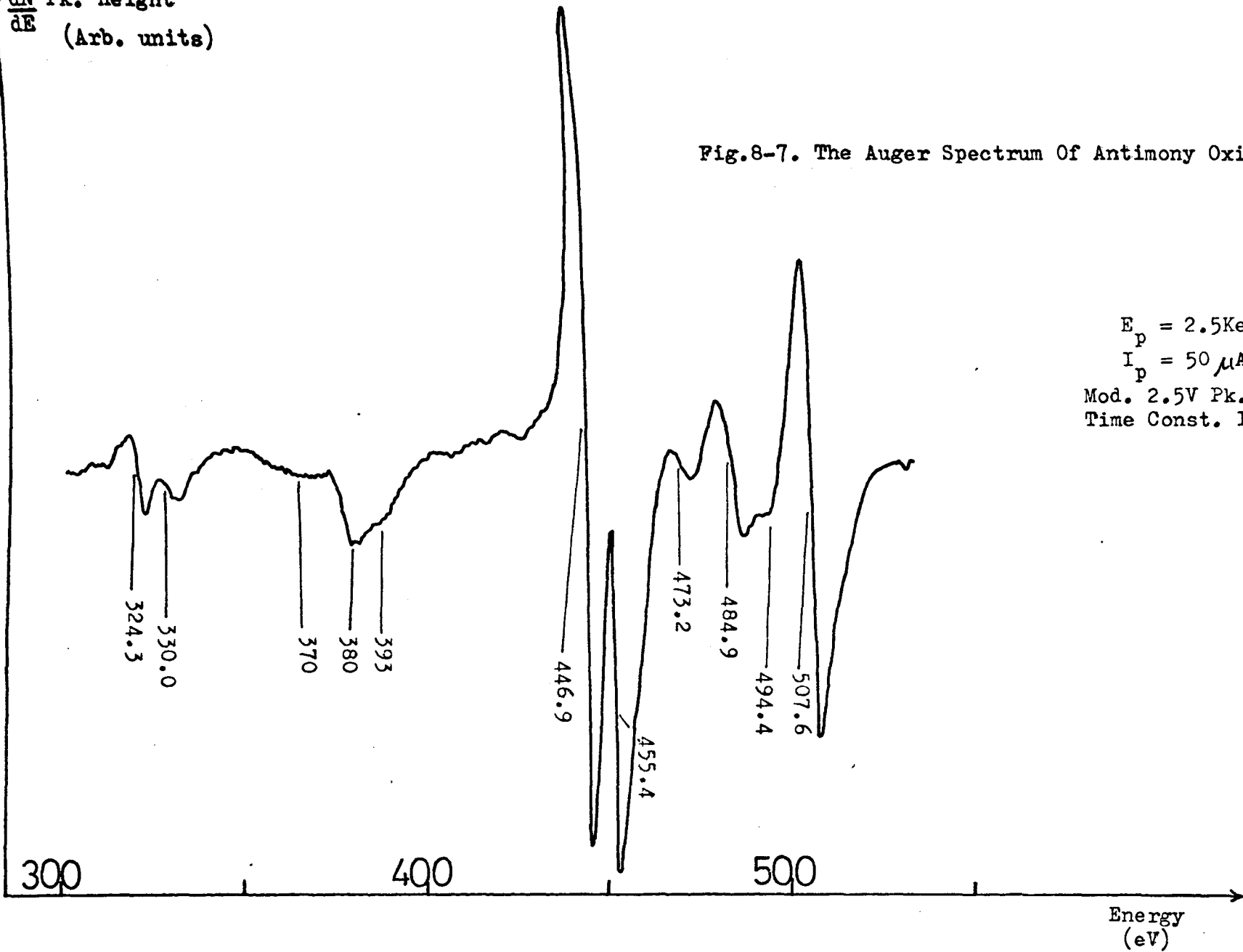


TABLE 8-5

AUGER PEAK ENERGIES OBSERVED FROM  $Sb_2O_3$

<u><math>Sb_2O_3</math> (eV)</u>	<u>Sb (100) (eV)</u>	<u>Peak Shift (eV)</u>
<u>peaks</u>	<u>peaks</u>	
324.3 $\pm$ 0.5	333.5	9.2eV
333.0 $\pm$ 0.5	341.7	8.7
370	378	8
380	388	8
393	400	9.7
446.9 $\pm$ 0.5	455.1	8.2
455.4 $\pm$ 0.5	463.2	8.8
473.2 $\pm$ 0.5	)	
484.9 $\pm$ 0.5	) Oxygen	
494.4 $\pm$ 0.5	) + Sb	
507.6 $\pm$ 0.5	) Peaks	
	)	

TABLE 8-6

ASSIGNMENT OF OBSERVED PEAKS FROM Sb<sub>2</sub>O<sub>3</sub>

<u>Observed Energy of Prominent Peaks</u>	
324.3	Sb M <sub>5</sub> N <sub>2/3</sub> N <sub>2/3</sub> , M <sub>5</sub> N <sub>1</sub> N <sub>4/5</sub>
333.0	Sb M <sub>4</sub> N <sub>2/3</sub> N <sub>2/3</sub> , M <sub>4</sub> N <sub>1</sub> N <sub>4/5</sub>
446.9	Sb M <sub>5</sub> N <sub>4/5</sub> N <sub>4/5</sub>
455.4	Sb M <sub>4</sub> N <sub>4/5</sub> N <sub>4/5</sub>
473.2	O K L <sub>1</sub> L <sub>1</sub>
484.9	O K L <sub>1</sub> L <sub>2/3</sub>
494.4	Sb M <sub>5</sub> N <sub>4/5</sub> O <sub>2/3</sub> O (K) O(L <sub>1</sub> ) Sb (O <sub>2/3</sub> )
507.6	O K L <sub>2/3</sub> L <sub>2/3</sub>

thought to be due to a chemical shift of the Auger peaks and not a surface charging effect. This explanation is justified to some extent later on in this section.

The higher energy peaks between 470 and 510 eV are due to antimony and oxygen, Auger transitions. It is to be noted that the strong peak at 438.7 eV in the antimony spectra of Fig. 8-2 is not observed in the  $Sb_2O_3$  Auger spectra of Fig. 8-7, confirming the assignment that it was probably a plasmon loss feature from the main antimony peaks. The feature at 447.4 eV in the Sb Auger spectra is also absent for the same reason. The prominent peaks in the Auger spectra of  $Sb_2O_3$  are assigned transitions using the tables of Coghlan and Clausing<sup>36</sup> in Table 8-6. A possible interatomic transitions may be contributing to the 494.4 eV peak.

As can be seen in Table 8-5 the Auger peaks of Sb are shifted to lower energies by about 8 - 9 eV when the element combines with oxygen. If we confine our discussion to the Sb,  $M_5 N_{4/5} N_{4/5}$  peak, which is identified at 446.9 eV in the Auger spectrum of  $Sb_2O_3$  and use some of the ideas discussed in Section 2.9 of Chapter 2, then the observed shift in the  $M_5 N_{4/5} N_{4/5}$  peak is given by

$$\Delta E_{M_5 N_{4/5} N_{4/5}} \text{ (observed)} = \Delta E_{M_5} - 2\Delta E_{N_{4/5}} + \Delta R_S, \quad \text{Eq. 8-1.}$$

Where  $\Delta E_{M_5}$  and  $\Delta E_{N_{4/5}}$  are the shifts in the binding energy of the  $M_5$  and  $N_{4/5}$  electrons.

Now an estimate of  $\Delta E_{M_5}$  is given by the photo electron measurements on antimony compounds due to Birchall et al (1975)<sup>194</sup> who found it to be 2.2 eV for  $Sb_2O_3$ . No data could be found on the shift of the  $N_{4/5}$  (4d) core level of Sb when it combines with oxygen, but data is available on the shift of the 3d ( $M_{4/5}$ ) core level of arsenic when it combines to form  $As_2O_3$ . The 3d level of As (binding energy 41.8 eV) and the 4 d level of Sb (binding energy 32 eV) can be regarded as being

in an equivalent configuration as far as chemical combination is concerned. Bahl et al (1976)<sup>206</sup> has measured a shift of 2.6 eV in the 3d level of As when it forms  $\text{As}_2\text{O}_3$  and if the approximation is made that there is a similar shift of the 4d level of Sb when it forms  $\text{Sb}_2\text{O}_3$ . Thus in Equation 8-1, as  $\Delta E_{M_{4/5}N_{2/3}N_{2/3}} = 8.2$  eV, then the static relaxation energy  $\Delta R_S = -5.2$  eV. That is to say the static relaxation energy has decreased by  $\approx 5$  eV relative to its value in pure antimony and as mentioned in Section 2.9 this is predominantly a change in extra-atomic relaxation energy as a consequence of the chemical combination with oxygen. The value deduced by Bahl et al for arsenic when it forms  $\text{As}_2\text{O}_3$  is  $\Delta R_S = -3.4$  eV, our value is probably a little high due to the approximations used.

The chemical shifts observed for the other peaks are similar so that the change in the relaxation energy is possibly the same and may be characteristic of antimony oxide, although further information is needed about core level shifts to test this suggestion.

#### 8.2.4 Electron Beam Effects in the Auger Spectra of $\text{Sb}_2\text{O}_3$

To study electron beam artifacts in the Auger spectra of  $\text{Sb}_2\text{O}_3$  an experiment was performed in which the  $M_{4/5}N_{4/5}N_{4/5}$  Auger peaks were recorded as a function of exposure time T, to the electron beam, whilst all other conditions were maintained constant. The results, recorded with an electron beam of 2 KeV energy and 50 $\mu$ A current, are shown in Figs. 8-8(a) and (b). The initial spectra at T = 0 was on a fresh part (i.e. not previously bombarded) of the antimony oxide film and the energies of the peaks were characteristic of  $\text{Sb}_2\text{O}_3$ . Changes were observed in the appearance of the spectra as a function of time and after 30 minutes exposure an additional peak became apparent, whose intensity grows with T. The position of this peak agrees well with the

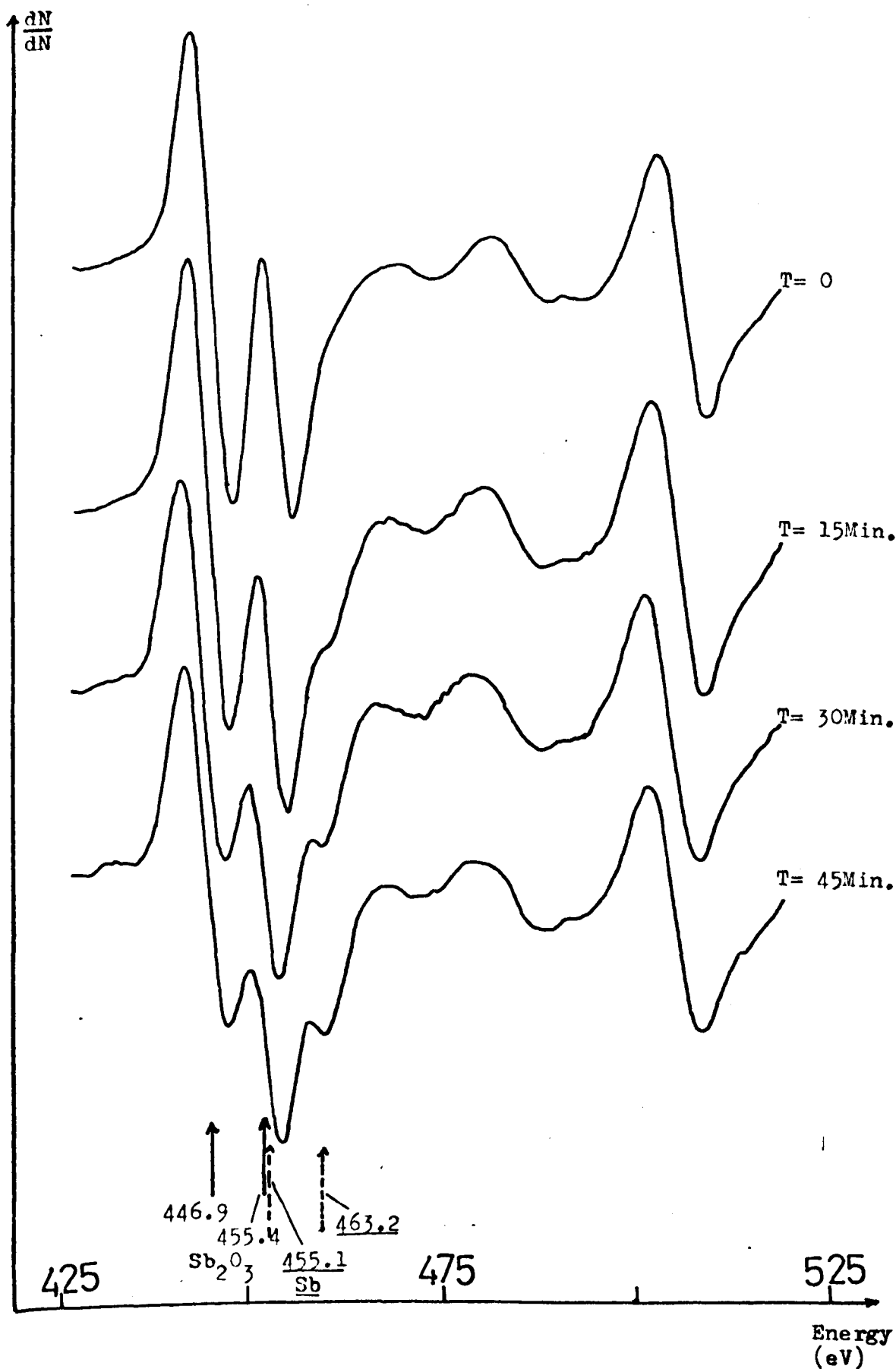


Fig.8-8(a). Electron Beam Effects In The Auger Spectra Of Antimony Oxide. The Spectra Are Recorded At Different Beam Exposure Times T.

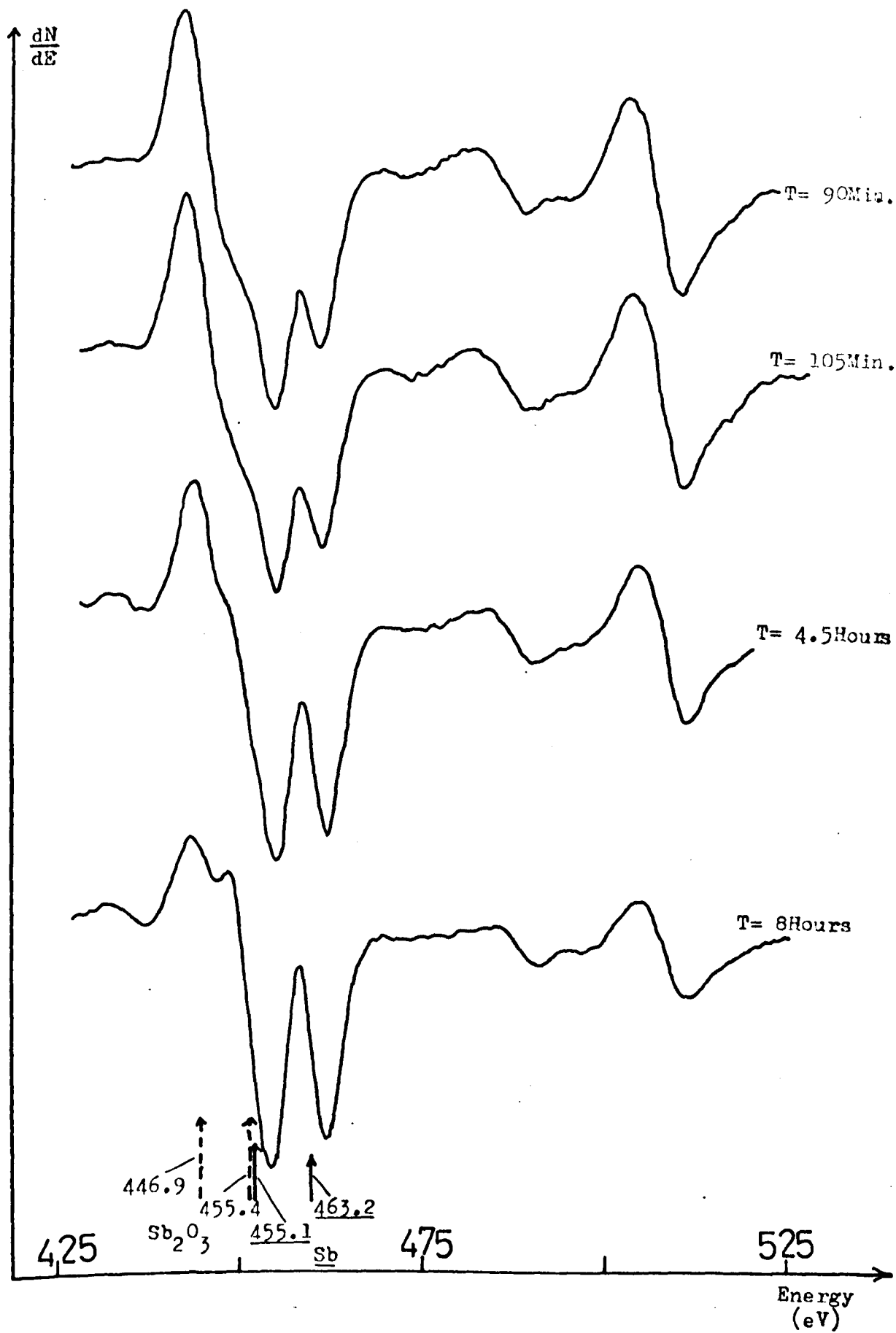
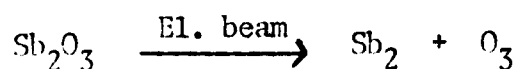


Fig.8-8(b). Continuation Of 8-8(a).

$M_4 N_{4/5} N_{4/5}$  transition observed from the Sb crystal. Eventually after bombardment of the  $Sb_2O_3$  surface with electrons for 8 hours, the two peaks observed were characteristic of a Sb single crystal although some influence due to the oxide could still be detected as shown in Fig. 8-8(b).

The electron beam is believed to be dissociating the antimony oxide:



So that with the time of exposure to the bombarding electrons the relative concentration of the antimony to the  $Sb_2O_3$  increases within the bombarded region and the Auger spectra recorded becomes more characteristic of Sb rather than  $Sb_2O_3$ . Some oxygen is thought to be desorbed from the surface as its Auger peak height relative to antimony peak height has decreased during bombardment.

As Auger spectrum of the surface in the energy range 0 - 700 eV, after such a long period of electron bombardment revealed no contamination due to sulphur or carbon and nor could the substrate Auger peaks of Molybdenum be detected.

### 8.2.5 Results and Discussion of the Energy Loss Spectra

The typical loss spectra from  $Sb_2O_3$  recorded with 300 eV and 500 eV primary electrons are shown in Figs. 8-9 and 8-10 and the spectra recorded with 1000 eV primary electrons is shown in Fig. 8-11. The losses observed from  $Sb_2O_3$  at different primary energies are summarised in Table 8-7, from which the mean values are obtained.

There were no optical measurements available in the energy range of interest to aid the identification of the observed losses of  $Sb_2O_3$ , nor could any previous energy loss measurements be discovered for antimony oxide. Electron beam effects, described later, were useful in

$\frac{dN}{dE}$  Spectra, Mod. 1.5V Pk-pk.  
 $I_p = 3\mu A$   
 Time Const.(T.C.) 1 Sec.

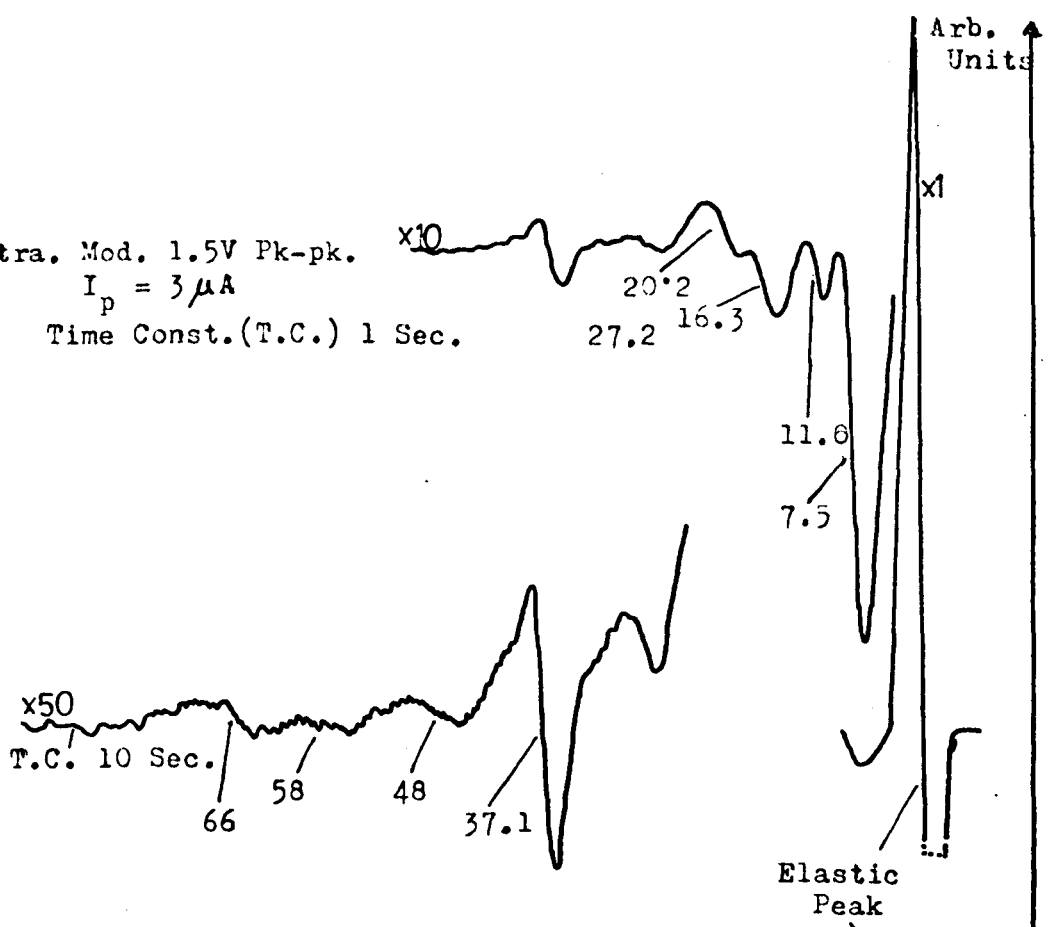
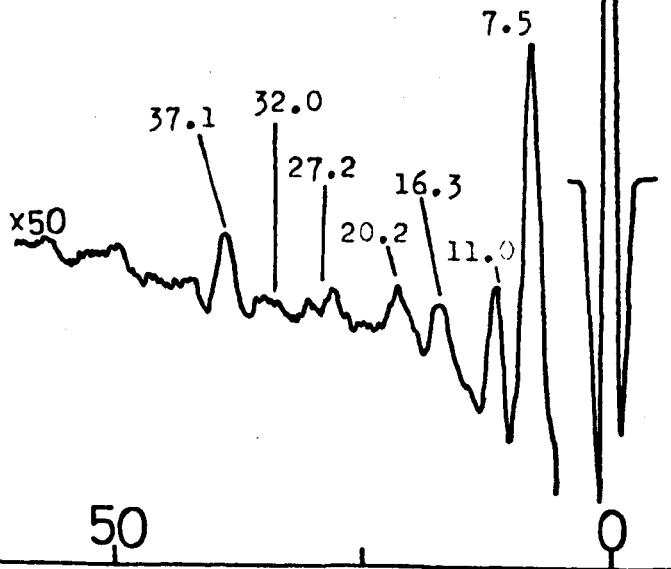


Fig.8-9. Energy Loss Spectra Of Antimony Oxide Excited With 300eV Electrons.

$\frac{d^2N}{dE^2}$  Spectra, Mod. 1.5V Pk-pk.  
 Time Const. 10 Sec.



100 50 0  
 ← Energy (eV)

Arb. Unit

$\frac{dN}{dE}$  Spectra, Mod. 2V Pk.-pk.  
Time Const. 1 Sec.  
 $I_p = 9 \mu A$

T.C. 10 Sec.

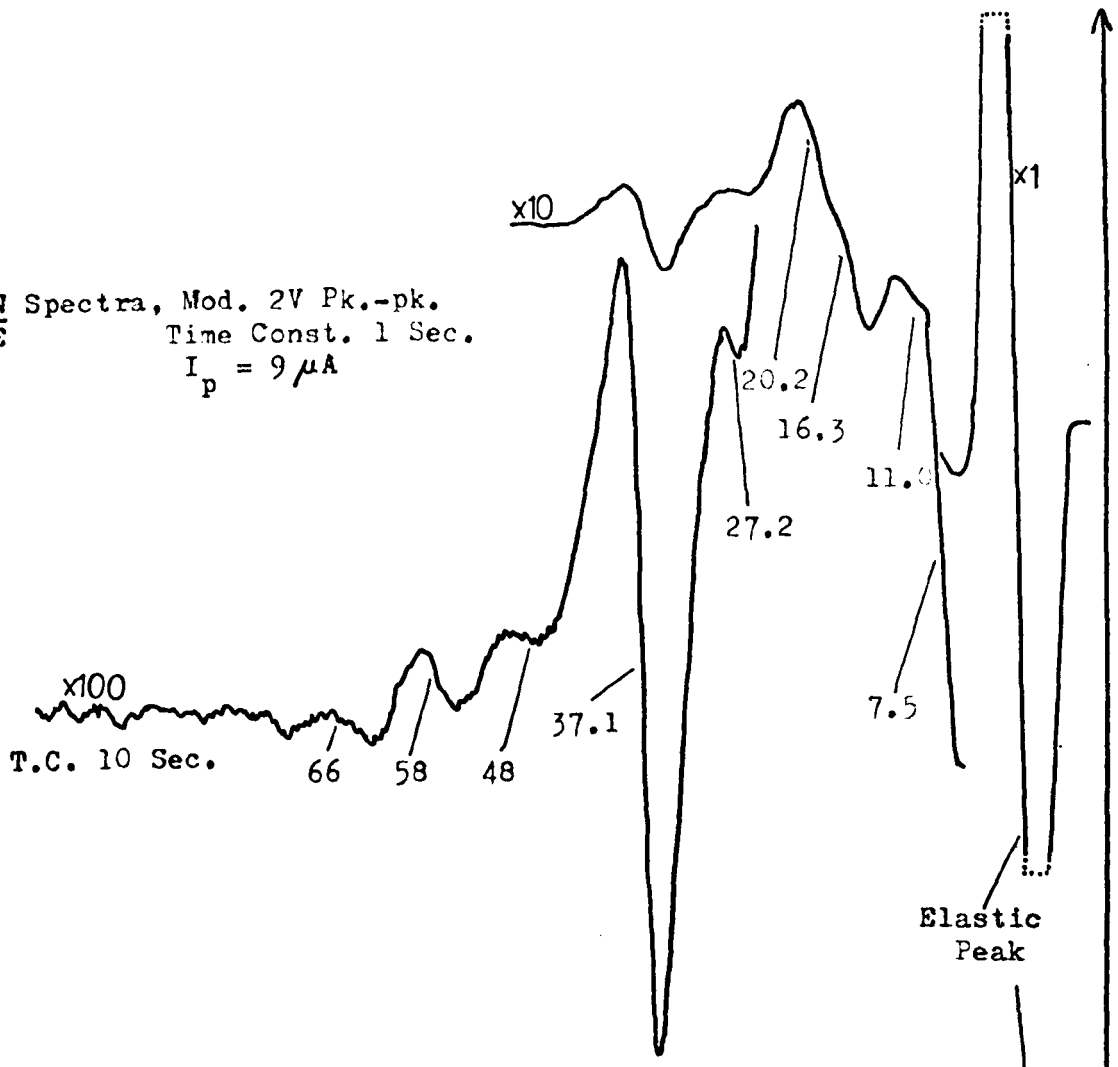


Fig.8-10. Energy Loss Spectra Of Antimony Oxide Excited With 500eV Electrons.

$\frac{d^2N}{dE^2}$  Spectra, Mod. 2V Pk-pk.  
Time Const. 10 Sec.

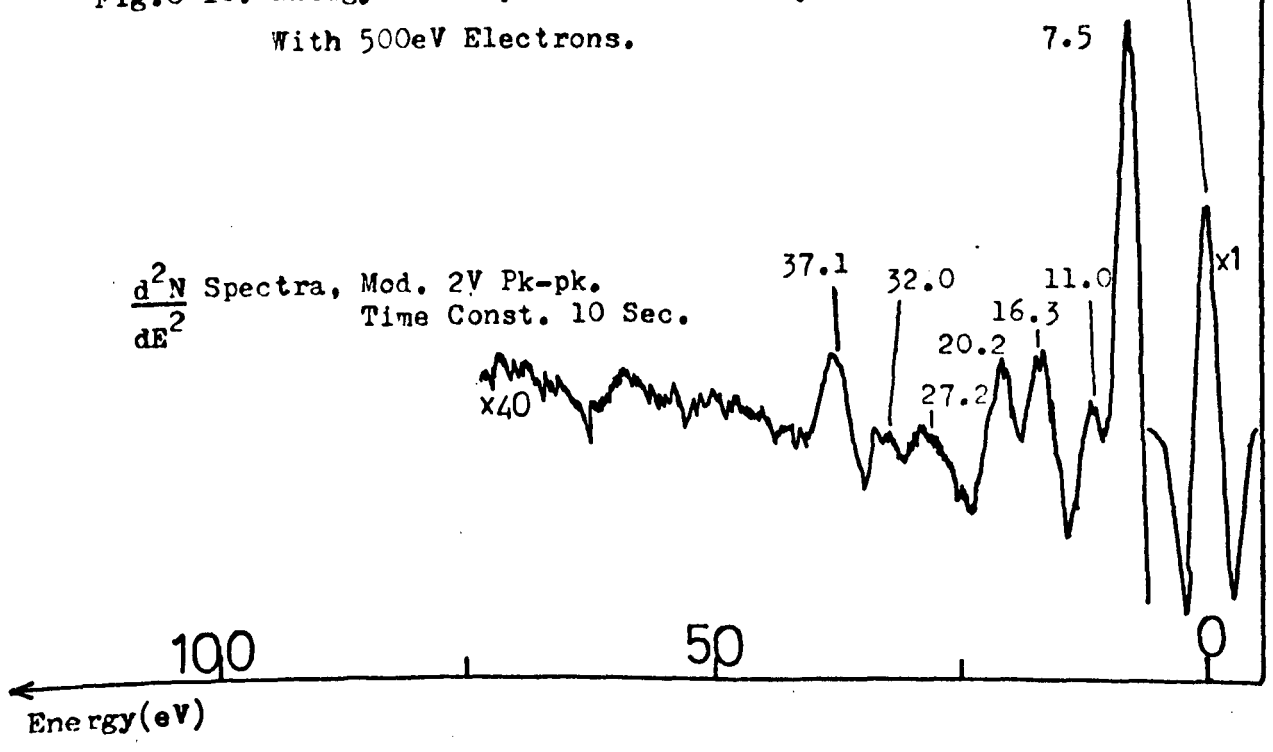


Fig.8-11. Energy Loss Spectra Of Antimony Oxide Excited  
With 1000eV Electrons.

$\frac{dN}{dE}$   
Arb.  
Units

$I_p = 14 \mu A$   
Mod. 3V Pk-pk.  
Time Const. 1 Sec.

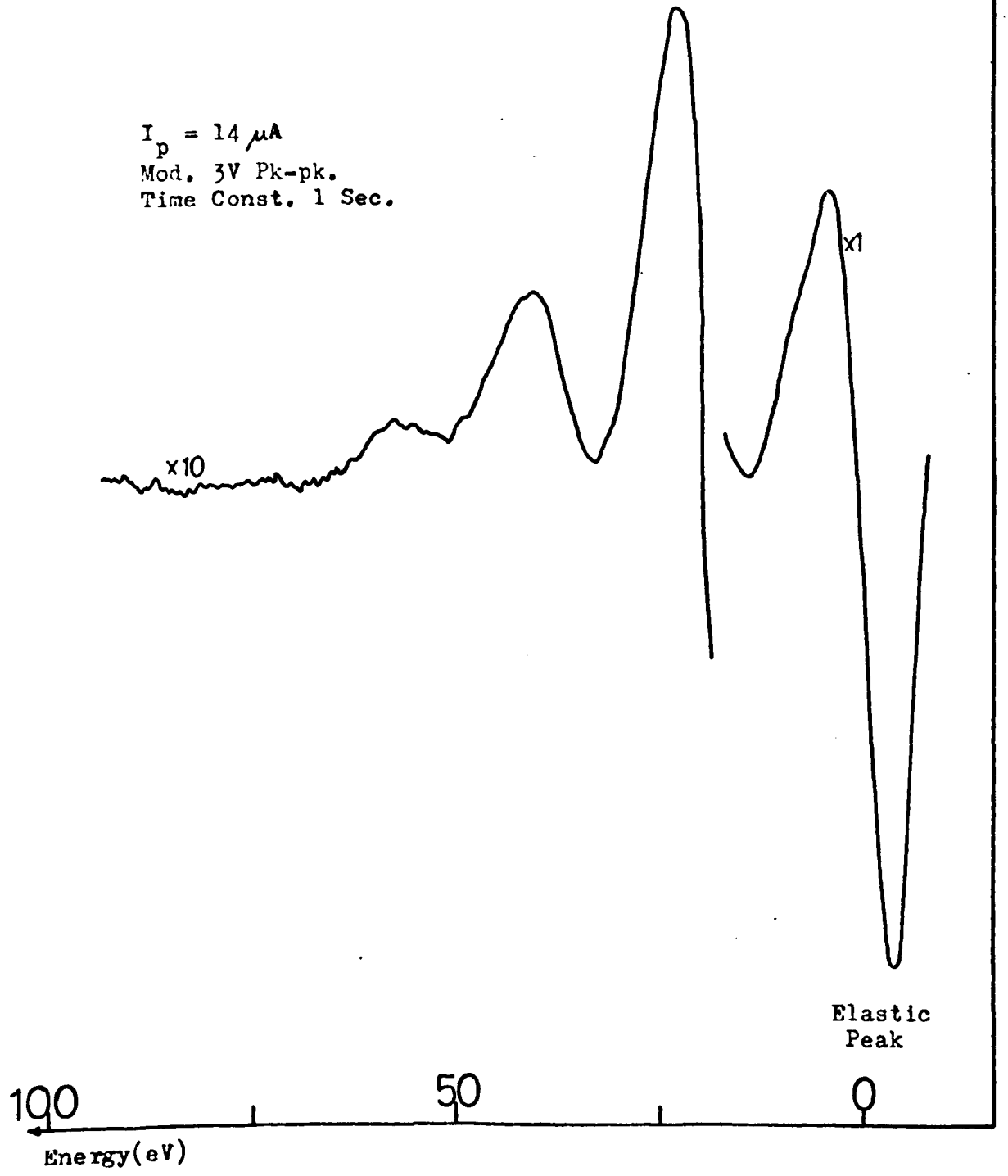


TABLE 8-7

THE OBSERVED LOSSES OF  $\text{SB}_2\text{O}_3$

<u><math>E_p</math> (eV)</u>	<u>Analysers</u>	<u>Observed Losses (eV)</u>								
	<u>Operation</u>	<u>Mode</u>								
500	$\frac{d^2N}{dE}$		7.4	10.8	16.1	19.8	27.2		36.9	
			8.0		16.5	20.4	28.7		37.4	
			7.6	11.6	16.5	20.4	28.1	31.7	37.2	
			7.5	11.2	16.0	19.8	27.6	31.6	36.7	
			7.4	10.0		20.1	27.0		37.1	48.7, 57.2 65.5
300	$\frac{d^2N}{dE}$		7.2	11.2	16.4	20.1	25.9	32.8	37.0	
			7.7	11.4	16.4	20.7	27.6		37.6	47.9, 59.1 67.5
Mean			7.5	11.0	16.3	20.2	27.2	32.0	37.1	
			$\pm 0.3$		$\pm 0.3$					
							48	58	66	

identifying the origin of the losses. If the loss spectra recorded from  $\text{Sb}_2\text{O}_3$  are compared with those recorded from the Sb crystal then it is clear that the intensity of the low energy feature, now measured at 7.5 eV has increased in intensity. This loss is still believed to be due to the excitation of antimony  $O_1$  electrons to states near the Fermi level, but the intensity has been increased by an additional contribution from the four oxygen  $L_{2/3}$  electrons which have a binding energy of 7 eV (Beardon and Barr)<sup>30</sup>, and which are also believed to be excited to the Fermi level.

The 11.0 eV and the 16.3 eV losses are identified as due to the surface (SP) and volume plasmon (VP) excitations of antimony, respectively. As already mentioned in the AES of  $\text{Sb}_2\text{O}_3$ , the primary electron beam is thought to have a dissociating effect on the oxide. Thus a reasonable explanation for the observation of the surface and volume plasmons of Sb from a  $\text{Sb}_2\text{O}_3$  surface may be that in the region under bombardment the electrons dissociate the top layers first from which the oxygen atoms are desorbed leaving behind a predominantly antimony layer, which will increase in thickness as bombardment is continued. The volume and surface plasmons of antimony are then excited in this layer and because the first monolayer is predominantly composed of antimony atoms the surface plasmon energy is characteristic of antimony rather than antimony oxide. The small differences in energy with the values obtained from pure antimony are probably due to a different packing density of the Sb atoms.

The valence band of antimony oxide is expected to be composed of the  $L_1$ ,  $L_{2/3}$  electrons of oxygen together with the  $O_1$  and  $O_{2/3}$  electrons of antimony, a total of 28 electrons per  $\text{Sb}_2\text{O}_3$  molecule. These are the electrons actively involved in the chemical bond formation of  $\text{Sb}_2\text{O}_3$  and by regarding these electrons as a free electron like gas in which

TABLE 8-8  
ASSIGNMENT OF THE LOSSES  
of  $Sb_2O_3$

<u>Loss (eV)</u>	<u>Assignment</u>
1) 7.5	{ $L_{2/3} \rightarrow$ Fermi level (O) $O_1 \rightarrow$ Fermi level (Sb)
2) 11.0	SP of Sb
3) 16.3	VP of Sb
4) 20.2	VP of $Sb_2O_3$
5) 27.2	(2) + (3)
6) 32.0	(2) + (4), 2 x (3)
7) 37.1	$N_{4/5} \rightarrow$ Fermi Level (Sb)
8) 48	3 x (3)
9) 58	$N_1 \rightarrow N_{2/3}$
10) 66	{ 4 x (3) $N_{2/3} \rightarrow N_{4/5}$ (Sb)

charge oscillations can be excited, a plasmon energy of 20.4 eV can be calculated in good agreement with the observed loss at 20.2 eV.

Multiples of this volume plasmon loss are believed to be excited by the 1000 eV primary electrons shown in Fig. 8-11. In this loss spectra up to 3 volume plasmon losses can be detected. This Fig. 8-11 should be compared with Fig. 8-5 (1000 eV loss spectra from Sb) in which 5 volumes plasmon losses are detected, this result possibly indicating that the possibility for plasmon excitation in  $\text{Sb}_2\text{O}_3$  is not as high as in Sb for 1000 eV primary electrons.

The 37.1 eV loss is identified as the excitation of  $N_{4/5}$  electrons to states near the Fermi level. This peak has a shape similar to the 34.1 eV peak in the loss spectra of Sb and the slight lowering of the binding energy is believed to be a chemical effect. Usually the binding energies of electrons in core levels are increased by a few electron volts when the (metal) atom forms a chemical bond, because charge is transferred from it to the non-metal atom. The observation of such chemical shifts has already been mentioned for the antimony  $M_4$ ,  $M_5$  levels (Section 8.2.3).

The remaining losses are identified as being due to primary electrons which have undergone multiple losses before emerging from the solid. The assignments are summarised in Table 8-8 and Fig. 8-12. The 58 eV feature was not observed in the loss spectra of Sb although it is identified as the excitation of the Sb,  $N_1 \rightarrow N_{2/3}$  electron transitions possibly due to the stronger volume plasmon losses in Sb in this energy range. Also in Table 8-8 peaks due to multiple antimony plasmon losses are identified whereas no peaks could be associated with multiple antimony oxide plasmon losses. Possibly in the depth of penetration of the primary beam the Sb/ $\text{Sb}_2\text{O}_3$  concentration ratio is significantly large due to the dissociation produced because the recording of the loss

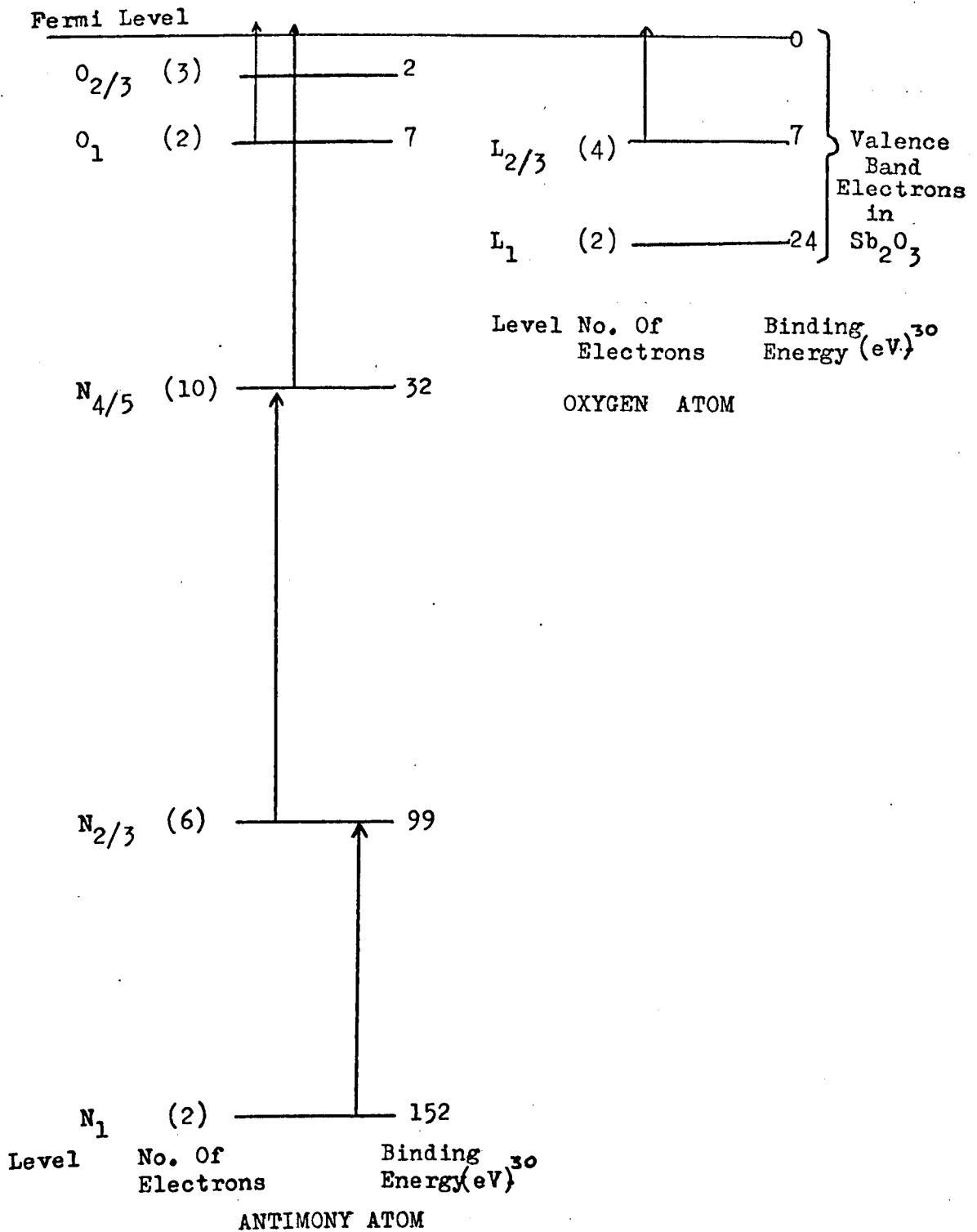


Fig.8-12. The Outer Electronic Levels Of Antimony And Oxygen Showing Possible Characteristic Losses.

spectra did require long scanning times of 15 - 30 minutes. Thus an electron is more likely to lose energy by exciting a Sb volume plasmon than a  $\text{Sb}_2\text{O}_3$  volume plasmon.

#### 8.2.6 Electron Beam Effects in the Loss Spectra

Electron beam effects in the loss spectra of antimony oxide were detected. These are shown in Fig. 8-13 where the loss spectra are recorded after an exposure time T to the electron beam, in the same way as the Auger spectra were recorded in Section 8.2.4.

The results obtained in Fig. 8-13 show that the 16.1 eV loss increases in strength at the expense of the 20.1 eV loss. This behaviour is consistent with the dissociation of the antimony oxide by the electron beam as deduced from the Auger measurements because as the Sb concentration increases its volume plasmon intensity would be expected to increase and this is indeed what is observed. Powell et al (1975)<sup>195</sup> has also recently used the increase in intensity of the volume plasmons of potassium and lithium to study the dissociation of KCl and LiF by impinging electrons.

One important observation of note is that the Auger spectrum, in which primary currents of 50 $\mu\text{A}$  were used, revealed electron beam effects after approximately 15 - 30 minutes of bombardment, whereas in the characteristic loss spectra recorded with lower primary currents ( $\sim 10\mu\text{A}$ ), a peak due to the volume plasmon of Sb could always be detected. The reason for this effect is not clear but it is possible that during the deposition of the thin film two intermingled phases are formed i.e. the thin evaporated film consists of  $\text{Sb}_2\text{O}_3 + \text{Sb}$ , although predominantly a  $\text{Sb}_2\text{O}_3$  phase. Alternatively electron beam effects occur much more rapidly than indicated by AES, so that as soon as the beam is switched on, significant dissociation of the oxide films has occurred for volume

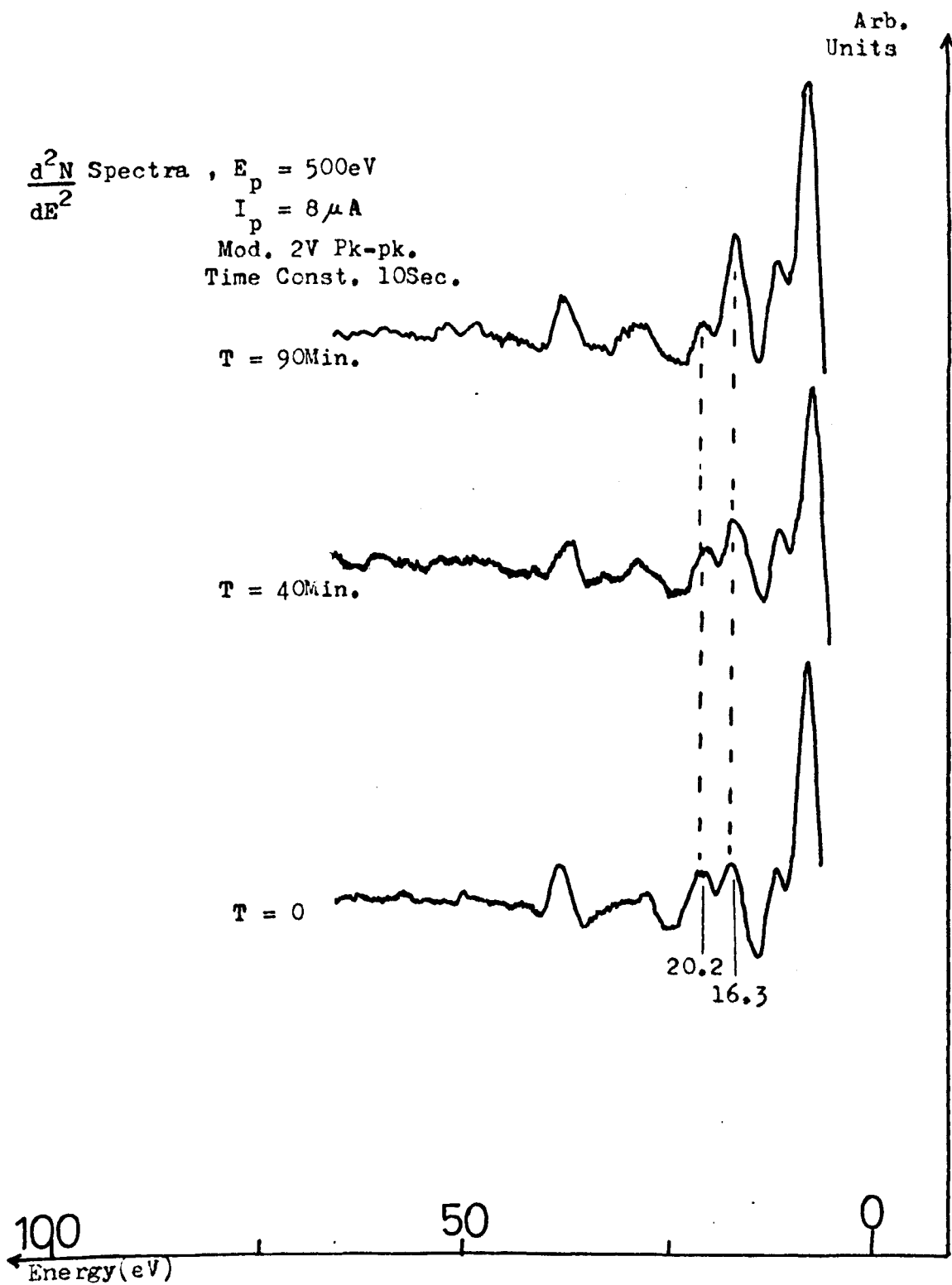


Fig.8-13. The Changes In The Energy Loss Spectra Of  $\text{Sb}_2\text{O}_3$   
 With Beam Exposure T.

plasmons characteristic of Sb to be observed in the energy loss spectra.

The results obtained indicate that CELS may be a more sensitive technique for the detection of two phases in a thin film. From the measurements recorded on the  $\text{Sb}_2\text{O}_3$  surface the initial AES spectra indicated the presence of pure oxide only whereas the initial CELS spectra indicated the presence of antimony element as well as the oxide. The study of thin films may potentially be a useful application for CELS, certainly the information obtained will complement the Auger spectroscopy particularly about the chemical state of the surface.

### 8.3 Antimony Sulphide

#### 8.3.1 Introduction

As a part of the programme to study chemical effects the Auger and characteristic loss spectra of antimony sulphide were obtained. Antimony sulphide ( $\text{Sb}_2\text{S}_3$ ) is another simple compound of Sb and one reason for investigating its surface was to see if it behaved in the same way as antimony oxide, ( $\text{Sb}_2\text{O}_3$ ).

#### 8.3.2 Experimental

An antimony sulphide surface was prepared by the same method as the antimony oxide surface, that is by evaporating from a molybdenum boat on to a clean polished molybdenum substrate. The antimony sulphide was obtained in chip form from BDI<sup>193</sup> and these were ground to a powder before placing into an outgassed Mo boat. The sulphide was slowly evaporated by heating the boat to a temperature between 300 - 500°C, as recommended, and a thin film deposited on to the molybdenum substrate in

a UHV environment. Auger spectra were recorded periodically to confirm the growth of the sulphide film and evaporation was continued until a sufficiently thick film, absent of any substrate influences, had been prepared. The evaporated film had a glassy appearance and care had to be exercised not to evaporate too thick a film as then surface charging became so acute during electron bombardment that Auger spectra could not be satisfactorily recorded.

### 8.3.3 Results and Discussion of the Auger Spectra from $Sb_2S_3$

The Auger spectrum from a  $Sb_2S_3$  evaporated thin film is shown in Fig. 8-14 and the antimony Auger peaks are shown in more detail in Fig. 8-15. The signal to noise ratio in the Auger spectrum was not as good as obtained from a clean, polished antimony surface and a small amount of impurity chlorine, probably originating from the  $Sb_2S_3$  powder, was detected on the surface as evidenced by the  $Cl_{1s}, L_{2/3}^M, M_{2/3}^M$  Auger peak at 181 eV. No other contaminants were observed.

As seen in Fig. 8-14 the antimony Auger peaks from  $Sb_2S_3$  are observed at higher energies than the same peak from pure antimony. The amount of the shift to higher energies depended on the thickness of the antimony sulphide film, for the thicker films the shift was greater. This shift is believed to be due to negative surface charging of the antimony sulphide film, so that with an increasing thickness there is a greater negative charge stored in the surface region and hence the greater is the shift in the Auger peak position. For "thick" films, Auger peaks could not be observed due to the surface charging and the glassy antimony sulphide film was observed to "crack up" under the impact of the primary electron beam.

It is difficult to be quantitative about the thickness of the antimony sulphide films prepared as no thickness monitor was used. The

a UHV environment. Auger spectra were recorded periodically to confirm the growth of the sulphide film and evaporation was continued until a sufficiently thick film, absent of any substrate influences, had been prepared. The evaporated film had a glassy appearance and care had to be exercised not to evaporate too thick a film as then surface charging became so acute during electron bombardment that Auger spectra could not be satisfactorily recorded.

### 8.3.3 Results and Discussion of the Auger Spectra from $Sb_2S_3$

The Auger spectrum from a  $Sb_2S_3$  evaporated thin film is shown in Fig. 8-14 and the antimony Auger peaks are shown in more detail in Fig. 8-15. The signal to noise ratio in the Auger spectrum was not as good as obtained from a clean, polished antimony surface and a small amount of impurity chlorine, probably originating from the  $Sb_2S_3$  powder, was detected on the surface as evidenced by the  $Cl, L_3^M, 2/3 M_{2/3}$  Auger peak at 181 eV. No other contaminants were observed.

As seen in Fig. 8-14 the antimony Auger peaks from  $Sb_2S_3$  are observed at higher energies than the same peak from pure antimony. The amount of the shift to higher energies depended on the thickness of the antimony sulphide film, for the thicker films the shift was greater. This shift is believed to be due to negative surface charging of the antimony sulphide film, so that with an increasing thickness there is a greater negative charge stored in the surface region and hence the greater is the shift in the Auger peak position. For "thick" films, Auger peaks could not be observed due to the surface charging and the glassy antimony sulphide film was observed to "crack up" under the impact of the primary electron beam.

It is difficult to be quantitative about the thickness of the antimony sulphide films prepared as no thickness monitor was used. The

$\frac{dN}{dE}$  Arb. Units

$E_p = 2.5 \text{ KeV}$   
 $I_p = 20 \mu\text{A}$   
Mod. 3V Pk-pk.  
Time Const. 1Sec.

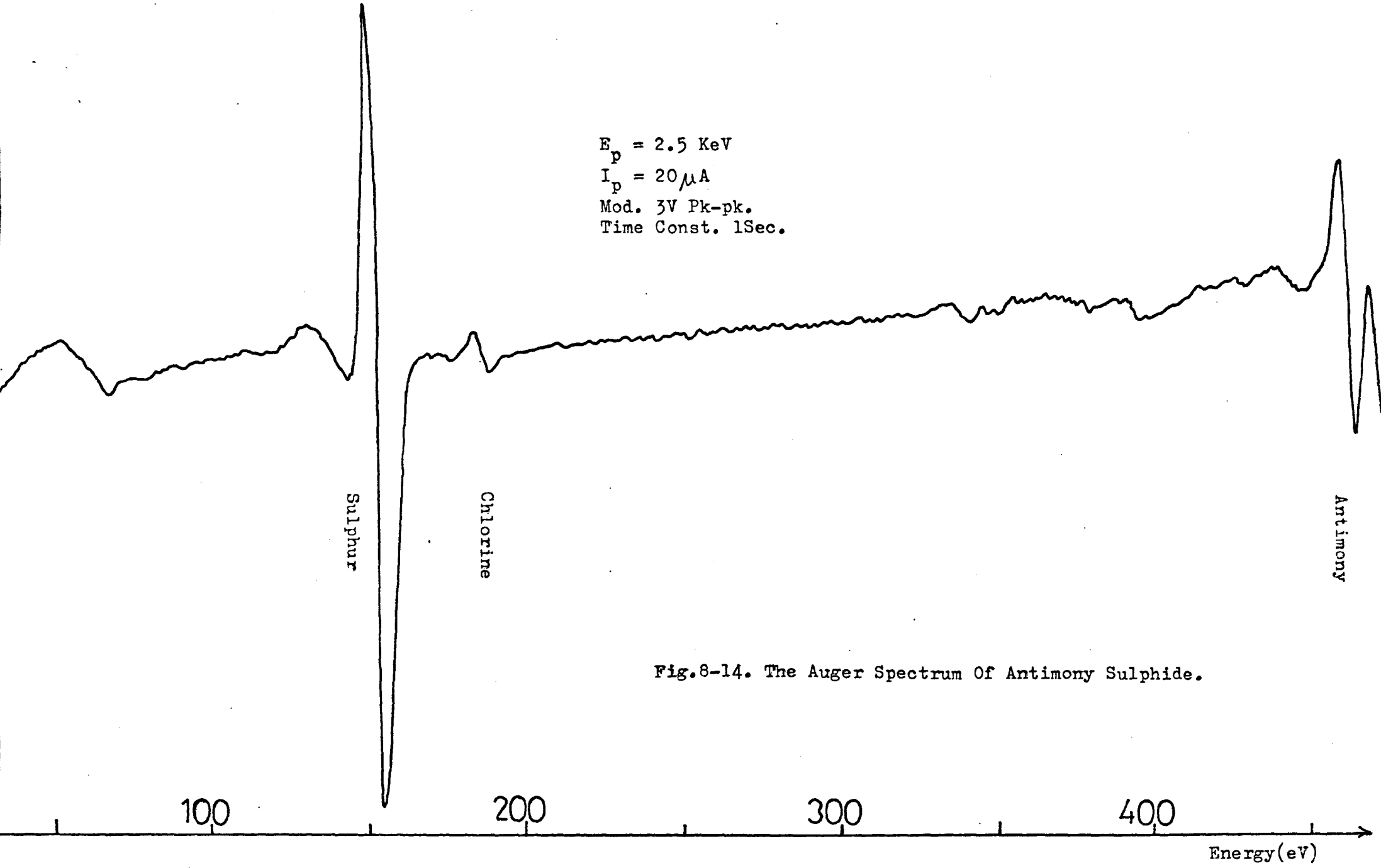


Fig.8-14. The Auger Spectrum Of Antimony Sulphide.

$\frac{dN}{dE}$  Pk.Ht.  
Arb. Units

$E_p = 2.5 \text{ KeV}$   
 $I_p = 35 \mu\text{A}$   
Mod. 3V Pk-pk.  
Time Const. 1 Sec.

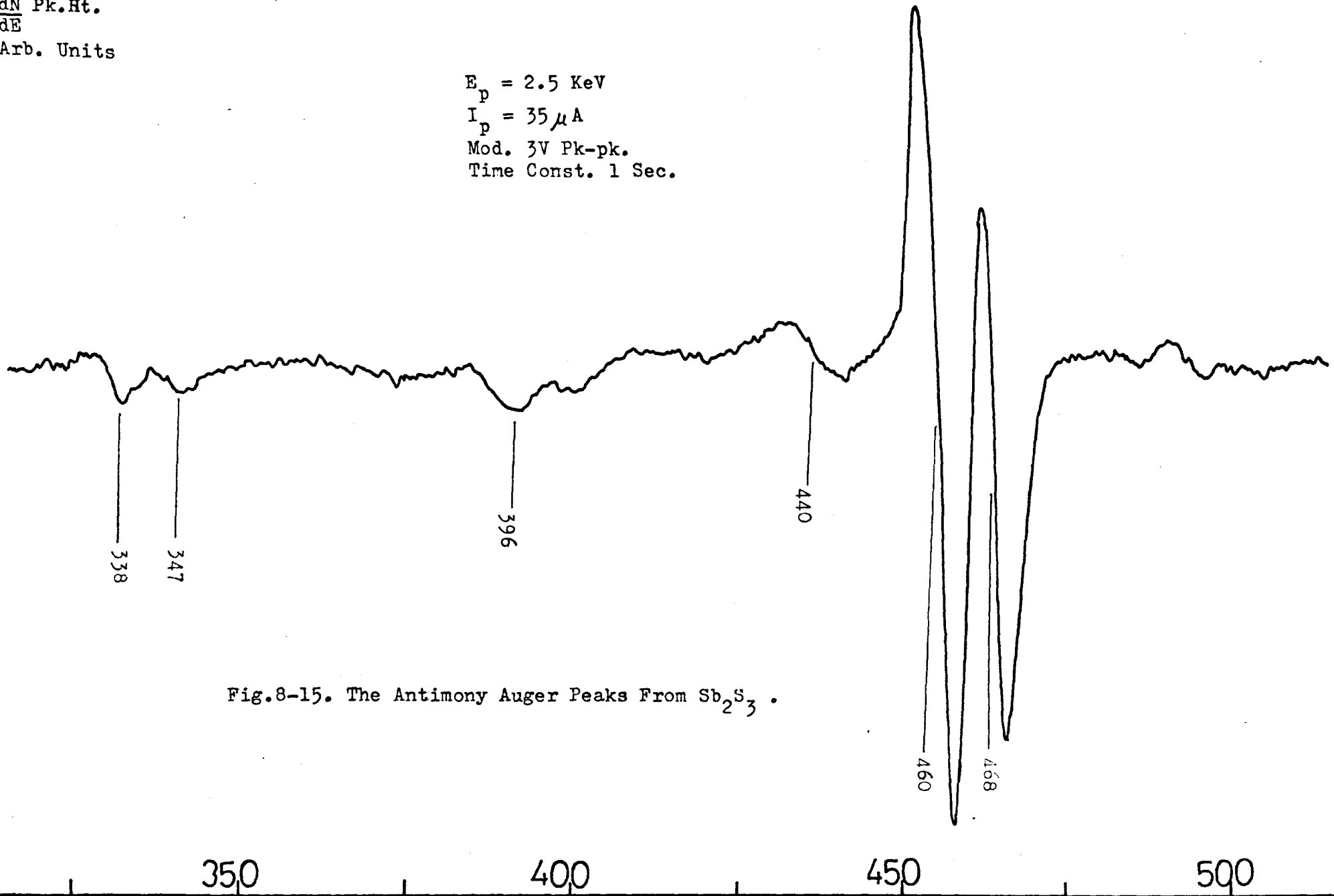


Fig.8-15. The Antimony Auger Peaks From  $\text{Sb}_2\text{S}_3$ .

Energy (eV)

TABLE 8-9

OBSERVED PEAKS FROM  $Sb_2S_3$  (eV)

Present Work (eV)

157	S	$L_{2/3}$ $M_{2/3}$ $M_{2/3}$	(150eV in Mo spectra)
338	Sb (333.5)	)	$M_5$ $N_1$ $N_{4/5}$
347	Sb (341.7)	)	$M_4$ $N_1$ $N_{4/5}$
396	Sb (388)		$M_{4/5}$ $N_{2/3}$ $N_{4/5}$
440	Plasmon loss	on	$M_5$ $N_{4/5}$ $N_{4/5}$
460	Sb (455.1)		$M_5$ $N_{4/5}$ $N_{4/5}$
468	Sb (463.2)		$M_4$ $N_{4/5}$ $N_{4/5}$

spectra presented here are from a film of sufficient thickness so that substrate influences are negligible but not so thick that Auger spectra could be not recorded from them.

The Auger spectra recorded in Figs. 8-14 and 8-15 are from a suitable antimony sulphide film and the energy positions of the observed peaks are summarised in Table 8-9 together with the origin of the observed peaks. The energy values quoted for the antimony peaks in Table 8-9 are from the single crystal results. The peak at 440 eV is identified as a plasmon loss of the  $M_5 N_{4/5} N_{4/5}$  electrons as they exit from the solid, it is later shown that the volume plasmon energy of  $Sb_2S_3 \approx 20\text{eV}$ .

In most of the spectra recorded from the antimony sulphide surface the ratio of the sulphur  $L_{2/3}$  MM peak height to the antimony  $M_5 N_{4/5} N_{4/5}$  peak height was approximately 2:1, although some spectra were recorded in which the ratio was greater, eg. Fig. 8-14.

#### 8.3.4 Electron Beam Effects

Considerable electron beam effects had been detected in the Auger spectrum of antimony oxide, so a similar experiment was performed to observe the effect of electron bombardment on the Auger spectra from  $Sb_2S_3$ . The  $M_{4/5} N_{4/5} N_{4/5}$  Auger peaks of antimony and the  $L_{2/3} M_{2/3} M_{2/3}$  Auger peak of sulphur were monitored as function of beam exposure and the results are shown in Fig. 8-16. During the experiment the pressure within the chamber increased to  $5 \times 10^{-8}$  Torr from an initial ultra high vacuum and subsequently decreased when the electron beam was switched off indicating that desorption stimulated by the electron beam was occurring from the antimony sulphide surface.

As can be seen in Fig. 8-16 the peaks are gradually shifting downwards in energy with beam exposure. No appearance of new peaks characteristic of elemental antimony could be detected although the peaks

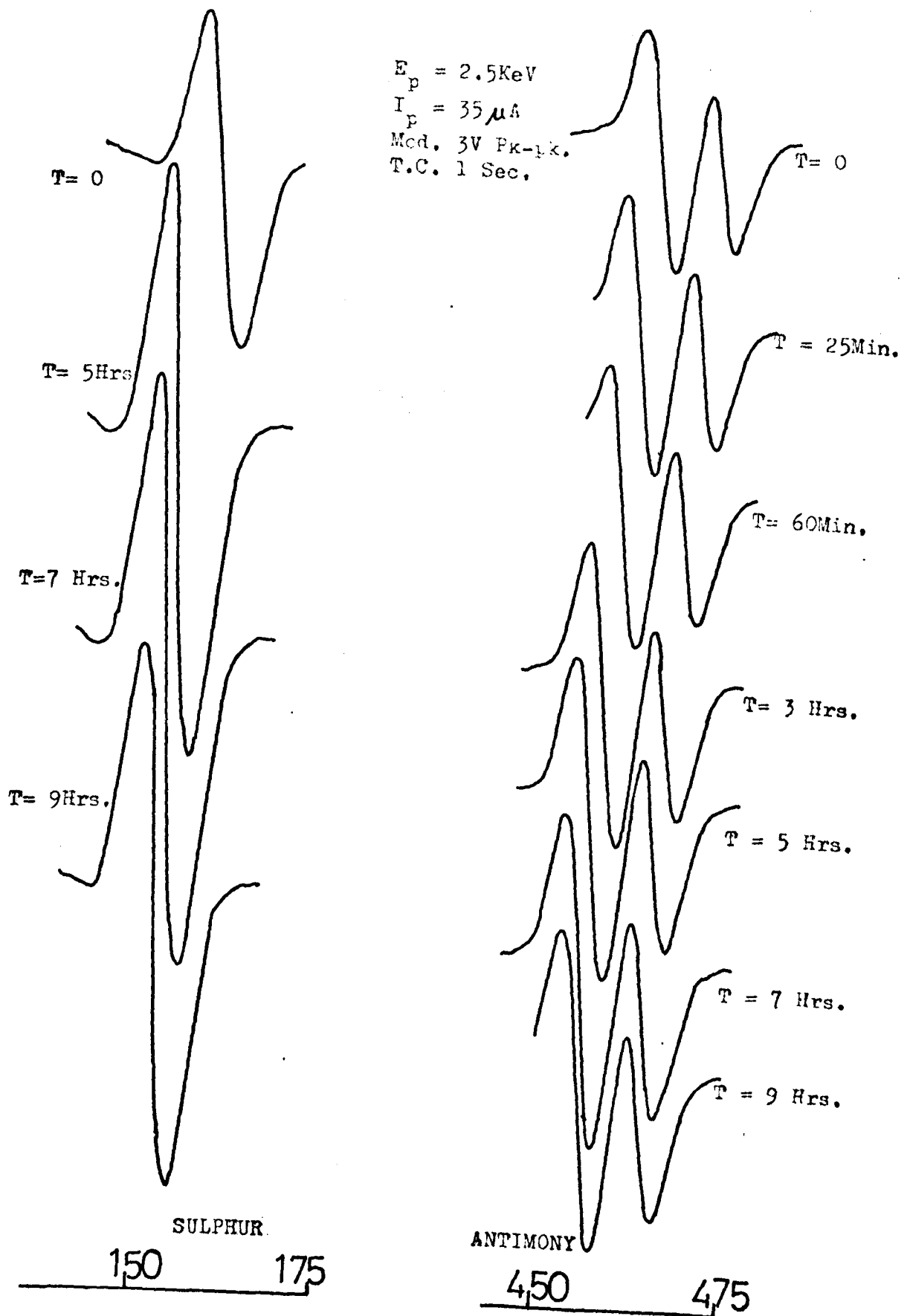


Fig.8-16. The Change In Position Of The S(150eV) And Sb( $\sim$ 450) Peaks From  $\text{Sb}_2\text{S}_3$  -With Beam Exposure T.

in Fig. 8-16 have shifted to such an extent that after five hours bombardment the energies are almost characteristic of the pure elements.

It is thought that the electron beam is adsorbing entire molecules of  $\text{Sb}_2\text{S}_3$  from the surface, thus gradually decreasing the thickness of the evaporated film and increasing the pressure within the chamber. The ratio of the sulphur  $L_{2/3} M_{2/3} M_{2/3}$  peak height to the antimony  $M_5 N_{4/5} N_{4/5}$  peak height also remained constant at approximately 2 during electron bombardment, indicating no preferential desorption of antimony or sulphur was occurring. As the film thickness decreases it stores less charge in its surface region so that the peak shift gradually decreases.

The antimony Auger peaks from  $\text{Sb}_2\text{S}_3$  are expected to be at energies below the values from elemental Sb by analogy with antimony oxide. In fact the antimony Auger peaks from  $\text{Sb}_2\text{S}_3$  are observed at higher energies and even after about 5 hours of bombardment, as shown in Fig. 8-16, the energy of the antimony peak did not fall below their value from elemental Sb. Further bombardment for 4 hours produced no detectable change in the position of the Sb peaks. It is possible that an equilibrium has developed due to molecules diffusing from the unbombarded surface to the region of the surface under the impact of the electron beam effectively maintaining a constant thickness of film and thus a constant fixed energy for the Auger peaks. It is noteworthy that the interaction of the electron beam with the  $\text{Sb}_2\text{S}_3$  thin film is of a different character than the interaction of the electron beam with the  $\text{Sb}_2\text{O}_3$  film as evidenced by the Figs. 8-16 and 8-8.

### 8.3.5 Results and Discussion of the Energy Losses of $Sb_2S_3$

The energy losses of  $Sb_2S_3$  were recorded with 300 eV and 500 eV primary electrons in the first derivative (500 eV only) and the second derivative mode of operation of the spectrometer. The losses were recorded from a freshly evaporated suitable film surface of  $Sb_2S_3$  on which the AES results indicated minor contamination due to chlorine, as shown in Fig. 8-14.

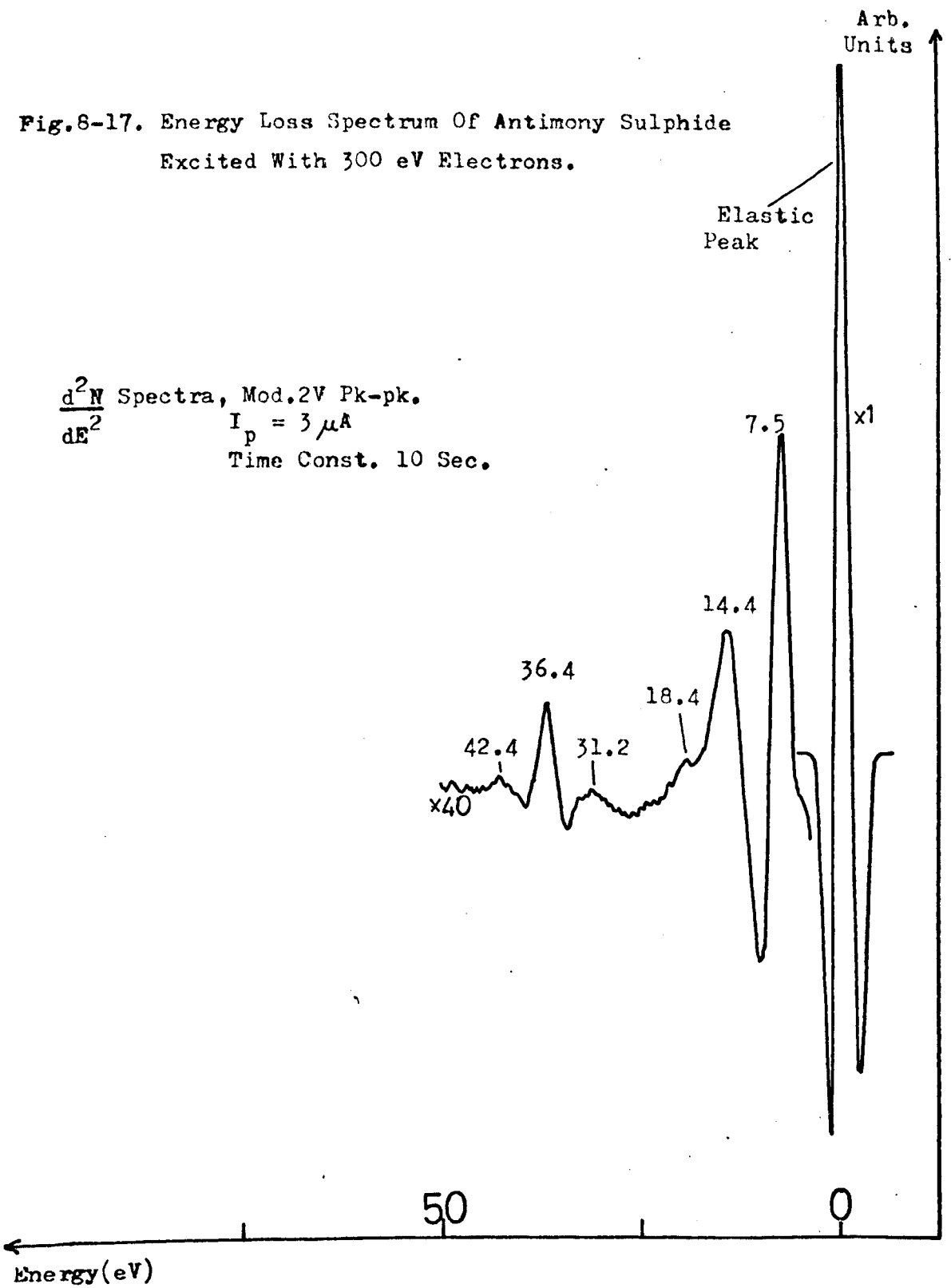
The typical loss spectra observed are shown in Figs. 8-17 and 8-18 and the energies of the observed losses are summarised in Table 8-10. Only one previous measurement of the characteristic losses of  $Sb_2S_3$  could be discovered and that was by Leder and Marton (1954)<sup>109</sup> who obtained their values by transmission of 30 KeV electrons through thin films. Their results are also summarised in Table 8-11 for comparison.

The antimony sulphide losses originate from the same phenomenon as the losses of Sb and  $Sb_2O_3$ . There were no optical measurements available to aid the identification of the observed losses. The 7.5 eV loss is believed to be due to the excitation of the  $O_1$  electrons of Sb and  $M_{2/3}$  electrons of sulphur to empty states close to Fermi level, as shown in Fig. 8-19. This loss has increased in relative intensity when it is compared with the 6.6 eV loss of Sb crystal due to the additional contribution of the 4 sulphur electrons having a binding energy of about 8 eV.

The 18.4 eV loss is thought to be due to volume plasmon oscillations of the valence band electrons of  $Sb_2S_3$ . The valence band electron density is composed of 5 electrons from each Sb atom and 6 electrons from each sulphur atom, a total of 28 electrons per  $Sb_2S_3$  molecule. The plasmon energy for free electron like oscillations is calculated to be 17.8 eV in good agreement with the observed value.

The origin of the 14.4 eV loss is not clear. In the loss spectra

Fig.8-17. Energy Loss Spectrum Of Antimony Sulphide  
Excited With 300 eV Electrons.



$\frac{dN}{dE}$  Spectra. Mod. 2V Pk-pk.  
 Time Const. 1 Sec.  
 $I_p = 8 \mu A$

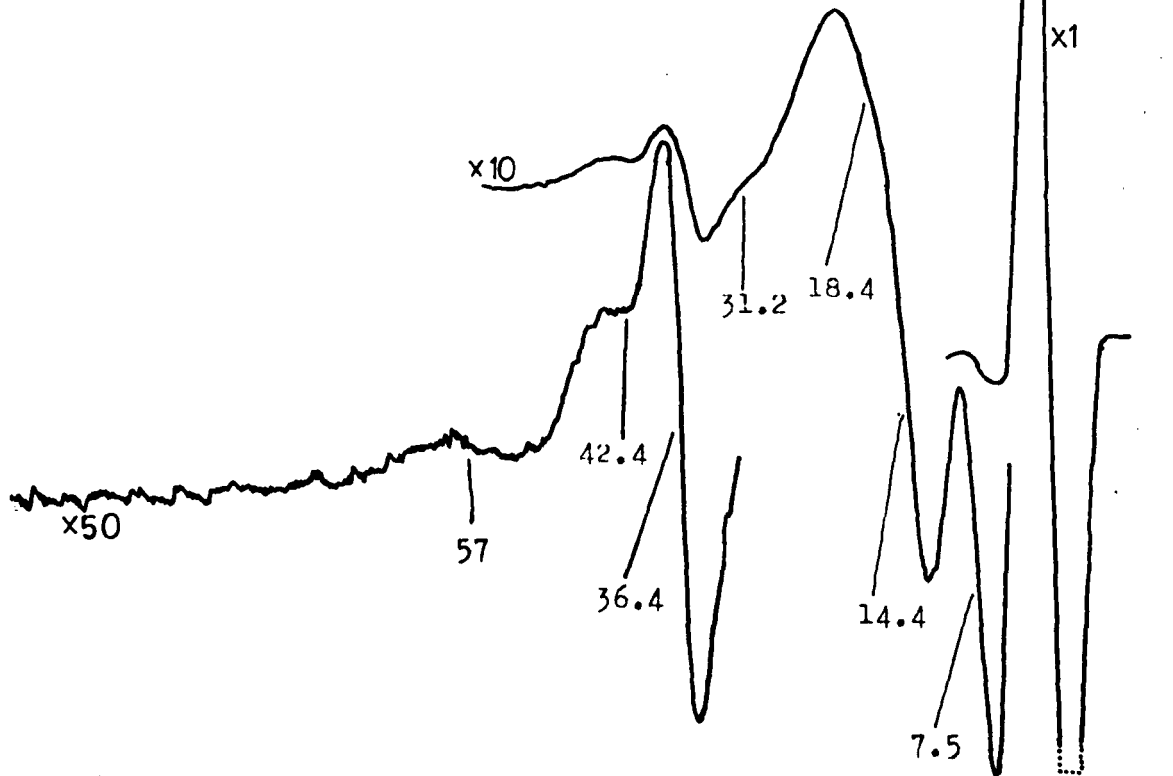


Fig.8-18. Energy Loss Spectra Of Antimony Sulphide  
 Excited With 500eV Electrons.

$\frac{d^2N}{dE^2}$  Spectra, Mod. 2V Pk-pk.  
 Time Const. 10 Sec.

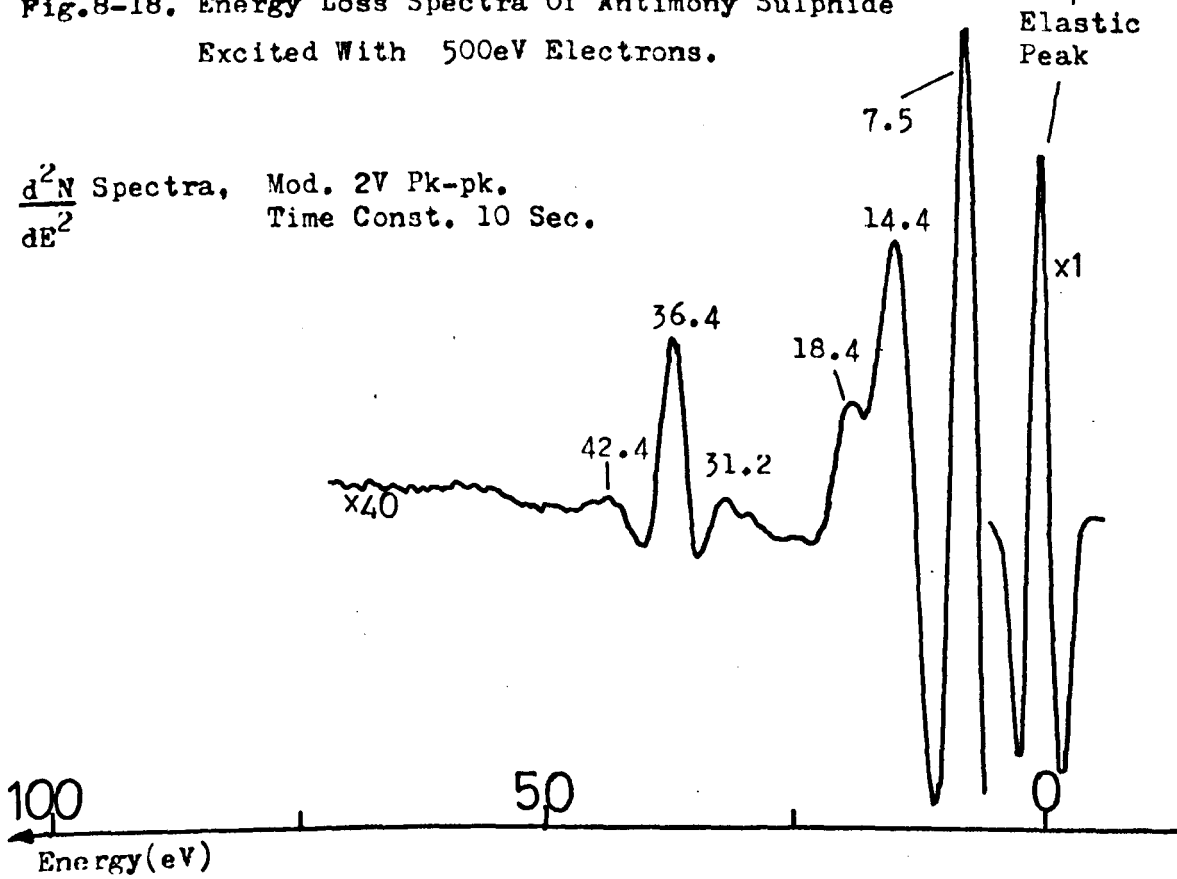


TABLE 8-10  
OBSERVED LOSSES OF  $Sb_2S_3$

<u>Ep (eV)</u>	<u>Analyser Operation Mode</u>	<u>Observed Losses (eV)</u>						
500	$\frac{d^2N}{dE}$	7.2	14.1	18.4	31.3	36.1	42.2	
		7.4	15.0	17.7	30.1	36.3	42.4	
		7.7	14.2	18.0	31.4	36.3		
		7.5	14.3	18.8	31.1	36.1	41.8	
		7.4	14.6	18.6	31.4	36.8	43.6	
		7.7	14.2	18.1	31.7	36.3	42.8	
		7.4	14.5	18.7	31.5	36.5		
	dN/dE					41.2	57	
300	$\frac{d^2N}{dE}$	7.4	14.7	18.8	31.0	36.4	42.2	
<b>Mean Values (eV)</b>		7.5 ± 0.2	14.4 ± 0.2	18.4 ± 0.3	31.2 ± 0.4	36.4 ± 0.3	42.4 ± 0.5	57

it is observed as a relatively strong feature and its energy is slightly higher than the calculated surface plasmon energy (13.0 eV). Additionally it is probably not to be associated with the presence of a Sb phase in the evaporated film as its intensity did not change with beam exposure, nor is it associated with a sulphur phase, in the evaporated film, whose plasmon energy is calculated to be 18.4 eV (on the basis of all 6 outer electrons undergoing oscillations). Further information especially from optical measurements is needed for an identification of this feature.

The 36.4 eV loss peak agrees in shape with the 37.1 eV loss peak of  $\text{Sb}_2\text{O}_3$  and the 341 eV loss peak of Sb so that it is identified as the excitation of  $N_{4/5}$  electrons to empty states close to the Fermi level. The increase in binding energy of the  $N_{4/5}$  electrons has occurred due to the chemical bonding with sulphur. The transfer of outer electrons from the antimony atom to the sulphur atom has effectively increased the influence of the ion core on the remaining electrons of the Sb ion, resulting in higher binding energies for them.

The 57 eV loss is identified as being due to the excitation of  $N_1$  electrons to the  $N_{2/3}$  level by the primary beam. The remaining losses are interpreted as being due to multiple loss processes and their assignments are summarised in Table 8-11. Some of the losses are identified on the energy level diagram of Fig. 8-19.

The effect of electron beam bombardment on the characteristic losses was studied by carrying out an experiment similar to the one performed on antimony oxide. No electron beam effects could be detected in the loss spectra after two hours of bombardment and so the experiment was discontinued at this stage.

TABLE 8-11

ASSIGNMENT OF THE CHARACTERISTIC LOSSES OF  $Sb_2S_3$

<u>Present Work</u> (eV)	<u>Leder &amp; Marton<sup>109</sup></u> (1954)	<u>Assignment</u>
1) 7.5	6.3	$O_1 \rightarrow$ Fermi Level (Sb)
		$M_{23} \rightarrow$ Fermi Level (S)
2) 14.4		?
3) 18.4	18.0	VP of $Sb_2S_3$
4) 31.2		(2) + (3)
5) 36.4	35.4	$N_{4/5} \rightarrow$ Fermi Level (Sb)
6) 42.4		(5) + (1)
7) 57.0		$N_1 \rightarrow N_{2/3}$ (Sb)

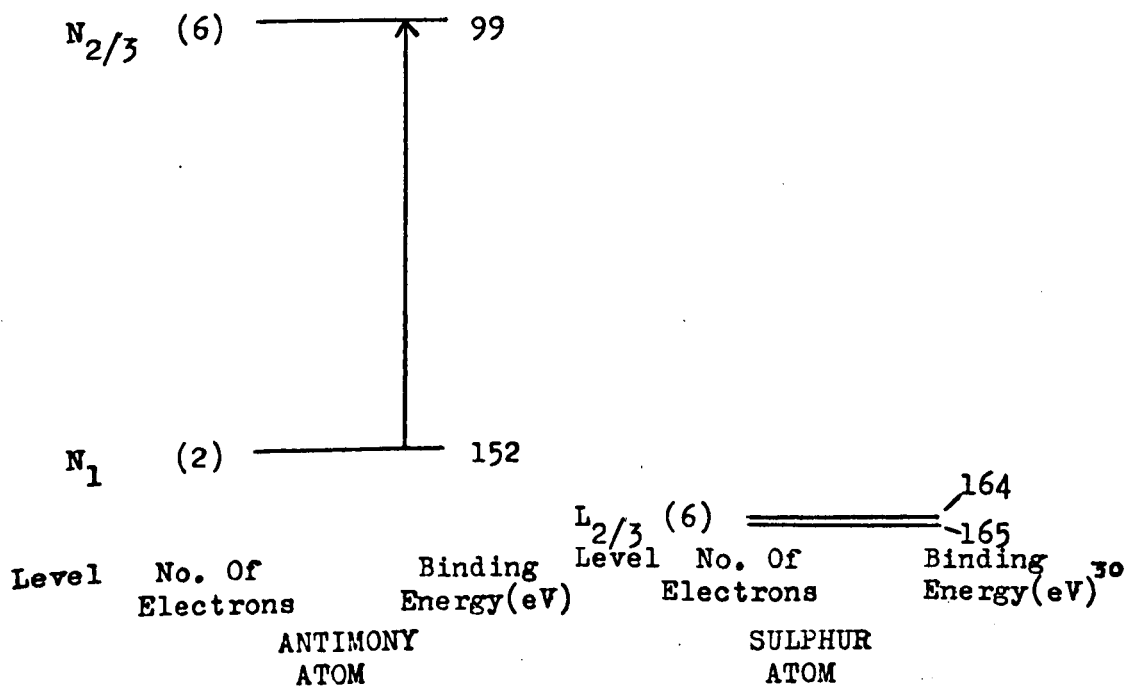
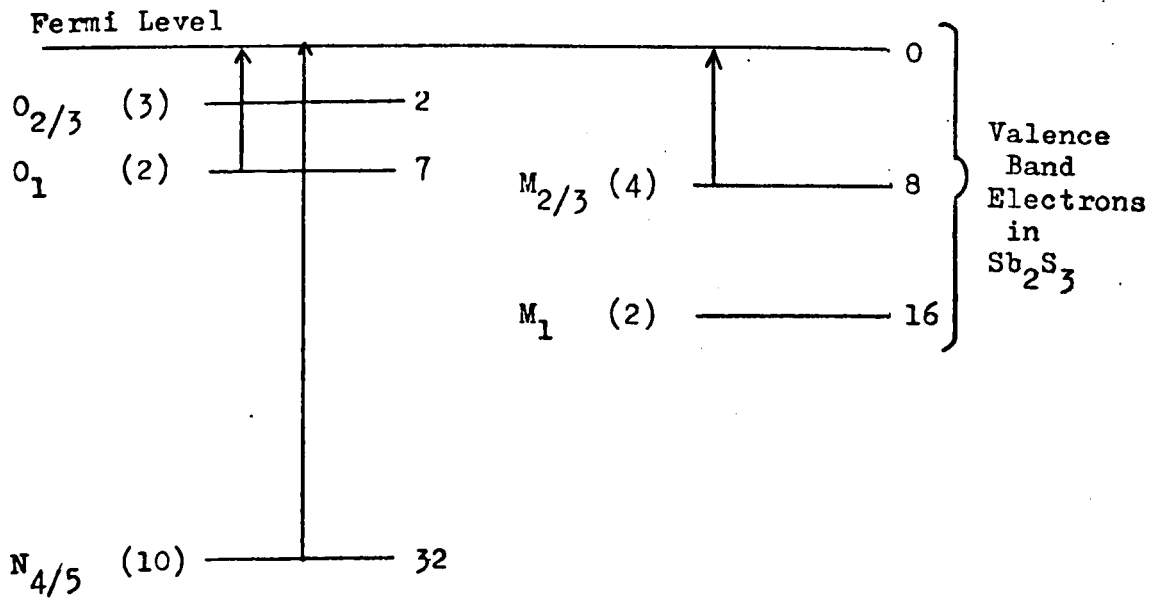


Fig.8-19. The Outer Electronic Levels Of Antimony And Sulphur Showing Possible Characteristic Losses.

#### 8.4 Summary

In this chapter the Auger spectra and the characteristic energy loss spectra of Sb (100),  $\text{Sb}_2\text{O}_3$  and  $\text{Sb}_2\text{S}_3$  have been presented. The positions of the Auger peaks of Sb (100) in the energy range 0 - 550 eV were determined and transitions assigned to them. The influence of Coster-Kronig transitions in the Auger spectra of the pure element was noted.

The Sb Auger peaks were found to shift to lower energies by a small amount when recorded from a  $\text{Sb}_2\text{O}_3$  thin film. Some of this chemical shift was identified as being due to the change in binding energy of the core level electrons involved and the remainder was interpreted as a change in the extra-atomic relaxation energy of Sb. This was deduced to be lowered by about 5 eV in antimony oxide.

The Sb Auger peaks detected from a  $\text{Sb}_2\text{S}_3$  thin film surface were found to be strongly influenced by surface charging effects so that chemical shifts could not be identified. Strong electron beam induced effects were observed on  $\text{Sb}_2\text{O}_3$  and  $\text{Sb}_2\text{S}_3$  surfaces. The results obtained suggested that the electron beam dissociates the antimony oxide molecules whereas the antimony sulphide molecules were desorbed.

The characteristic energy losses from all three materials were obtained and interpreted in terms of surface plasmons, volume plasmons and interband transitions. The common features of the observed losses are summarised in Table 8-12. Peaks in the loss spectra were identified with free-electron like plasmon oscillations of the valence band electrons in all three materials. The Sb ( $N_{4/5} \rightarrow$  Fermi level) transition energy was found to be dependent on the chemical environment of the antimony atoms and additionally a strong peak was always detected at lower energies which was interpreted as being due to the excitation of valence band electrons to empty states close to the Fermi level.

TABLE 8-12

SUMMARY OF COMMON LOSSES OF SB,  $Sb_2O_3$ ,  $Sb_2S_3$

	<u>Valence band → Fermi level (Observed Energy)</u>	<u>Volume Plasmon (Observed Energy)</u>	<u><math>N_{4/5} \rightarrow</math> Fermi level (Observed Energy)</u>	<u>Volume Plasmon <math>\hbar\omega_p</math> (Calculated Energy)</u>
Sb	6.6	15.8	34.1	15.1
$Sb_2O_3$	7.5	20.2	37.1	20.4
$Sb_2S_3$ ,	7.5	18.4	36.4	17.8

## CHAPTER 9

### AUGER ELECTRON AND ENERGY LOSS SPECTROSCOPY OF BISMUTH AND BISMUTH OXIDE

#### 9.1 Bismuth

##### 9.1.1 Introduction

The interesting results obtained from the study of antimony and its compounds in the previous chapter provided a stimulus to proceed with further work on the group V semi metals. Bismuth is the heaviest of the group V elements having an outer electron configuration of  $6s^2 6p^3$ . The surface of this material has been little studied previously and no report could be found in the literature about an Auger spectroscopy study, although the Auger spectra has been published by P.E.I. in their handbook <sup>140</sup>.

An AES study of bismuth is of practical importance because the material shows promise of important future uses. Two particular applications in a state <sup>of</sup> current development are mentioned here. Olsen (1974) <sup>196</sup> has developed bismuth thin films on glass substrates as a useful holographic recording material with sensitivity extending into the infra red wavelengths and MnBi is one of the materials currently being developed for potential use in computer memory devices <sup>197</sup>.

The Auger spectrum from a clean bismuth thin film surface is presented in this chapter with some, previously unreported fine structure being resolved. The energy losses, which were obtained from an AES characterised surface, are then presented and compared with previous studies.

### 9.1.2 Experimental

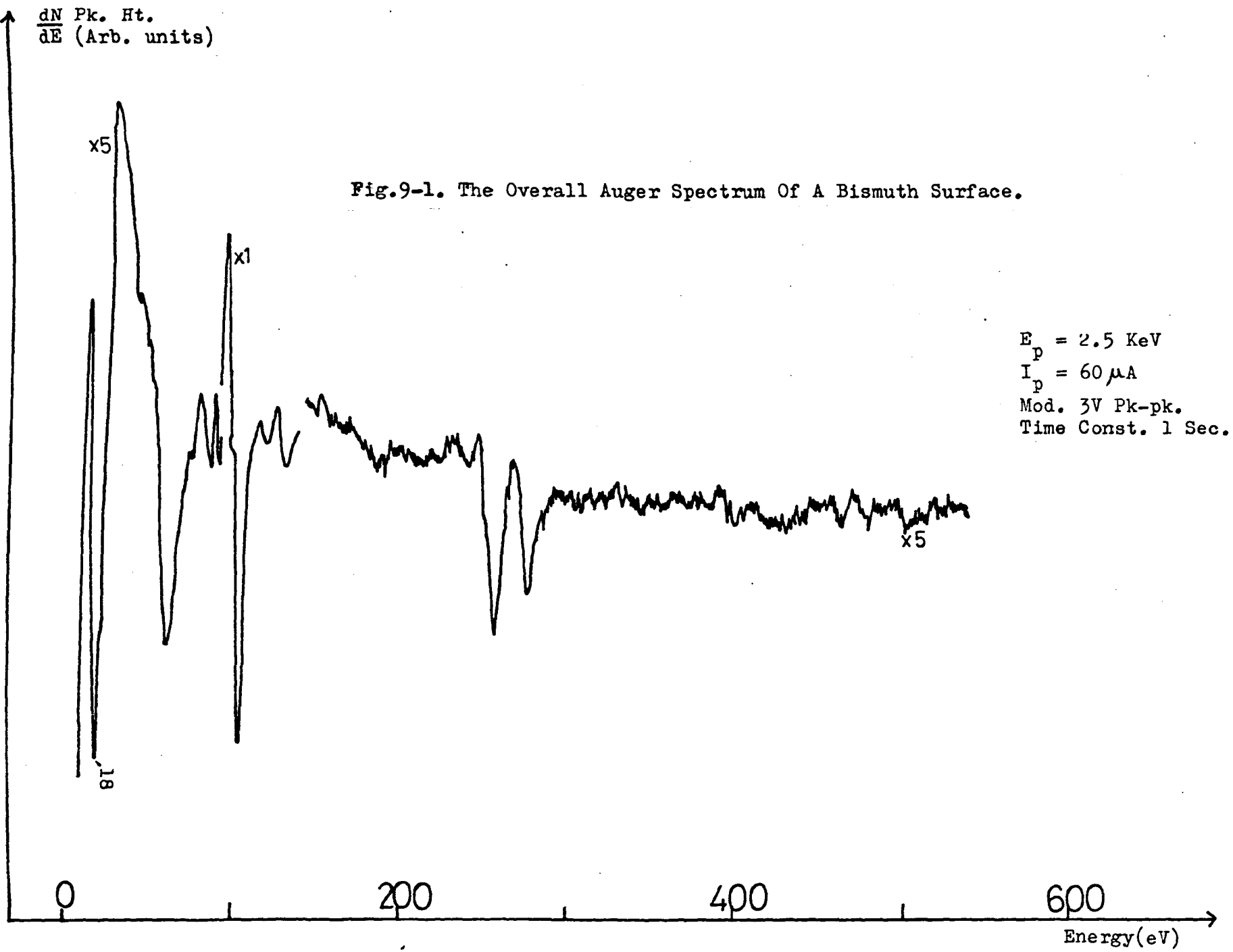
Initially it was attempted to record results from a solid bismuth target. A disc of 1cms diameter and 2mm thick was cut from a polycrystalline rod of 99.99% purity supplied by Metals Research Ltd. One face of the disc was mechanically polished with the usual techniques as described for the stainless steel and molybdenum samples. The target was mounted in the chamber and the system evacuated to UHV pressures  $\approx 5 \times 10^{-10}$  Torr. Auger spectra of the bismuth surface showed considerable contamination due to sulphur and carbon, a small peak due to bismuth could be detected and the major peaks heights observed from the elements were in the ration 1:3:8 for Bi:S:C.

Attempts were made to remove the contaminants by heating the target with electron bombardment with out acheiving any success. A difficulty arose because the Bi has a low melting temperature of 540<sup>o</sup>K, so that the target would melt before any contaminants were removed from the surface. Additionally the primary electron beam did not appear to have the same cleaning effect on Bi, as was observed on the antimony crystal.

Attempts to obtain a clean solid target were eventually abandoned and it was decided to try to prepare a clean bismuth surface by evaporating a thin film on to a molybdenum substrate, in a UHV environment. 99.99% pure bismuth was evaporated from an outgassed tungsten filament on to the molybdenum substrate which was at room temperature. The substrate was prepared using the same method as was used to prepare the molybdenum target of Chapter 7 and it was flashed clean of any contaminants before evaporating the bismuth film. The film was deposited by flashing the tungsten filament to white heat (Approx.50 amps through the filament) and gradually the thickness of bismuth on the substrate increased. During the evaporation the pressure within the

$\frac{dN}{dE}$  Pk. Ht.  
(Arb. units)

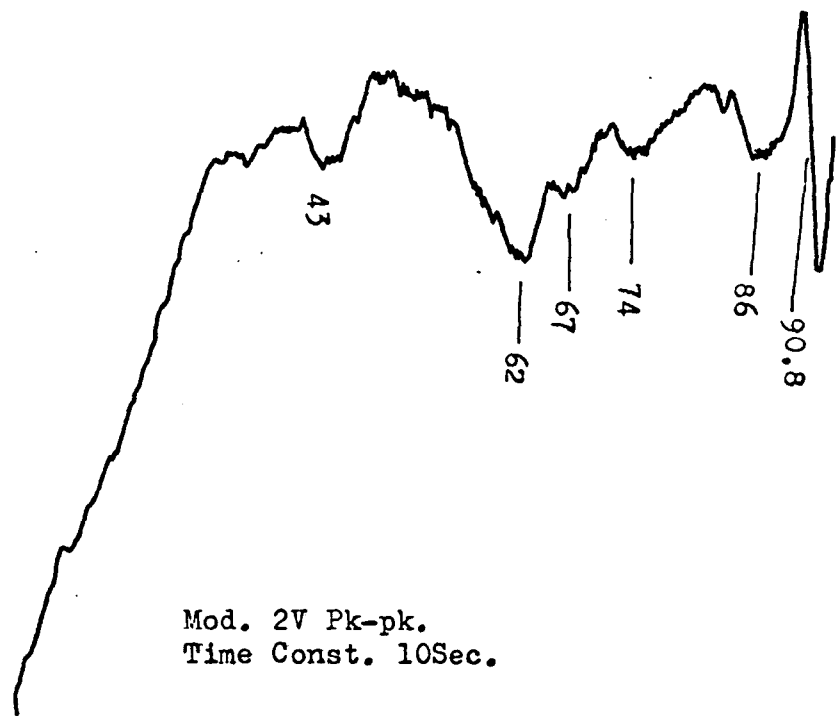
Fig.9-1. The Overall Auger Spectrum Of A Bismuth Surface.



$E_p = 2.5$  KeV  
 $I_p = 60 \mu A$   
Mod. 3V Pk-pk.  
Time Const. 1 Sec.

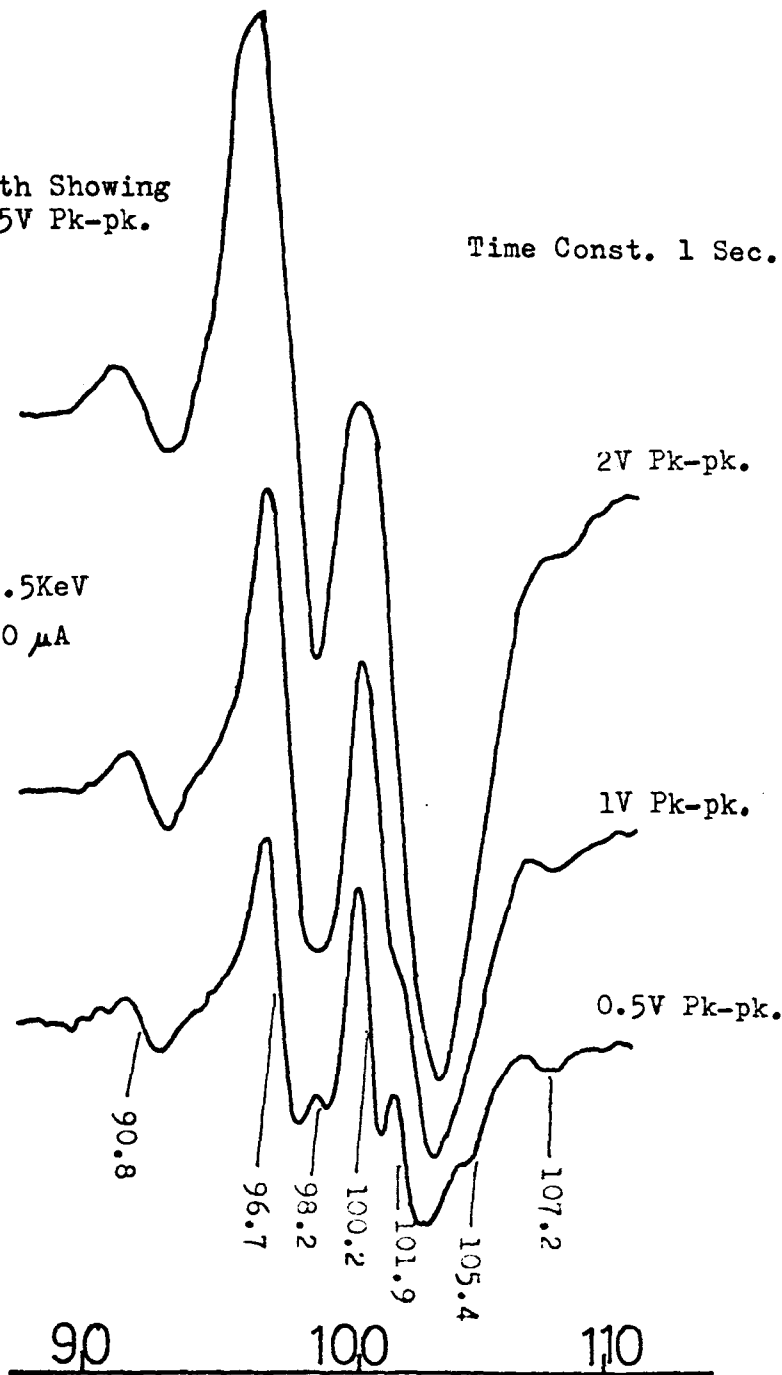
$\frac{dN}{dE}$  Pk.-Ht.  
(Arb. units)

Fig.9-2(a). The Low Energy Auger Spectrum Of Bismuth Showing Fine Structure In The Major Peak At 0.5V Pk-pk. Modulation.



Time Const. 1 Sec.

$E_p = 2.5\text{KeV}$   
 $I_p = 60 \mu\text{A}$



Energy(eV)

$\frac{dN}{dE}$  Pk-pk.  
(Arb. units)

Fig.9-2(b). The Auger Spectrum Of Bismuth Continued From  
9-2(a).

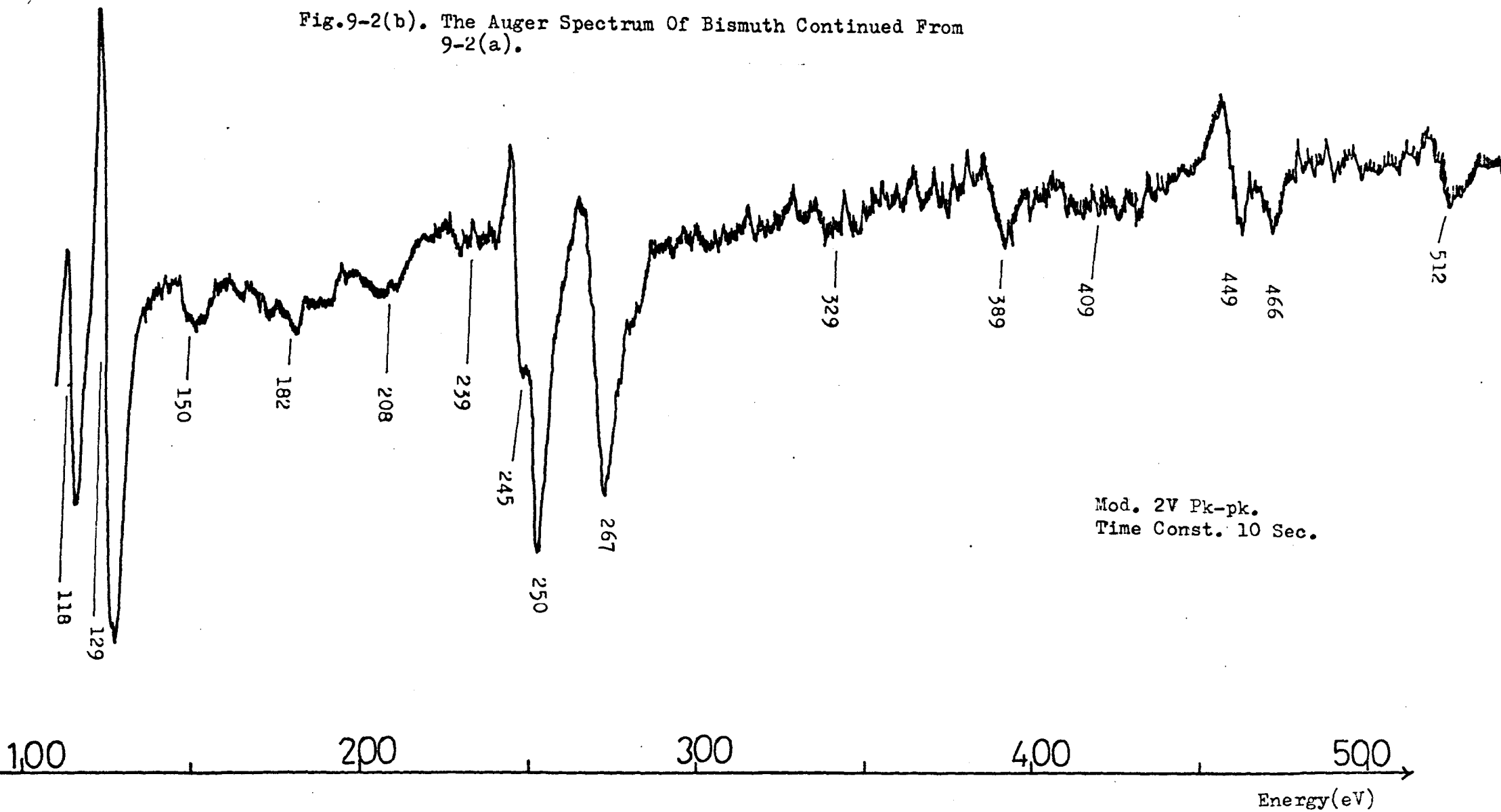


TABLE 9-1

ENERGY OF OBSERVED PEAKS FROM BISMUTH

<u>Present Work (eV)</u>	<u>P.E.I. <sup>140</sup>(eV)</u>
18	17
43	
62	
67	
74	
86	
90.8	
96.7	96
98.2	
100.2	101
101.9	
105.4	
107.2	
118	
129	129
182	180
208	203
239	234
245	
250	249
267	268
329	332
389	384
409	404
	416
449	
466	460
	487
512	510

chamber increased to  $\sim 10^{-6}$  Torr.

The bismuth surface thus prepared revealed no contamination, as detected by AES. Consequently we proceeded to obtain results from this surface. No electron beam induced effects could be observed so that longer scan times for recording the Auger and energy loss spectra could be used.

### 9.1.3 Results and Discussion of the Auger Spectrum of Bismuth

The overall Auger spectrum from Bi in the energy range 0 - 550 eV is shown in Fig. 9-1. The appearance of this spectrum is similar to that published by P.E.I.<sup>140</sup>. The Auger spectrum of Bi is characterised by a large peak of energy about 100 eV, the remaining peaks are of much lower intensity and these were examined using a longer time constant on the lock-in amplifier, together with a slower scanning rate. The results are presented in Fig. 9-2(a) and (b). Also shown in Fig. 9-2(a) is the large Bi peak ( $\sim 100$  eV) observed with lower modulation amplitudes to increase the resolution of the instrument. The P.E.I. spectrum of Bi detected two peaks at 96 and 101 eV in this energy range and we also detect two peaks using a modulation of 2v pk-pk, but on decreasing the amplitude of modulation additional fine structure becomes apparent and with 0.5v pk-pk modulation six features can be identified in this energy range. At these energies the resolution of the analyser is approximately 0.7 eV, so that using 0.5 volts pk-pk modulation the instrument is operating near optimum resolution and sensitivity.

The energies of the observed peaks are summarised in Table 9-1, together with the values obtained by P.E.I. The energies of the fine structure features are an average of three measurements and an error of  $\pm 0.2$  eV is estimated in these values, the remaining peak energies are accurate to  $\pm 1$  eV.

TABLE 9-2

## THE ASSIGNMENT OF THE AUGER PEAKS OF BISMUTH

<u>Observed Energy (eV)</u>	<u>Transition</u>	<u>Calculated<sup>36</sup> Energy</u>	<u>Multiplicity</u>
18	O <sub>5</sub> V V	17.0 eV	14
	N <sub>3</sub> N <sub>4</sub> N <sub>6</sub>	22.0 eV	25
43	N <sub>7</sub> O <sub>3</sub> O <sub>5</sub>	32.0 eV	50
	N <sub>6</sub> O <sub>3</sub> O <sub>5</sub>	37.0 eV	37
	O <sub>3</sub> O <sub>5</sub> O <sub>5</sub>	38.0 eV	37
	N <sub>3</sub> N <sub>5</sub> N <sub>6</sub>	48.0 eV	37
	N <sub>3</sub> N <sub>5</sub> N <sub>7</sub>	53.0 eV	56
	N <sub>7</sub> O <sub>3</sub> V	56.0 eV	25
62	N <sub>6</sub> O <sub>3</sub> V	61.0 eV	18
	O <sub>3</sub> O <sub>5</sub> V	62.0 eV	18
67	O <sub>2</sub> O <sub>5</sub> O <sub>5</sub>	62.0 eV	18
86	N <sub>2</sub> N <sub>3</sub> O <sub>5</sub>	87.0 eV	12
90.8	N <sub>5</sub> N <sub>6</sub> N <sub>6</sub>	90.5 eV	56
96.7	N <sub>5</sub> N <sub>6</sub> N <sub>7</sub>	95.5 eV	75
98.2	N <sub>7</sub> O <sub>4</sub> O <sub>4</sub>	99.0 eV	33
100.2	N <sub>5</sub> N <sub>7</sub> N <sub>7</sub>	100.5 eV	100
101.9	N <sub>7</sub> O <sub>4</sub> O <sub>5</sub>	101.0 eV	50
105.4	{ N <sub>7</sub> O <sub>5</sub> O <sub>5</sub>	103.0 eV	75
	{ N <sub>6</sub> O <sub>4</sub> O <sub>4</sub>	104.0 eV	25
107.2	N <sub>6</sub> O <sub>5</sub> O <sub>5</sub>	108.0 eV	50
118	N <sub>4</sub> N <sub>6</sub> N <sub>7</sub>	119.0 eV	50
129	N <sub>4</sub> N <sub>7</sub> N <sub>7</sub>	125.0 eV	66
182	N <sub>5</sub> N <sub>7</sub> O <sub>3</sub>	172.0 eV	50
208	N <sub>3</sub> N <sub>5</sub> O <sub>5</sub>	195.0 eV	37
	N <sub>4</sub> N <sub>7</sub> O <sub>3</sub>	198.0 eV	33

/...

TABLE 9-2 contd.

<u>Observed Energy (eV)</u>	<u>Transition</u>	<u>Calculated Energy</u>	<u>Multiplicity</u>
239	{ N <sub>5</sub> N <sub>6</sub> O <sub>5</sub>	238.0 eV	56
	{ N <sub>5</sub> N <sub>7</sub> O <sub>4</sub>	241.0 eV	50
245	N <sub>5</sub> N <sub>7</sub> O <sub>5</sub>	243.0 eV	75
250	N <sub>5</sub> N <sub>7</sub> P <sub>1</sub>	256.0 eV	18
267	N <sub>5</sub> N <sub>7</sub> V	266.0 eV	37
	N <sub>4</sub> N <sub>7</sub> O <sub>5</sub>	267.0 eV	50
329	N <sub>3</sub> N <sub>6</sub> N <sub>6</sub>	330.0 eV	37
	N <sub>3</sub> N <sub>6</sub> N <sub>7</sub>	334.0 eV	50
389	N <sub>5</sub> O <sub>5</sub> O <sub>5</sub>	385.0 eV	56
409	N <sub>4</sub> O <sub>5</sub> O <sub>5</sub>	409.0 eV	37
	N <sub>3</sub> N <sub>7</sub> N <sub>7</sub>	411.0 eV	33
449	N <sub>4</sub> P <sub>1</sub> V	450.0 eV	6
466	N <sub>2</sub> N <sub>7</sub> N <sub>7</sub>	467.0 eV	33
512	N <sub>3</sub> N <sub>7</sub> V	506.0 eV	25

Transitions are assigned to the observed peaks using the tables of Coghlan and Clausing<sup>36</sup> and are summarised in Table 9-2. The broad peaks observed at 43, 62 and 67 eV could not be assigned a specific transition and it is thought that they are probably due to several unresolved peaks in this energy range. The energy of the primary beam, 2.5 keV, is such that the M levels are not ionized due to their greater binding energy.

The electronic structure of bismuth is such that the most populated subshells are the core levels  $N_5$  (6 electron),  $N_6$  (6 electrons),  $N_7$  (8 electrons),  $O_5$  (6 electrons) so that Auger transitions involving these levels are expected to be the strongest and not transitions involving the valence band of bismuth. In this respect bismuth is similar to antimony whereas in molybdenum and gold the strongest transitions are those which involve the valence band. Thus the fine structure in the strong bismuth peak shown in Fig. 9-2(a) is due to transitions between core levels and does not reflect the valence band density of occupied states.

The influence of Coster-Kronig type transitions is to be noted. Vacancies created in the lower N levels are filled by Auger transitions involving the higher N levels rather than direct transitions to the outer electrons of the atom. Thus  $N_5O_5O_5$  (389 eV) and  $N_4O_5O_5$  (401 eV) are much weaker than the  $N_6O_5O_5$  and  $N_7O_5O_5$  transitions whereas Coster-Kronig transitions such as  $N_5N_6N_6$  and  $N_5N_6N_7$  are observed to be relatively strong.

#### 9.1.4 Results and Discussion of the Energy Losses of Bismuth

The characteristic energy losses of bismuth were studied with 300 eV and 500 eV primary electrons. The loss spectra were recorded in the first derivative and second derivative mode of operation of the

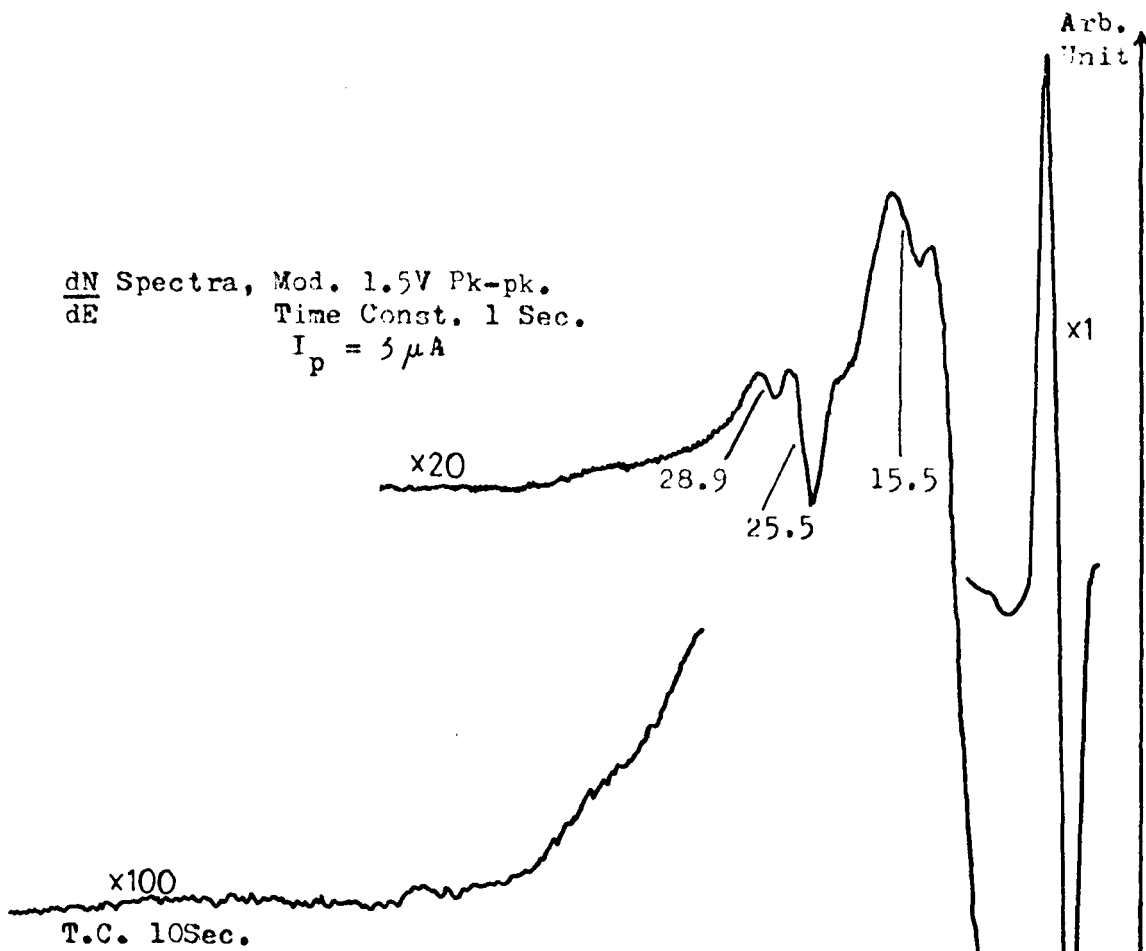
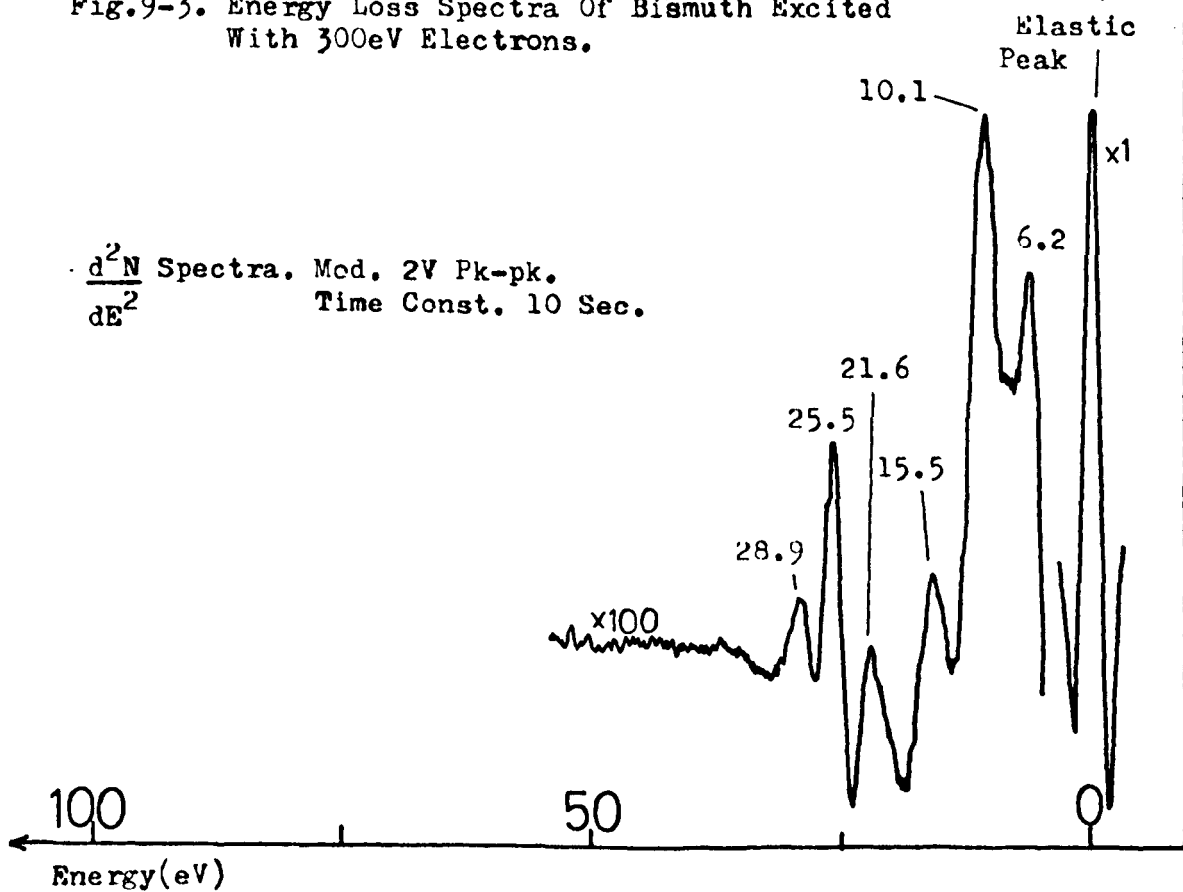


Fig.9-3. Energy Loss Spectra Of Bismuth Excited With 300eV Electrons.



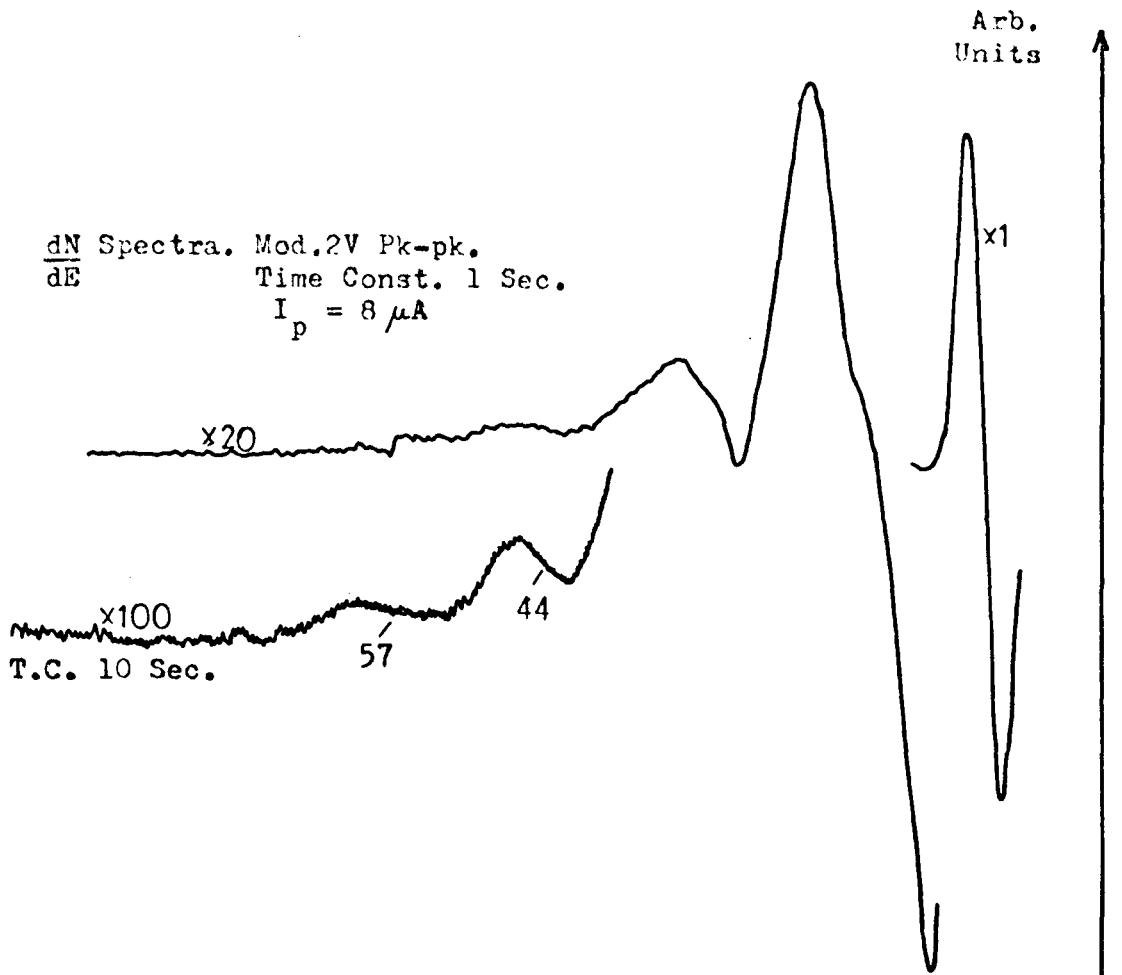


Fig.9-4. Energy Loss Spectra Of Bismuth Excited With 500eV Electrons.

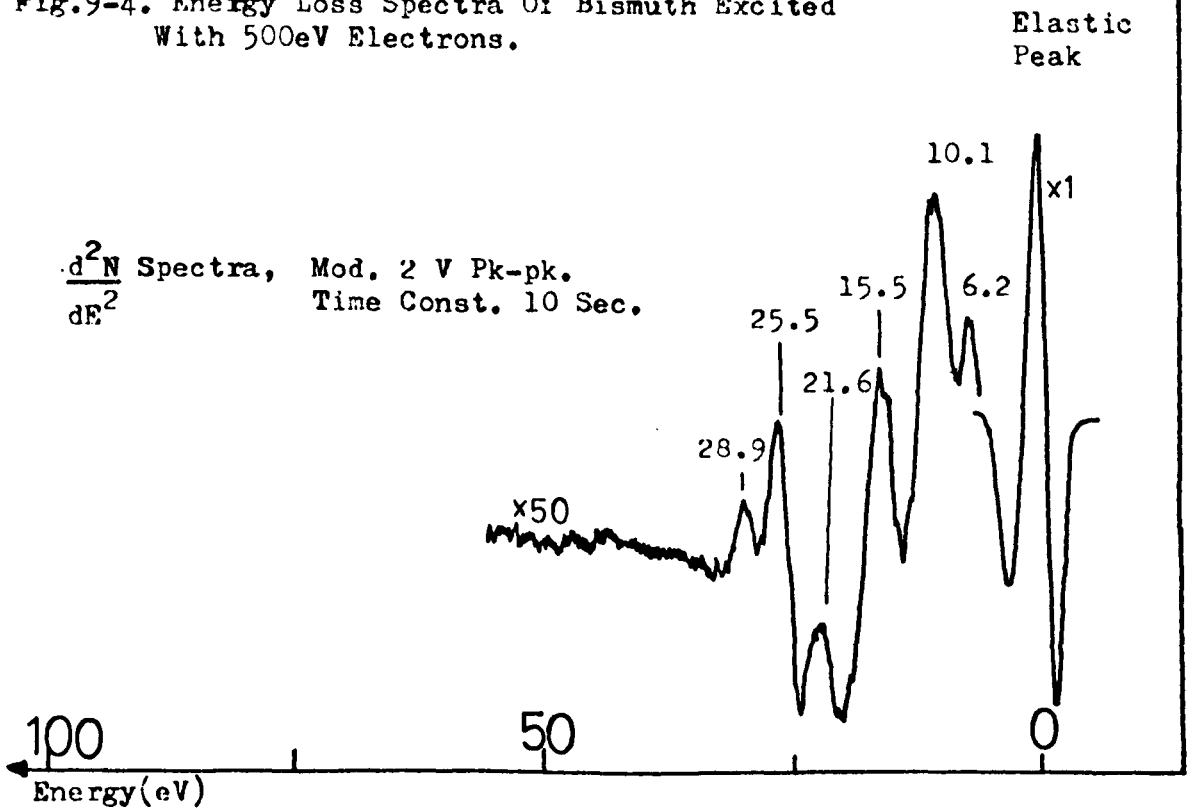


TABLE 9-3

ENERGY OF OBSERVED LOSSES OF BISMUTH

<u>Primary Energy E<sub>p</sub></u> (eV)	<u>Analyser Operation mode</u>	<u>Observed Losses (eV)</u>							
300	$\frac{d^2N}{dE}$	6.0	10.8	15.6	21.6	25.8	28.9		
		5.9	10.2	15.1	21.7	25.4	28.7		
500	$\frac{d^2N}{dE}$	6.3	9.6	15.6	21.6	25.8	29.4		
		6.1	9.8	15.3	21.4	25.2	28.4		
	$\frac{d^2N}{dE}$	6.5	10.4	15.6	21.5	25.4	28.9		
		6.3	9.9	15.6	21.8	25.7	28.8		
	$\frac{dN}{dE}$							43	57
								44	57
<u>Mean Value (eV)</u>		6.2	10.1	15.5	21.6	25.5	28.9	44	57
		± 0.1	± 0.2	± 0.1	± 0.1	± 0.2	± 0.2		

analyser from the evaporated uncontaminated thin film surface. The observed spectra are shown in Figs. 9-3 and 9-4.

The energies of the observed losses are summarised in Table 9-3 and the mean values calculated. The error bars represent a confidence limit of 66%. The high energy losses at 44 and 57 eV were only observed in the  $dN/dE$  spectra for 500 eV primary exciting electrons, presumably due to the greater instrumental sensitivity with the higher beam currents available for this primary energy.

The loss values obtained are compared with the losses observed by other authors, in Table 9-4 and as can be seen our values are in good agreement. The origins of the observed losses are identified by comparison with the optical properties of bismuth, which have been determined by Hunter et al (1965)<sup>201</sup> and by Toots et al (1969)<sup>202</sup>. The results of both these authors show a strong broad maxima in the energy loss function  $\text{Im} \left( \frac{-1}{\epsilon} \right)$  at 14 - 15 eV, so that the observed 15.5eV loss is identified as a volume plasmon oscillation (VP). The plasmon energy for free electron like oscillation of the 5 valence band electrons of bismuth ( $6s^2 6p^3$ ) is calculated to be 13.9 eV. The higher energy of the observed plasmon loss possibly indicates a strong interband transition at lower energies, Raither (1965)<sup>91</sup>.

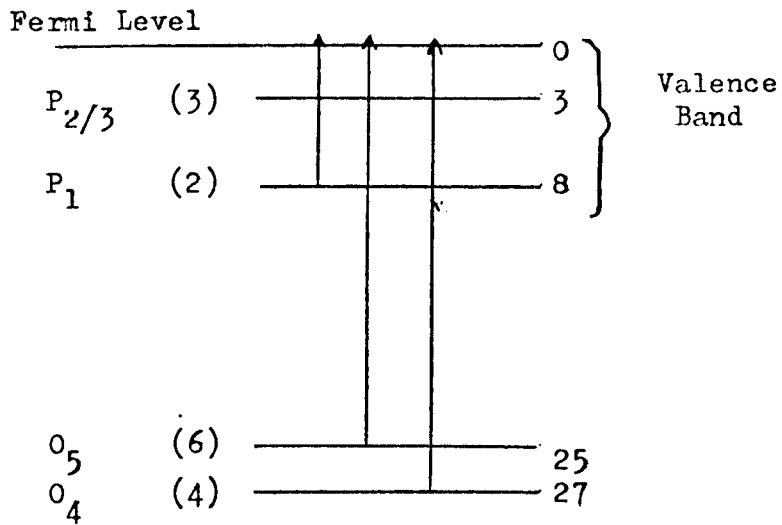
The 10.1 eV loss is identified as being due to a surface plasmon (SP) oscillation although the observed energy is lower than the calculated value of 11.0 eV. There were no graphs available of the surface loss function  $\text{Im} \left( \frac{-1}{\epsilon + \epsilon_0} \right)$  to confirm this assignment.

The 6.2 eV loss is identified as the excitation of the  $P_1$  electrons ( $6s^2$ ) to states near the Fermi level and similarly the 28.9 eV loss is identified as the excitation of  $O_{4/5}$  electrons to states near the Fermi level, as shown in Fig. 9-5. These assignments are indicated by the optical properties of Hunter<sup>201</sup> which have structure in the bulk loss

TABLE 9-4

ASSIGNMENT OF THE OBSERVED LOSSES

<u>Observed Values (eV)</u>	<u>Powell (1960)<sup>188</sup></u>	<u>Wehenkel (1974)<sup>198,199</sup></u>		<u>Zachrais (1973)<sup>200</sup></u>	<u>Assignment</u>
1) 6.2		5	5	5.3	$P_1 \rightarrow$ Fermi level
2) 10.1	9.9		10	9.5	SP
3) 15.5	14.7	13.95	14	14.4	VP
4) 21.6			24	24.6	VP + (1)
5) 25.5	24.8	24.45	27	27.8	VP + SP
6) 28.9	29.0	27.3	29	29.7	$O_{4/5} \rightarrow$ Fermi level
7) 44					3VP
		52			
8) 57					4VP



Level	No. Of Electrons	Binding Energy (eV) <sup>30</sup>
$O_3$	(4)	93

Fig. 9-5. The Outer Electronic Levels Of Bismuth Showing Possible Characteristic Losses.

function at 6 - 7 eV and in the region 25 - 30 eV.

The remaining observed losses are thought to be due to primary electrons undergoing multiple in-elastic collisions before emerging from the solid. The assignments are summarised in Table 9-4. The bismuth losses are by no means conclusively identified due to the presence of core level excitations and multiple losses at energies very close to each other. Thus the  $O_4, O_5$  level splitting of  $\approx 2$  eV cannot be identified in the loss spectra due to the presence of the (VP + SP) loss and a possible contribution due to a ZVP loss at 30 - 31 eV.

## 9.2 Bismuth Oxide

### 9.2.1 Experimental

To study the chemical effects on the Auger spectrum of bismuth we proceeded to obtain results from bismuth oxide,  $Bi_2O_3$ . The oxide was obtained in tablet form from BDH<sup>193</sup> and ground to a powder before placing in an outgassed molybdenum boat for evaporation. Again a molybdenum substrate was used, prepared in the normal way and flashed clean in a UHV atmosphere, prior to evaporating the oxide film.

The evaporation temperature of bismuth oxide is in the region of 800 - 1000°C and it was found on depositing the oxide films that there was still some molybdenum contamination, as detected by AES, present. We were satisfied that there was a sufficiently thick oxide film to neglect substrate influences. It is thought that at the high evaporation temperatures needed for  $Bi_2O_3$ , the oxide was reacting with the molybdenum boat to form a molybdenum oxide  $MoO_2$  and this is known to sublime appreciably at temperatures of 1000°C<sup>203</sup>. Consequently not only was  $Bi_2O_3$  being deposited on the substrate but also  $MoO_2$  contamination.

Subsequently we used a platinum evaporation boat and a stainless steel substrate, as a precaution to eliminate the possibility of the molybdenum substrate being the cause of the contamination.

The stainless steel substrate was flashed to a high temperature to desorb surface contaminants, although small amounts of C, S and oxygen were still present. The bismuth oxide was then evaporated on to the polished face of the stainless steel target. The pressure within the chamber increased from an initial value  $\sim 10^{-10}$  Torr to  $\sim 10^{-6}$  Torr during evaporation. A sufficient thickness of film was evaporated to eliminate substrate influences.

From such a film, which had a dull greyish appearance, the Auger and energy loss measurements were recorded. During electron beam bombardment of the surface the pressure within the chamber increased to  $4 \times 10^{-8}$  Torr, from an initial UHV possibly due to desorption from the surface, although no electron beam effects could be detected in the Auger spectra.

### 9.2.2 Results and Discussion of the Auger Spectrum of Bismuth Oxide

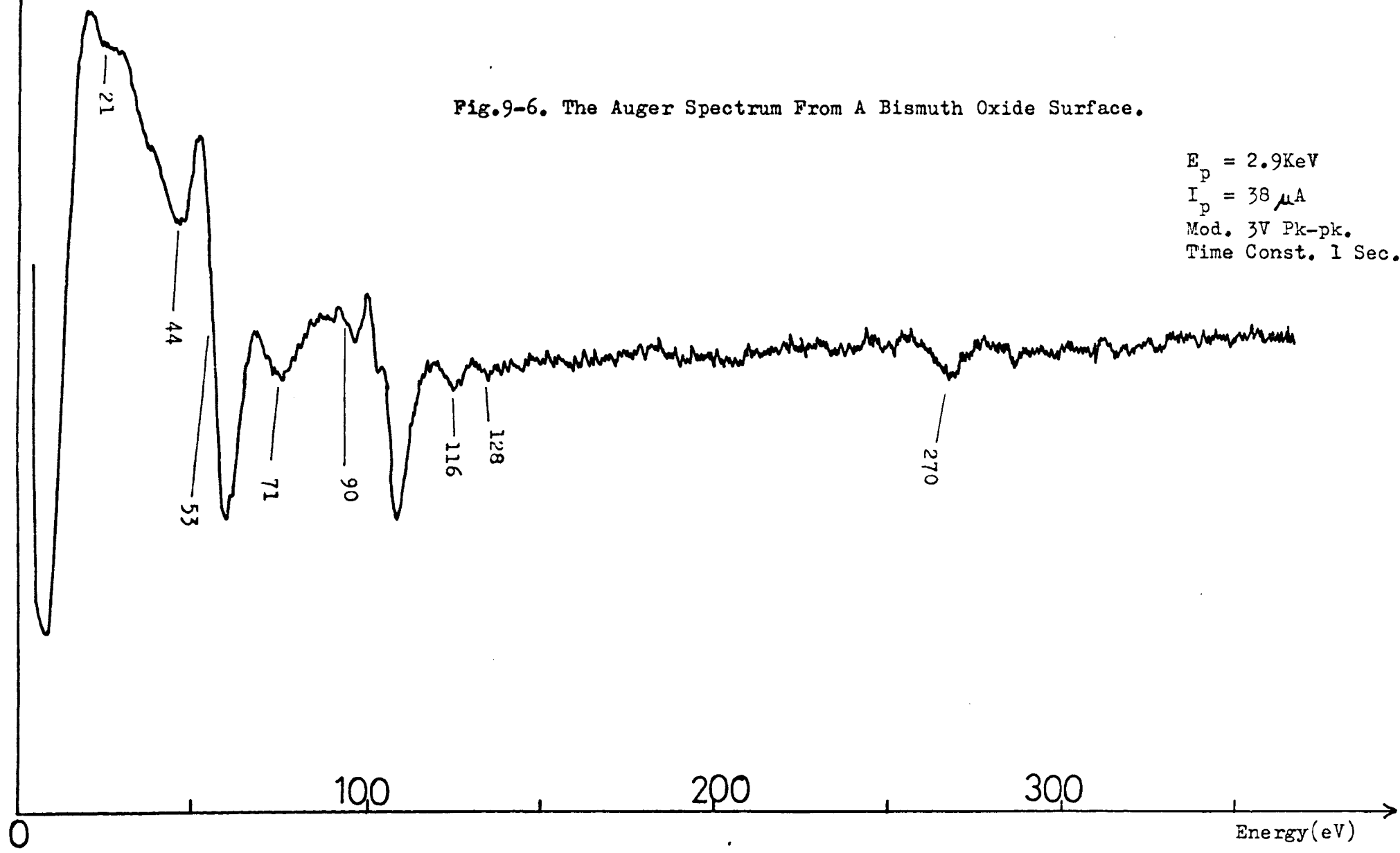
The Auger spectrum from a contamination free bismuth oxide surface is shown in Fig. 9-6 and the fine structure in the major bismuth peak is shown in Fig. 9-7. The appearance of this spectrum remained unchanged with electron beam exposure indicating that the pressure increase observed in the chamber was probably due to desorption of entire molecules of  $\text{Bi}_2\text{O}_3$  rather than the desorption of oxygen by dissociation of the molecules. In this respect  $\text{Bi}_2\text{O}_3$  appears to differ from antimony oxide.

The energies of the observed peaks in the Auger spectrum of bismuth oxide are summarized in Table 9-5. These energies are the average of a number of spectra and are accurate to  $\pm 1$  eV.

$\frac{dN}{dE}$  Pk.Ht.  
(Arb. units)

Fig.9-6. The Auger Spectrum From A Bismuth Oxide Surface.

$E_p = 2.9\text{KeV}$   
 $I_p = 38\mu\text{A}$   
Mod. 3V Pk-pk.  
Time Const. 1 Sec.



$\frac{dN}{dE}$  Pk.Ht.  
(Arb. units)

Fig.9-6. Continued

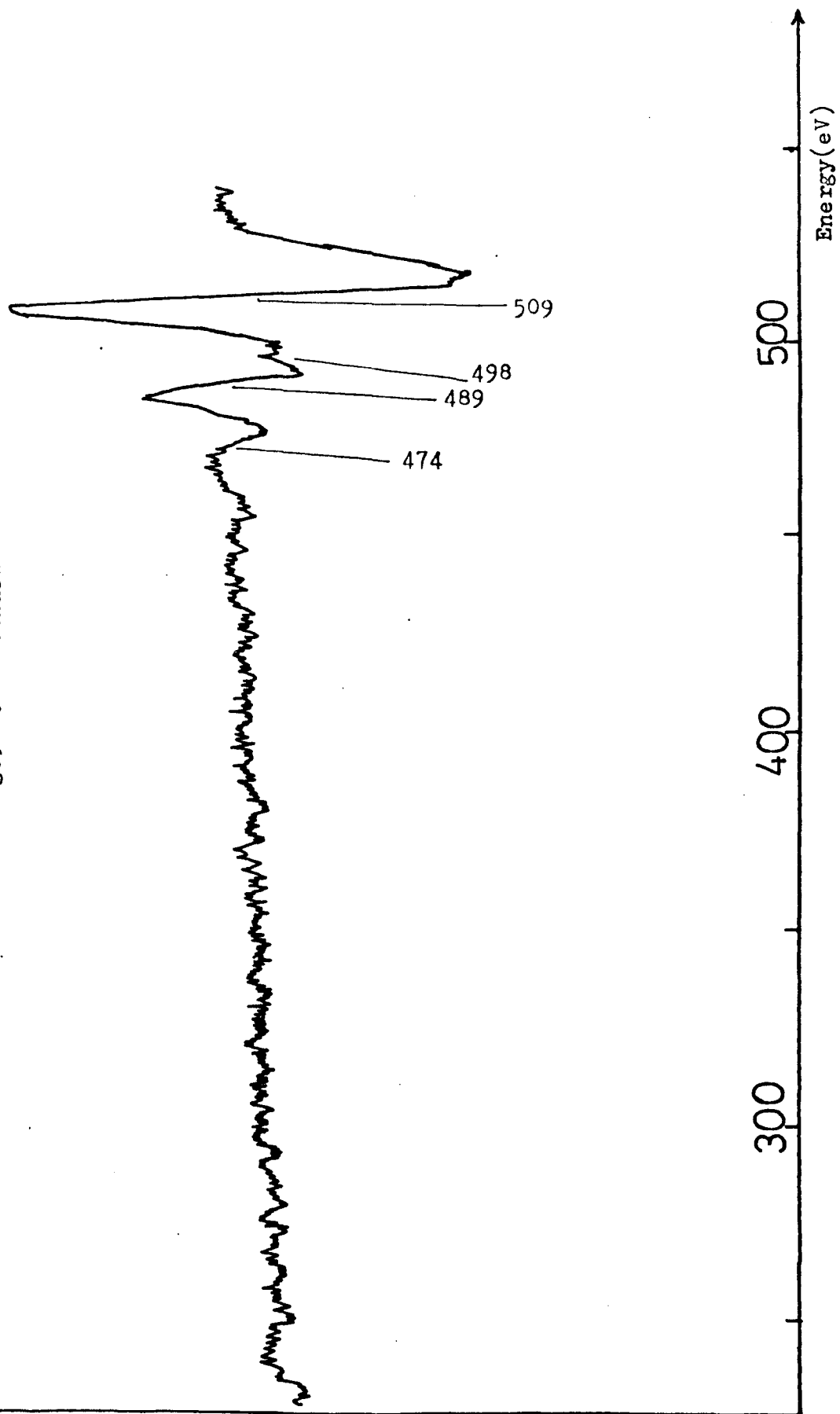


TABLE 9-5

ENERGIES OF THE PEAKS OBSERVED FROM  $\text{Bi}_2\text{O}_3$ 

<u>Observed Energy (eV)</u> ( $\text{Bi}_2\text{O}_3$ )	<u>Transition Assigned</u>	<u>Observed Energy (eV) in Bi</u> <u>from 9-1</u>	
21	Bi $\text{O}_5\text{V V}$	18	
	Bi $\text{N}_3\text{N}_4\text{N}_6$		
44	Bi Broad feature	43	
53	Bi( $\text{N}_7$ ) Bi( $\text{O}_3$ ) O ( $\text{L}_{2/3}$ )		
	Bi( $\text{N}_6$ ) Bi( $\text{O}_3$ ) O ( $\text{L}_{2/3}$ )		
71	Bi ( $\text{O}_3$ ) O( $\text{L}_{2/3}$ ) O( $\text{L}_{2/3}$ )		
90	Bi $\text{N}_5\text{N}_6\text{N}_6$	90.8	
96.0 $\pm 0.2$	Bi $\text{N}_5\text{N}_6\text{N}_7$	96.7	
100.9 $\pm 0.2$	Bi $\text{N}_5\text{N}_7\text{N}_7$	100.2	
102.4 $\pm 0.2$	Bi $\text{N}_7\text{O}_4\text{O}_5$	101.9	
116	Bi $\text{N}_4\text{N}_6\text{N}_7$	118	
128	Bi $\text{N}_4\text{N}_7\text{N}_7$	129	
270	Bi $\text{N}_4\text{N}_7\text{O}_5$	267	
		<u>Calculated<sup>36</sup> Energy</u>	<u>Multiplicity</u>
474	O K $\text{L}_1\text{L}_1$	477	25
489	O K $\text{L}_1\text{L}_{2/3}$	496	50
498	O (K) O ( $\text{L}_1$ ) Bi ( $\text{P}_{2/3}$ )		
509	O K $\text{L}_{2/3}\text{L}_{2/3}$	516	100

The origins of the peaks are also identified in this table together with the energy of the same peak as detected from the element bismuth in the previous section. The calculated energies and multiplicities of the  $O_2$  Auger peaks are summarised from the tables of Coghlan and Clausing<sup>36</sup>.

The Auger spectrum of bismuth oxide is different from the bismuth Auger spectrum in a number of ways. Apart from the obvious additional peaks due to oxygen, the fine structure in the Bi 100 eV peak from  $Bi_2O_3$  is not so apparent as shown in Fig. 9-7. Two reasons are suggested for this. Firstly, the signal to noise ratio in the  $Bi_2O_3$  Auger spectrum is not as good as in the Bi spectrum probably due to a surface topography effect and secondly, some broadening of the Auger peaks is thought to occur so that not as much fine structure is resolved by the instrument.

In the Auger spectrum of bismuth oxide a strong peak is identified at 53 eV which is only observed as a broad shallow peak, in the Bi spectrum (labelled at 62 eV), see Fig. 9-2. The assignments for the observed bismuth peaks in Table 9-2 indicate the presence of transitions at about 50 - 60 eV calculated energy involving the valence electrons. Thus in bismuth oxide, the additional electrons introduced by the oxygen atom into the valence band are thought to be enhancing the intensity of the 53 eV peak with a cross transition (or interatomic Auger peak) of type Bi ( $N_{6/7}$ ) Bi ( $O_3$ ) O ( $L_{2/3}$ ), Fig. 9-8. The calculated energy of such a transition is estimated to be 58 eV, in good agreement with the observed value. Similarly the 71 eV peak is also identified as a cross transition as indicated in Table 9-5 and shown in Fig. 9-8. The 498 eV feature is also thought to be a cross transition, a similar peak was observed in the Auger spectrum of antimony oxide, but there no other strong cross transitions, similar to the 53 eV and 71 eV structures in  $Bi_2O_3$ , could be identified.

Because the 53 eV peak involved electrons from the valence band

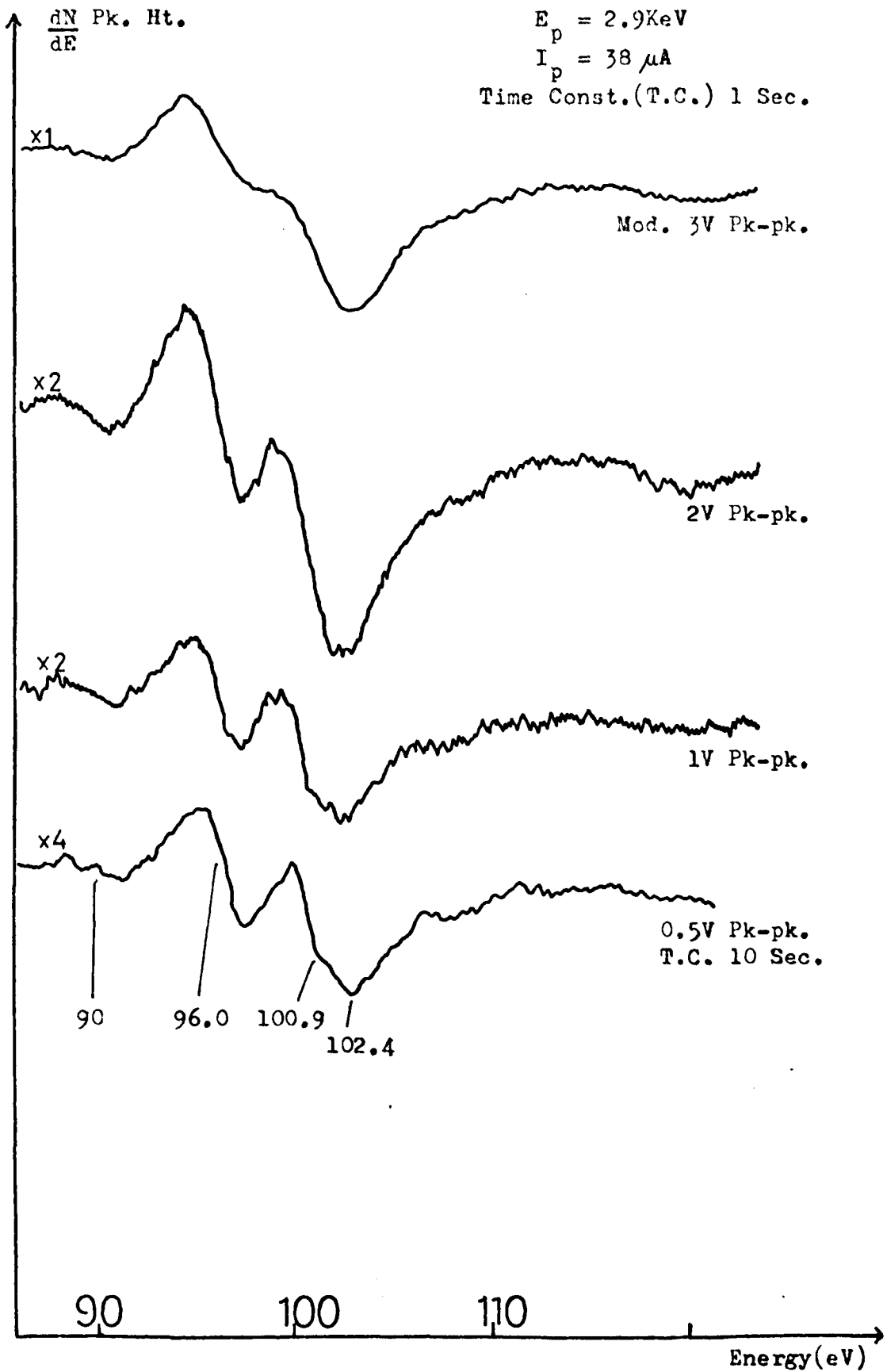


Fig.9-7. Fine Structure In The Major Auger Peak Of Bismuth  
 From  $\text{Bi}_2\text{O}_3$  .

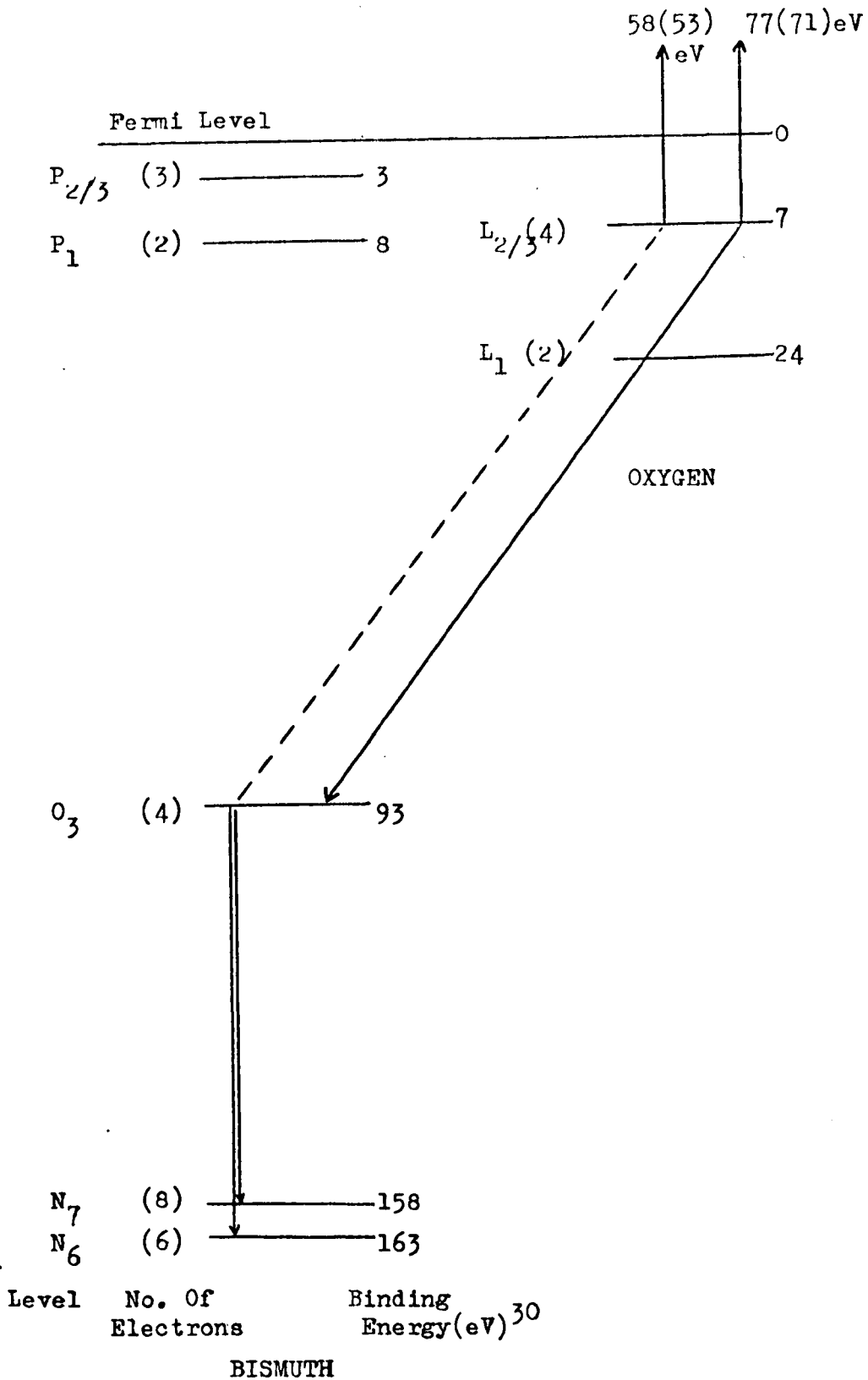


Fig.9-8. The Energy Levels Involved In The Cross-Transitions Observed From  $Bi_2O_3$  .

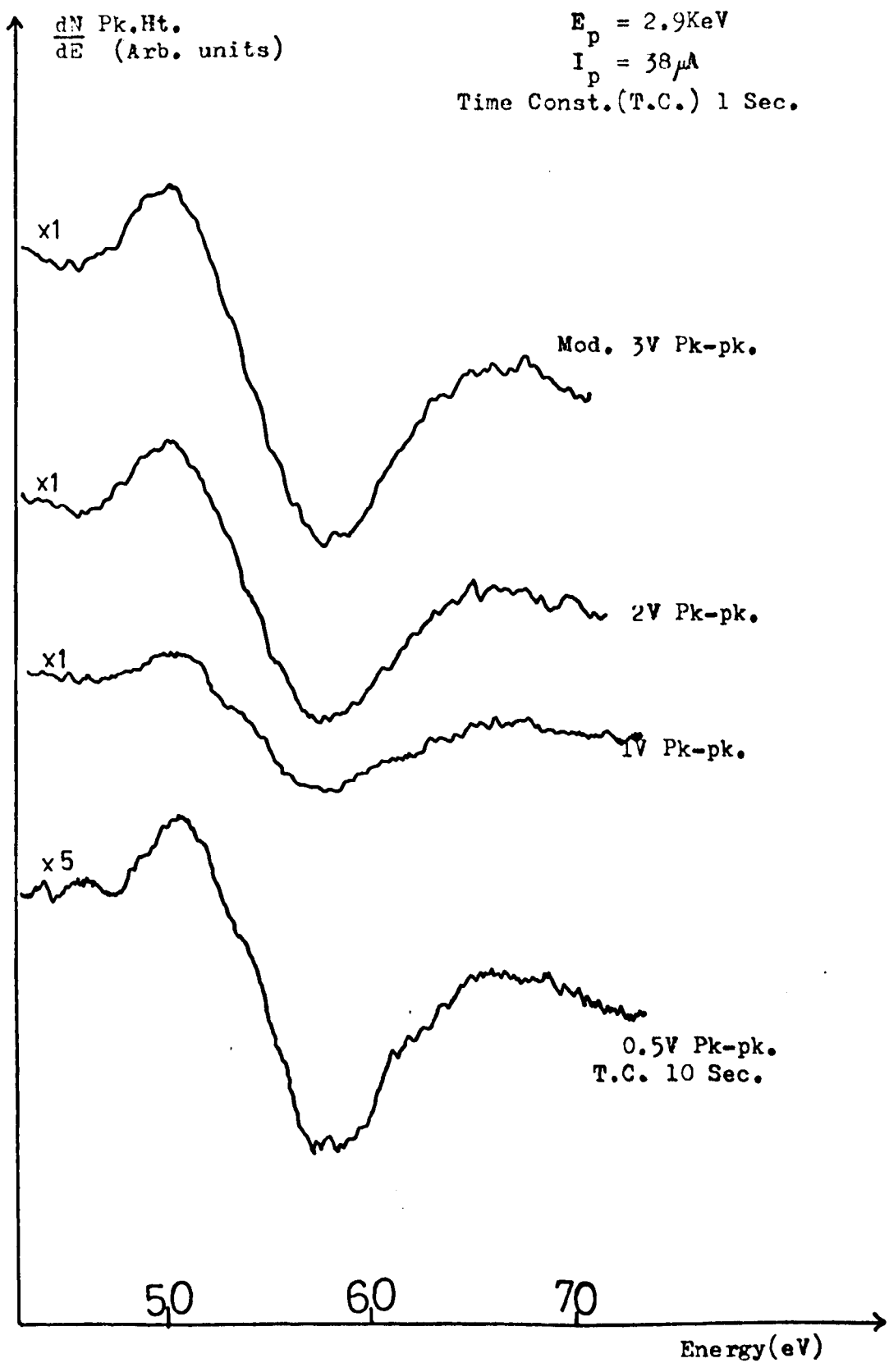


Fig.9-9. Fine Structure In The 53eV Peak.

it was thought that it may contain features reflecting the valence band density of occupied states. Consequently it was examined with a low amplitude modulation of 0.5 v pk-pk, as shown in Fig. 9-9. As can be seen no fine structure could be identified, although the peak is observed to be 6 - 7 eV broad (pk-pk width), indicating that possibly a broad region of the valence band is participating in this transition.

Chemical shifts similar to those observed in the Auger spectrum of antimony oxide were not detected in the spectrum of bismuth oxide, certainly the results on the major bismuth peak revealed no systematic shifting of these peaks. The antimony oxide evaporated film had a polycrystalline appearance whereas the bismuth oxide evaporated film was of a powdery texture, which could be easily removed from the substrate by rubbing. In Chapter 8.2 a significant proportion of the chemical shift of the antimony Auger peaks was explained as a change in the extra-atomic relaxation energy which has a structure dependent term in it as it involves the lattice electrons. Because of the "powdery" structure of the evaporated bismuth oxide film little change is expected in the extra atomic relaxation energy and hence chemical shifts would be small.

### 9.2.3 Results and Discussion of the Energy Losses of Bismuth Oxide

The energy losses were recorded with 300 eV and 500 eV primary electrons from an AES characterised, freshly evaporated, bismuth oxide surface. The typical spectra observed are shown in Figs. 9-10 and 9-11.

The energies of the observed losses at different primary energies are summarised in Table 9-6 and the mean values obtained. There appears to be only one previous measurement of the characteristic losses of  $\text{Bi}_2\text{O}_3$ , as far as we could discover, and this was by Wehenkel

$\frac{dN}{dE}$  Spectra,  $I_p = 2.8 \mu A$   
 Mod. 2V Pk-pk.  
 TimeConst. 1Sec.

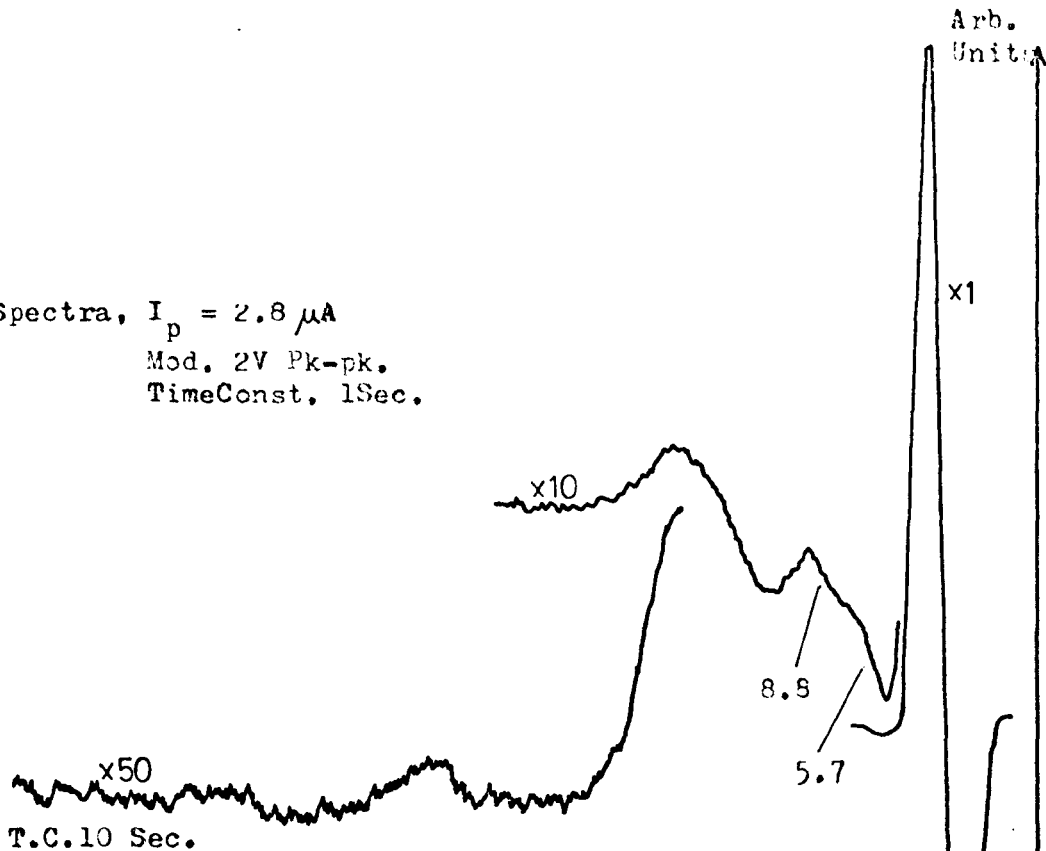
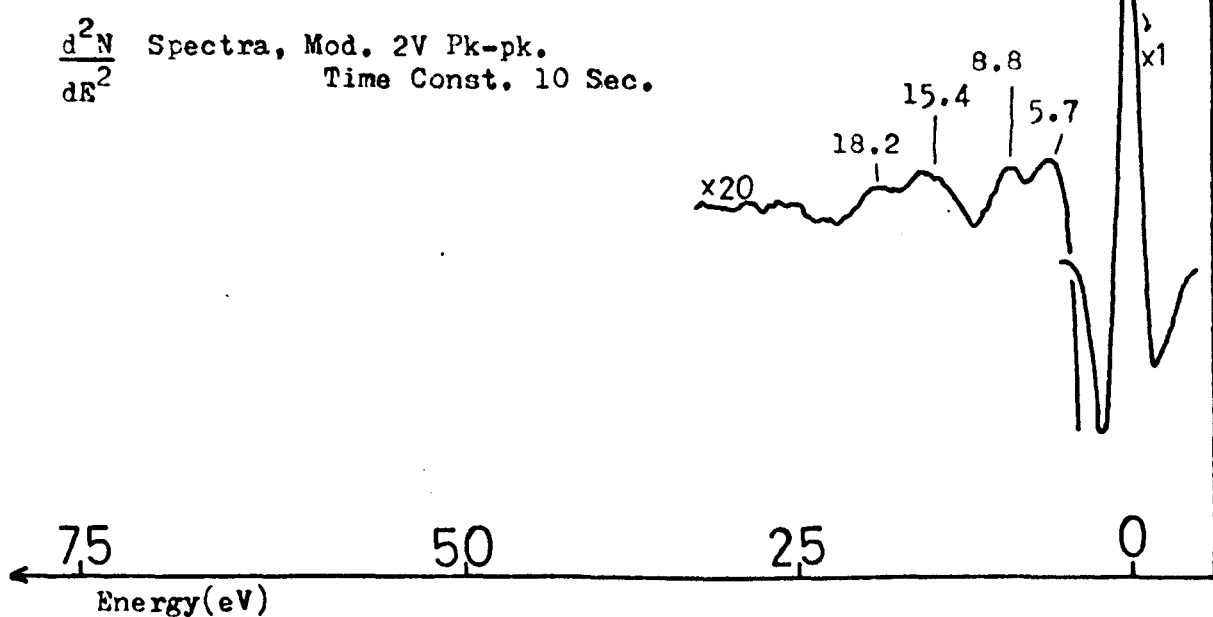


Fig.9-10. Energy Loss Spectra Of Bismuth Oxide  
 Excited With 300eV Electrons.

$\frac{d^2N}{dE^2}$  Spectra, Mod. 2V Pk-pk.  
 Time Const. 10 Sec.



Arb.  
Units

$\frac{dN}{dE}$  Spectra,  $I_p = 7.6 \mu A$   
Mod. 3V Pk-pk.  
Time Const. 1 Sec.

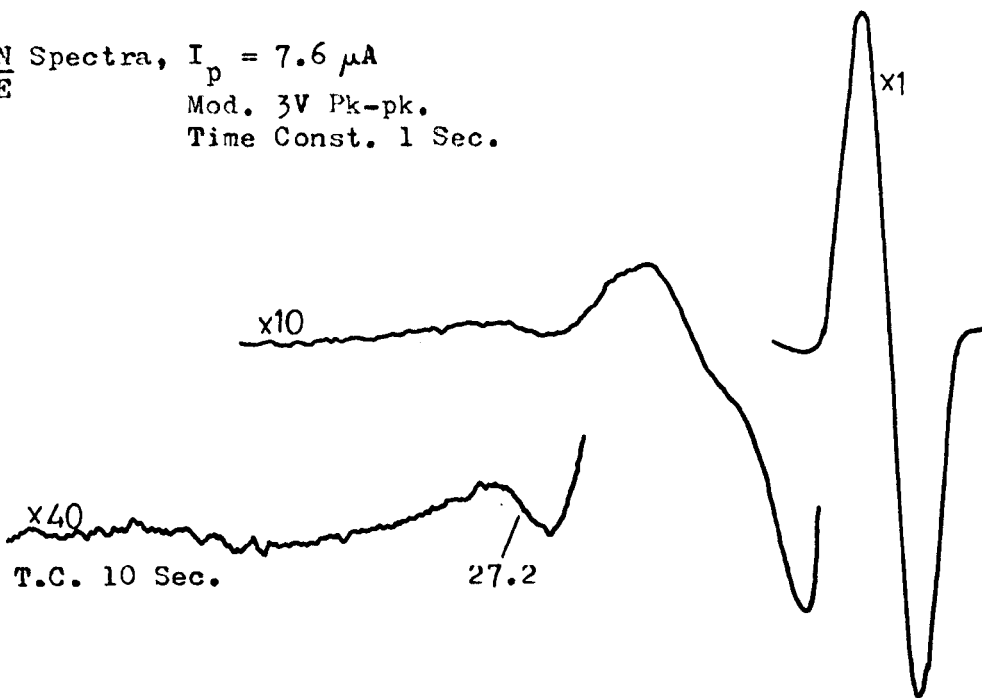
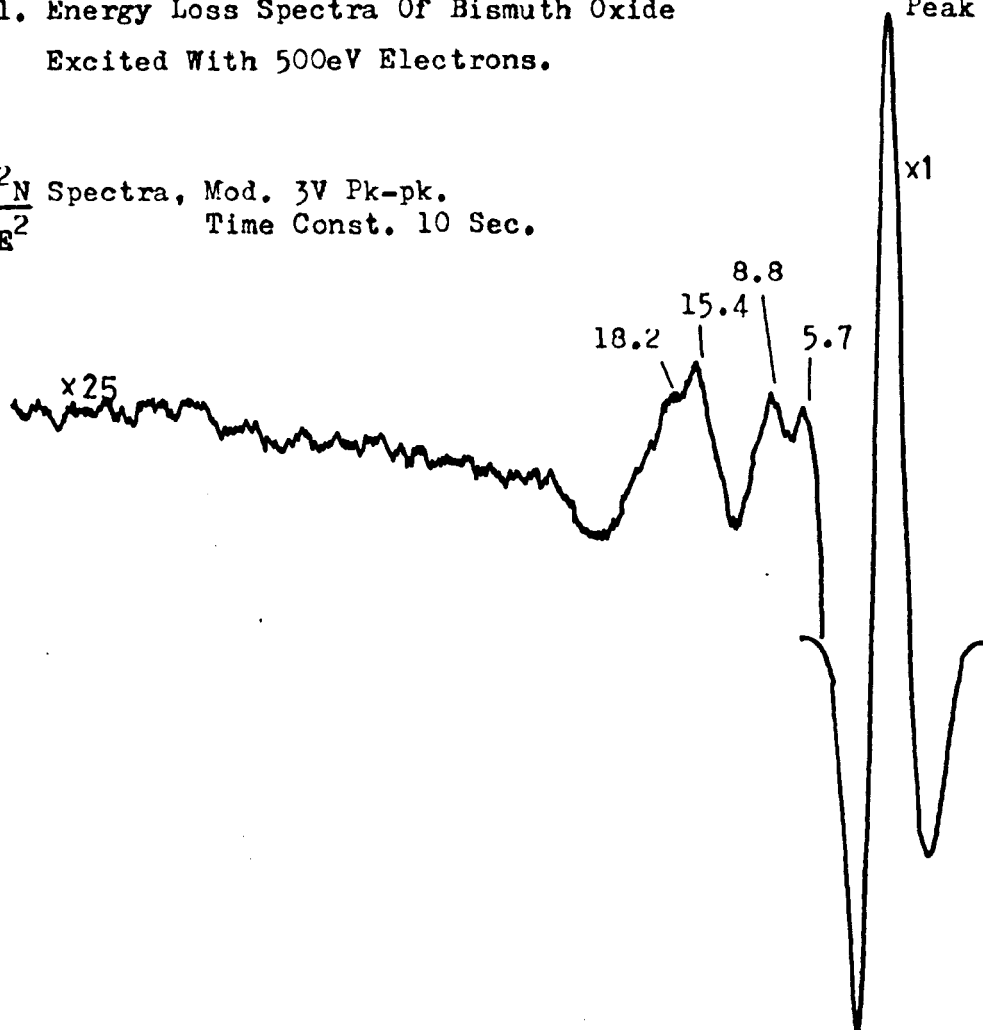


Fig.9-11. Energy Loss Spectra Of Bismuth Oxide  
Excited With 500eV Electrons.

$\frac{d^2N}{dE^2}$  Spectra, Mod. 3V Pk-pk.  
Time Const. 10 Sec.



75  
50  
25  
0  
Energy (eV)

TABLE 9-6

ENERGIES OF LOSSES OBSERVED FROM  $\text{Bi}_2\text{O}_3$

Primary Electron Energy (eV)	Analyser Operation Mode	Observed Losses (eV)				
300	$\frac{d^2N}{dE^2}$	5.0	8.9	15.1		
300	"	5.8	9.0	15.6	19.1	
500	"	6.2	8.5	14.3	17.2	27.8
500	"		8.9	16.0	18.4	28.2
500	$\frac{dN}{dE}$		8.6	16.7		27.1
500	"		8.9	14.9		25.6
Mean Value		5.7	8.8	15.4	18.2	27.2
		- 0.2	$\pm 0.2$	$\pm 0.5$		$\pm 1$

TABLE 9-7

ASSIGNMENT OF THE CHARACTERISTIC LOSSES OF  $\text{Bi}_2\text{O}_3$

Present Work (eV)	Wehenkel (1974) 198	Assignment
5.7		O ( $L_{2/3}$ ) Bi ( $P_1$ ) $\rightarrow$ Fermi level
8.8		SP ?
15.4	11	VP of Bi
18.2	18.5	VP of $\text{Bi}_2\text{O}_3$
27.2	29	Bi ( $O_{4/5}$ ) $\rightarrow$ Fermi level
		O ( $L_1$ ) $\rightarrow$ Fermi level

et al (1974)<sup>198</sup>. Our results are compared with this author's work in Table 9-7. Wehenkel et al prepared his bismuth oxide film by heating bismuth samples in humid air and his results were obtained by the transmission of high energy electrons.

On the basis of the 6 outer electrons of each oxygen atom and the 5 outer electrons of each bismuth atom contributing to the valence band of bismuth oxide (28 electrons per molecule), a plasmon energy of 19.6 eV can be calculated for free-electrons like oscillations of these electrons. Thus the peak observed at 18.2 eV is identified as a volume plasmon loss, although this is difficult to resolve on the high energy side of the 15.4 eV loss.

The 15.4 eV peak is identified as the volume plasmon loss of bismuth (identified at 15.5 eV in elemental Bi). The strong presence of this loss indicates that possibly a bismuth phase exists in the evaporated thin film. No change in the intensity of this loss could be observed with time of electron beam exposure so that the presence of the bismuth is probably due to evaporation from the platinum boat and not due to a dissociation of the bismuth oxide thin film by the primary electron beam.

The energy loss at 8.8 eV is tentatively identified as a surface plasmon oscillation although it is at a much lower energy than the predicted surface plasmon energy of bismuth ( $\approx 11$  eV) or bismuth oxide ( $\approx 12.9$  eV). No reason can be suggested why the plasmon energy should be lowered.

The 5.7 eV loss and the 27.2 eV loss are identified as excitations to empty states near the Fermi level of the material. The oxygen  $L_{2/3}$  electrons and the bismuth  $P_1$  electrons have a binding energy of 7-8 eV so that the 5.7 eV loss is identified with the excitation of these electrons and similarly the 27.2 loss is identified as the excitation of the bismuth  $O_{4/5}$  electron with a possible additional contribution due to

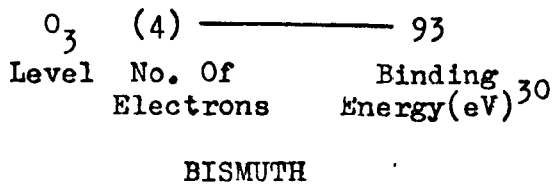
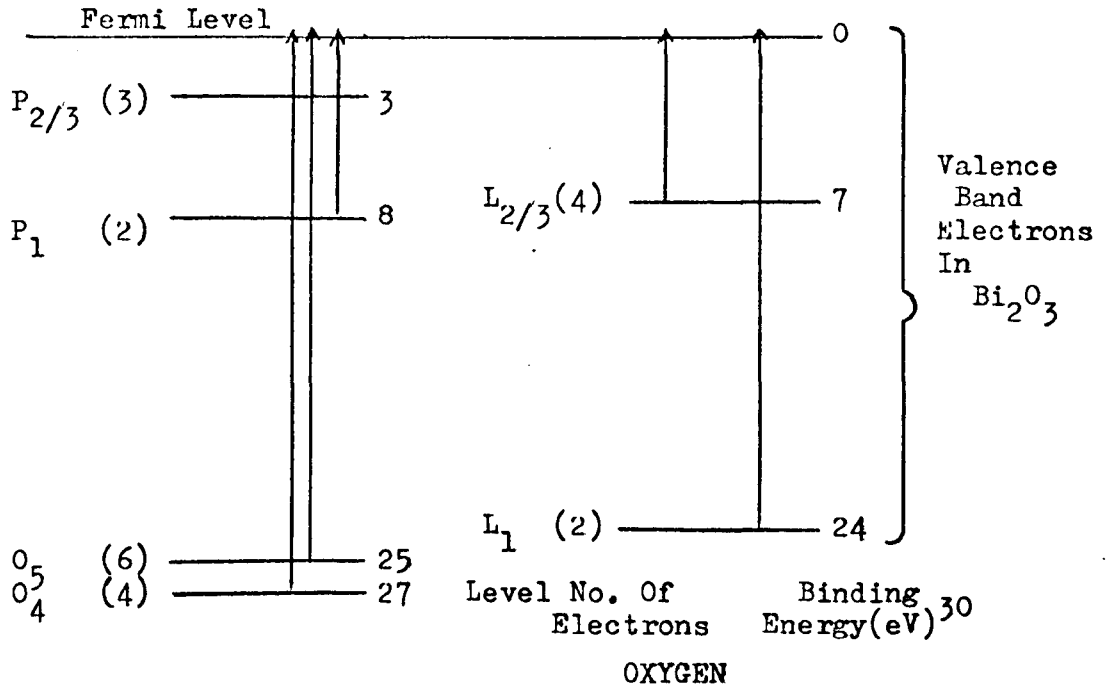


Fig.9-12. The Outer Electronic Levels Of Bismuth And Oxygen Showing Possible Characteristic Losses.

the oxygen  $L_1$  electrons being excited, see Fig. 9-12. The assignments of the  $\text{Bi}_2\text{O}_3$  losses are summarised in Table 9-7.

### 9.3 Summary

In this chapter the Auger spectra characteristic of bismuth and bismuth oxide have been studied in the energy range 0 - 550 eV. The energies of the peaks were determined and transitions assigned to them. In the Auger spectrum of bismuth, previously unreported, fine structure in the main peak ( $\approx 100$  eV) was resolved. This fine structure becomes smeared out in the bismuth Auger peaks from  $\text{Bi}_2\text{O}_3$ . No chemical shifts of the bismuth Auger peaks could be identified when they were detected from the oxide surface, although some cross transitions (or inter-atomic peaks) involving both bismuth and oxygen energy levels were thought to be detected.

The characteristic energy losses of these materials were also obtained but the assignments of the observed losses from bismuth and bismuth oxide are somewhat tentative, partly due to the absence of any corroborative data from optical measurements. Nevertheless, free-electron like volume plasmon oscillations of the valence electrons can be identified in both these materials as well as excitations of bound electrons to states near the Fermi level.

## CHAPTER 10

### GENERAL CONCLUSIONS AND SUGGESTIONS FOR FURTHER WORK

In this thesis the main conclusions about each material have been summarized at the end of each chapter. In this final chapter an overall picture of the work is presented together with suggestions for future studies.

In Chapter 4 the design and construction of a cylindrical mirror type of Auger Spectrometer was described and this double pass analyser was shown to operate successfully with an energy resolution of 0.7 - 0.8%. It was shown that the instrument can be operated to yield an output which is proportional to  $N(E)$ ,  $\frac{dN(E)}{dE}$  or  $\frac{d^2N(E)}{dE^2}$ , where  $N(E)$  is the secondary electron emission spectrum. Although the instrument can continue to yield many useful results in its present form, two modifications are suggested which may further improve its performance:-

(i) The size of the central aperture can be reduced from its present value of 2mm. to say 1mm. The size of this sperture effectively determines the source size for the second stage of the instrument and hence the resolution, so that a reduction in the size of the central aperture will result in an improvement in resolution, although some loss of transmission may occur.

(ii) The incorporation of retarding grids at the entrance of the analyser could lead to significant improvements. This type of instrument which has recently become commercially available from P.E.I., would then consist of three energy analysers in series - one hemispherical retarding grid system and two cylindrical mirror analysers. The electrons emitted from the target are first accelerated to higher or lower energies by the retarding grids which are concentric with the source point. The energy with which they are injected into the double pass CMA is thus

controlled to yield the desired energy resolution  $\Delta E$ . Thus Auger peaks at different energies can be recorded with a constant energy resolution and a constant electron multiplier gain; (which is known to vary slightly with energy). This will be a considerable advantage in quantitative AES when Auger peak heights at different energies need to be compared.

The apparatus constructed was used to study the detailed Auger spectra of four elements Au, Mo, Sb and Bi, the peaks from each element were identified and transitions assigned to them. A common feature of all the spectra studied was the influence of Coster-Kronig transitions enhancing the vacancy distribution in the higher subshells thus increasing the relative intensity of the Auger peaks involving these sub-shells. In the peaks identified as Auger transitions, with at least one final state hole in the valence band, no valence band density of occupied states effect could be detected. The peaks identified as involving the valence band, such as the  $M_{4/5}VV$  peak of Mo, were observed to be of sufficiently narrow width as to have the appearance of quasi-atomic Auger transitions instead of displaying the solid state influences expected.

It would be useful to study an element eg. silicon in whose Auger spectrum valence band effects have already been identified. Elements having a strong low energy peak involving the valence band (eg.  $L_{2/3}VV$  peak of Si at 91 eV) can be particularly well investigated because of the good energy resolution of the instrument at these low energies. Fine structure similar to that observed in the main bismuth ( $Z = 83$ ) peak is also expected in the main lead ( $Z = 82$ ) and thallium ( $Z = 81$ ) peaks and this may be worth investigating particularly as it has not been reported in the literature. There is also the possibility of performing adsorption studies similar to the one performed on

molybdenum.

The Auger spectra of three compounds  $\text{Sb}_2\text{O}_3$ ,  $\text{Sb}_2\text{S}_3$ , and  $\text{Bi}_2\text{O}_3$  were studied and some chemical effects identified. The antimony Auger peaks detected from an antimony oxide surface were shifted to lower energies and some of this shift was identified as due to a lowering of the binding energies of the core electrons involved and the remainder ( $\approx 5$  eV) as a reduction in the extra-atomic relaxation energy of the antimony due to the chemical combination with oxygen. No chemical shift of the metallic Auger peaks could be detected from the other two compounds because of surface charging effects on the antimony sulphide and possibly poor structure of the bismuth oxide film although cross-transitions were identified in the  $\text{Bi}_2\text{O}_3$  Auger spectrum. Further work on these compounds could be attempted by evaporating the thin films on to different substrate materials and an alternative method to prepare  $\text{Bi}_2\text{O}_3$ , by heating a bismuth target in a pure oxygen atmosphere, may be worth investigating.

The characteristic energy losses of the various elements and compounds were obtained and free-electron like plasmon oscillations of the valence band electrons identified, as summarised in Table 10-1. Excitation of core level electrons to empty states near the Fermi level were also identified. Further characterisation work on other materials is possible with the apparatus, using AES to specify the surface under investigation, and another line of enquiry worth pursuing may be to obtain the dielectric response of the material from the characteristic energy loss measurements. The energy loss measurements carried out by transmission of high energy electrons have been used to determine the energy loss function  $\text{Im} \left( \frac{-1}{\epsilon} \right)$  from which the real and imaginary parts of the dielectric constant  $\epsilon_1$ ,  $\epsilon_2$  have been determined for a material<sup>205</sup>. It would be useful if  $\epsilon_1$  and  $\epsilon_2$  could be similarly

TABLE 10-1

<u>Material</u>	<u>Calculated volume plasmon</u>		<u>Observed Volume Plasmon</u>
	<u>Energy of VB electrons (eV)</u>		<u>Energy (eV)</u>
Au	29.7	(5d <sup>10</sup> + 6s')	25.1
Mo	21.9	(4d <sup>5</sup> + 5s')	22.6
Sb	15.1	(5s <sup>2</sup> + 5p <sup>3</sup> )	15.8
Bi	13.9	(6s <sup>2</sup> + 6p <sup>3</sup> )	15.5
Sb <sub>2</sub> O <sub>3</sub>	27.4	(Sb (5s <sup>2</sup> + 5p <sup>3</sup> ) 2 + O(2s <sup>2</sup> + 2p <sup>4</sup> ) 3)	20.2
Sb <sub>2</sub> S <sub>3</sub>	17.8	(Sb (5s <sup>2</sup> + 5p <sup>3</sup> ) 2 + O(2s <sup>2</sup> + 2p <sup>4</sup> ) 3)	18.4
Bi <sub>2</sub> O <sub>3</sub>	19.6	(Bi (6s <sup>2</sup> + 6p <sup>3</sup> ) 2 + O(2s <sup>2</sup> + 2p <sup>4</sup> ) 3)	18.2

determined over a wide energy range from the reflection energy loss measurements.

The characteristic losses of chromium and tungsten may be worth investigating to compare with the results obtained on molybdenum in this thesis. Of particular interest would be the possible detection of the surface plasmon and a second type of volume plasmon as was identified for molybdenum.

By detecting the volume plasmon of a material in the characteristic energy loss measurements the presence of a phase of that material can be identified as was shown by detecting the Sb volume plasmon in the loss measurements on antimony oxide. In this respect CELS may complement the results obtained from AES and it is suggested that whenever AES studies are performed on a surface containing a number of elements CELS studies also be performed and these may yield additional useful information.

It is suggested that an electron gun capable of operating at lower voltages (50 - 100 eV) with high beam currents (up to 10 $\mu$ A) be incorporated into the apparatus to carry out characteristic energy loss measurements. The present gun did not function well at these low energies. The advantages of a low energy gun are that it is more surface sensitive, the analyser is operating at a much better energy resolution and the excitation of multiple plasmon features does not dominate the loss spectrum, see Rowe et al (1975)<sup>99</sup>.

In summary the work presented in this thesis has described the successful design and construction of a suitable spectrometer operating in ultra high vacuum environment and capable of investigating solid surfaces. This instrument was used to study a number of materials and the Auger spectra and characteristic energy losses of Au, Mo, Sb, Sb<sub>2</sub>O<sub>3</sub>, Sb<sub>2</sub>S<sub>3</sub>, Bi and Bi<sub>2</sub>O<sub>3</sub> have been presented. An adsorption study was also performed and the thesis concludes with suggestions for future work.

## REFERENCES

- 1 Tamm, Phys. Z. SU., 1, 733, (1932).
- 2 V. Heine, Surf. Sci., 2, 1-7, (1964).
- 3 Science Research Council Summer School on Surface Science, Warwick University, (July, 1974).
- 4 Vacuum Generators Ltd., Charlwoods Road, East Grinstead, Sussex, RH19 2HR, England.
- 5 L. A. Harris, J. of Appl. Phys., 39 (3), 1419, (1968).
- 6 T. E. Gallon, J. A. D. Matthew, Reviews of Physics in Technology, 3, 18, (1972).
7. K. Seigbahn et al, "ESCA - Atomic, Molecular and Solid State Structure Studied by means of Electron Spectroscopy", Almquist and Wicksell, Upsalla, Sweden, (1967).
- 8 E. W. Muller, Z. Phys., 131, 136, (1951).
- 9 E. W. Muller, T.T. Tsong, "Field Ion Microscopy" Elsevier, New York, (1969).
- 10 R. L. Park, J. E. Houston, D. G. Shreiner, Rev. Sci. Instr., 41, 1810, (1970).
11. R. L. Park, Surf. Sci., 48, 80, (1975).
- 12 H. D. Hagstrum, Phys. Rev., 150, 495, (1966).
- 13 C. J. Powell, Surf. Sci., 44, 29, (1974).
- 14 P. Auger, J. Phys. Radium, 6, 205, (1925).
- 15 E.H.S. Burhop, "Auger and other Radiationless Transitions" (Cambridge monographs on Physics), (1952).
- 16 J. Lander, Phys. Rev., 91, 1382, (1953).
- 17 L. A. Harris, J. Appl. Phys., 39, 1428, (1968).
- 18 R. E. Weber, W. T. Peria, J. Appl. Phys., 38, 4355, (1967).
- 19 P. W. Palmberg, P2901 - 2918 of "Structure and Chemistry of Solid Surfaces". Ed. G. A. Somorjai, Wiley, New York, (1969).

- 20 P. W. Palmberg, G. K. Bohn, J. C. Tracy, *Appl. Phys. Lett.*, 15, 254, (1969).
- 21 C. C. Chang, *Surf. Sci.*, 25, 53, (1971).
- 22 J. C. Tracy, 1972 Nato Summer School, Gent, Belgium.
- 23 E. N. Sickafus, *J. Vac. Sci. Technol.*, 11(1), 299, (1974).
- 24 D. F. Stein, *J. Vac. Sci., Technol.*, 12(1), 268, (1975).
- 25 A. Barrie, *J. Elec. Spec.*, 7, 75, (1975).
- 26 J. J. Mackey et al, *J. Phys. B* , 7(16), L447, (1974).
- 27 L. Viel et al, *Surf. Sci.*, 54, 635, (1976).
- 28 R. G. Musket et al, *Appl. Phys. Lett.*, 20, 455, (1972).
- 29 K. O. Groeneve, *Vacuum*, 25(1), 9, (1975).
- 30 J. A. Beardon, A. F. Burr, *Rev. Mod. Phys.*, 39, 125, (1967).
- 31 K. D. Servier, "Low Energy Electron Spectrometry", Wiley, (1972).
- 32 M. E. Packer, J. M. Wilson, "Auger Transitions" Unwin Press Ltd., (1973).
- 33 I. Bergstrom, R. D. Hill, *Arbiv. Fysik*, 8, 21, (1954).
- 34 M. F. Chung, L. H. Jenkins, *Surf. Sci.*, 22, 479, (1970).
- 35 W. A. Coghlan, R. E. Clausing, *Surf. Sci.*, 33, 411, (1972).
- 36 W. A. Coghlan, R. E. Clausing, "A Catalogue of Calculated Auger transitions for the Elements". Oak Ridge National Laboratory, Oak Ridge, Tennessee, 37830.
- 37 D. A. Shirley, *Phys. Rev.*, A7, 1520, (1973).
- 38 E. D. Roberts, P. Weightman, C. E. Johnson, *J. Phys. C*, 8 (8), 1301, (1975).
- 39 E. D. Roberts, P. Weightman, C. E. Johnson, *J. Phys. C*, 8 (14), 2336, (1975).
- 40 J. A. D. Matthews, *Surf. Sci.*, 40, 451, (1973).
- 41 E. J. McGuire, *Phys. Rev.*, A3, 1801, (1971).
- 42 E. J. McGuire, *Phys. Rev.*, A3, 1587, (1971).

- 43 E. J. McGuire, Phys. Rev., A5, 1043, (1972).
- 44 J. C. Tracy, Surf. Sci., 38, 265, (1973).
- 45 J. H. Neave, C. T. Foxon, B. A. Joyce, Surf. Sci., 29,411, (1972).
- 46 T. Gallon, J. Phys. D., 5, 822, (1972).
- 47 F. Meyer, J. J. Vrakking, Surf. Sci., 33, 271, (1972).
- 48 M. L. Tarn, G. K. Wehner, J. Appl. Phys., 44, 1534, (1973).
- 49 F. Meyer, J. J. Vrakking, Surf. Sci., 47, 50, (1975).
- 50 P. W. Plamberg, Appl. Phys. Lett., 13, 183, (1968).
- 51 M. Suleman, Ph. D. Thesis, Physics Dept., University of Keele, (1971).
- 52 P. Harris, Ph. D. Thesis, Physics Dept., University of Keele, (1972).
- 53 B. Wright, Ph.D. Thesis, Physics Dept., University of Keele, (1974).
- 54 B. Wright, E. B. Pattinson, J. Phys. F, 3, 1237, (1973).
- 55 B. D. Powell, D. P. Woodruff, B. W. Griffiths, J. Phys. E, 8, 548, (1975).
- 56 Physical Electronics Industries, 7317 South Washington Avenue, Edina, Minnesota 55435, U.S.A.
- 57 R. Bouwman et al, Vacuum, 23(5), 169, (1972).
- 58 H. J. Mathieu, D. Landolt, Surf. Sci., 53, 228, (1975).
- 59 J. V. Florio, W. D. Robertson, Surf. Sci., 18, 398, (1969).
- 60 R. G. Musket, J. Ferrante, J. Vac. Sci. Technol., 7, 14, (1970).
- 61 D. C. Jackson, T. E. Gallon, A. Chambers, Surf. Sci., 36, 381, (1973).
- 62 R. E. Kirby, D. Lichman, Surf. Sci., 41, 447, (1974).
- 63 F. J. Szalkowski, G. A. Somorjai, J. Chem. Phys., 61(5), 2064, (1974).
- 64 T. W. Haas, J. T. Grant, G. J. Dooley, J. Appl. Phys., 43(4), 1853, (1972).
- 65 J. M. Baker et al, J. Vac. Sci. Technol., 9(2), 792, (1972).

- 66 A. Barrie, *J. Elec. Spectro.*, 7, 1, (1975).
- 67 J. S. Soloman, W. L. Baun, *Surf. Sci.*, 51, 228, (1975).
- 68 P. H. Holloway, *Surf. Sci.*, 54, 506, (1976).
- 69 G. W. Simmons, D. J. Dwyer, *Surf. Sci.* 48, 375, (1975).
- 70 K. L. Wang, A. Joshi, *J. Vac. Sci. Technol.*, 12, 927, (1975).
- 71 M. Seo et al, *Surf. Sci.*, 50, 541, (1975).
- 72 S. P. Kowalozyk et al, *Phys. Rev.*, B8, 2387, (1973).
- 73 T. Gallon, J. A. D. Matthews, *Phys. Stat. Sol.*, 41, 343, (1970).
- 74 A. P. Jansen et al, *Surf. Sci.*, 47(1), 45, (1975).
- 75 A. P. Jansen et al, *Surf. Sci.*, 49, 143, (1975).
- 76 P. H. Citrin, *J. Elec. Spectro.*, 5, 273, (1974).
- 77 F. Meyer, J. J. Vrakking, *Surf. Sci.*, 45, 409, (1974).
- 78 E. N. Sickafus, *Phys. Rev.*, B7, 5100, (1973).
- 79 G. F. Amelio, *Surf. Sci.*, 22, 301, (1970).
- 80 M. Salmeron, A. M. Baro, *Surf. Sci.*, 49, 356, (1975).
- 81 P. J. Bassett, *Surf. Sci.*, 35, 63, (1974).
- 82 R. W. Joyner, M. Wyn Roberts, *J. Chem. S.*, F1, 69(7), 1242, (1973).
- 83 M. Salmeron, A. M. Baro, J. M. Rojo, *J. Phys. F. (G.B.)* 5(4), 826, (1975).
- 84 N. A. Gjostein, N. G. Chauka, *J. Testing and Evaluation*, 1(3), 183, (1973).
- 85 D. F. Stein, *J. Vac. Sci. Technol.*, 12(1), 275, (1975).
- 86 S. W. Pepper, *J. Appl. Phys.*, 45(7), 2947, (1974).
- 87 A. Van Oostrom, L. A. West, *J. Vac. Sci. Technol.*, 13(1), 224, (1976).
- 88 J. R. Noonan et al, *J. Vac. Sci. Technol*, 13(1), 183, (1976).
- 89 L. McDonnell, D. P. Woodruff, B. W. Holland, *Surf. Sci.*, 51, 249, (1975).
- 90 M. F. Moyaux, "Solid State Plasmas". (London, Pion) (1970).

- 91 H. Raether, Springer Tracts in Modern Physics, 38, 84, (1965).
- 92 D. Pines, "Elementary Excitations in Solids", Benjamin, (1963).
- 93 J. J. Quinn, Phys. Rev., 126(4), 1453, (1962).
- 94 E. Rudberg, J. C. Slater, Phys. Rev., 129(4), 1550, (1964).
- 95 H. R. Phillip, H. Ehrenreich, Phys. Rev., 129 (4), 1550, (1964).
- 96 R. H. Ritchie, Phys. Rev., 106, 874, (1957).
- 97 E. A. Stern, R. A. Ferrell, Phys. Rev., 120, 130, (1960).
- 98 R. H. Ritchie, Surf. Sci., 34, 1, (1973).
- 99 J. E. Rowe, Surf. Sci., 48, 44, (1975).
- 100 A. J. Braudmeier, D. G. Hall, Surf. Sci., 48, 44, (1975).
- 101 H. Raether, Surf. Sci., 8, 233, (1967).
- 102 J. E. Rowe, H. Ibach, H. Froitzheim, Surf. Sci., 52(2), 281, (1975).
- 103 J. L. Powell, Proc. Phys. Soc., 79, 119, (1962).
- 104 B. M. Hartley, J. B. Swan, Aus. J. Phys., 23, 655, (1970).
- 105 E. A. Bakalin et al, Sov. Phys. - Solid State, 13(10), 2536, (1972).
- 106 M. D. Rechtin, B. L. Averbach, Phys. Rev., B9(8), 3464, (1974).
- 107 D. A. Porter, P. Doig, J. W. Edington, Philos. Mag., 29, 437, (1974).
- 108 P. E. Best, Proc. Phys. Soc., 79, 133, (1962).
- 109 L. Marton, L.B. Leder, Phys. Rev., 94, 203, (1954).
- 110 H. Watanabe, J. Phys. Soc. Japan, 9, 1035, (1954).
- 111 G. Mollenstedt, Optik, 5, 499, (1949).
- 112 T. T. Katonak, R. L. Hengehold, J. Appl. Phys., 46(10), 4294, (1975).
- 113 R. L. Hengehold, F. L. Pedrotti, J. Appl. Phys., 46(12), 5202, (1975).
- 114 H. Luth, G. J. Russell, Surf. Sci., 45, 329, (1974).

- 115 R. Ludeke, L. Esaki, Phys. Rev. Lett., 33(11), 653, (1974).
- 116 J. E. Rowe, Sol. St. Commun., 15, 1505, (1974).
- 117 Ferranti, Gem Mill, Chadderton, Oldham, Lancs.
- 118 Associated Electrical Industries (A.E.I.), P.O. Box 1, Edinburgh Way, Harlow, Essex, England.
- 119 20th Century Electronics Ltd., King Henry's Drive, New Addington, Croydon, CR9 OB6, England.
- 120 Perfection Mica Company, 740 Thomas Drive, Bensenville, Ill. 60106, U.S.A.
- 121 Superior Electronics Ltd., U.S.A.
- 122 Nuclear Products Co., 15635 Saranac Road, Cleveland 10, Ohio, U.S.A.
- 123 The assistance of Mr. W.R.C. Stewert is acknowledged in the construction of this device. Physics Dept., University of Keele, Staffordshire.
- 124 R. K. Fitch, T. Mulvey, W. J. Thatcher, A. H. McIlraith, J. Phys. D. Appl. Phys., 3, 1399, (1970).
- 125 R. K. Fitch, T. Mulvey, W. J. Thatcher, A. H. McIlraith, J. Phys. D, Appl. Phys., 4, 553, (1971).
- 126 E. Blauth, Z Physik, 147, 288, (1957).
- 127 H. Z. Sar-El, Rev. Sci. Instr., 38(9), 1210, (1967).
- 128 V. V. Zashkvara, M. I. Korsunskii, O. S. Kosmachev, Sov. Phys. - Technical Phys., 11(1), 96, (1966).
- 129 Mullard Ltd., Mullard House, Torrington Place, London, WC1E 7HD.
- 130 Brookdeal Electronics Ltd., Market Street, Bracknell, Berks, RG12 1JU, England.
- 131 M. P. Seah, Reprint, N.P.L., Teddington, U.K.
- 132 D. L. Arnott, J. A. Ramsey, Vacuum, 22(9), 355, (1972).
- 133 H. E. Bishop, I. P. Coad, J. C. Riviere, J. Electron. Spec., 1, 389, (1972/3).

- 134 F. Meyer, J. J. Vrakking, Surf. Sci., 45, 409, (1974).
- 135 D. F. Stein, A. Joshi, R. P. Laforce, Transactions of the American Society of Metals, 62, 776, (1969).
- 136 G. Betz et al, J. Appl. Phys., 45(12), 5312, (1974).
- 137 J. P. Coad, J. G. Cunningham, J. Elec. Spec., 3, 435, (1974).
- 138 Grade A diamond paste, supplied by the Struers Company, Copenhagen, Denmark.
- 139 John Cashmores Ltd., Upper Brook Street, Walsall, Staffordshire.
- 140 "Handbook of Auger Electron Spectroscopy" by P. W. Palmberg et al Published by Physical Electronics Industries, 7317, South Washington Avenue, Edina, Minnesota, 55435, U.S.A.
- 141 J. P. Coad, J. C. Riviere, U.K.A.E.A. Research report AERE - R6589 Harwell, (1970).
- 142 K. Ueda, R. Shimizu, Surf. Sci., 43, 77, (1974).
- 143 T. W. Haas, J. T. Grant, G. J. Dooley, Phys. Rev. B, 1, 1449, (1970).
- 144 D. G. Fedak, J. V. Florio, W. D. Robertson, Paper 74 in "Structure and Chemistry of Solid Surfaces", Ed. G. A. Somorjai, (Wiley, New York, 1969).
- 145 P. W. Palmberg, T. N. Rhodin, J. Appl. Phys., 39, 2425, (1970).
- 146 Johnson Matthey Metals Ltd., 81 Hatton Garden, London, EC1P 1AE.
- 147 I. Lindau, L. Wilson, Phys. Lett., 42A, 279, (1972).
- 148 J. Freeouf, M. Erbudak, D. E. Eastman, Solid St. Commun., 13, 771-3, (1973).
- 149 P. J. Bassett, Surf. Sci., 35, 63, (1973).
- 150 J. L. Robins, Proc. Phys. Soc. (Lond.), 78, 1177, (1961).
- 151 C. J. Powell, Phys. Rev., 175(3), 972, (1968).
- 152 B. R. Cooper, H. Ehrenreich, H. R. Phillip, Phys. Rev., 138, A494, (1965).

- 153 L. R. Canfield, G. Hass, W. R. Hunter, *J. Phys.*, 25, 124, (1964).
- 154 G. J. Barnes et al, *J. Electrochemical Soc.*, 119(6), 684, (1972).
- 155 S. Thomas, T. W. Haas, *Surf. Sci.*, 28, 632, (1971).
- 156 S. Thomas, T. W. Haas, *J. Vac. Sci., Technol.*, 9 (2), 840, (1972).
- 157 A. G. Jackson, M. P. Hooker, *Surf. Sci.*, 28, 373, (1971).
- 158 A. G. Jackson, M. P. Hooker, *Surf. Sci.*, 27, 197 (1971).
- 159 T. Kawai, K. Kunimori, T. Kondo, T. Onishi, K. Tamaru, *Phys. Rev. Lett.*, 33(9), 533, (1974).
- 160 K. Kunimori et al, *Surf. Sci.*, 54, 525, (1976).
- 161 R. M. Lambert, J. W. Linnett, J. A. Schwarz, *Surf. Sci.*, 26, 372, (1974).
- 162 M. P. Hooker, J. T. Grant, *J. Vac. Sci. Technol.*, 12(1), 325, (1975).
- 163 T. W. Haas, J. T. Grant, G. J. Dooley, *J. Appl. Phys.*, 43(4), 1853, (1972).
- 164 Murex Ltd., Rainham, Essex.
- 165 T. Murotani et al, *Proc. 2nd. International Conf. on Solid Surfaces*, *Jap. J. Appl. Phys. Suppl. 2 Pt. 2*, (1974).
- 166 R. Ducros et al, *Surf. Sci.*, 54, 513, (1976).
- 167 K. Kunimori et al, *Surf. Sci.*, 46, 567, (1974).
- 168 M. P. Hooker, J. T. Grant, T. W. Haas, *J. Vac. Sci. Technol.*, 12(1), 325, (1975).
- 169 S. Thomas, E. B. Pattinson, *J. of Phys. D*, 3, 1469, (1970).
- 170 R. M. Lambert, J. W. Linnett, J. A. Schwarz, *Surf. Sci.*, 26, 572, (1972).
- 171 T. Miura, Y. Tuzi, *Proc. 2nd. International Conf. on Solid Surfaces*, *Jap. J. Appl. Phys., Suppl. 2 Pt. 2*, 85, (1974).
- 172 H. E. Bishop, J. C. Riviere, *J. Appl. Phys.*, 40, 1740, (1969).

- 173 M. Gryzinski, Phys. Rev., 115, 374, (1959).
- 174 M. Gryzinski, Phys. Rev., 138, 305, (1965).
- 175 R. M. Lambert, J. W. Linnett, J. A. Schwarz, Surf. Sci., 26, 572, (1971).
- 176 K. Hayek et al, Surf. Sci., 10, 429, (1968).
- 177 A. M. Morgan, D. A. King, Surf. Sci., 23, 259, (1970).
- 178 V. V. Zashkvara et al, Sov. Phys. - Solid State, 11(12), 30383, (1970).
- 179 V. V. Zashkvara, V.S. Red'kin, Sov. Phys. - Solid State, 14(9), 2410, (1973).
- 180 G. A. Harrower, Phys. Rev., 102, 340, (1956).
- 181 T. Kawai, K. Kunimori, T. Kondow, T. Onishi, K. Tamaru, J. Chem. Soc., Faraday Trans., I(G.B.), 70(1), 137, (1974).
- 182 D. W. Juenker, L. J. Le Blanc, C. R. Martin, J. of Opt. Soc. of America, 58(2), 164, (1968).
- 183 J. H. Weaver, D. W. Lynch, C. G. Olson, Phys. Rev. B, 10(2), 501, (1974).
- 184 I. Petroff, C. R. Viswanathan, Phys. Rev. B4, 799, (1971).
- 185 J. Lecante, International Symposium on Adsorption Desorption phenomenon, April 1971, Florence, Italy.
- 186 E. A. Taft, H. R. Phillip, Phys. Rev., A138, 197, (1965).
- 187 J. M. Burkstrand, F. M. Propst, T. L. Cooper, D. E. Edwards, Surf. Sci., 29, 663, (1972).
- 188 C. J. Powell, Proc. Phys. Soc., 76, 593, (1960).
- 189 Metals Research Ltd., Melbourn, Royston, Herts., SG8 6EJ, U.K.
- 190 'Metals Reference Book', C. J. Smithells, Butterworths, London, (1955).
- 191 J. C. Lemonier, J. Thomas, Mme S. Robin, J. Phys. E. (G.B.), 6(6), 553, (1973).

- 192 W. P. Ellis, Surf. Sci., 41, 125, (1974).
- 193 British Drug House Ltd., range of patinal tablets suitable for vacuum deposition. Broom Road, Poole, Dorset, BH12 4NN, U.K.
- 194 T. Birchall, J.C.S. Dalton Transactions, 2003, (1975).
- 195 B. D. Powell, Surf. Sci., 57, 504, (1975).
- 196 J. N. Olsen, Appl. Phys. Lett., 24(5), 220, (1974).
- 197 Y. Ono et al, Jap. J. Appl. Phys. 12(12), 1907, (1973).
- 198 C. Wehenkel, B. Gauthe, Solid St. Commun., 15, 555, (1974).
- 199 B. Gauthe, C. Wehenkel, Phys. Lett. 39A, 171, (1972).
- 200 P. Zacharias, Opt. Comm., 8, 142, (1973).
- 201 W. R. Hunter, D. W. Angel, R. Toussey, Appl. Opt., 4, 891, (1965).
- 202 J. Toots, L. Marton, J. Opt. Soc. Am., 59, 1305, (1969).
- 203 "Handbook of physiochemical properties of the elements" Ed. G. V. Samsonov. (I.F.I./Olenum), (1968).
- 204 A. Ignatiev et al, Phys. Rev. B., 11(12), 4787, (1975).
- 205 U. Bucchner, J. Phys. C, 8(17), 2679, (1975).
- 206 M. K. Bahl et al, J. Chem. Phys., 64(1), 1210, (1976).